Indications of CP Violation in the Lepton Sector from a Combined Analysis of Neutrino and Antineutrino Data in the T2K Experiment

Thesis submitted in accordance with the requirements of the University of Liverpool for the degree of Doctor in Philosophy by Christopher Barry

October 2018

Abstract

The T2K long baseline experiment studies neutrino oscillations over a distance of 295 km, by observation of the flavour change in a ν_μ or $\bar{\nu}_\mu$ beam starting at J-PARC travelling to the 50 kt water Cherenkov detector, Super-Kamiokande. The beam can be run in either neutrino or antineutrino mode and operates with a peak energy of 0.6 GeV. The ratio of baseline to energy was designed for optimal sensitivity to oscillations at the atmospheric neutrino mass squared splitting. The beam composition is also determined 280 m from the production target and in combination with far detector the flavour change in the beam can be determined.

This thesis consists of an analysis of data from neutrino mode and antineutrino mode and the ν_e appearance, and ν_μ disappearance channels, performed using a hybrid frequentist-bayesian approach, for three active neutrino flavour oscillations in constant-density matter. Data is used from the T2K Run 1-8 which corresponds to an integrated neutrino beam exposure of 1.4734×10^{21} POT in FHC mode and 7.558×10^{20} POT in RHC mode. The four oscillation parameters $\sin^2\theta_{23}$, $\sin^2\theta_{13}$, $|\Delta m^2_{32}|(\Delta m^2_{13})$, and δ_{CP} for Normal Hierarchy (Inverted Hierarchy) are determined by a joint fit of the energy spectra for muon-like samples, and energy vs lepton angle spectra for the electron-like samples at Super-Kamiokande. The 1σ intervals for each of the parameters are, with the confidence intervals for δ_{CP} extracted using the constant $\Delta\chi^2$ method and T2K data only

$$\begin{aligned}
\delta_{\mathrm{CP}} &= -2.083\ ^{+0.932}_{-0.889} \quad (\ -1.157\ ^{+0.754}_{-0.808}) \\
\sin^2\theta_{13} &= 0.0277\ ^{+0.0053}_{-0.0047} \quad (\ 0.0331\ ^{+0.0047}_{-0.0065}) \\
\sin^2\theta_{23} &= 0.530\ ^{+0.031}_{-0.037} \quad (\ 0.530\ ^{+0.029}_{-0.034}) \\
|\Delta m^2_{32}|(\Delta m^2_{13}) &= [2.462\ ^{+0.057}_{-0.055} \quad (\ 2.436\ ^{+0.055}_{-0.053})] \times \mathrm{c}10^{-3}\,\mathrm{eV}^2.
\end{aligned}$$

Using the most precise available measurements, $[3\sigma]$ range, of $\sin^2\theta_{13} = 0.0215\,[0.0190 - 0.0240]$ $(0.0216\,[0.0190 - 0.0242])$, determined by reactor experiments, ranges for the value of δ_{CP} can be determined using the Feldman-Cousins method and are shown below including an exclusion of the CP conserving values of 0 and π,

$$\begin{aligned}
&[-2.805, -0.830] \quad 90\,\%\mathrm{CL} \\
&[-2.981, -0.600]\,([-1.531, -1.184]) \quad 2\sigma.
\end{aligned}$$

Declaration

Chapter 2 is a description of the theoretical background and experimental results in the field. This is constructed from the available literature on the topic. Chapter 3 describes the elements which compose the T2K experiment which is the source of the data analysed. Both internally and externally published documents are the source of the information in this chapter. Chapter 4 describes how the data which is used as input to my analysis was developed and validated by the T2K collaboration. Chapter 5 is a physics analysis that is my original work which uses information of chapter 4 as input. The "VALOR" analysis group was the environment in which the work was performed and was actively developed by myself, Costas Andreopolous, Andrew Chappell, Thomas Dealtry, Steve Dennis, Davide Sgalaberna, and Raj Shah.

Contents

List of Figures

List of Tables

Abbreviations

2p2h two particle two hole.

BANFF Beam And Near Detector Task Force.

BDT Boosted Decision Tree.

BeRPA Bernstein RPA.

CνB Cosmic Neutrino Background.

CC Charged Current.

CCQE Charged Current Quasi-Elastic.

ΛCDM Lambda Cold Dark Matter.

CERN European Organization for Nuclear Research, Conseil Européen pour la Recherche Nucléaire.

C.L. Confidence Level.

CUORE Cryogenic Underground Observatory for Rare Events.

CUORE-0 Cryogenic Underground Observatory for Rare Events-0.

CUORICINO CUORICINO.

CVN Convolutional Visual Network.

DIS Deep Inelastic Scattering.

DOM Digital Optical Module.

DUNE Deep Underground Neutrino Experiment.

ECal Electromagnetic Calorimeter.

ERPA Effective RPA.

ES Elastic Scattering.

EXO-200 Enriched Xenon Observatory-200.

FGD Fine Grained Detector.

FHC Forward Horn Current.

FSI Final State Interactions.

GERDA GERmanium Detector Array.

GLoBES General Long Baseline Experiment Simulator.

Hyper-K Hyper-Kamiokande.

INGRID Interactive Neutrino GRID.

IO Inverted Ordering.

J-PARC Japan Proton Accelerator Research Centre.

KamLAND Kamioka Liquid scintillator Anti-Neutrino Detector.

KATRIN Karlsruhe Tritium Neutrino Experiment.

LINAC Linear Accelerator.

LMPD Low Momentum Particle Detector.

LSND Liquid Scintillator Neutrino Detector.

MaCh3 MaCh3 Oscillation Analysis Framework.

MAJORANA MAJORANA.

MEC Meson Exchange Current.

MiniBooNE Mini Booster Neutrino Experiment.

MINOS Main Injector Neutrino Oscillation Search.

MPPC Multi Pixel Photon Counter.

MR Main Ring.

MSW Mikheyev Smirnov Wolfenstein.

MUMON Muon Monitor.

NA61/SHINE SPS Heavy Ion and Neutrino Experiment.

NC Neutral Current.

ND Near Detector.

ND280 Near Detector (at) 280m.

NN Nucleon-Nucleon.

NO Normal Ordering.

NOνA NuMI Off-axis ν_e Appearance.

PDG Particle Data Group.

PINGU Precision IceCube Next Generation Upgrade.

PMNS Pontecorvo Maki Nakagawa Sakata.

PMT Photomultiplier Tube.

POT Protons On Target.

PSD Particle Spectator Detector.

RCS Rapid-Cycling Synchrotron.

RENO Reactor Experiment for Neutrino Oscillation.

RHC Reverse Horn Current.

RPA Random Phase Approximation.

SBN Short-Baseline Neutrino.

SI Secondary Interactions.

SMRD Side Muon Range Detector.

Super-K Super-Kamiokande.

T2K Tokai to Kamioka.

ToF time of flight.

TPC Time Projection Chamber.

VALOR VALOR Oscillation Analysis Framework.

1 Introduction

The neutrino, a weakly interacting neutral particle of spin 1/2, which forms a part of the Standard Model of Particle Physics, has been a source of several surprises. The Standard Model has been very successful at describing nature, predicting: the W and Z gauge bosons, gluons, top and charm quarks, and the Higgs boson. There are also several areas where the Standard Model does not fully describe nature. In the Standard Model neutrinos are massless, however neutrino oscillation experiments have shown at least two neutrino states must be massive. The Standard Model also does not explain the observed $\mathcal{CP}$ violation in cosmology, with most of the universe observed as matter and requiring a set of three conditions to generate this asymmetry. Some details of neutrino interactions, mass, and probing $\mathcal{CP}$ violation in the lepton sector are presented in chapter 2.

This thesis analyses data collected by the T2K long baseline neutrino oscillation experiment. The T2K experiment probes the neutrinos oscillation parameters, and better characterises neutrino cross sections, by measurements of neutrino interactions induced by an accelerator produced ν_μ or $\bar{\nu}_\mu$ beam, depending on running mode. The neutrino beam is generated at J-PARC, by focussing the hadrons resulting from the collision of a proton beam with a graphite target. A set of detectors located 280 m from the target, both on and off the beam axis, measure beam interactions. At a distance of 295 km downstream, the Super-K 50 kt water Cherenkov detector makes the final set of beam interaction measurements. The details of the T2K experiment are outlined in chapter 3.

The oscillation analysis that is described in this thesis depends on a set of inputs which are generated by the T2K experiment. A description of these inputs is made in chapter 4, and are made up of flux, cross section and detector central values along with systematics and constraints. These values are modelled at T2K, and a constraint that is propagated to the prediction of the spectra at the far detector is generated using near detector data. This constraint provides tuned central values of flux and cross section parameters in conjunction with their covariance matrix. The beam flux model is tuned using external hadron production data, from the NA61/SHINE experiment at CERN. The cross section central values and uncertainties are tuned using external data with the FSI model used at both the near and far detectors. Systematic uncertainties at Super-K are evaluated using cosmic data. A description is made of how the data events for each sample are selected at Super-K, which are subsequently fit in the analysis.

The analysis in this thesis, presented in chapter 5, is composed of data from the transitions $\overset{(-)}{\nu}_\mu \to \overset{(-)}{\nu}_\mu$ and $\overset{(-)}{\nu}_e \to \overset{(-)}{\nu}_e$, and shows for the first time an exclusion of the $\mathcal{CP}$ conserving

values $0, \pi$ at 2σ. The analysis is carried out in the framework of three flavour oscillations in constant density matter, and a hybrid bayesian-frequentist approach is used to fit the parameters, where nuisance parameters are marginalised instead of profiled. Energy, and energy vs lepton angle spectra are fit, and confidence intervals are built using a $\Delta\chi^2$ method or the Feldman-Cousins method. A discussion of the implications of these results is presented in chapter 6 along with a description of future prospects in neutrino physics.

2 Neutrino Physics

2.1 Neutrinos in the Standard Model

The Standard Model of particle physics is a quantum field theory which describes the known interactions between particles excluding the gravitational force. The standard model is a gauge theory based on a local symmetry group $SU(3)_C \times SU(2)_L \times U(1)_Y$, where the first symmetry group, C corresponds to colour, L is for left-handed chirality, and Y is weak hypercharge. The colour charge of a fermion determines whether they participate in strong interactions and form hadrons, quarks have color charge and leptons do not. The symmetry group $SU(2)_L \times U(1)_Y$ determines the interactions of leptons and hence neutrinos. The observation of neutrino oscillations is evidence of physics beyond the standard model, and requires a mechanism for generating their mass. Two possible natures of the neutrino, Dirac or Majorana, lead to different consequences for neutrino mass.

2.1.1 Weak Interaction

Since leptons have no colour and neutrinos have no charge they only participate in the weak interaction, (which is somewhat of a misnomer, although it appears *weaker* than the other forces it is just short ranged) this means that they only couple to either the $W^{\pm}$ or Z^0 bosons. Both W and Z bosons are very massive, with masses of $\sim$80 GeV and $\sim$91 GeV respectively, unlike the massless photon and gluon which mediate the electromagnetic and strong forces. As neutrinos only couple to the weak force they have very a small interaction cross section see section 2.2.3. Since the interaction rate is dependent on the cross section, flux, and target density, neutrino experiments seek to maximise the flux of particles and the target mass available for interaction. The charged $W^{\pm}$ bosons lead to interactions which are called CC and the neutral Z boson, leads to NC processes, these are further discussed in section 2.2.3. Both CC and NC interactions conserve lepton flavour with CC interactions producing the corresponding charged lepton, whilst neutral current processes are blind to the flavour of the incoming neutrino and only produce charged particles indirectly. In the Charged Current Quasi-Elastic (CCQE) interaction mode a neutrino scatters from a nucleon converting the nucleon and producing a charged lepton. CCQE events will form the bulk of the analysed signal mode for this thesis. A charged current mode with the production of a single positively charged pion from an electron neutrino interaction CC 1 π^+ makes up a smaller part of the signal.

2.2 Neutrino Interaction Lagrangian

Without modification the Standard Model of particle physics includes a charged-current (CC) interaction Lagrangian, $\mathcal{L}^{(CC)}$, of the form

$$\mathcal{L}^{(CC)} = -\frac{g}{\sqrt{2}} \sum_{\substack{\alpha=e,\mu,\tau \\ i=1,2,3}} \left(\overline{\ell_{L\alpha}} \gamma^\lambda U_{\alpha i} \nu_{Li} W_\lambda^- + \overline{\nu_{Li}} \gamma^\lambda U_{\alpha i}^* \ell_{L\alpha} W_\lambda^+ \right), \tag{2.1}$$

where g is the semi-weak coupling constant, neutrino and lepton fields of flavour α, are ν_α and ℓ_α respectively, $\ell_{L\alpha} = \frac{1}{2}(1-\gamma^5)\ell_\alpha$, the left handed chiral projections of ℓ_α and ν_α, and $W_\lambda^\pm$ the W boson fields, and γ^λ are the gamma matrices. Mixing between neutrino flavours which will be discussed in section 2.4 in detail is included in the term $U_{\alpha i}$ the Pontecorvo Maki Nakagawa Sakata (PMNS) matrix element. The NC interaction Lagrangian $\mathcal{L}^{(NC)}$ is,

$$\mathcal{L}^{(NC)} = -\frac{g}{2\cos\theta_W} \sum_{i=1,2,3} \left(\overline{\nu_{Li}} \gamma^\lambda \nu_{Li} Z_\lambda^0 \right), \tag{2.2}$$

where θ_W is the weak mixing or Weinberg angle and Z_λ is the Z boson field. Combining the above Lagrangians with a Dirac mass term (which requires both handed neutrinos, and therefore an extension of the Standard Model), neutrino interactions within the Standard model are fully described.

$$\mathcal{L} \supset \sum_{i=1,2,3} \left[i\bar{\nu}_i \partial\!\!\!/ \nu_i - m_i \bar{\nu}_i \nu_i \right] + \mathcal{L}^{(NC)} + \mathcal{L}^{(CC)} \tag{2.3}$$

where $\partial\!\!\!/ = \gamma^\lambda \partial_\lambda$. The mass term considered in eq. (2.3) is the Dirac term which is discussed in section 2.3.

2.2.1 Helicity and Chirality

The handedness of a particle is a vital component of the Standard Model, as the weak interaction only couples to particles of one handedness. The related concepts of helicity and chirality are used to determine a particle's handedness. The parity operator $\mathcal{P}$, takes the spatial components of a four vector x^μ to $\vec{x} \xrightarrow{\mathcal{P}} -\vec{x}$, but in the case of axial-vectors (or pseudovectors) which are of the form, $\vec{c} = \vec{a} \times \vec{b}$, the parity transformation leaves the vector unchanged $\vec{c} \xrightarrow{\mathcal{P}} \vec{c}$.

The helicity of a particle is defined as the dot product of the particle's spin and its momentum. In the case of massless particles this is well defined in all frames, however for massive particles a Lorentz boosted frame can be found in which the helicity of the particle is reversed, to deal with this situation we introduce the related concept of chirality. To do this we decompose the particle's Dirac spinor, ϕ, into left and right handed

components by applying Lorentz invariant operators which project these components.

$$\chi_L = \frac{1}{2}(1-\gamma^5) \; ; \; \chi_R = \frac{1}{2}(1+\gamma^5) \tag{2.4}$$

here γ^5 is defined as $i\gamma^0\gamma^1\gamma^2\gamma^3$ where the γ matrices are those used in the Dirac equation [1]. Using these operators we can see $\phi = \phi_R + \phi_L$, using the additional properties that $\{\gamma^\mu, \gamma^5\} = 0$ and that, $\gamma^{5\dagger} = \gamma^5$, we can derive

$$\bar{\phi_L}\phi_L = \bar{\phi_R}\phi_R = 0. \tag{2.5}$$

This allows the construction of a Dirac mass term for a chiral state, which is complicated by the fact that ν_R and $\bar{\nu}_L$ have not be observed.

2.2.2 V-A form of Weak Interaction

The condition that any matrix element in the Standard Model must be Lorentz invariant limits the number of possible forms of the interaction vertex. Taking these limitations into consideration there are only 5 allowed combinations of 2 spinors and gamma matrices which form invariant currents. These five categories are classified according to the rank of the tensor and how they transform under the parity operator. In section 2.1.1 the axial vector remained the same under parity transformation as do scalars, whilst pseudoscalars and vectors change sign.

An experiment to determine the helicity of the neutrino [2] observed that all neutrinos were left handed. The previous observation requires a combination of vector and axial vector terms, $V-A = \gamma^\mu(1-\gamma^5)$, whose form maximally violates symmetry under charge conjugation. The terms in the Lagrangians for neutrinos can be found in eq. (2.1) for the charged current and eq. (2.2) for the neutral currents. The form of the weak neutral current contains vector (g_V^f) and axial vector (g_A^f) terms for interactions with each of the fermions, f, with $g_V^f V - g_A^f A$ and for the case of the neutrinos $g_V^\nu = g_A^\nu = \frac{1}{2}$.

2.2.3 Interaction channels

Observation of neutrino interactions requires the production of a charged particle either directly or as the result of a capture mechanism. A review of neutrino interactions across energy scales can be found in [3]. There are several different modes by which a charged particle can be produced at the energies that are covered by the T2K flux which are discussed in more detail in section 4.2. Each of these processes has an associated cross section which is required in order to predict the expected interaction rate for a particular neutrino flux. The neutrino nucleus interaction kinematics are described by the invariant

amplitude $\mathcal{M}$, and the cross section is this quantity squared

$$\overline{|\mathcal{M}|^2} = 4G_F^2 L_{\mu\nu} W^{\mu\nu}, \tag{2.6}$$

where G_F is the Fermi constant, $L_{\mu\nu}$ is the leptonic tensor, and $W^{\mu\nu}$ is the hadronic tensor. The Standard Model can make precise predictions of $W^{\mu\nu}$ for quarks, however, neutrino interactions as considered in this thesis are on nucleons, which are gluon bound structures of valence quarks and also contain sea quarks, which are bound in nuclei. The nucleon structure complicates the picture so that $W^{\mu\nu}$ is not known.

The most general form of the hadronic tensor for neutrino nucleus scattering is described by [4]

$$\begin{aligned}\frac{1}{2M} W^{\mu\nu} = &- W_1 g^{\mu\nu} + W_2 \frac{p^\mu p^\nu}{M^2} + W_4 \frac{q^\mu q^\nu}{M^2} + W_5 \frac{p^\mu q^\mu + q^\mu p^\nu}{2M^2} \\ &- iW_3 \epsilon^{\mu\nu\alpha\beta} \frac{p_\alpha q_\beta}{2M^2} + W_6 \frac{p^\mu q^\mu - q^\mu p^\nu}{2M^2},\end{aligned} \tag{2.7}$$

the W_i for $i = 1, 2, \ldots, 6$ are structure functions which parameterise our ignorance of the nucleon structure, and need to be determined experimentally. The binding of nucleons within the nucleus also introduces the additional effects of Fermi motion, due to the positional confinement of the nucleons within the nucleus. Nuclear binding of the nucleons also introduces effects from the uncertainty in the nucleons momentum, and nucleon-nucleon correlations. Reinteractions within the nuclear medium of the hadrons resulting from the primary interaction can also occur, these are termed final state interactions (FSI) in the literature. These have a particularly significant effect where the neutrino energy is of the order of a few GeV, and make determination of the true topology difficult or impossible and will bias neutrino energy reconstruction. These effects examined in greater detail in section 4.2.

In ascending energy the interaction modes are, charged current quasi-elastic interactions (CCQE), the neutrino interacts with a nucleon, and leaves it in the ground state. In resonant interactions (RES) the neutrino excites the nucleon into a resonant state, which typically then decays to a state with a nucleon and a pion in the final state, but many other decays are possible. Pions can also be produced coherently, in this process the interaction is on the whole nucleus which stays in its ground state without much energy transfer. This results in a forward scattered pion. Going to higher energies the neutrino can interact with a single quark and cause a hadronic shower from the final state quark in deep inelastic scattering (DIS). There are also neutral current versions of the processes discussed, where a final state pion is not observed. Plots of the CC inclusive cross section which includes all the previously discussed interaction modes are shown in fig. 2.1.

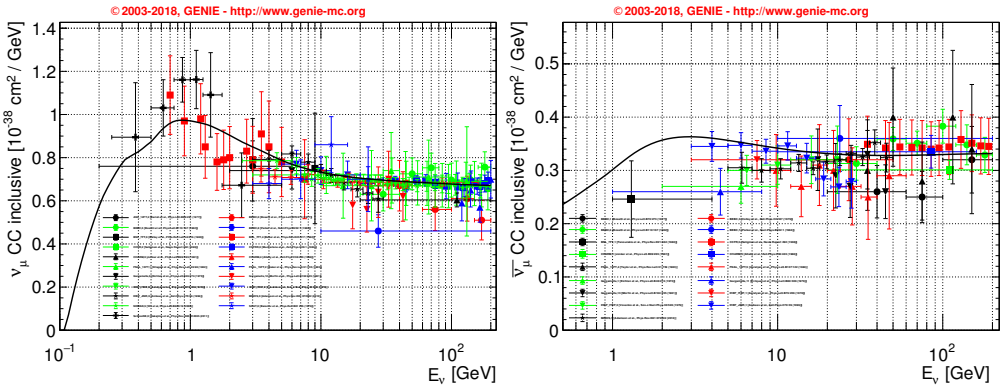

(a) ν_μ CC inclusive cross section. **(b)** $\bar{\nu}_\mu$CC inclusive cross section.

Figure 2.1: Neutrino (a), and antineutrino (b), CC inclusive cross section as a function of the neutrino energy per target nucleon. The prediction is provided by the GENIE neutrino MC generator [5].

2.3 Neutrino Mass

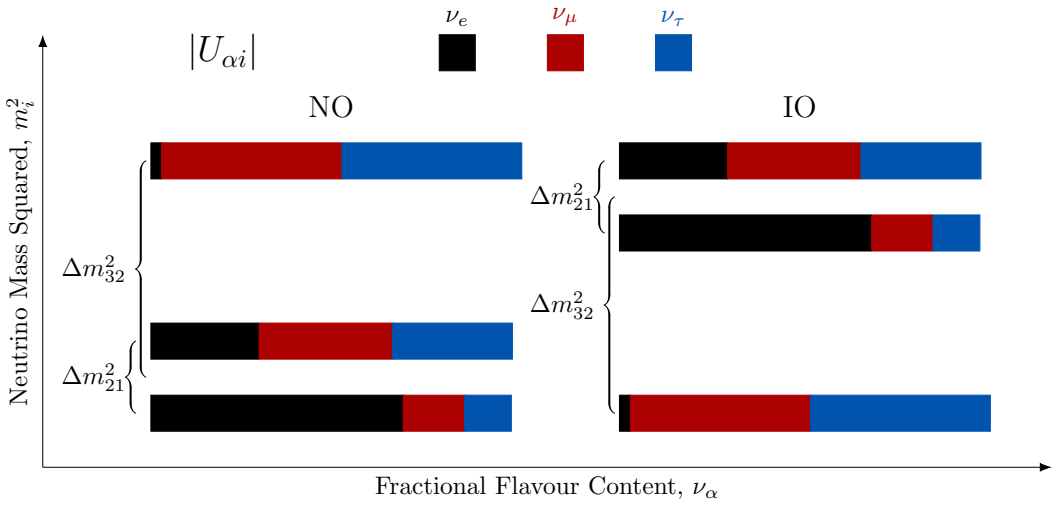

Figure 2.2: Probability of finding the flavour, α, in the ith mass eigenstate, representation of the Pontecorvo Maki Nakagawa Sakata matrix mixing elements for the two different mass orderings, left showing the Normal Ordering (NO) and right showing the Inverted Ordering (IO). Here the convention $\Delta m^2_{ij} = m^2_i - m^2_j$ is used

We now know from oscillation experiments that neutrinos have small masses with tiny mass splittings, illustrated in fig. 2.2 see section 2.4 for further details. However oscillation experiments can only probe the mass difference $\Delta m^2_{ij} = m^2_i - m^2_j$, and cannot determine the mass of a particular neutrino. Methods for directly determining the masses of the neutrinos exist, and are described in section 2.3.1. The pattern of mass splittings is very different to the quark sector, and generating the masses in the same manner as the quarks seems unlikely as the ratio of the neutrino mass to the quark mass is of $\mathcal{O}(10^{-6})$.

There are only left handed neutrinos in the standard model, due to the maximally parity violating nature of the weak interaction.

To introduce mass to neutrinos requires an extension of the Standard Model, a *minimally extended Standard Model* introduces the right handed neutrino fields $\nu_{\alpha R}$, $\alpha = e, \mu, \tau$. Such fields are fundamentally different to the rest of the fermion sector due to their invariance under $\mathrm{SU}(3)_C \times \mathrm{SU}(2)_L$, they are singlets, and have hypercharge $Y = 0$, and are known as *sterile* due to their only interaction being with the gravitational force.

In the Dirac case a massless fermion can be described by a spinor with left and right handed components. The mass term in case is

$$\mathcal{L}^{\mathrm{Dirac}} = \sum_{i=1,2,3} -m_i \bar{\nu}_i \nu \tag{2.8}$$

where each of the, $m_i = y_i \dfrac{v}{\sqrt{2}}$, is made up of the Yukawa couplings, y_i.

The Majorana case, makes the particle its own antiparticle, by making the spinor the sum of left handed field and its conjugate [6],

$$\nu = \nu_L + \nu_L^C = \nu^C, \tag{2.9}$$

this does not violate charge conservation since the neutrino is neutral. This spinor leads to a mass term

$$\mathcal{L}^{Majorana} = -\frac{1}{2} m (\overline{\nu_L^C} \nu_L + \nu_L^C \overline{\nu_L}), \tag{2.10}$$

where the expression is for a single neutrino field. Although eq. (2.10) only contains the standard model left-handed neutrino fields, Majorana mass terms break $SU(2)$ gauge symmetry, and violate $B - L$, where B is baryon number and L is lepton number, a symmetry of the standard model. An expression for the kinetic terms including the Majorana mass is

$$\mathcal{L}^{Majorana} = \overline{\nu_L^C} i \overleftrightarrow{\partial\!\!\!/} \nu_L - \frac{m}{2} \left(-\nu_L^T \mathcal{C}^\dagger \nu_L + \overline{\nu_L} \mathcal{C} \overline{\nu_L}^T \right). \tag{2.11}$$

where the notation $\overleftrightarrow{\partial\!\!\!/} \equiv \frac{1}{2} \left(\overrightarrow{\partial\!\!\!/} - \overleftarrow{\partial\!\!\!/} \right)$ acts to the right and to the left.

For a massless neutrino the Dirac and Majorana descriptions of the neutrino coincide and in both cases the right handed chiral fields do interact. This means that measurements of the effect of neutrino mass are necessary in order to distinguish between the two possibilities. This measurement cannot be made from neutrino oscillations as the effect of the Majorana phase cannot be seen in oscillation experiments. A promising way of determining the nature of neutrinos is via neutrinoless double beta decay which is discussed in section 2.3.2.

2.3.1 Direct Measurements of Neutrino Mass

Radioactive decay offers a model independent way of determining the neutrino mass. The decay models are not dependent on whether neutrinos are Dirac or Majorana and also do not suffer from dependence on cosmological models as in section 2.3.3. The process

$$(A, Z) \rightarrow (A, Z+1) + e^- + \bar{\nu}_e, \tag{2.12}$$

results in an electron whose kinematics depend on the momentum of the neutrino. Isotopes with the lowest accessible endpoint are used to improve the sensitivity of the experiments. These experiments probe the limit of the effective mass, $m_\beta = \sqrt{\sum_i |U_{ei}|^2 m_i^2}$. Tritium is the isotope used in the Karlsruhe Tritium Neutrino Experiment (KATRIN) experiment [7], and the Troitsk and Mainz experiments [8, 9] have determined the limit $m_\beta < 2\,\text{eV}$. KATRIN is designed to reach $0.200\,\text{eV}$ at $90\,\%$ Confidence Level (C.L.) after 3 years running [10].

Since the decay

$$\pi^+ \rightarrow \mu^+ + \nu_\mu, \tag{2.13}$$

has two bodies in the final state, energy conservation can be used to determine the mass of the neutrino. Measurements of the μ^+ momentum resulted in upper limits for $m_{\nu_\mu} < 0.17\,\text{MeV}$ at $90\,\%$ C.L. [11].

The following decays of τ particles have been used to determine neutrino mass,

$$\tau^- \rightarrow 2\pi^- + \pi^+ + \nu_\tau, \quad \tau^- \rightarrow 3\pi^- + 2\pi^+ + \nu_\tau(+\pi^0) \tag{2.14}$$

resulting in an upper limit of $m_{\nu_\tau} < 18.2\,\text{MeV}$ at $95\,\%$ C.L.. Both these limits are less stringent than those determined by the single beta decay

2.3.2 Neutrinoless Double Beta Decay

If neutrinos are Majorana particles the decay processes

$$\begin{aligned} {}^A_Z N &\rightarrow {}^A_{Z+2} N + 2e^- \\ {}^A_Z N &\rightarrow {}^A_{Z-2} N + 2e^+, \end{aligned} \tag{2.15}$$

known as neutrinoless double beta decay ($2\beta^\mp_{0\nu}$) can occur, these violate lepton number conservation $\Delta L = \pm 2$, and observing either of these process is enough to confirm the Majorana nature of neutrinos. In fig. 2.3 a $2\beta^\mp_{0\nu}$ process is shown at tree level, incorporating three neutrino mixing which adds a factor of U_{ek} at each vertex, to take into account of helicity matching a term m_k is incorporated. The *effective Majorana*

mass is then the sum over three massive neutrinos

$$m_{2\beta} = \sum_{k=1}^{3} U_{ek}^2 m_k. \tag{2.16}$$

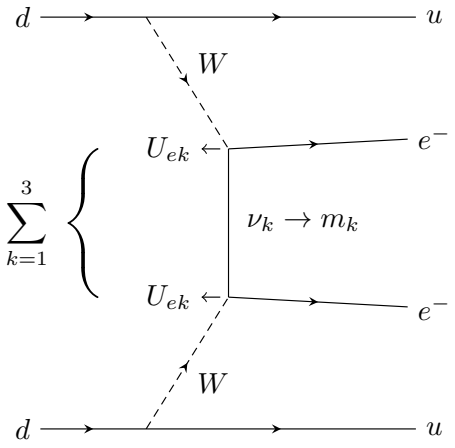

Figure 2.3: Tree level diagram of the neutrinoless beta decay ($2\beta^-_{0\nu}$) process, since the $\nu_e = \bar{\nu}_e$ are the same particle, helicity also matching in the process introduces a term m_k for each of the massive neutrinos. Mixing between the three massive neutrinos introduces the sum, and the elements of the Pontecorvo Maki Nakagawa Sakata matrix U_{ek}, which leads to eq. (2.16). This process is forbidden in the standard model

In the standard model the particle and anti-particle difference in addition to the helicity difference mean that $2\beta^{\mp}_{0\nu}$ is not possible. It is also possible for the decays to go via the lepton number conserving decays with either $2\nu_e/2\bar{\nu}_e$. If a nucleus can decay via a single β process then the 2β process is not observable in practice due to its much longer lifetime. Isotopes with energetically forbidden or suppressed β decay are selected for experiment. The lifetime of the $2\beta^{\mp}_{0\nu}$ decay depends on the effective Majorana mass, $m_{2\beta}$

$$\left[T^{0\nu}_{1/2}(N)\right]^{-1} = G^N_{0\nu}\left|M^N_{0\nu}\right|^2 \frac{|m_{2\beta}|}{m_e^2} \tag{2.17}$$

where $M^N_{0\nu}$ is the nuclear matrix element, and $G^N_{0\nu}$ is the phase space factor, and $m_{2\beta} = \sum_i U_{ei} m_i$. To date lower bounds, and no signal, have observed on elements which can decay via $2\beta^{\mp}_{0\nu}$. A lower bound has been set on the decay of ^{136}Xe of $T^{0\nu}_{1/2} > 1.07 \times 10^{26}$ yr at 90 % C.L. by the KamLAND [12] experiment. A bound set by the GERmanium Detector Array (GERDA) experiment on ^{76}Ge at $T^{0\nu}_{1/2} > 8 \times 10^{25}$ yr at 90 % C.L. has also been observed [13]. Three other experiments have also measured limits: Cryogenic Underground Observatory for Rare Events (CUORE) ^{130}Te at $T^{0\nu}_{1/2} > 1.3 \times 10^{25}$ yr at 90 % C.L. and $T^{0\nu}_{1/2} > 1.5 \times 10^{25}$ yr at 90 % C.L. [14] combined with Cryogenic Underground Observatory for Rare Events-0 (CUORE-0) [15] and CUORICINO (CUORICINO) [16], Enriched Xenon Observatory-200 (EXO-200)

^{136}Xe at $T^{0\nu}_{1/2} > 1.8 \times 10^{25}$ yr at 90 % C.L. [17], MAJORANA (MAJORANA) ^{76}Ge at $T^{0\nu}_{1/2} > 1.9 \times 10^{25}$ yr at 90 % C.L. [18].

2.3.3 Astrophysical Neutrino Constraints

The cosmological evolution of the universe is affected by the density of the neutrinos which is related to the number of active neutrino species and the value of their masses. Information from neutrinos after a hot Big Bang model in a Cosmic Neutrino Background (CνB) modelled by the Lambda Cold Dark Matter (ΛCDM) formalism which currently fits most cosmological parameters well [19]. Constraints for the sum of the neutrino masses $\sum m_\nu = \sum_{i=1,2,3} m_i$, come from a variety of data sets with the most robust constraints coming from the Planck temperature data. The constraint is subject to some model dependence with some weakening of the upper bounds of $\sum m_\nu$ when including additional parameters. The result $\sum m_\nu < 0.12\,\text{eV}$ at the 95 % C.L., does not include data from Lyman-α absorption data which is much more sensitive to modelling, a plot of $\sum m_\nu$ against the Hubble parameter H_0, and coloured by the matter fluctuation amplitude σ_8 [20] is shown in fig. 2.4.

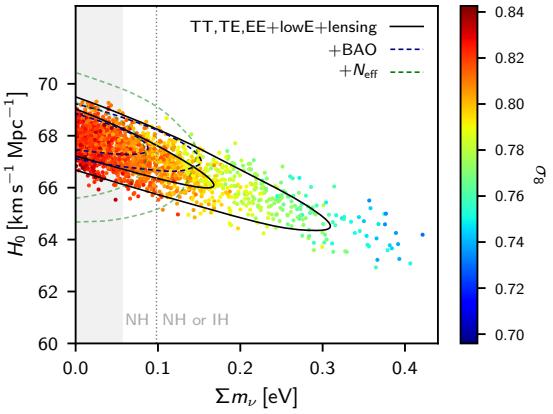

Figure 2.4: Sum of the neutrino masses $\sum m_\nu$ against the Hubble parameter H_0. The grey zone is excluded by limits from neutrino oscillation data $\sum m_\nu < 0.056\,\text{eV}$, colour coded by σ_8, the matter fluctuation amplitude. The parameter space left of the vertical dotted line implies Normal Hierarchy/Ordering whilst to the right either Normal or Inverted Hierarchy/Ordering are possible. Reproduced from [20] .

The effective number of neutrino families N_{eff} can be obtained from the transition when neutrinos decouple from the plasma present in the early Universe. In this model the neutrinos are treated as a part of the parameterisation of the energy density of the Universe in addition to photons. Recent results from the Planck experiment give $N_{eff} = 2.99 \pm 0.17$ at 95 % C.L. which can be seen in fig. 2.5 where N_{eff} is plotted against the Hubble parameter, H_0 and data sets are coloured by the matter fluctuation amplitude σ_8.

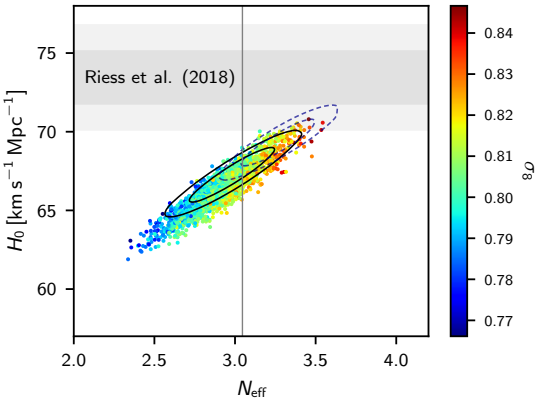

Figure 2.5: Number of effective neutrino species which are relativistic, N_{eff} with the local Hubble parameter, H_0, colour coded by σ_8, the matter fluctuation amplitude. The solid contours use data from Planck alone, limits for H_0 from [21] are shown in the grey region and joint constraints with that data set are shown in dashed lines. The vertical line shows $N_{eff} = 3.046$, the standard neutrino decoupling model expectation. Reproduced from [20].

2.4 Neutrino Oscillations

The primary focus of this thesis is the measurement of neutrino oscillations, the observation that a flux of neutrinos can change flavour in flight. We will consider three flavour oscillations in this thesis and in the following treatment although there are mechanisms for the addition of non-active or sterile neutrinos. The measurement of the Z^0 width by experiments at LEP and SLD constrained the number of light mass neutrino species to 2.9840 ± 0.0082 [22]. The observation of neutrino oscillations implies that neutrinos have mass and their mass and flavour eigenstates are not equivalent. Since we only observe neutrinos via their weak interactions we can define the neutrino that is produced with a lepton of a particular flavour, for instance an electron, as a neutrino of that flavour, an electron neutrino in this case. The propagation of neutrinos occurs via their mass eigenstates, and each flavour state is a superposition of the mass eigenstates, since these mass states are not identical each has a different velocity and will become out of phase as the particle propagates. When a neutrino is detected it will have a different superposition of probability amplitudes for each mass state to its initial composition which in turn describe another set of flavour eigenstates.

To calculate oscillation probabilities we need to relate the flavour states, ν_α for $\alpha = e, \mu, \tau$, to the mass states, ν_i for $i = 1, 2, 3$, via a matrix U

$$|\nu_\alpha\rangle = \sum_i U_{\alpha i} |\nu_i\rangle \tag{2.18}$$

$$|\nu_i\rangle = \sum_{\alpha} U^*_{\alpha i} |\nu_\alpha\rangle \,. \tag{2.19}$$

The transformation matrix, in this case a rotation matrix which is called the PMNS matrix U_{pmns}: Pontecorvo, Maki, Nakagawa, Sakata (PMNS)

$$\begin{aligned} U_{\text{pmns}} &= \begin{pmatrix} U_{e1} & U_{e2} & U_{e3} \\ U_{\mu 1} & U_{\mu 2} & U_{\mu 3} \\ U_{\tau 1} & U_{\tau 2} & U_{\tau 3} \end{pmatrix} \\ &= \begin{pmatrix} 1 & 0 & 0 \\ 0 & c_{23} & s_{23} \\ 0 & -s_{23} & c_{23} \end{pmatrix} \begin{pmatrix} c_{13} & 0 & s_{13}e^{-i\delta_{\text{CP}}} \\ 0 & 1 & 0 \\ -s_{13}e^{-i\delta_{\text{CP}}} & 0 & c_{13} \end{pmatrix} \begin{pmatrix} c_{12} & s_{12} & 0 \\ -s_{12} & c_{12} & 0 \\ 1 & 0 & 1 \end{pmatrix} \\ &= \begin{pmatrix} c_{12}\,c_{13} & s_{12}\,c_{13} & s_{13}e^{-i\delta_{\text{CP}}} \\ -s_{12}\,c_{23} - c_{12}\,s_{23}\,s_{13}e^{i\delta_{\text{CP}}} & c_{12}\,c_{23} - s_{12}\,s_{23}\,s_{13}e^{i\delta_{\text{CP}}} & s_{23}\,c_{13} \\ s_{12}\,s_{23} - c_{12}\,c_{23}\,s_{13}e^{i\delta_{\text{CP}}} & -c_{12}\,s_{23} - s_{12}\,c_{23}\,s_{13}e^{i\delta_{\text{CP}}} & c_{23}\,c_{13} \end{pmatrix}, \end{aligned} \tag{2.20}$$

encodes the transformation between the neutrino mass and flavour states as a three dimensional rotation matrix. In eq. (2.20) the notation c_{lm}, s_{lm} for $\cos\theta_{lm}$ and $\sin\theta_{lm}$ is used, where θ_{lm} is a mixing angle between the state l and m, and the physical phase δ_{CP}. An additional complex phase factor can be multiplied with the matrix in order to take into consideration a possible Majorana mass which can be expressed as a diagonal unitary matrix

$$\text{diag}(e^{i\lambda_1}, e^{i\lambda_2}, e^{i\lambda_3}), \tag{2.21}$$

where $\lambda_1 = 0$, this cannot be observed in oscillation experiments and will not be considered in the the rest of the treatment. This matrix must be unitary in order to preserve probability .

Since only the mass squared splittings Δm^2_{21} and $\left|\Delta m^2_{32}\right|$ are known from neutrino oscillations, and the sign of Δm^2_{31} is not known, this introduces two possibilities for how the absolute values of the masses are ordered. One case is $m_1 < m_2 < m_3$, the Normal Ordering (NO) and $m_3 < m_2 < m_1$, Inverted Ordering (IO) The case where $\Delta m^2_{31} > 0$ is called the Normal Hierarchy/Ordering (NH,NO) and the other possibility, Inverted Hierarchy/Ordering (IH,IO) where $\Delta m^2_{32} < 0$, a diagram of the splittings is shown in fig. 2.2. The results in this thesis, and those for global fits, are presented for both of these cases considered separately.

The calculation of the probablility of observing a particular flavour state α after the beam of neutrinos has propagated a distance, L can be performed in several different ways . It can be shown that taking the wave packets in consideration as opposed to the plane wave approach taken here results in the same expression for the transition probabilities [23]. A method of generating neutrinos is from the decay of pions, from this

consideration an expression for the energy and the momentum of the mass eigenstates can be derived, and ignoring variations of the group speeds of the neutrinos of order m_j^2 an expression for the state $|\nu_\alpha\rangle$ after time t, $|\nu_\alpha(t)\rangle$, can be derived

$$|\nu_\alpha(t)\rangle = U^*_{\alpha j} e^{-im_j^2 t/2E} |\nu_j\rangle \,, \tag{2.22}$$

from the previous expression in eq. (2.22), the oscillation probability can be obtained assuming the orthogonality of the flavour states

$$\begin{aligned} P(\nu_\alpha \to \nu_\beta) &= |\langle \nu_\beta | \nu_\alpha(t)\rangle|^2 && (2.23)\\ &= \left| \sum_j U_{\beta j} U^*_{\alpha j} e^{-im_j^2 t/2E} \right|^2 && (2.24)\\ &= \sum_{k,j} U^*_{\beta k} U_{\alpha k} U_{\beta j} U^*_{\alpha j} e^{-i\Delta m^2_{kj} t/2E} && (2.25) \end{aligned}$$

where in the last line the notation $\Delta m^2_{kj} = m^2_k - m^2_j$ is used. If we make the approximation that the neutrinos are ultrarelativistic (and time of flight for neutrinos is not usually experimentally measured) we can say that $t = L$, this assumption is reasonable based on the current bounds for the neutrino masses. As a consequence we can express the phase in eq. (2.25) as

$$\Phi_{kj} = \frac{\Delta m^2_{kj} L}{2E}, \tag{2.26}$$

and the amplitude is determined by the magnitude of the elements of U, $|U_{\alpha i}|^2$. The expression in eq. (2.25) can be written as

$$\begin{aligned} P(\nu_\alpha \to \nu_\beta) = \delta_{\alpha\beta} &- 4 \sum_{j>k} \mathrm{Re}\left[U^*_{\beta k} U_{\alpha k} U_{\beta j} U^*_{\alpha j}\right] \sin^2\left(\frac{\Delta m^2_{kj} L}{4E}\right) \\ &+ 2 \sum_{j>k} \mathrm{Im}\left[U^*_{\beta k} U_{\alpha k} U_{\beta j} U^*_{\alpha j}\right] \sin\left(\frac{\Delta m^2_{kj} L}{2E}\right). \end{aligned} \tag{2.27}$$

In eq. (2.27) flavour changing channels, where $\alpha \neq \beta$ are called *transition*, or in the case of beam based experiments, *disappearance* probabilities (which could also in principle be caused by neutrino decays, which are not considered in this thesis and also require "new physics"). Channels where $\alpha = \beta$ are called *survival* probabilities.

A similar expression to eq. (2.23) can be derived for antineutrinos, where the elements of U are complex conjugated wrt eq. (2.25)

$$P(\bar\nu_\alpha \to \bar\nu_\beta) = \sum_{k,j} U_{\beta k} U^*_{\alpha k} U^*_{\beta j} U_{\alpha j} e^{-i\Phi_{kj}}, \tag{2.28}$$

expressing eq. (2.28) in the same form as eq. (2.27),

$$\begin{aligned} P(\bar{\nu}_\alpha \to \bar{\nu}_\beta) = \delta_{\alpha\beta} &- 4\sum_{j>k} \mathrm{Re}\left[U^*_{\beta k}U_{\alpha k}U_{\beta j}U^*_{\alpha j}\right] \sin^2\left(\frac{\Delta m^2_{kj}L}{4E}\right) \\ &- 2\sum_{j>k} \mathrm{Im}\left[U^*_{\beta k}U_{\alpha k}U_{\beta j}U^*_{\alpha j}\right] \sin\left(\frac{\Delta m^2_{kj}L}{2E}\right), \end{aligned} \tag{2.29}$$

this expression only differs in the sign of the imaginary part from the expression for neutrinos in eq. (2.27). $\mathcal{CPT}$ violating transitions are not considered in this thesis, which implies the equality $P(\nu_\alpha \to \nu_\beta) = P(\bar{\nu}_\beta \to \bar{\nu}_\alpha)$, which can be seen by interchanging α and β in eq. (2.28) and comparing with eq. (2.27), this equality also holds for the case where $\alpha = \beta$. $\mathcal{CP}$ asymmetry can be characterised by the difference between the transitions $P(\nu_\alpha \to \nu_\beta)$ and $P(\bar{\nu}_\alpha \to \bar{\nu}_\beta)$ and the time reversed versions of both these transitions. Using the expressions for these transitions from eqs. (2.27) and (2.29), the terms which contribute to $\mathcal{CP}$ asymmetry are,

$$4\sum_{j>k} \mathrm{Im}\left[U^*_{\beta k}U_{\alpha k}U_{\beta j}U^*_{\alpha j}\right] \sin\left(\frac{\Delta m^2_{kj}L}{2E}\right), \tag{2.30}$$

where in the case of a *survival* transition the imaginary terms vanish.

As a consequence of the unitarity of the matrix U, the sum $\sum_\beta P(\nu_\alpha \to \nu_\beta) = 1$, that is the sum of all the transitions from a flavour α, to all flavours $\beta(=\alpha)$ covers all of probablility space. Also for $\alpha(=\beta)$, $\sum_\alpha P(\nu_\alpha \to \nu_\beta) = 1$.

Using the PMNS matrix elements, an expression for the disappearance probability of ν_μ can be written

$$\begin{aligned} P(\nu_\mu \to \nu_\mu) = 1 &- \left(c^4_{13}\sin^2 2\theta_{23} + s^2_{23}\sin^2 2\theta_{13}\right)\sin^2\Delta_{31} \\ &+ \left[c^2_{13}(c^2_{12} - s^2_{13}s^2_{12})\sin^2 2\theta_{23} + s^2_{12}s^2_{23}\sin^2 2\theta_{13}\right. \\ &\left. - s^2_{23}c^2_{13}\sin^2 2\theta_{13}\sin^2 2\theta_{23}\sin^2 2\theta_{12}\cos\delta_{\mathrm{CP}}\right] \\ &\times \left[\frac{1}{2}\sin 2\Delta_{21}\sin 2\Delta_{31} + 2\sin^2 2\Delta_{21}\sin^2 2\Delta_{31}\right] \\ &- \left[\sin^2\theta_{12}(c^2_{23} - s^2_{13}s^2_{23})^2 + s^2_{13}\sin^2\theta_{23}(1 - \cos^2\delta_{\mathrm{CP}}\sin^2 2\theta_{12})\right. \\ &+ 2s^2_{13}\sin^2 2\theta_{12}\cos 2\theta_{12}\sin 2\theta_{23}\sin 2\theta_{23}\cos\delta_{\mathrm{CP}} \\ &- 2s^2_{23}s^2_{12}c^2_{13}\sin 2\theta_{13}\sin 2\theta_{23}\sin 2\theta_{12}\cos\delta_{\mathrm{CP}} \\ &\left. + \sin^2 2\theta_{23}c^2_{13}(c^2_{12} - s^2_{13}s^2_{12}) + s^2_{12}s^2_{23}\sin^2 2\theta_{13}\right]\sin^2\Delta_{21}, \end{aligned} \tag{2.31}$$

where $\Delta_{ij} = \Delta m^2_{ij}L/2E$, and the θ_{ij} are the mixing angles. Measurements of the ratio $\Delta m^2_{31}/\Delta m^2_{21} \sim 30$ have been made, and experiments are designed to maximise either $\sin^2\Delta_{31}$ or $\sin^2\Delta_{21}$ through the ratio of L/E. This allows the approximation

$\Delta m^2_{21} \ll \Delta m^2_{31}$ to be made, the resulting expression is

$$\begin{aligned} P(\nu_\mu \to \nu_\mu) \simeq & 1 - \left(c^4_{13} \sin^2 2\theta_{23} + s^2_{23} \sin^2 2\theta_{13}\right) \sin^2 \Delta_{31} \\ = & 1 - 4\cos^2_{13} \sin^2_{23} \left(1 - \cos^2 \theta_{13} \sin^2 \theta_{23}\right) \sin^2 \Delta_{31}, \end{aligned} \tag{2.32}$$

due to the symmetry of this expression about $\sin^2 2\theta_{23}$ there is a degeneracy in the octant of this parameter. The approximate expression for electron neutrino appearance to leading order is

$$P(\nu_\mu \to \nu_e) \simeq \sin^2 \theta_{23} \sin^2 2\theta_{13} \sin^2 \Phi_{31}, \tag{2.33}$$

this approximate expression can be used to lift the degeneracy in ν_μ survival. Matter effects which modify the expressions eqs. (2.32) and (2.33) are discussed in section 2.4.1.

2.4.1 Matter Effects

The discussion in section 2.4 was for neutrinos propagating in a vacuum and did not take into account the effects introduced by propagation through matter, where an additional potential is introduced by those same atoms. This potential modifies the oscillation probabilities introducing additional terms which can significantly alter the resulting probabilities. This is a significant effect when neutrinos created in nuclear interactions in the core of sun propagate and leave the sun. Since ordinary matter which composes the sun is composed of electrons orbiting nuclei and does not contain muonic or tau matter an effect from this asymmetry needs to be included. In ordinary matter NC interactions take place for, $\nu_{e,\mu,\tau}$, whilst for ν_e CC interactions with the e^- also take place. Coherent forward elastic scattering introduces a potential which can enhance oscillations [24], the amount of incoherent scattering is small. A charged current potential is introduced in a addition to a neutral current potential due to matter.

In the case of three-neutrino mixing an effective hamiltonian $\mathcal{H}_\mathrm{F}$ can be used to describe the evolution of the neutrino states, and is defined as

$$\mathcal{H}_\mathrm{F} = \frac{1}{2E}\left(U\boldsymbol{M}^2 U^\dagger + \boldsymbol{A}\right), \tag{2.34}$$

with

$$\boldsymbol{M}^2 = \begin{pmatrix} 0 & 0 & 0 \\ 0 & \Delta m^2_{21} & 0 \\ 0 & 0 & \Delta m^2_{31} \end{pmatrix}, \ \boldsymbol{A}^2 = \begin{pmatrix} A_\mathrm{cc} & 0 & 0 \\ 0 & 0 & 0 \\ 0 & 0 & 0 \end{pmatrix} \tag{2.35}$$

where $A_\mathrm{cc} \equiv 2EV_\mathrm{cc} = 2E\sqrt{2}G_\mathrm{F}N_e$, where N_e is the electron density in matter, and G_F is the Fermi coupling constant. The neutral current potential is given by $V_\mathrm{nc} = -\frac{1}{2}\sqrt{2}G_\mathrm{F}N_n$, where N_n is the neutron density in matter. The signs of the two potentials are reversed for interactions of antineutrinos in ordinary matter.

For three flavour oscillations the probability of the transition $\nu_\mu \to \nu_e$ can be approximated by [25]

$$
\begin{aligned}
P(\nu_\mu \to \nu_e) \simeq & \sin^2\theta_{23} \sin 2\theta_{13} \frac{\sin^2(\Delta_{31} - aL)}{(\Delta_{31} - aL)^2} \Delta_{31}^2 \\
& + \sin 2\theta_{23} \sin 2\theta_{13} \sin 2\theta_{12} \frac{\sin(\Delta_{31} - aL)}{(\Delta_{31} - aL)} \Delta_{31} \frac{\sin(aL)}{(aL)} \Delta_{21} \cos(\Delta_{31} + \delta_{\mathrm{CP}}) \\
& + \cos^2\theta_{23} \sin^2 2\theta_{12} \frac{\sin^2(aL)}{(aL)^2} \Delta_{21}^2
\end{aligned}
\tag{2.36}
$$

where $\Delta_{ij} = \Delta m_{ij}^2 L/4E$, and $a = V_{\mathrm{cc}}/2$. The $\mathcal{CP}$ conjugate process changes the signs of both δ_{CP} and the matter potential V_{cc}, and hence a. This introduces a degeneracy, where matter effects can mimic the effects of $\mathcal{CP}$ violation. The effect of varying the phase of δ_{CP} with the inclusion of matter effects are shown in fig. 2.12 for a baseline where the degeneracy between matter effects and $\mathcal{CP}$ violation can be resolved. In fig. 2.6 the T2K experiment baseline and energy is shown with degeneracies for both the mass hierarchy and the value of δ_{CP}. Additional degeneracies come from the octant of θ_{23} as the ν_μ survival probability depends on $\sin^2 2\theta_{23}$ which further limits the resolution of the experiment, this is also shown in fig. 2.6.

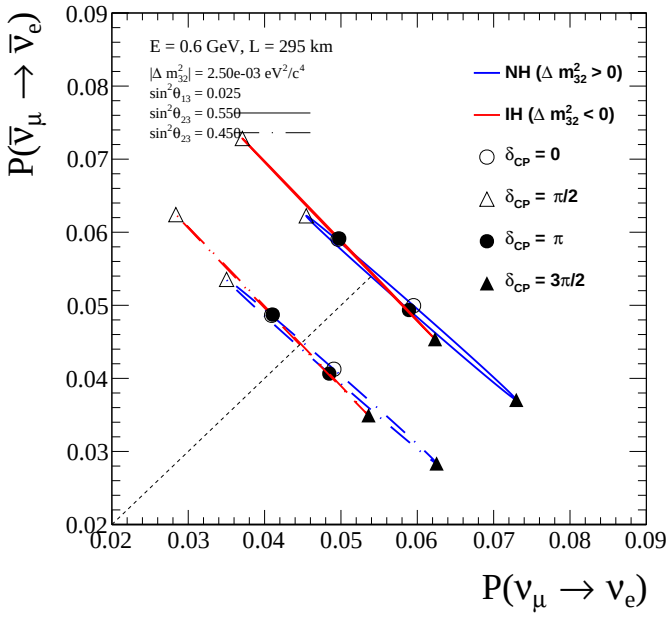

Figure 2.6: Biprobability diagram in the space $P(\nu_\mu \to \nu_e)$, $P(\bar{\nu}_\mu \to \bar{\nu}_e)$ the $\mathcal{CP}$ transformed transition for the T2K experiment baseline and energy. The oscillation parameters are fixed apart from δ_{CP} which varies between $\delta_{\mathrm{CP}} \in [0, 2\pi]$, the red and blue curves show the normal and inverted hierarchies respectively. The solid and dashed lines show different solutions to the octant of θ_{23} which introduces an additional degeneracy beyond that of the mass hierarchy.

2.4.2 MSW Effect

Considering the case of two neutrino mixing is useful to illustrate the enhancement that matter can have on the oscillation probability, the treatment in this section follows [26]. Considering the case of ν_e, ν_μ and ν_1, ν_2, which is the same as mixing between ν_e, ν_τ since they have the same matter potential. The mixing matrix contains one mixing angle, θ and a single mass splitting Δm. The time evolution of the neutrino state can be written

$$i\frac{d}{dx}\begin{pmatrix}\phi_{ee}\\ \phi_{e\mu}\end{pmatrix} = \frac{1}{4E}\begin{pmatrix}-\Delta m^2\cos 2\theta + A_{\mathrm{cc}} & \Delta m^2 \sin 2\theta \\ \Delta m^2 \sin 2\theta & \Delta m^2 \sin 2\theta - A_{\mathrm{cc}}\end{pmatrix}\begin{pmatrix}\phi_{ee}\\ \phi_{e\mu}\end{pmatrix} \tag{2.37}$$

with the effective Hamiltonian contained in the first two terms after the equality. An effective mixing matrix is described by

$$U_{\mathrm{M}} = \begin{pmatrix}\cos\theta_{\mathrm{M}} & \sin\theta_{\mathrm{M}} \\ -\sin\theta_{\mathrm{M}} & \cos\theta_{\mathrm{M},}\end{pmatrix} \tag{2.38}$$

along with an effective Δm^2 difference

$$\Delta m^2_{\mathrm{M}} = \sqrt{\left(\Delta m^2\cos 2\theta - A_{\mathrm{cc}}\right)^2 + \left(\Delta m^2 \sin 2\theta\right)^2}, \tag{2.39}$$

and the effective mixisng angle θ_{M} given by

$$\tan 2\theta_{\mathrm{M}} = \frac{\tan 2\theta}{1 - \dfrac{A_{\mathrm{cc}}}{\Delta m^2 \cos 2\theta}}. \tag{2.40}$$

When the electron density in matter is a specific value, N_e^{R}, a resonance for the transitions between the flavour states occurs,

$$N_e^{\mathrm{R}} = \frac{\Delta m^2 \cos 2\theta}{2E\sqrt{2}G_F}. \tag{2.41}$$

The angle at resonance is $\pi/4$, and if the region of matter at the resonant electron density is wide enough, a complete transition between the two flavours can occur and is called the Mikheyev Smirnov Wolfenstein (MSW) effect [27, 28]. These conditions are present for neutrinos propagating outwards from the core of stars, in the case of solar neutrinos and for supernova neutrinos. Star are composed of a plasma smoothly varying varying in density in a radial direction. The core of the Sun has a high electron density, $N_e \gg N_e^{\mathrm{R}}$ and so the initial production of neutrinos, where $\theta_{\mathrm{M}} \sim \pi/2$ and is therefore almost pure ν_2 will cross the resonance and do so adiabatically. The state will then remain in $\nu_2 = \sin\theta\nu_e + \cos\theta\nu_\mu$ and will primarily be composed of ν_μ even in the case of a small vacuum mixing angle θ.

2.4.3 Neutrino Oscillation Measurements

Several experiments have been designed and run to measure the oscillation parameters in the parameterisation of the PMNS matrix described in section 2.4.

Knowledge of the oscillation parameters θ_{12} and Δm^2_{21} comes from solar and reactor experiments with baselines of $\sim$100 km. The θ_{23} parameter is determined by atmospheric experiments and accelerator experiments with long baselines $\sim$100 km. θ_{13} has best been determined by reactor experiments with baselines $\mathcal{O}(1\,\text{km})$ and is also determined with long baseline accelerator experiments. $\left|\Delta m^2_{32}\right|$ is measured using atmospheric, long baseline accelerator and reactor experiments with baselines $\sim$1 km. The determination of the sign of Δm^2_{32} requires lifting the degeneracy between matter effects and the effect of δ_{CP} as illustrated in fig. 2.12. δ_{CP} is determined by long baseline experiments. A brief description of the experiments follows with the experimental best knowledge of the parameters presented in section 2.4.6.

2.4.3.1 Solar Experiments

Copious neutrinos are produced in the sun in several thermonuclear reactions, making up the standard solar model [29], which each have an associated energy spectrum shown in fig. 2.8. Experimentally observable quantities are used as input into the standard solar model and have been verified using data from satellite based experiments [30]. An experiment at the Homestake mine [31] measured the number of ^{37}Ar atoms that were produced in the reaction $\nu_e + {}^{37}\text{Cl} \rightarrow {}^{37}\text{Ar} + e^-$ on 615 t of tetrachloroethylene C_2Cl_4, and measured one third of the expected flux relative to the prediction from the solar model. The precursor to the Super-Kamiokande experiment, Kamiokande, measured the solar neutrino flux and specifically neutrinos from the ^{8}B reaction [32]. Gallium based experiments have also been performed, which are sensitive to lower energy neutrinos from the *pp* reactions, GALLEX [33, 34] and SAGE [35], and observed a deficit of about a half, suggesting an energy dependence. The Super-K experiment made more precise measurements [36] of the same process the Kamiokande experiment, consistent with the previous measurements. The SNO experiment made measurements with 1000 t of D_2O which allowed it to measure interactions in the CC, NC and ES channels. Each of these channels has a different sensitivity to the neutrino flavour states, with NC $\nu_\alpha + d \rightarrow p + n + \nu_\alpha$ being equally sensitive to all neutrino flavours, the CC channel $\nu_e + d \rightarrow p + p + e^-$ sensitive to the ν_e and the ES channel $\nu_\alpha + e^- \rightarrow \nu_\alpha + e^-$ sensitive to a mixture of the fluxes with the contribution from the ν_e dominant. Using the sensitivity to the ν_μ, ν_τ components of the flux the hypothesis that neutrinos oscillate in flight could be tested, finding that the measurements were consistent with a mixture of neutrino flavours in the solar neutrino flux, this is shown in fig. 2.7. The Borexino experiment [37] had the ability to measure the lower energy neutrinos which are much more abundant,

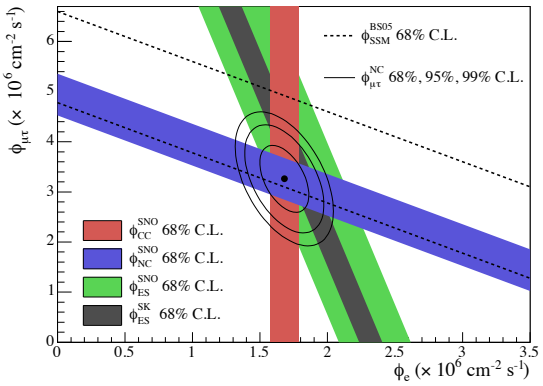

Figure 2.7: ^{8}B flux of $\nu_\mu + \nu_\tau$ vs flux of ν_e for the CC, NC, and ES channels as indicated by the filled bands. The black band shows the result from Super-K reported in [40]. Reproduced from[41].

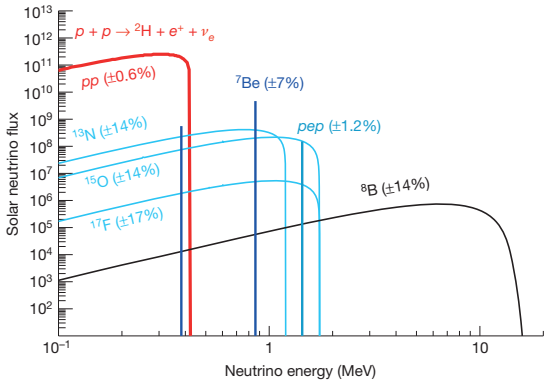

Figure 2.8: The solar neutrino flux as a function of energy for the thermonuclear processes considered in the standard solar model. Reproduced from [38]

including those originating from the *pp* reaction [38, 39], and better characterising the majority of the neutrino flux.

2.4.3.2 Atmospheric Neutrino Experiments

The Super-K experiment also made measurements of neutrinos originating from cosmic ray interactions and subsequent hadronic decays. The interaction model predicted a ratio of the flux ratio $(\nu_\mu + \bar{\nu}_\mu)/(\nu_e + \bar{\nu}_e) \simeq 2$. Measurements of the flux ratio as a function of zenith angle were made, which samples interactions from regions of the atmosphere at different distances from the detector. These measurements, shown in fig. 2.9 showed deviations from the ratio predicted by the flux model [42] and were consistent with two flavour oscillations [43].

The IceCube detector is an ice Cherenkov detector consisting of an array of 5160 10 inch Photomultiplier Tubes (PMTs) facing downwards at depths between 1450–2450 m in the ice at the South Pole. The PMTs are arranged on strings protected by pressure spheres (Digital Optical Modules (DOMs)) with a vertical spacing of 17 m between

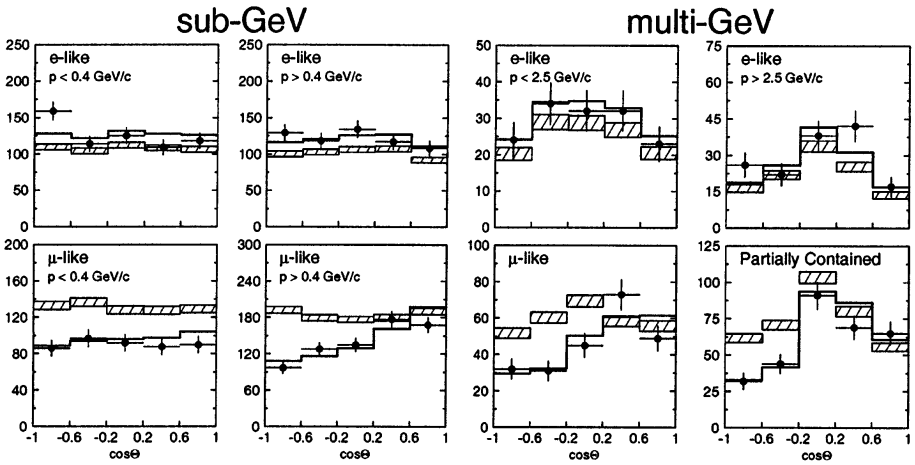

Figure 2.9: Super-K zenith angle distributions for the events in the sub-GeV range and the multi-GeV producing e-like or μ-like signatures. The hatched regions show the expectation based on the atmospheric flux model with no oscillations, whilst the bold line shows the best fit expectation for $\nu_\mu \leftrightarrow \nu_\tau$. Reproduced from [43]

DOMs on the strings, the strings are sunk into the ice in a triangular grid spaced at 125 m [44]. A more densely instrumented region with DOM spacing of 7 m and smaller (40–70 m) string spacing along with 50 % of PMTs having higher quantum efficiency and a threshold of 10 GeV is known as DeepCore [45]. A planned upgrade Precision IceCube Next Generation Upgrade (PINGU) will be able to determine the neutrino mass ordering to 3σ with less than 4 yr of data [46].

2.4.3.3 Reactor Experiments

Experiments using the intense $\bar{\nu}_e$ flux from nuclear reactors at different baselines can probe either θ_{13} and Δm^2_{32} at $\mathcal{O}(1\,\text{km})$ or at longer baselines $\mathcal{O}(10\,\text{km})$ the parameters θ_{12} and Δm^2_{21}. These are typically accomplished via the measurement of $\Delta m^2_{ee} \approx \cos^2\theta_{12}\left|\Delta m^2_{31}\right| + \sin^2\theta_{12}\left|\Delta m^2_{32}\right|$ [47]. Inverse β-decay $\bar{\nu}_e + p \rightarrow e^+ + n$ is used as the reaction channel.

The KamLAND experiment uses 1 kt liquid scintillator surrounded by 55 reactors at an average distance of 180 km, the exposure consists of 2881 t yr [48]. A plot of the data gathered showing the data to no oscillation expectation fig. 2.10 shows a characteristic oscillation pattern.

The Chooz experiment was a 0.09 % Gd loaded scintillator with a target mass of 5 t surrounded by a 17 t region of scintillator optically separated from a final 90 t region of scintillator to veto cosmic ray muons. The total live time of the experiment was 342.1 days[49, 50].

The Palo Verde experiment consisted of 11.3 t of 0.1 % Gd loaded scintillator [51] shielded

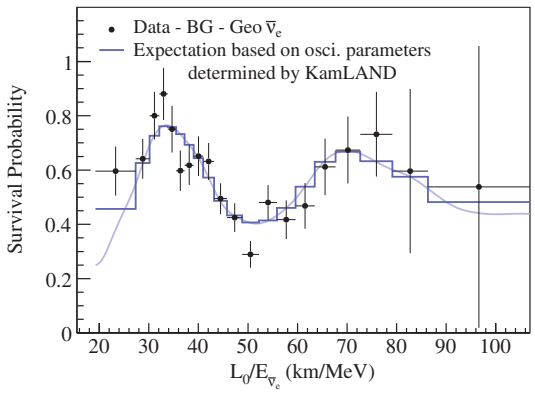

Figure 2.10: Figure from [48] showing the background and geoneutrino subtracted $\bar{\nu}_e$ spectrum from the average reactor flux as a ratio to the no-oscillation expectation measured by the KamLAND experimentx. This ratio is plotted as a function of L_0/E where the average distance L_0 is 180 km.

by oil and 105 t of water, non equidistant from three reactors, one at 750 m and two at 890 m, and took data for 350 days [52].

Double Chooz uses the same site as the Chooz experiment and uses two detectors a near detector, 400 m from the two reactors and far detector near the oscillation maximum at 1.05 km. The neutrino target consists of 10.3 m^3 of liquid scintillator loaded with Gd ($1\,g\,l^{-1}$) surrounded by a plain scintillator region 55 cm (22.3 m^3) thick to catch γ-rays itself surrounded by a shielding/veto region 105 cm thick (110 m^3) 462.72 days [53].

The Daya Bay experiment consists of identical modular detectors, with two sets of two near detectors and four far detectors. Each detector contains 20 t of liquid scintillator loaded with 0.1 % Gd by mass which are in turn nested within 20 t of plain scintillator, and an outer layer of mineral oil. The data collected corresponded to 1230 days of operation, and the flux originates from 6 reactor pairs [54].

The Reactor Experiment for Neutrino Oscillation (RENO) consists of two identical detectors, 290 m and 1380 m from a flux from 6 linearly arranged equidistant (260 m)reactors. The detectors contain 16 t of liquid scintillator loaded with 0.1 % Gd as the target, with 29 t plain scintillator, a buffer region and an outer detector acting as a shield and veto [55].

2.4.3.4 Accelerator Experiments

Accelerators can be used to produce beams of primarily ν_μ or $\bar{\nu}_\mu$ neutrinos via hadron production and decay. A proton beam is incident on a target and the charged hadrons that are produced are focussed with magnetic horns to increase the beam intensity and select the primary ν_μ or $\bar{\nu}_\mu$ beam mode.

Main Injector Neutrino Oscillation Search (MINOS) was a long baseline experiment with near (0.1 kt) and far (3.3 kt) detectors 1.04 km and 795 km from beam target and on the beam axis. These were tracking calorimetric detectors of the same technology made up of layers of magnetised steel and scintillator to measure particle momentum [56].

The long baseline T2K experiment is described in more detail in chapter 3, briefly it operates 2.5°(22.9 mrad) off-axis with a beam peak $E_\nu \sim 0.6$ GeV with a near detector (ND280) and far detector (Super-K) at 280 m and 295 km from the beam target.

NuMI Off-axis ν_e Appearance (NOνA) is a 0.84°(14.6 mrad) long baseline off-axis experiment with near and far detectors 1 km and 810 km from the beam target with a beam peak $E_\nu \sim 1.9$ GeV. The near and far detectors are composed of the same polyvinyl chloride scintillator cells in layers alternately oriented in the vertical and horizontal directions, the total mass of the far detector is 14 kt. The events are fed into a Convolutional Visual Network (CVN), which selects from beam induced CC reactions from $\nu_{e,\mu,\tau}$ and NC events and cosmogenic events. Muon-like tracks are selected after Kalman filtering [57] by a k-nearest neighbour classifier [58] which scores tracks based on: likelihoods in dE/dx and scattering consistent with a single particle, the total track length, and consistency with having minimum-ionizing-like dE/dx in the detector planes. Far detector events must also be signal like based on a Boosted Decision Tree (BDT) which is trained on simulation and cosmic data.A similar process is applied for the selection of ν_e events, where ν_e CC events are initially selected by the same CVN then further selected by building event vertices using a Hough transforms in the two available two dimensional views for both near and far detectors. Events are removed: if they have large amounts of transverse energy as they are typically cosmogenic, are not contained in the detector, have too many hits for reconstruction, or are close in time or space in the detector. A different BDT is used at the far detector to select for signal like events. [59]

The Liquid Scintillator Neutrino Detector (LSND) experiment measured oscillations in a short baseline (30 m) accelerator based experiment and observed an excess of $\bar{\nu}_e$ events at 3.8 σ[60]. The Mini Booster Neutrino Experiment (MiniBooNE) experiment was designed in part to search for the excess found by the LSND experiment at the same L/E. Results with 12.84×10^{20} POT in neutrino mode show an excess of ν_e events at 4.5 σ, and in combination with the antineutrino mode 11.27×10^{20} POT an excess at 4.8 σ is found. Taken in combination the MiniBooNE and LSND experiments show an excess at 6.1 σ [61]. The Short-Baseline Neutrino (SBN) program, made up of a set of three detectors, at Fermilab is designed to resolve this anomaly [62], with the MiniBooNE detector continuing to operate in the same beamline.

2.4.4 Charge Parity ($\mathcal{CP}$) Violation

One of the major unresolved questions in modern physics is the reason for the observed matter antimatter asymmetry in the universe. The Standard Model contains a mechanism for violating $\mathcal{CP}$ (CPV) through the Cabbibo-Kobayashi-Masakawa (CKM) quark mixing matrix which was designed to accommodate the observed CPV decays of K mesons [63]. Evidence for $\mathcal{CP}$ in λ_b^0 baryons has been observed [64]. However the predominance of matter over antimatter in the universe cannot be explained using these observations. A possible mechanism for this asymmetry to manifest in the universe requires that: baryon number is not conserved, the $\mathcal{C}$ and $\mathcal{CP}$ symmetries must be violated, unless $\mathcal{CPT}$ violating transitions are allowed these previous two conditions must proceed out of thermal equilibrium [65]. The discovery of neutrino masses suggests that an additional source of $\mathcal{CP}$ violation may come from the lepton sector. The resulting lepton number asymmetry may be converted to a baryon number asymetery via sphaleron transitions [66] in a process called leptogenesis.

The charge conjugation operator $\mathcal{C}$ takes a particle, p, to its antiparticle, $|p\rangle \xrightarrow{\mathcal{C}} -|p\rangle$, and is not a symmetry of weak interactions, neither left handed antineutrinos nor right handed neutrinos have been observed. The operator $\mathcal{P}$ was defined in section 2.1.1, and was first shown to be maximally violated in the decay of ^{60}Co [67] and verified in an experiment from a π^+ decay [68]. Both $\mathcal{C}$ and $\mathcal{P}$ when applied twice return the particle to its initial state $\mathcal{C}^2 = \mathcal{P}^2 = I$, and the parity of a composite system, in its ground state, is the product of the parities of the constituent particles. The eigenvalues taken by the operators $\mathcal{C}$ and $\mathcal{P}$ are ± 1, with the convention that the parities of the fermions and antifermions are 1 and -1 respectively.

The product $\mathcal{CPT}$, where the operator $\mathcal{T}$, reverses the sign of the time component $x^\mu \xrightarrow{\mathcal{T}} (-x^0, \vec{x})$, must be conserved as shown by the $\mathcal{CPT}$-theorem, which shows that it is not possible to construct a quantum field theory without this symmetry, although from a phenomenological point view it is conceivable that $\mathcal{CPT}$ violation could occur in the neutrino sector and limits set from cosmological data [69]. $\mathcal{CP}$ invariance can be checked by comparing $P(\nu_\alpha \to \nu_\beta; t)$ with $P(\bar{\nu}_\alpha \to \bar{\nu}_\beta; t)$ which are appearance channels, and are used in this thesis. $\mathcal{T}$ violation can be searched for in the neutrino transition $P(\nu_\beta \to \nu_\alpha; t)$.x The combination CPT can be searched for by looking at $P(\nu_\alpha \to \nu_\beta; t)$ with $P(\bar{\nu}_\beta \to \bar{\nu}_\alpha; t)$, a diagrammatic representation of the symmetries can be seen in fig. 2.11, although it is extremely difficult to search for transitions which involve ν_τ. Looking at the transition probabilities in the space $P(\nu_\mu \to \nu_e)$, $P(\bar{\nu}_\mu \to \bar{\nu}_e)/P(\nu_e \to \nu_\mu)$ as shown in fig. 2.12 shows how a search for $\mathcal{CP}$ might be carried out experimentally, oscillation probabilities are calculated with matter effects (solid) and in vacuum (dashed) for several transitions with normal hierarchy (red) and the inverted hierarchy (blue) $P(\nu_\mu \to \nu_e)$, $P(\bar{\nu}_\mu \to \bar{\nu}_e)$. The yellow (normal hierarchy) curve and the green (inverted hierarchy) show $P(\nu_\mu \to \nu_e)$, $P(\nu_e \to \nu_\mu)$.

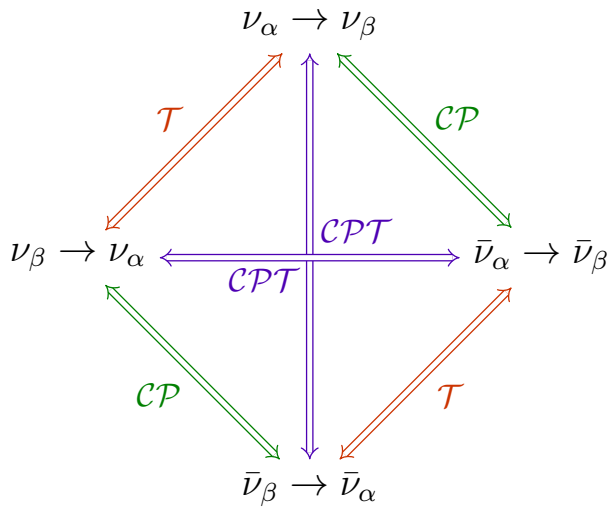

Figure 2.11: Diagram illustrating action of the $\mathcal{T}$, $\mathcal{CP}$, $\mathcal{CPT}$ operators when acting on the neutrino flavour transitions, $\nu_\alpha \to \nu_\beta$, for neutrinos of flavour $\alpha = e, \mu, \tau$ where α can equal β.

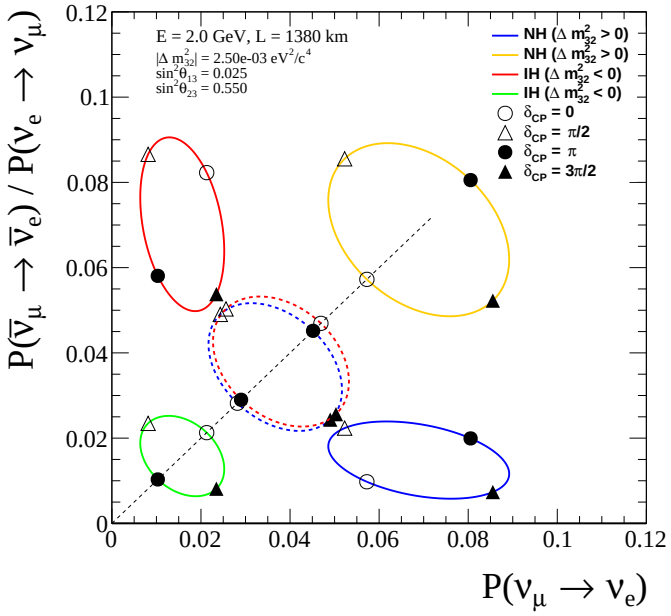

Figure 2.12: Biprobability diagram in the space $P(\nu_\mu \to \nu_e)$, $P(\bar{\nu}_\mu \to \bar{\nu}_e)/P(\nu_e \to \nu_\mu)$, the $\mathcal{CP}$ and $\mathcal{T}$ transformed spaces, oscillation parameters are fixed apart from δ_{CP} which varies between $\delta_{\text{CP}} \in [0, 2\pi]$. The red and blue solid curves show the normal and inverted hierarchies with matter effects, whilst the dashed curves show oscillations in vacuum in both cases for $P(\nu_\mu \to \nu_e)$ vs $P(\bar{\nu}_\mu \to \bar{\nu}_e)$. The yellow and green curves show the normal and inverted hierarchies for $P(\nu_\mu \to \nu_e)$ and $P(\nu_e \to \nu_\mu)$ respectively. The baseline and energy correspond to a DUNE like scenario where matter effects mimicking $\mathcal{CP}$ violation can be separated.

2.4.5 Jarlskog Invariant

An expression for $\mathcal{CP}$ violation in a way which is independent of the rephasing of the leptonic (or quark) fields can be accomplished using the Jarlskog Invariant, J, [70]

$$J = \mathfrak{Im}\left[U_{\mu 3} U_{e2} U^*_{\mu 2} U^*_{e3}\right] \tag{2.42}$$

where the U are elements of the matrix eq. (2.20). For the case of mixing of three active neutrinos all the imaginary parts of the rephasing invariant quartic products $U^*_{\alpha k} U_{\beta k} U_{\alpha j} U^*_{\beta j}$ are equal apart from a sign due to unitarity relations. In the parameterisation of the PMNS matrix U, J is ,

$$J = c_{12} s_{12} c_{23} s_{23} c^2_{13} s_{13} \sin\delta_{\rm CP} = \frac{1}{8} \sin 2\theta_{12} \sin 2\theta_{13} \sin 2\theta_{23} \cos\theta_{13} \sin\delta_{\rm CP}. \tag{2.43}$$

In the quark sector the value of $J_{\rm CKM} = (3.18 \pm 0.15) \times 10^{-5}$ [71] which is significantly different from that which is found for the lepton sector, $0.026(0.027)|\sin\delta_{\rm CP}| \lesssim |J_{\rm CP}| \lesssim 0.035|\sin\delta_{\rm CP}|$ [71], where the size of the $\mathcal{CP}$ violation effects are mainly dependent on the value of $\delta_{\rm CP}$.

2.4.6 Global fit results

Global fits to the data [72, 73] are used to extract the six oscillation parameters using data gathered from the categories of experiments listed in section 2.4.3. Results of these analysis are shown in fig. 2.13, showing the parameter values with respect to a local minimum of either the NO or IO or with and fig. 2.14.

The fit results from the analysis in [72] determine a maximum allowed value of $\mathcal{CP}$ violation of $J^{max}_{\rm CP} = 0.0329 \pm 0.0007\,(^{+0.0021}_{-0.0024})$ at 1 σ and (3σ) where this is expressed using the Jarlskog Invariant in eq. (2.43).

	Normal Ordering (best fit)		Inverted Ordering ($\Delta\chi^2 = 0.83$)		Any Ordering
	bfp $\pm 1\sigma$	3σ range	bfp $\pm 1\sigma$	3σ range	3σ range
$\sin^2\theta_{12}$	$0.306^{+0.012}_{-0.012}$	$0.271 \to 0.345$	$0.306^{+0.012}_{-0.012}$	$0.271 \to 0.345$	$0.271 \to 0.345$
$\theta_{12}/^\circ$	$33.56^{+0.77}_{-0.75}$	$31.38 \to 35.99$	$33.56^{+0.77}_{-0.75}$	$31.38 \to 35.99$	$31.38 \to 35.99$
$\sin^2\theta_{23}$	$0.441^{+0.027}_{-0.021}$	$0.385 \to 0.635$	$0.587^{+0.020}_{-0.024}$	$0.393 \to 0.640$	$0.385 \to 0.638$
$\theta_{23}/^\circ$	$41.6^{+1.5}_{-1.2}$	$38.4 \to 52.8$	$50.0^{+1.1}_{-1.4}$	$38.8 \to 53.1$	$38.4 \to 53.0$
$\sin^2\theta_{13}$	$0.02166^{+0.00075}_{-0.00075}$	$0.01934 \to 0.02392$	$0.02179^{+0.00076}_{-0.00076}$	$0.01953 \to 0.02408$	$0.01934 \to 0.02397$
$\theta_{13}/^\circ$	$8.46^{+0.15}_{-0.15}$	$7.99 \to 8.90$	$8.49^{+0.15}_{-0.15}$	$8.03 \to 8.93$	$7.99 \to 8.91$
$\delta_{\mathrm{CP}}/^\circ$	261^{+51}_{-59}	$0 \to 360$	277^{+40}_{-46}	$145 \to 391$	$0 \to 360$
$\frac{\Delta m^2_{21}}{10^{-5}\ \mathrm{eV}^2}$	$7.50^{+0.19}_{-0.17}$	$7.03 \to 8.09$	$7.50^{+0.19}_{-0.17}$	$7.03 \to 8.09$	$7.03 \to 8.09$
$\frac{\Delta m^2_{3\ell}}{10^{-3}\ \mathrm{eV}^2}$	$+2.524^{+0.039}_{-0.040}$	$+2.407 \to +2.643$	$-2.514^{+0.038}_{-0.041}$	$-2.635 \to -2.399$	$\begin{bmatrix} +2.407 \to +2.643 \\ -2.629 \to -2.405 \end{bmatrix}$

Figure 2.13: Oscillation parameters for the three flavour case, from a global fit to data extant after NEUTRINO 2016 [74]. The numbers in the first two columns are relative to the local minimum for the ordering hypothesis, the third column minimises also with respect to the ordering. Reproduced from [72].

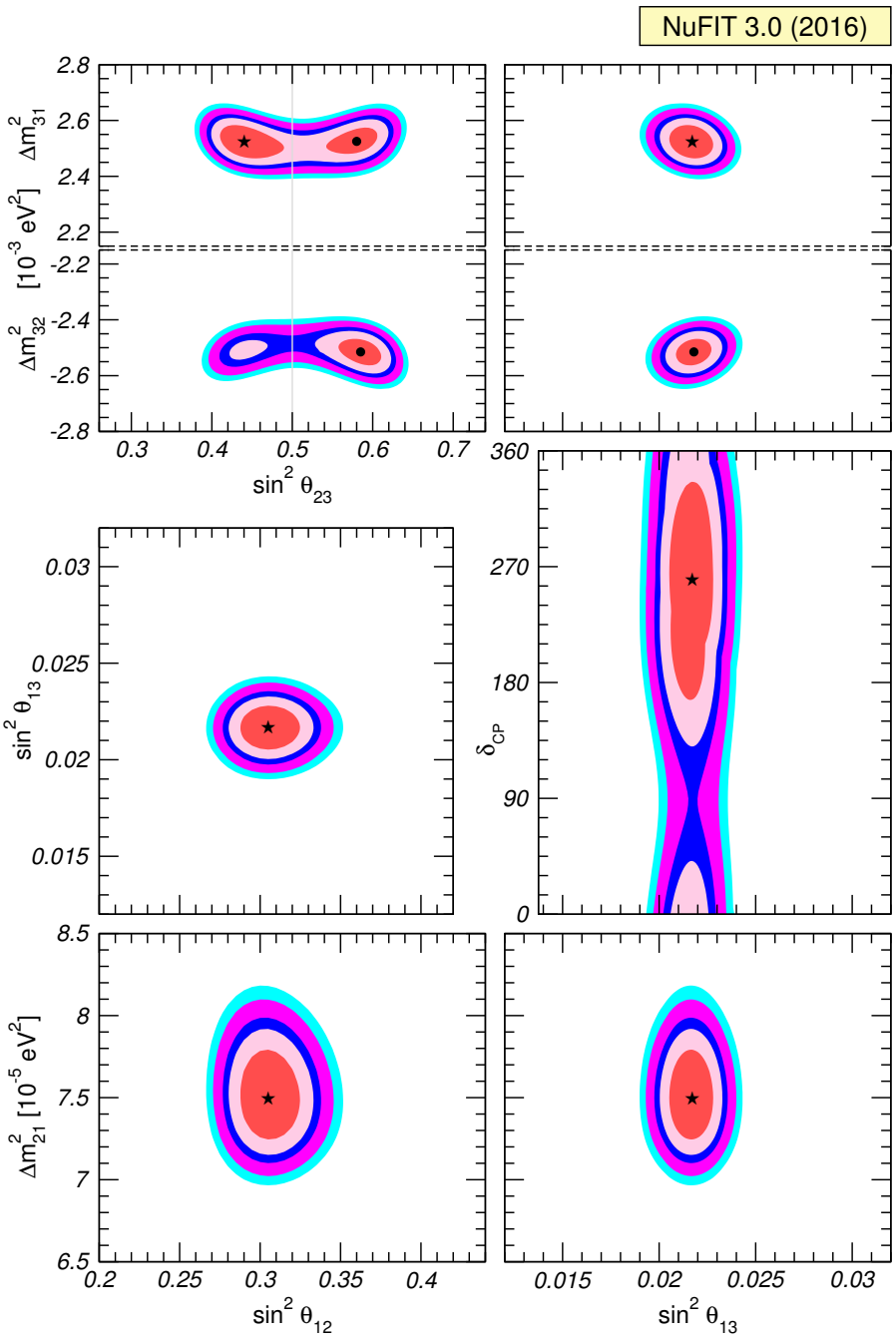

Figure 2.14: Global fit results from a 3 ν oscillation analysis reproduced from [72]. Each of the contours correspond to 1σ, 90 %, 2σ, 99 %, 3σ confidence levels, these are the result of marginalising the oscillation parameters not shown in the plot. Data from reactor experiments is used in the fits, including short <100 m baseline experiments. The atmospheric mass squared splitting uses Δm^2_{31} for NO and Δm^2_{32} for IO. The lower four plots are obrained from minimising $\Delta\chi^2$ with respect to the mass ordering.

At the time that the analysis described in chapter 5 together with validation studies were performed using the value for θ_{13} and its uncertainty derived from reactor experiments, the "reactor constraint" in the 2016 compilation of the Particle Data Group (PDG). Due

to time constraints it was not possible to reproduce the whole analysis with the, at the time, newly available PDG values for the reactor constraint.

3 T2K Experiment

The T2K long baseline neutrino experiment is made up of three primary constituent parts: the neutrino beam and parent proton beamline located in the Japan Proton Accelerator Research Centre (J-PARC), a ND280, and a far detector, Super-Kamiokande (Super-K). A neutrino beam, initially composed primarily of ν_μ, or $\bar{\nu}_\mu$, depending on the running mode, is produced at J-PARC by hadron decays resulting from proton interactions in a graphite target. The ND280 complex of detectors is located ~280 m from the target, where the first set of neutrino beam induced interactions are observed. The beam continues to propagate 295 km through Japan to Super-K where neutrino interactions are once again observed. The location of the detectors and the path that the beam takes is shown in fig. 3.1.

3.1 J-PARC Proton Accelerator and Neutrino Beam

The proton beam (which ultimately generates the neutrino beam) at J-PARC is created by a series of three accelerators: a Linear Accelerator (LINAC) and two synchrotrons, the Rapid-Cycling Synchrotron (RCS) and the Main Ring (MR), their arrangement at J-PARC is depicted in fig. 3.2. An initial beam of H^- ions are accelerated to 400 MeV in the LINAC, injected into the RCS where they are stripped of e^- and accelerated to 3 GeV. The RCS cycles at 25 Hz, and contains two proton bunches per cycle [76] which are injected into the MR. The MR accelerates the protons to 30 GeV, and achieved 470 kW in Run 8 (2017), with planned upgrades to reach its design power of 750 kW in 2018-2023 and eventually 1.3 MW beyond 2023 [77].

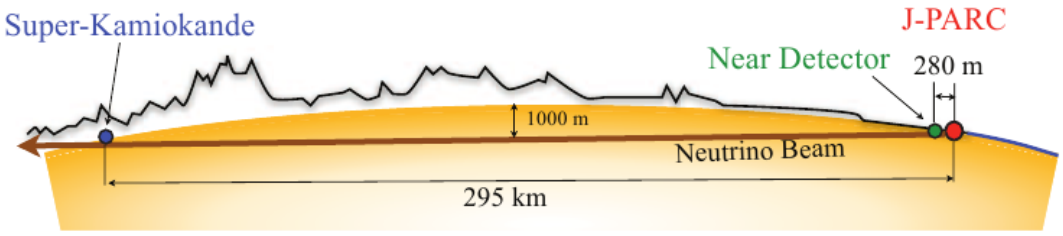

Figure 3.1: A diagramatic overview of the T2K experiment near and far detector sites and path through Japan. Reproduced from [75]

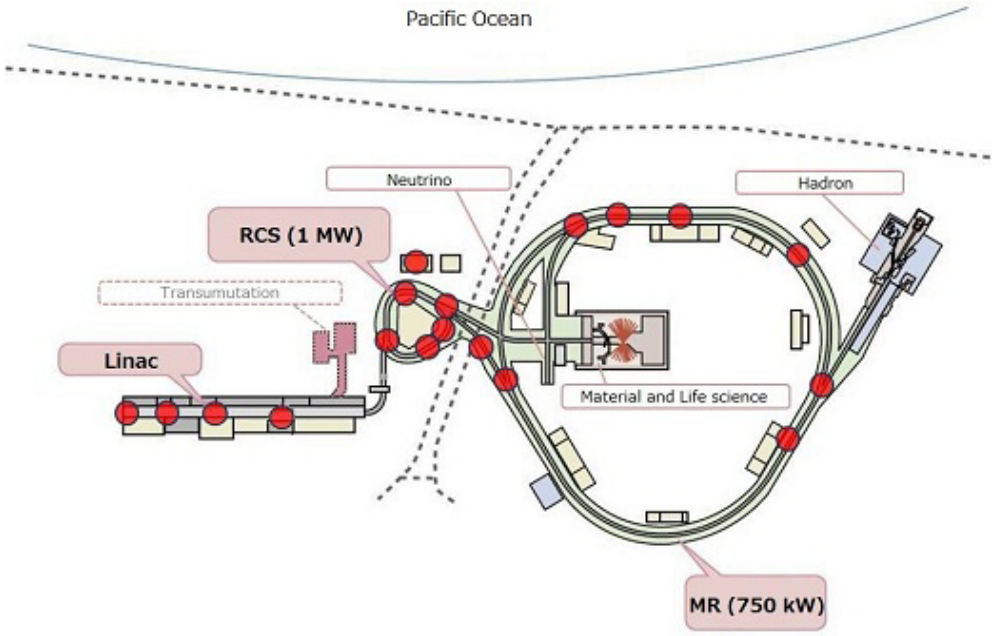

Figure 3.2: Diagram of the J-PARC proton beam accelerator facility showing the position on site of: the linear accelerator (LINAC), rapid cycling synchrotron (RCS), and the main ring (MR)– source JPARC public website

3.1.1 Primary Beamline

The proton bunches are extracted from MR to the neutrino beamline, which is composed of two sections as depicted in fig. 3.3. The primary section steers the proton beam towards Kamioka and allows for a range off-axis angles, 2–3°, with respect to Super-K and is operated at 2.5° or 43 mrad off-axis. Each beam spill extracted from the MR consists of an 8-bunch structure with 80 ns bunch width and 581 ns bucket length, which repeats every 2.48 s [77], see fig. 3.4..

The primary beamline is made up of an initial preparation section which contains 11

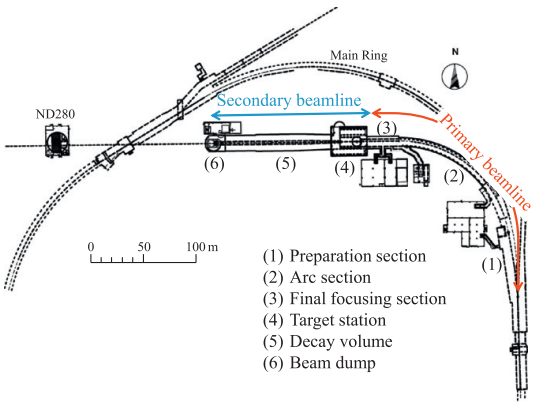

Figure 3.3: Schematic of the neutrino beam facility at J-PARC, marked "Neutrino" in fig. 3.2 detailing the dedicated beamline components for the neutrino beam production.

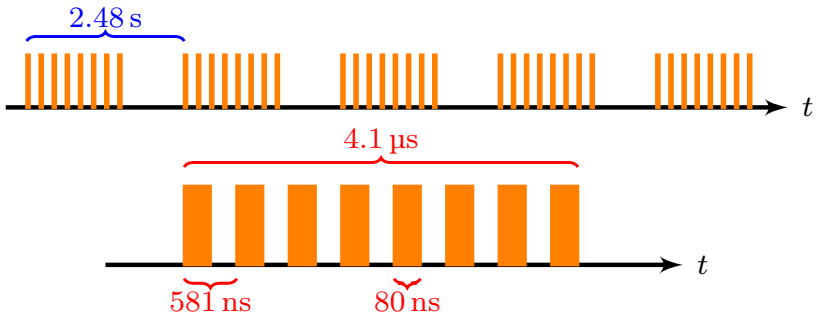

Figure 3.4: Beam bunch structure at T2K, showing the bunch repetition rate (top), and the bunch timing structure (bottom).

normal conducting magnets, a more strongly curved arc section with 28 superconducting combined function magnets (SCFMs) and a final focussing section with 10 conducting magnets. Following the beam through the described beamline sequence, these sections perform an initial bending and focussing of the proton beam from the MR and ready the beam for transport through the arc section. The arc section strongly deflects the beam towards Super-K, followed by fine adjustment of the beam's position, angle, and size at the target in the final focussing section. There are a series of instruments in the primary beamline which monitor beam intensity, loss, position and profile. Beam intensity is monitored by 5 current transformers (CTs), loss is instrumented by 50 beam loss monitors (BLMs), position is monitored by 21 electrostatic monitors (ESMs), 19 segmented secondary emission monitors (SSEMs) measure the beam profile during beam tuning. The beam intensity monitors are used to measure T2K's exposure, recorded in POT. Table 3.1 shows the exposures achieved in each T2K run period. A plot of the cumulative POT in each run period and the beam power can be seen in fig. 3.5.

	Period	Dates	POT$\times 10^{20}$	
ν	Run 1	01/2010 – 06/2010	0.323	
ν	Run 2	11/2010 – 04/2011	1.108	
ν	Run 3	03/2012 – 06/2012	1.579	
ν	Run 4	09/2012 – 05/2013	3.560	6.57
$\bar{\nu}$	Run 5	05/2014 – 06/2014	0.506	
$\bar{\nu}$	Run 6	11/2014 – 06/2015	3.505	4.011
$\bar{\nu}$ / ν	Run 7	02/2016 – 05/2016	2.18 / 1.12	
ν	Run 8	10/2016 – 05/2017	7.170	

Table 3.1: Table of run periods and exposure in protons on target at T2K, separated into neutrino and antineutrino running

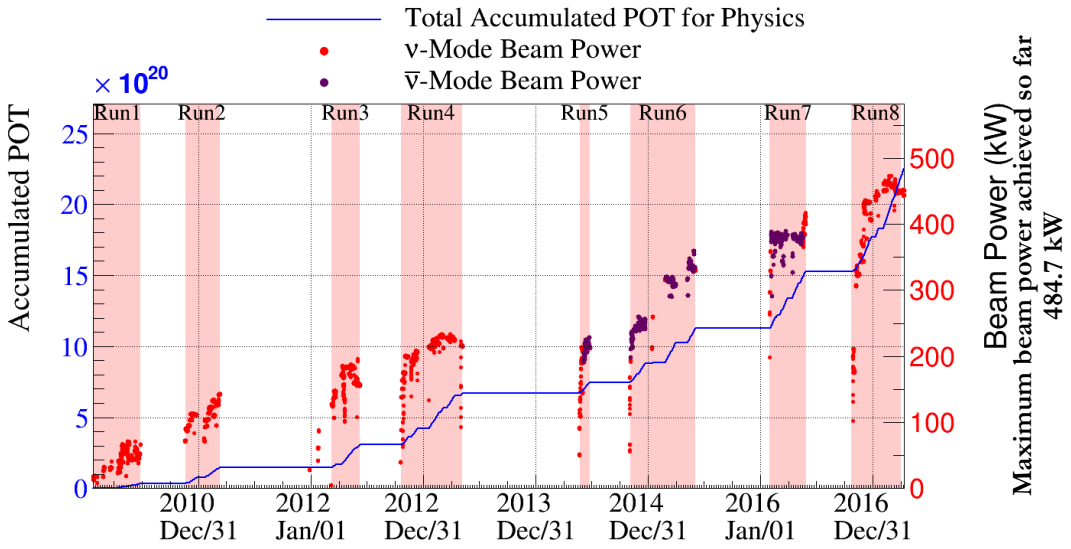

Figure 3.5: Cumulative delivered Protons On Target (POT) and beam power ν, and $\bar{\nu}$ for the T2K running periods considered in this thesis.

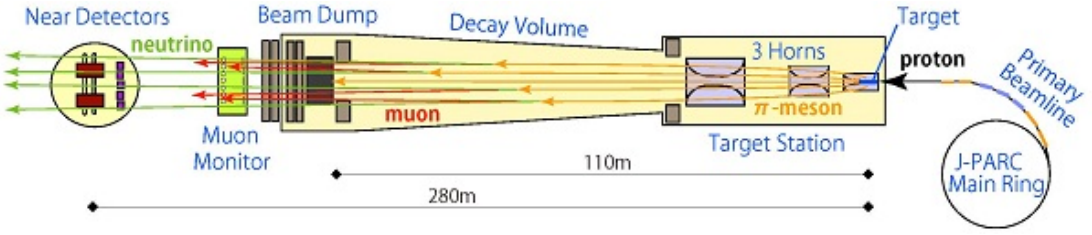

Figure 3.6: Schematic of the secondary neutrino beamline at J-PARC. The primary proton beam is shown impinging the target, the resulting hadrons are focussed by the horns. The hadrons and any decaying particles impinge on the beam dump, any muons passing through monitored by the muon monitor, neutrinos then interact with the detectors in the near pit. The target station section does not depict the carbon baffle located upstream of the target in the target station which collimates the proton beam

3.1.2 Secondary Beamline

The secondary beamline which is shown in fig. 3.6 consists of a baffle, target, focussing horns, decay volume, beam dump and two beam monitors. The target station contains a graphite baffle, which is 1.7 m long with a bore 30 mm in diameter which serves to collimate the beam. An optical transition monitor (OTR) [78] monitors the 30 GeV proton beam from the primary beam profile just before it strikes the target. The beam then interacts with the 91.4 cm, (1.9 interaction length, 85 % of protons interact) graphite target, producing primarily pions and kaons, this is further discussed in section 4.1. The particles are then focussed by the set of three magnetic focussing horns and propagate down a water cooled decay volume filled with helium to minimise pion absorption and the production of tritium and NO_x products. At the end of the decay volume particles impinge on the beam dump, and any particles which pass through the beam dump are monitored by the muon monitor.

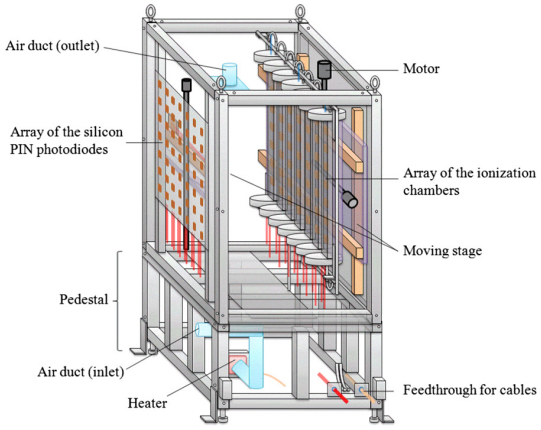

Figure 3.7: The Muon Monitor (MUMON) located after the beam dump designed to monitor the secondary beam. The incoming beam is incident on the left side of the detector, reproduced from [80]

The charged mesons resulting from the proton interaction with the graphite target are focussed by the previously mentioned system of three magnetic horns. Each of these consists of a pair of coaxial conductors, which generate a magnetic field of 2.1 T when at their design current of 320 kA, although are currently operated at 250 kA. The first horn serves to collect the generated mesons while the two downstream horns focus the mesons [79]. Depending on the direction of the current in the horns, termed either forward horn current (FHC) or reverse horn current (RHC), the neutrino beam composition can be primarily ν, in FHC mode or $\bar{\nu}$ in RHC mode. The analysis in this thesis is performed on data collected in both running modes. Further details on the composition of the beam can be found in section 4.1.

A beam dump consisting of 75 t of graphite sandwiched by iron plates, is located at the end of the ∼96 m decay volume, and is designed to only allow muons with $p_\mu \gtrsim 5\,\text{GeV}$ to pass through and absorb most other remaining particles. The secondary beam is continuously monitored, bunch by bunch, after the beam dump, by a muon monitor (MUMON) [80]. This makes measurements of the beam profile using the arrangement shown in fig. 3.7 of 49 sensors in each of two detection technologies, a columnar arrangement of seven argon filled ionisation chambers each containing seven sensors, preceded by a seven by seven array of silicon PIN photodiodes. Using MUMON the beam direction is tuned to within the systematic error of 0.3 mrad [80].

3.1.3 Off-Axis Beam

Neutrino oscillation has a dependence on L/E_ν, where E_ν is the neutrino energy and L is the propagation length see section 2.4. This implies that a more sharply defined neutrino energy is desirable to observe a clear oscillation signal, due to the difficulty in reconstructing the interaction neutrino's energy. The approach taken at T2K is to use

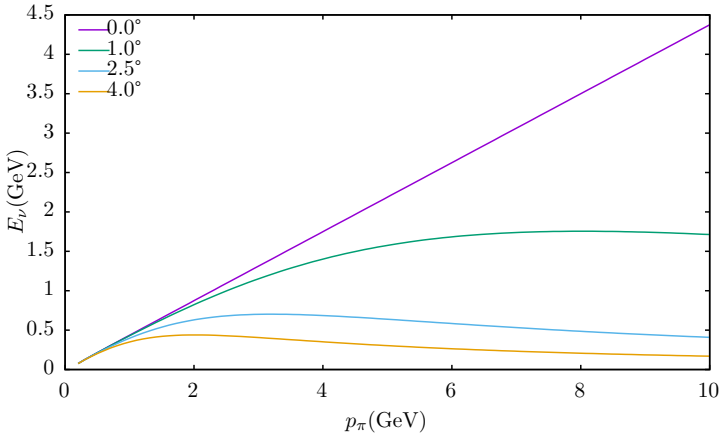

Figure 3.8: Neutrino energy vs pion momentum for several off-axis angles, θ_{OA} from eq. (3.1), including the 2.5° T2K operating angle.

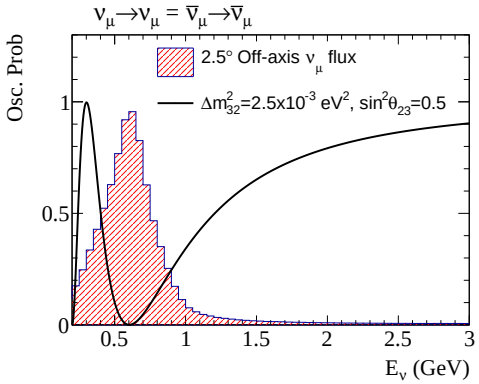

Figure 3.9: Oscillation probability for $P(\nu_\mu \to \nu_\mu)$ overlaid with the flux for the T2K experiment at Super-Kamiokande.

the angular dependence of pion (and other mesons) decay to select the desired neutrino energy .

$$E_\nu = \frac{m_\pi^2 - m_\mu^2}{2(E_\pi - p_\pi \cos\theta_{\mathrm{OA}})} \tag{3.1}$$

where $m_{\pi,\mu}$ are the masses of the pion and muon respectively, E_π is the energy and p_π is the momentum of the pion and θ_{OA} is the angle from the pion momentum vector, following from the proposal in [81]. When the off axis angle increases the contribution that the momentum term makes to the denominator decreases, which flattens the variation in neutrino energy. This results in a peaked neutrino energy distribution fig. 3.8, where the energy can be selected by variation of the off-axis angle. The 2.5° (or 43.63 mrad) angle that is chosen for T2K gives a peak neutrino flux energy of 0.6 GeV, see fig. 3.9 which corresponds to the location of the first oscillation maximum for ν_μ disappearance at Super-K, the corresponding probabilities for $\nu_e/\bar{\nu}_e$ appearance are shown in fig. 3.10. A discussion of how the flux prediction is generated can be found in section 4.1, and the flux composition for FHC and RHC modes for each flavour in fig. 4.6.

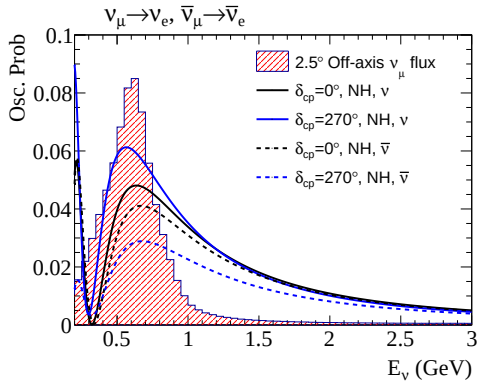

Figure 3.10: Oscillation probability for $P(\nu_\mu \to \nu_e)$ and $P(\bar{\nu}_\mu \to \bar{\nu}_e)$ overlaid with the flux for the T2K experiment at Super-Kamiokande, showing the $\mathcal{CP}$ conserving value of 0° and the maximally violating value 270°, for Normal Hierarchy.

3.2 Near Detector Complex

The T2K near detectors are a heterogeneous set of detectors designed in order to satisfy a number of physics goals, including the measurement of long baseline and to a lesser extent short baseline neutrino oscillations. A precise determination of the energy spectrum and flavour composition of the neutrino beam is required for the measurement of neutrino oscillations. The primary physics goal is the precise characterisation of the unoscillated neutrino flux and the measurement of cross sections, for which a number of different sub detectors are used [75], the arrangement of the detector is illustrated in fig. 3.11.

After the beam has travelled through the muon monitor it passes through the soil/sand at J-PARC towards a site which is located 280 m from the target. This site contains a number of detectors, of which the primary detector is a magnetised tracking detector known as ND280, located 2.5° off-axis. This detector consists of a number of subdetectors contained within a dipole magnet from the UA1 experiment [82], which operates at 0.2 T. The magnet flux return yokes are composed of 16 iron plates separated by air gaps whose three innermost gaps are populated with scintillator slabs threaded with wavelength shifting (WLS) fibre of radius 1 mm matched to Multi Pixel Photon Counter (MPPC) of dimension $1.3 \times 1.3\,\mathrm{mm}^2$ developed specially for the T2K experiment [83]. The scintillator plates inserted in the magnet make up the Side Muon Range Detector (SMRD). The SMRD is designed so that areas where lower energy loss are expected due to the detector material composition are more heavily instrumented [84]. The previously described detection technology of scintillator bars threaded with WLS fibres readout by MPPCs are used extensively throughout the detector, due the MPPCs insensitivity to the detector's magnetic field. Inside the magnet solenoid coil a number of electromagnetic calorimeters (ECals) surround the innermost portions of the detector, these are designed to detect γ-rays and any other electromagnetic radiation not converted in the inner detector. The upstream portion of the detector consists of a π^0 detector (PØD), and downstream of this is the tracking portion of the detector which is an alternating stack

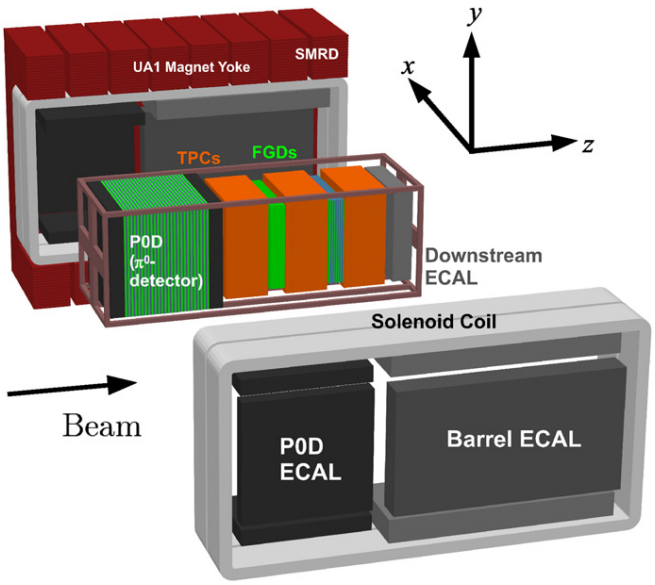

Figure 3.11: ND280 off axis constituent detectors, PØD, Ecals, FGDs, TPCs, magnet solenoid coil, and SMRD, within the UA1 magnet – reproduced from [75]

of three time projection chambers (TPCs) and two fine grained detectors (FGDs), an event display from the tracker region is shown in fig. 3.12.

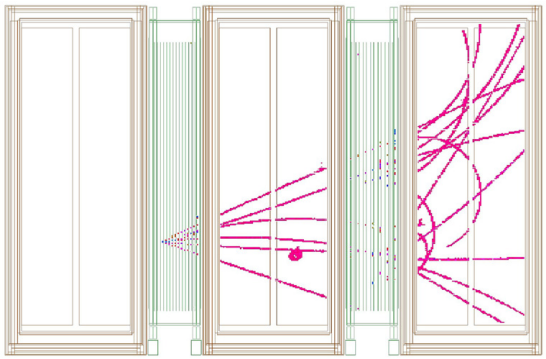

Figure 3.12: An event display from the tracker region of ND280 showing a possible deep inelastic scatter originating in FGD1, figure reproduced from [85]

A separate modular cross shaped detector located on the beam axis made up of iron and scintillator planes, Interactive Neutrino GRID (INGRID), is also housed in the same pit as the primary ND280 detector. The cross shape of the detector spans the beam and makes measurements of the neutrino beam profile.

3.2.1 ND280 Detector

3.2.1.1 Pi-zero Detector (PØD)

The π^0 detector (PØD) is instrumented by triangular scintillator bars in perpendicular x and y views with WLS fibres read out by MPPCs. These bars are 2133 mm long vertically and 2272 mm horizontally. The scintillator planes are interleaved with stainless steel clad lead sheets (4.5 mm thick) in two ECal sections which are upstream and downstream of a water target section. The water target section is divided into an upstream section and a central section, this section is composed of high density polyethylene (HDPE) water bags and brass sheets as targets. The primary objective of this water filled section is to measure the neutral current process $\nu_\mu + N \rightarrow \nu_\mu + N + \pi^0 + X$ on the same nuclear target and with same neutrino beam as at Super-K [86]. The (PØD) detector can operate with (15 800 kg) or without water (12 900 kg) in the HDPE bags, and can determine the rate on water by using the difference in these two configurations.

3.2.1.2 Fine Grained Detectors (FGDs)

The two FGDs, FGD1 and FGD2, provide a neutrino interaction target mass and the tracking of charged particles originating from the interaction. Short-ranged particles are important in identifying the type of neutrino interaction, and the granularity of the FGDs is such that the tracks and their direction from the interaction can be resolved. The FGDs differ in composition: FGD1 is composed of 30 layers of 9.6×9.6 mm scintillator bars alternately oriented in x and y directions transverse to the beam and bonded together into 15 "xy" modules of dimensions $186.4 \times 186.4 \times 2.02$ cm, FGD2 has seven scintillator xy modules alternating with total of 6, 2.5 cm thick layers of water making up 42 % of the FGD mass, contained in hollow corrugated polycarbonate panels [85]. As will be discussed in section 3.3.1, any particles that are detected at Super-K have to be above an energy threshold for detection, this means that hadrons are often invisible. The FGDs are used to characterise these and other irreducible backgrounds. The FGDs work in conjunction with the TPCs (section 3.2.1.3) they are thin enough so that charged leptons can leave tracks in the TPCs, their particle identification can discriminate between protons and muons or pions, and measure short ranged particles.

Constraints from both FGD1 and FGD2 are used in this thesis and are the only targets at the near detector that are used in this thesis. The inclusion of FGD2 allows constraints on the neutrino oxygen cross section parameters to be imposed, see section 4.3, and is essential for the prediction of events at Super-K. A fiducial mass 1100 kg of CH_2 makes up FGD1 and the described structure of CH_2 and H_2O in FGD2 with a target mass of water 579 kg, the remainder CH_2 as in FGD1. The composition of the water filled panels in FGD2 is designed so that it nearly matches that of a mixture of water and

scintillator allowing for interactions on water to be determined by subtraction of the rates in the two FGDs. The speed dependent nature of energy deposition in the FGD is exploited for particle identification. The energy deposition for a particular track range has a different form for the protons, muons and pions that are produced in interactions, the expectation from MC and data are shown in fig. 3.13.

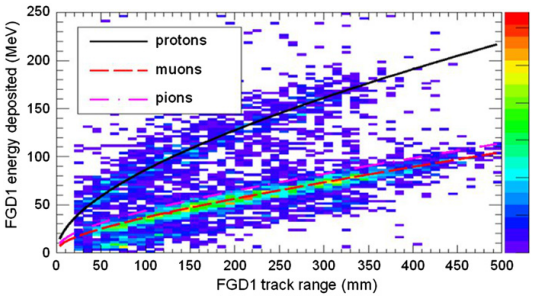

Figure 3.13: Track range and energy deposition in FGD1, for stopping particles. Data collected in neutrino beam running mode, and the curves show MC expectations for protons, muons and pions

3.2.1.3 Time Projection Chambers (TPCs)

The three identical time projection chambers (TPCs) are filled with a gas mixture of argon, tetrafluoromethane, and isobutane, Ar:CF_4:iC_4H_{10} in a ratio (95:3:2), this drift volume is surrounded a CO_2 filled insulating volume. A central cathode divides the drift volume which is of dimensions $1808 \times 2230 \times 854$ mm, the active tracking length in the volume is 720 mm. The 12 micromegas modules are arranged in two staggered columns so that the inactive regions are not aligned.

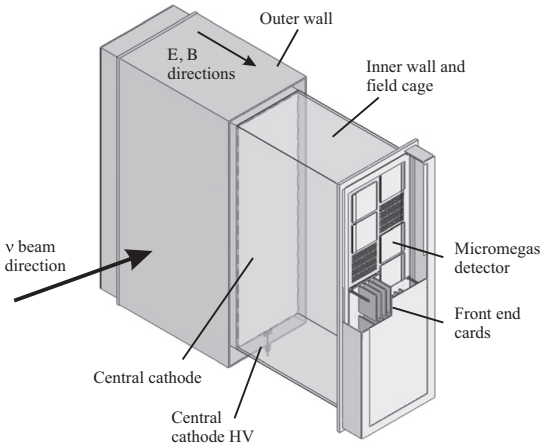

Figure 3.14: A cutaway diagram of a TPC module showing the arrangement of the micromegas detectors and the central cathode and nested structure of the two gas volumes.

Using the electric field from the inner volume and the magnetic field, which are roughly

aligned, charged particles are deflected and their momentum can be inferred. The ionisation electrons produced by the particles are readout by the micromegas detectors. Combining information from the energy deposition of a particle with its measured momenta allows for the identification of particle in the TPC, measurements for positively charged particles and MC expectations are shown in fig. 3.15. The requirements for energy loss in order to perform this identification are better than 10 % with a measured resolution of (7.8 ± 0.2) %, and a momentum resolution better than $0.1 p_\perp > \delta p_\perp / p_\perp$ GeV

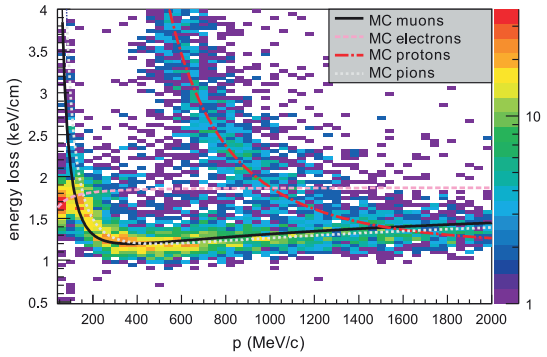

Figure 3.15: Measured energy loss distributions as a function of the particle momentum in the TPCs compared with the plotted MC expectations for the particle.

3.2.1.4 Electromagnetic Calorimeters (ECals)

The Electromagnetic Calorimeter (ECal) uses layers of rectangular scintillator bars (dimensions $186.4 \times 186.4 \times 2.02$ cm) alternately oriented in the x and y directions, containing WLS fibres, with lead absorber sheets between the scintillator layers. The three submodules of the ECal surround the inner detectors. The PØD ECal surrounds the PØD, the Barrel ECal surrounds the TPC and FGD tracking region and the downstream ECal is located after the final TPC in the beamline. The ECal detects, identifies, and measures the energy of charged particles which interact in the scintillator and from which tracks in the detector can be reconstructed [87]. The PØD, described in section 3.2.1.1, allows for reconstruction of the resulting electromagnetic showers from neutral pion decay and the PØD-ECal tags the escaping energy, provides separation between photons and muons, and a veto for events originating outside the PØD. Without the requirement of electromagnetic shower reconstruction the composition differs from the remaining Ecals with each of the PØD Ecals providing 4.9 radiation lengths of material. The remaining Ecals, known as the tracker-Ecal, provide detailed reconstruction of the electromagnetic showers from interactions that originate in the tracker region. Shower reconstruction complements the TPCs and FGDs by measurement of neutral particle energies and also by providing information on the presence of π^0 and potentially reconstructing the energy of the π^0, this is accomplished by having at least 10 electron radiation lengths of material in order to contain the photon initiated showers resulting from π^0 decays.

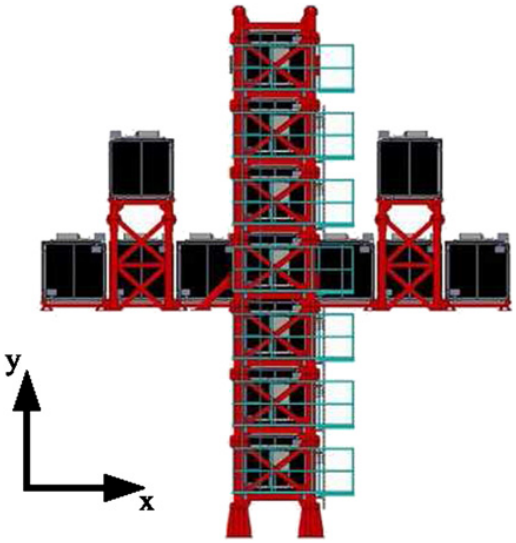

Figure 3.16: Diagram of the INGRID on axis detector – reproduced from [75]

3.2.2 Interactive Neutrino GRID (INGRID)

The Interactive Neutrino GRID (INGRID), is an on-axis neutrino detector which is designed to measure the beam centre, it does this by measuring neutrino interactions on 9 sheets of iron and 11 sheets of the same scintillator and MPPCs as the previously described detectors. Using the statistics collected, the beam centre is measured with a precision <10 cm, corresponding to a 0.4 mrad precision per day. The detector is arranged in a cross pattern consisting of 14 modules in a cross pattern and two outside this pattern see fig. 3.16 which measure the beam's axial symmetry[88]. The supplementary proton module, which has finer scintillator bars, in order to improve tracking, and no iron planes, is designed to detect the muons and protons due to neutrino beam interactions.

3.3 Super-Kamiokande Far Detector

The far detector, Super-Kamiokande is a water Cherenkov detector located in a mine below a mountain called Ikenoyama in the Japanese Gifu prefecture fig. 3.17. The detector has 1000 m overburden of rock or 2700 m-water-equivalent (m.w.e.), and muons with energies less than 1.3 TeV cannot reach this depth. Super-K was designed to search for proton decay, and to perform studies of neutrinos from several astrophysical sources, supernovae, gamma ray bursts, the Sun, atmospheric neutrinos and accelerator based beams. SK consists of a stainless steel tank containing 50 kt of water which is continually purified to maintain high optical clarity and to reduce radioactive backgrounds. The tank is separated into two optical regions the outer detector (OD) and inner detector (ID). The ID and OD are separated by a stainless steel frame, the ID is instrumented with 11 146 photomultiplier tubes (PMTs) which corresponds to 40 % coverage fig. 3.18.

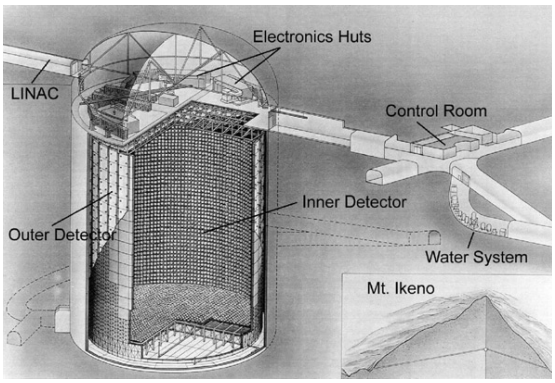

Figure 3.17: Super-Kamiokande Detector, location within the mine complex – reproduced from [89]

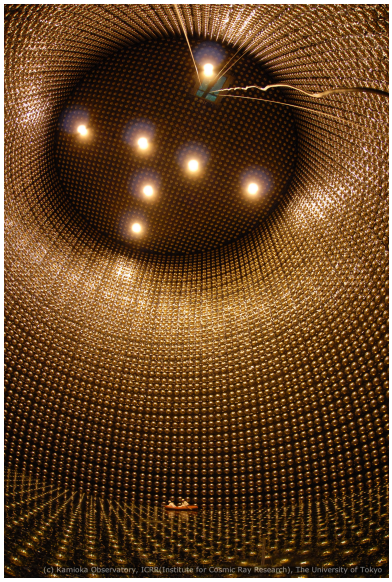

Figure 3.18: Super-Kamiokande, view of the inner detector partly filled with water, reproduced from the SuperK public website

The OD is more sparsely instrumented and used to veto events, with 1185 PMTs facing outward on the separating frame. The OD PMTs are mounted to acrylic plates and the OD itself is lined with a reflective material in order to increase light collection.

3.3.1 Super-Kamiokande Event Reconstruction

The Cherenkov effect is exploited in Super-K to detect interacting particles. The emitted Cherenkov light resulting from a charged particle propagating through the water is incident on the PMTs in the detector, detected light is shown in fig. 3.20. The conditions for Cherenkov emission are that the particle velocity exceed the phase velocity of light in the medium, $^{c}/_{n}$, where n is the refractive index of the medium, $n \approx 1.33$ for water. At this velocity a non zero dipole moment in the region around the charge will be induced, the energy deposited in the dipole is emitted as Cherenkov light in a cone at a

characteristic angle, θ from the particle's direction vector,

$$\cos\theta = \frac{1}{\beta n}. \tag{3.2}$$

Where $\beta = v/c$, and v is the particle velocity [90]. With the given value for n in water the threshold for Cherenkov emission is $\beta = 0.75$. Due to the interaction kinematics and the energy that is available in the neutrino beam, the more massive hadrons and nuclei are not usually above threshold. A proton requires a momentum of 1.064 GeV, pions require 158 MeV, they can also can be detected by the subsequent Michel decay electron tagging, if below threshold. The leptons that result from the interaction have momenta thresholds of 120 MeV for muons and 0.57 MeV for electrons.

This analysis uses the fiTQun reconstruction algorithm [91, 92]. The fiTQun algorithm has been used in previous analyses to reduce the NC π^0 background, and in this analysis is used to perform the selection of all the samples including a sample which observes the hadronic component of the system, in a ν_e CC $1\pi^+$ reaction, in addition to the charged current quasielastic (CCQE) samples that have been used for previous analyses see section 4.4.1 for further details. This algorithm also uses an expanded fiducial volume, determined using two variables which determine the distance to the walls of the inner detector, further details are in section 4.4 and the variables are depicted in fig. 4.27. The previously employed APFit algorithm uses an approach made up of various stages. A vertex fitting stage based on the difference between the photon arrival time and the time of flight is made, this is followed by a search for ring candidates using a Hough transformation [93], the contribution from other rings is subtracted in subsequent ring search stages. The identified rings are then classified in a particle identification (PID) stage, depending on whether they are showering or non showering using a likelihood function. Rings are then separated using the vertex position and direction to generate a predicted hit pattern on the PMTs. The particle momentum is then estimated by using the sum of the PMT hits that are detected for a particular ring within a 70° half opening angle from the particle direction vector [94].

FiTQun is based on a likelihood function approach using charge and time information from hit PMTs for each event. This likelihood aims to reconstruct the particle kinematics based on track variables, and compares the global maximum of likelihood for the hypothesis of higher multiplicity of numbers of tracks and in a similar way compares the likelihood ratio for different particles, with a revisited specific π^0 fit. It provides previously unavailable reconstruction and identification facilities for $\pi^\pm$, $K^\pm$ and p, which are employed for the additional electron-like sample containing a π^+.

Particle identification is included in the fiTQun likelihood by a function which contains the Cherenkov emission profile as a function of momentum, angle, and track length for a range of particles. The showers that are generated by electrons have broader angular emission distributions, which result in "fuzzy" cones [91]. The electron-like

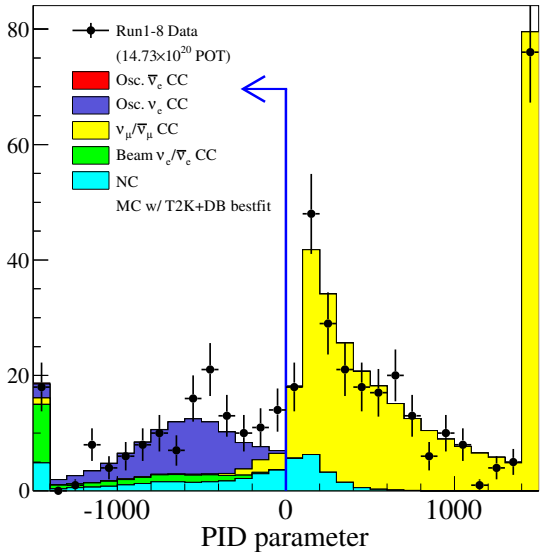

Figure 3.19: fiTQun PID distribution selecting between electron and muon like interactions with cut location – reproduced from [95]

particle identification (PID) cut for the ν_e sample is shown in fig. 3.19. As previously discussed the peak energy of the T2K beam lies at 0.6 GeV, this results in CCQE interactions making up the bulk of the signal with a smaller contribution coming from pion production channels. Measurements of channels with hadronic systems need to have the components above threshold in order to be measured. Studies of the data-MC difference in the stopping muon sample indicate that that largest difference between the vertex position is of the order of 1.5 cm in the fiTQun algorithm vs 5 cm as extracted by APFit. The energy scale was evaluated using APFit, unlike the rest of the analysis, at the time of the analysis no tuning was available for fiTQun which showed a larger uncertainty, hence the choice of the well understood APFit result.

3.4 Physics Results

The initial ν_μ character of the neutrino beam that is produced at T2K allows for better measurements of oscillation parameters accessible at the beam energy. The two detector setup and initial running in FHC mode, is suited to $P(\nu_\mu \to \nu_\mu)$, muon neutrino disappearance, and with sufficient statistics $P(\nu_\mu \to \nu_e)$ electron neutrino appearance. The disappearance of ν_μ allows access to the parameters $\sin^2\theta_{23}$ and $\left|\Delta m^2_{32}\right|$, whilst θ_{13} can be measured through ν_e appearance. Indications of ν_e appearance, and the first measurement of a θ_{13} angle inconsistent with zero [96] were followed by the measurement of electron neutrino appearance with a significance of $7.3\,\sigma$ [97]. Measurements of $\bar{\nu}_\mu$ disappearance have been made finding agreement with the parameters for ν_μ [98]. Transformations under $\mathcal{CP}$ of the previous channels can be combined to measure the δ_{CP} phase [99]. The current thesis aims to better characterise the phase of δ_{CP} in addition

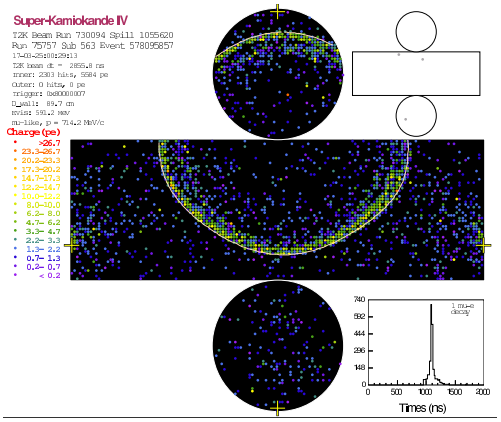

(a) Super-K Event Display, muon-like ring.

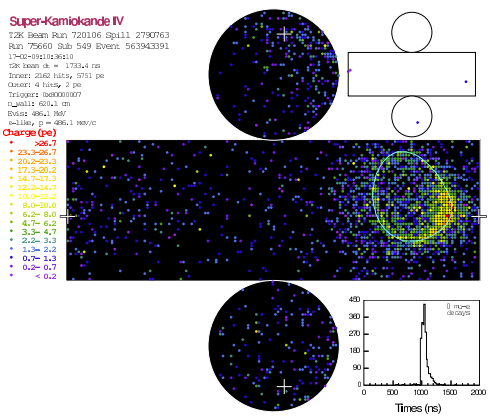

(b) Super-K Event Display, electron-like ring.

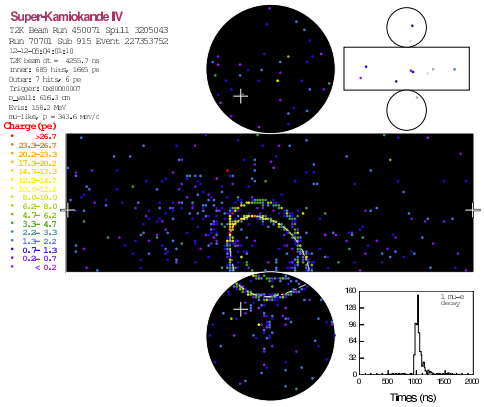

(c) Super-K Event Display, electron-like ring with 1 decay electron.

Figure 3.20: Super-K Event Displays for (a) μ-like, (b) e-like, (c) e-like with 1 decay electron. The coloured dots represent the charge measured by a PMT located on the inside of the detector, the figure in the upper right is the corresponding plot for the OD. reproduced from [95]

to measurements of the oscillation parameters from the disappearance and appearance channels.

A search for non-standard oscillations has been made using ND280 for indications of ν_e disappearance at short baseline [100]. A search for Lorentz Violation using INGRID based on sidereal time event rate variations indicates that any symmetry violations are suppressed by 1×10^{20} in the GeV region [101].

The composition of the near detector allows for the measurement of neutrino cross sections on many targets, and publications of these cross sections for the regions of phase space that T2K can access are have been published. A selection of these measurements ν_μ charged current single pion production on water [102] a flux-averaged cross section measurement for charged current coherent π^+ production on carbon for neutrino energies less than 1.5 GeV in the phase space of ND280 [103], charged current inclusive cross section induced by ν_μ and $\bar{\nu}_\mu$ on carbon, oxygen, hydrogen and copper [104], ν_μ on water without pions in the final state [105]. Single pion production in neutral current interactions on water has been measured [106], this is an important background to characterise since it forms an irreducible background to ν_e appearance. Better measurements of the interaction cross sections allow for a reduction in uncertainty in the observed event rates.

3.5 Future Developments and Physics Goals/Sensitivity

The original proposal which decided the final exposure of the T2K experiment was determined prior to the experimental result that the mixing angle θ_{13}, is large [107, 108, 109]. In the case of a large θ_{13}, systematic uncertainties are not dominant and increased statistics can improve the experimental sensitivity to exclude values of δ_{CP} at the 3σ level. As a result an extension of the running time to reach 20×10^{21} POT is proposed, known as T2K-II [110] with sensitivities for the oscillation parameters $\left|\Delta m^2_{32}\right|, \sin^2\theta_{23}$ shown in fig. 3.21, and δ_{CP} fig. 3.22.

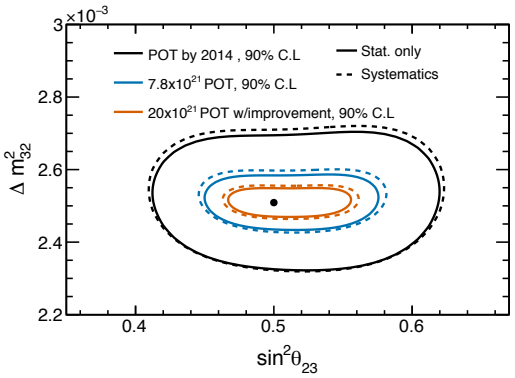

Figure 3.21: T2K-II sensitivity for the parameter space $\left|\Delta m^2_{32}\right|, \sin^2\theta_{23}$ with total exposure of 20×10^{21} POT, assuming that the true value of $\sin^2\theta_{23} = 0.5$, in the scenarios that that the evaluation of the systematic errors in the experiment remain the same or are improved to the order of 4 % – reproduced from [110].

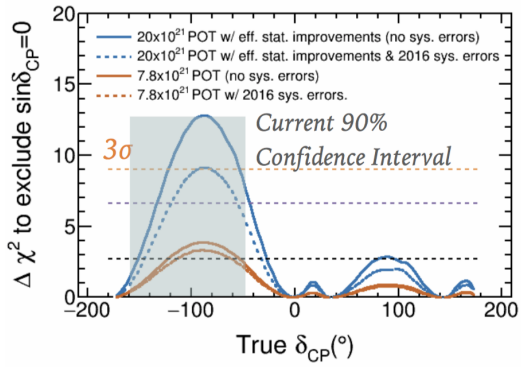

Figure 3.22: T2K-II sensitivity with total exposure of 20×10^{21} POT, assuming that the mass hierarchy is unknown as a function of δ_{CP} – reproduced from [111]

Gadolinium "doping" of Super-Kamiokande has been approved by both the T2K and Super-K collaborations. The addition of gadolinium at the level of 0.2 % in the form of a salt allows >90 % of thermalised neutrons to be captured by the gadolinum atom resulting in the emission of an 8 MeV γ cascade which allows detection by coincidence and discrimination between ν and $\bar{\nu}$ [112] allowing for the reduction of background in the measurement of δ_{CP}. Information about the final hadronic state will be gained from the ability to detect delayed neutron captures, and the ability to measure neutral current channels [113]. A 200 t prototype water Cherenkov detector has been run with the described 0.2 % gadolinium loading and experimental measurements of the neutron capture efficiency have been made with good agreement to simulation [114].

4 T2K Oscillation Analysis Inputs

The oscillation analysis which is described in chapter 5 depends on a variety of inputs which feed into the analysis as illustrated in fig. 4.1. A flux prediction is made based on simulation of the initial proton beam and the subsequent hadron production which results in a neutrino beam, this is tuned on external data and is described in section 4.1. A cross-section model is used which describes neutrino interactions in the $\sim$1 GeV region section 4.2, this is tuned on bubble chamber data. Event selections at ND280 are used to tune the flux and cross section parameters of the previous two models, via a fit, performed by Beam And Near Detector Task Force (BANFF) and MaCh3 (MaCh3) to those data sets section 4.3. Any correlated uncertainties are propagated to Super-K, and the covariance matrix that is obtained is used in the oscillation fits. Events are selected at Super-K in section 4.4 with event reconstruction based on: lepton kinematics approximating the CCQE interaction for the single ring samples, and on the production of a Δ resonance for the ν_e CC1π^+ sample. A new Super-K event reconstruction algorithm known as fiTQun, previously described in section 3.3.1, is further described in section 4.5 along with the procedure for evaluating the systematic uncertainties on these samples. A table of the versions of the software that are used in this thesis are listed in table 4.1.

4.1 Neutrino Flux Prediction

The neutrino flux is predicted by tracking the initial proton beam through the secondary beamline, and follows the produced secondary hadrons through the horns and allows for and tracks any tertiary hadron production. Finally the neutrinos resulting from hadronic decays whose direction vectors pass through the near and far detectors are passed to subsequent steps of the simulation. Energy thresholds for particle tracking are used, after which decays are forced using branching ratio information: 0.1 GeV for tracking hadrons and muons, and 1.0 GeV for gammas and electrons, with an additional

Input	Version
JNUBEAM flux	13av2
NEUT	5.3.2
SKDETSIM	v13p90
Super-K Software and MC	14a
fiTQun	v4r0
APFit	14c
Super-K FSI Systematics	FSIFitter (TN-325)

Table 4.1: Versions of the software used in the inputs to the oscillation analysis

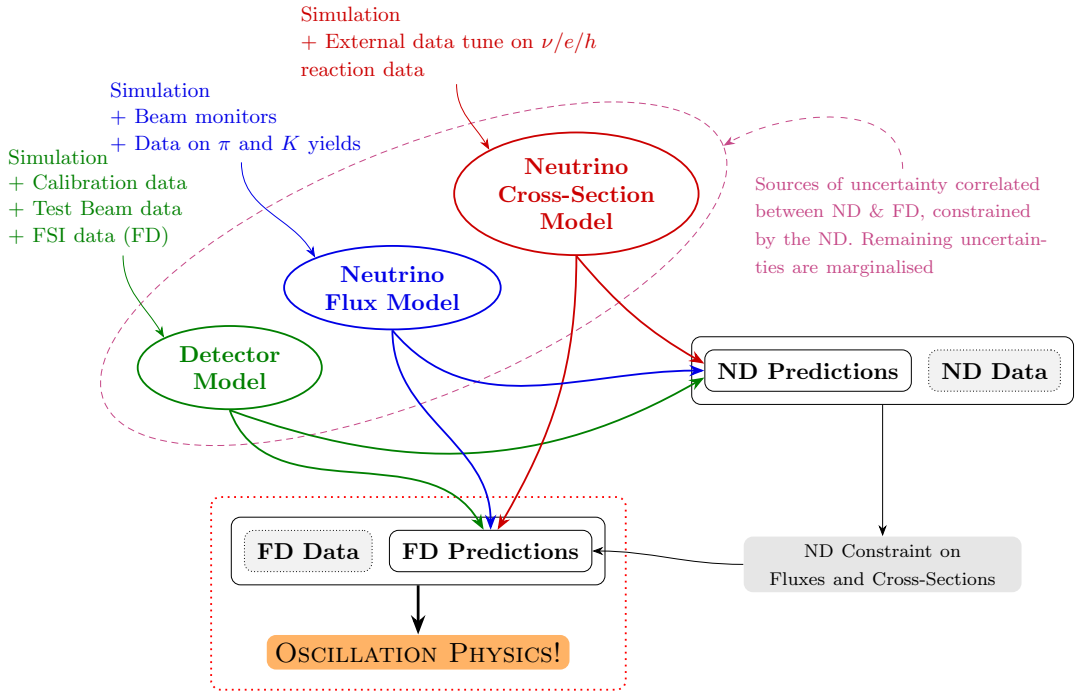

Figure 4.1: Inputs used in the oscillation analysis, categorised into flux, detector and cross section model. NEUT MC is used to simulate the neutrino cross-section model. The flux model is made up of several software packages, and the detector models are handled differently for both the near and far detectors. The red dashed box contains the work which is original to this thesis.

threshold of 1.0 GeV downstream of the beam dump for neutral hadrons and muons. Measurements of the beam characterising its profile and intensity are used together with measurements of the horn magnetic field and external measurements of hadron production to tune the simulation.

Hadron production and the associated decay channels ultimately determine the neutrino flux that is seen at the near and far detectors. Various hadron production channels from proton carbon collisions exist, and the contribution of each channel via branching ratio best knowledge [71] along with form factors and decay modes is considered in the flux prediction. Data from an external experiment, NA61, is used to tune the probabilities of producing various hadrons in bins of longitudinal and transverse momentum.

Proton interactions in the graphite target are simulated by using the FLUKA2011 code [115, 116] and in particular version FLUKA 2011.2c.3 [117] to simulate the interactions in the target followed by JNUBEAM (which is based on GEANT3)[118] to track the particles outside the target and the decay to neutrinos. Outside the target GCALOR [119, 120] simulates the hadronic interactions. This initial flux prediction is then tuned using both T2K data from ND280 and data from the NA61/SHINE (SPS Heavy Ion and Neutrino Experiment) at CERN [121] which has measured the hadron production on a thin target [122, 123, 124] and a replica T2K target [125, 126]. The neutrino tracks that are produced as a result of the simulation are extrapolated to both the near and

far detectors, to obtain the respective fluxes and energy spectra. These tracks are forced to point in the direction of the far detector or a random point in the near detector, with a corresponding weight, in order to save computation time.

The neutrino flux and energy spectra depend on the kinematics of the parent pions and kaons, which need to be accurately simulated in order to determine the neutrino flux which reaches the near and far detectors and participates in interactions. The off-axis E_ν technique limits the uncertainty originating from the parent pion spectrum. The hadronic interactions that contribute to the flux at Super-K are used to select the data that is used for tuning. The previously described interactions consist of: $\pi^\pm$, $K^\pm$, K^0, Λ production from the primary proton interaction, $p(n)$ production from both primary and secondary protons, $\pi^\pm$ production from secondary nucleons and from incident $\pi^\pm$ originating inside and outside of the target. The decay modes that produce neutrinos are listed in table 4.2, and are used along with the best knowledge of their branching ratios, and feed-down from strange particle decays K^0 and Λ.

Particle	Decay Products
π^+	$\rightarrow \nu_\mu \mu^+$
	$\rightarrow \nu_e e^+$
K^+	$\rightarrow \nu_\mu \mu^+$
	$\rightarrow \nu_\mu \pi^0 \mu^+$
	$\rightarrow \nu_e \pi^0 e^+$
K^0_L	$\rightarrow \nu_\mu \pi^\mp + \mu^\pm$
	$\rightarrow \nu_e \pi^\mp + e^\pm$
μ^+	$\rightarrow \bar{\nu}_\mu \nu_e e^+$
(Λ	$\rightarrow p\pi^-$)
(K^0_S	$\rightarrow \pi^+\pi^-$)

Table 4.2: Decay modes considered in the neutrino flux prediction, the antiparticle versions of the decays are also considered in the flux prediction but are not listed here for conciseness. The feed-down from the strange particle decays K^0_S and Λ are also considered.

The target materials that are considered in the flux tuning are carbon, which makes up the target and beam dump, the aluminium which composes the focussing horns and the iron which makes up the decay volume walls. Data is used to tune the interactions [127] and set systematic uncertainties that happen on the target materials which are simulated, which include Al, Cu and Ti. The flux is tuned via two weights, one for the probability of an interaction producing a secondary hadron W_1, and the second for the multiplicity of the final state in a double differential distribution W_2. The final weights as a function of energy for each neutrino species and each running mode are shown in

fig. 4.2. The first set of weights W_1,

$$\begin{aligned} W_1 = & \frac{\sigma_p^{\text{data}}(p_{\text{in}}, A)}{\sigma_p^{\text{MC}}(p_{\text{in}}, A)} \times \\ & \exp\left(-\rho d_0 \left[\sigma_p^{\text{data}}(p_{\text{in}}, A) - \sigma_p^{\text{MC}}(p_{\text{in}}, A)\right]\right) \times \\ & \exp\left(-\rho d_1 \left[\sigma_p^{\text{data}}(p_{\text{out}}, A) - \sigma_p^{\text{MC}}(p_{\text{out}}, A)\right]\right), \end{aligned} \tag{4.1}$$

where the secondary hadron production probability for an incoming proton, with momentum p_{in} which travels a distance d_0 before interacting in the medium of density ρ, and atomic number, A, depends on the production cross sections, σ_p^{MC} and σ_p^{data} which are momentum and atomic mass dependent, for Monte Carlo and data respectively. The production cross section is defined as $\sigma_{\text{p}} = \sigma_{\text{inel}} - \sigma_{\text{qe}}$. A particle of momentum p_{out} is created and travels a distance d_1 in the medium.

The second set of weights, W_2 that are calculated account for the multiplicity of the hadrons after the primary interaction

$$\frac{d^2n(p,\theta)}{dpd\theta} = \frac{1}{\sigma_{\text{prod}}} \frac{d^2\sigma(p,\theta)}{dpd\theta}, \tag{4.2}$$

$$W_2(p,\theta) = \left[\frac{d^2n(p,\theta)}{dpd\theta}\right]_{\text{data}} \Bigg/ \left[\frac{d^2n(p,\theta)}{dpd\theta}\right]_{\text{MC}}, \tag{4.3}$$

the double differential production weight eq. (4.2) is dependent on the momentum and the angle, θ relative to the incident particle. For the primary interaction eq. (4.3) can be constructed easily since the T2K beam and the NA61 data occupy the same phase space, as shown in figs. 4.4 and 4.5, for tertiary pion production extrapolation from the data is required. The extrapolation is required for the lower nucleon momenta and the interaction on the aluminium horn. A total weight for a particular neutrino is then the product of W_1 and W_2 for a particular ancestor particle.

The motivation of NA61/SHINE is to study the final hadronic states that are produced from several different beam particles that are available at the Super Proton Synchrotron (SPS), interacting on a variety of targets. Germane to this thesis are measurements which will improve the simulation of the neutrino beam produced as a result of the proton carbon interaction. The proton beam energy run at SPS is 31 GeV, which as described in section 3.1.1 is a near match to the 30 GeV run at T2K.

The NA61 detector, depicted in fig. 4.3, consists of 5 time projection chambers, and three time of flight (ToF) detectors. There is also a forward calorimeter Particle Spectator Detector (PSD), downstream of the other detectors and a Low Momentum Particle Detector (LMPD) which is located on either side of the target [121]. There is a group of detectors upstream of the target in the beamline which collect timing, charge, and position measurement of the incoming beam. Downstream of the detector are a set of interaction counters which trigger on the interactions. Two of the TPCs are located

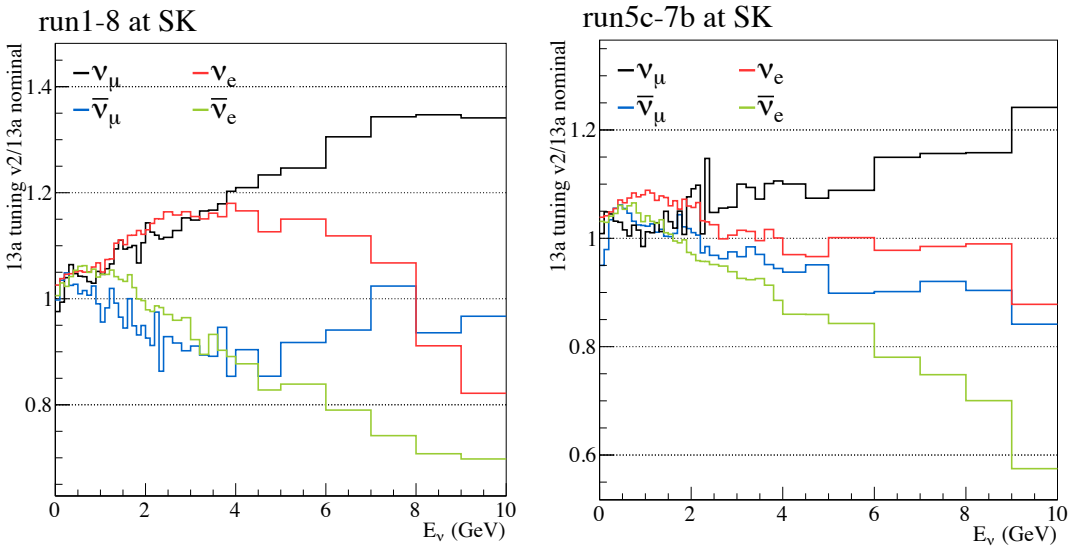

(a) Run 1-8 weights

(b) Run 5c-7b weights

Figure 4.2: Flux tuning weights for (a) forward horn running, and (b) reverse horn running for the neutrino species ν_μ ν_e $\bar{\nu}_\mu$ $\bar{\nu}_e$, from [128]

within magnetic fields and perform PID using dE/dx and the particle's momentum, the ToF detectors are also used to perform PID using the ToF information in combination with the information from the TPCs.

Data from two carbon targets has been collected, these are: a *thin* target which is 2 cm thick or $0.04\lambda_I$ interaction lengths in the direction of beam propagation, and a replica target $1.9\lambda_I$ of the same dimensions as the target used at T2K see section 3.1.2 for target details. The thin target provides data for the initial interaction and multiplicity of hadrons. Tertiary hadron production information within the target is provided by the replica target, leading to a better constraint of the T2K flux, increasing from 60 % to 90 % at the beam peak energy [125].

The final neutrino flux prediction broken down by neutrino flavour ν_μ ν_e $\bar{\nu}_\mu$ $\bar{\nu}_e$ for each running mode is presented in fig. 4.6.

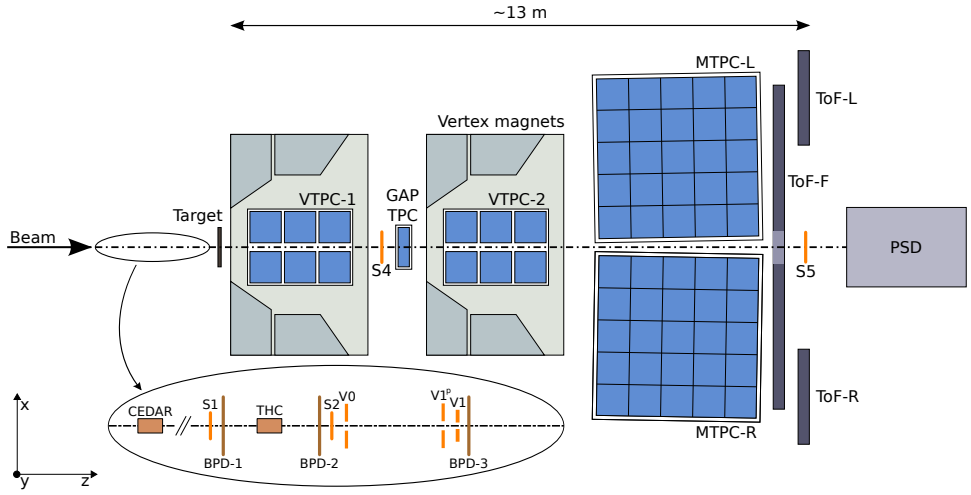

Figure 4.3: NA61/SHINE in the CERN SPS facility. The locations of the various components that determine the beam showing the location of the target which is either the thin target or the replica T2K target. Reproduced from[121]

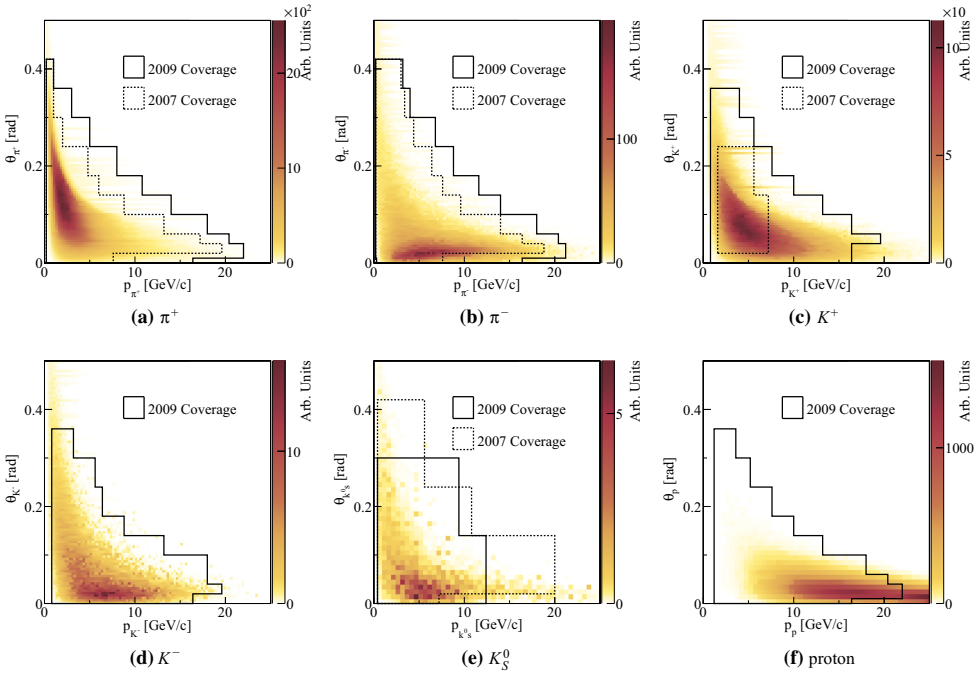

Figure 4.4: FHC mode phase space of the hadrons contributing to the flux at Super-K, with the coverage of the NA61/SHINE experiment for two data collection periods. Reproduced from [129]

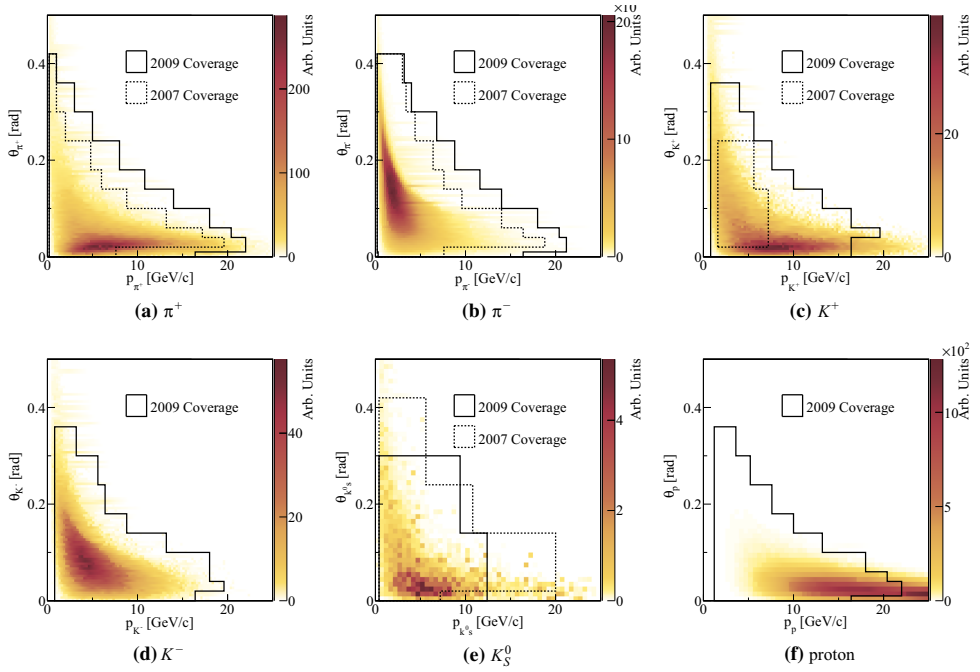

Figure 4.5: RHC mode phase space of the hadrons contributing to the flux at Super-K, with the coverage of the NA61/SHINE experiment for two data collection periods. Reproduced from [129]

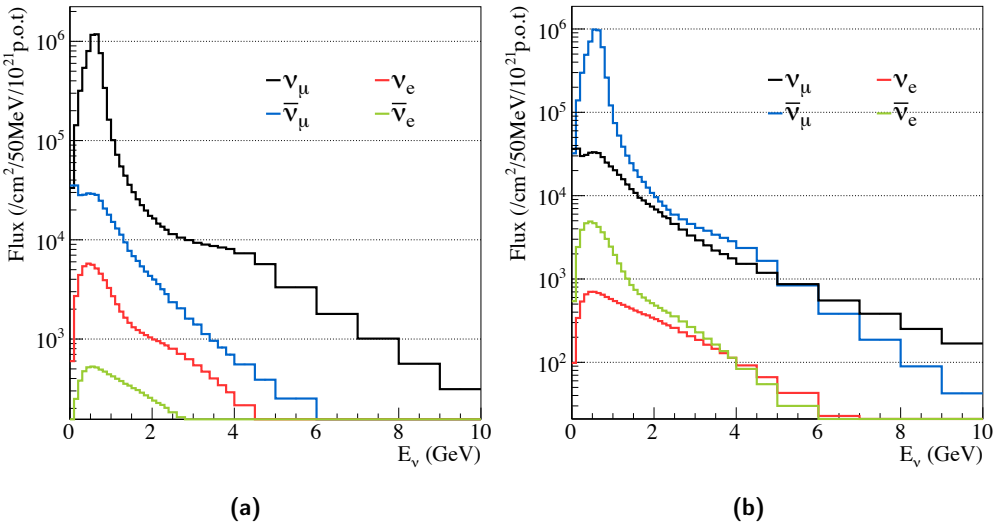

Figure 4.6: Neutrino flux prediction for (a) FHC mode Runs 1-8, and (b) RHC mode Runs 5c-7b, for each neutrino flavour at Super-K. Reproduced from [128].

4.1.1 Flux Uncertainties

There are five groups forming the sources uncertainty for the flux prediction, these are used to generate a prior flux covariance matrix. The sources of uncertainty considered are:

- **Hadron interaction:** the experimentally determined hadron production data have associated uncertainties. Extrapolating to the phase space not covered by NA61 carries a larger uncertainty, as does scaling the centre of mass energy to cover tertiary production. There are also uncertainties due to scaling for materials outside the target from the available data, and final state meson multiplicities. Secondary baryon production after the primary interaction is not simulated and forms a source of uncertainties

- **Proton beam and off-axis angle:** amongst the beam alignment parameters the Y beam center and θ_Y are the dominant sources of uncertainty [130, 131]. The proton beam profile is stable across all runs and allows for fully correlated variations to be applied across runs. The off-axis beam direction uncertainty is taken from the INGRID measurement.

- **Target and horn alignment:** the positions and angles of the target and horn system and the remaining two horns are another source of the uncertainty. The vertical displacement of horns 2 and 3, and together are of order 2 %. The uncertainty due to the target misalignment is of order 3 %, the angular alignment of horn 1 is of order 2 %.

- **Horn current magnetic field:** this uncertainty is dominated by the current monitoring stability. Measurements of the magnetic field's deviation from nominal have been made [131, 128]. The effect on the final neutrino flux is <1 % for bins <1 GeV and <4 % for bins >1 GeV.

- **Material out of target:** interactions on the cooling water inside the horns are simulated. The "striplines" carrying the current to the horn forms another source of uncertainty, each of these change the flux prediction by at most a few % over nominal [128].

The fractional flux uncertainties for the categories presented above are shown for ν_μ and $\bar{\nu}_\mu$ in FHC mode at Super-K in fig. 4.7, improvements in hadron interaction modelling using data from [129] have resulted in the right sign flux uncertainty has being reduced from ∼11 % to ∼8 % at the flux peak. Most bins show improvement compared to the previous flux prediction mainly due to improved hadron production modelling. The uncertainties for $\bar{\nu}_e$ at ND280 in RHC mode are shown in fig. 4.8 which does not have a previous flux version for comparison. The flux is parameterised as detailed in table 4.3.

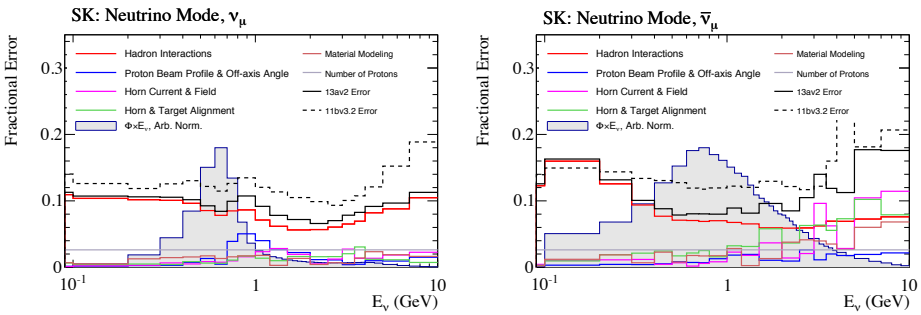

Figure 4.7: The fractional ν_μ and $\bar{\nu}_\mu$ flux uncertainties in FHC running mode at Super-K for each of the categories listed in section 4.1.1. The solid line represents the updated flux prediction, whereas the dashed line was the previous version. Reproduced from [128].

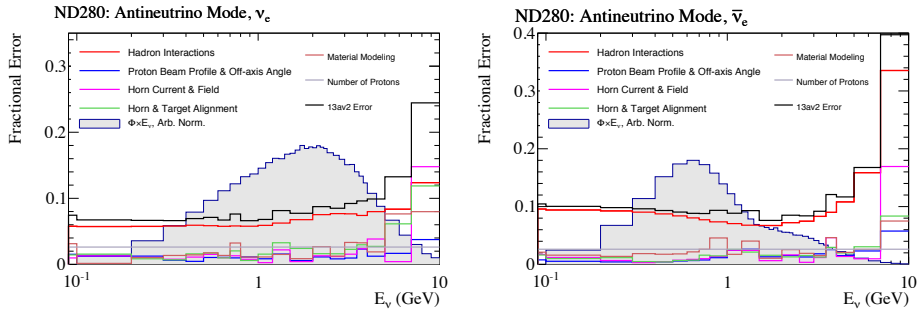

Figure 4.8: The fractional ν_e and $\bar{\nu}_e$ flux uncertainties in RHC running mode at ND280 for each of the categories listed in section 4.1.1. Reproduced from [128].

Beam mode	ν Flavour	Binning (GeV)
FHC	ν_μ	0–0.4, 0.4–0.5, 0.5–0.6, 0.6–0.7, 0.7–1.0, 1.0–1.5, 1.5–2.5, 2.5–3.5, 3.5–5.0, 5.0–7.0, 7.0–30.0
	ν_e	0–0.5, 0.5–0.7, 0.7–0.8, 0.8–1.5, 1.5–2.5, 2.5–4.0, 4.0–30.0
	$\bar{\nu}_\mu$	0–0.7, 0.7–1.0, 1.0–1.5, 1.5–2.5, 2.5–30.0
	$\bar{\nu}_e$	0–2.5, 2.5–30.0
RHC	ν_μ	0–0.7, 0.7–1.0, 1.0–1.5, 1.5–2.5, 2.5–30.0
	ν_e	0–2.5, 2.5–30.0
	$\bar{\nu}_\mu$	0–0.4, 0.4–0.5, 0.5–0.6, 0.6–0.7, 0.7–1.0, 1.0–1.5, 1.5–2.5, 2.5–3.5, 3.5–5.0, 5.0–7.0, 7.0–30.0
	$\bar{\nu}_e$	0–0.5, 0.5–0.7, 0.7–0.8, 0.8–1.5, 1.5–2.5, 2.5–4.0, 4.0–30.0

Table 4.3: Flux systematic parameters for each of the beam modes, as a function of true neutrino energy and flavour. These bins are mapped to the parameters in table 4.11 with `SKNuMode*` corresponds to FHC and `SKANuMode*` RHC, and `*Numu*`, `*Nue*`, `*Numub*`, `*Nueb*` mapping to ν_μ, ν_e, $\bar{\nu}_\mu$, $\bar{\nu}_e$, and each of the numbered parameters corresponding to a true energy bin.

4.2 Neutrino Interaction Simulation

The interactions of neutrinos, across the range of energies that is covered by the T2K beam flux, spans several different modes outlined in section 2.2.3. Ascribing the correct rate associated with a particular interaction mode depends on knowledge of its cross section. There are several different overlapping models for predicting cross sections in this energy region and they must all be incorporated into a coherent whole. Both the near detector inputs and the simulation of the far detector are produced by the NEUT Monte Carlo generator [132]. Since knowledge of neutrino cross sections is a major source of uncertainty in current oscillation experiments any treatment which better quantifies the uncertainty is valuable. NEUT version 5.3.2 is used as the reference in this analysis for the ND280 and Super-K. A description of the physics models used in NEUT 5.4.0 is available in [133] and are discussed below based primarily on [134].

4.2.1 Neutrino Interaction Modes

The interactions of neutrinos with atomic nuclei are simulated using a variety of models to cover the energy range at T2K. The "Impulse Approximation" is used along with a Random Phase Approximation (RPA) model parameterised using a functional form which minimises correlations. The primary interaction mode which makes up the signal in this thesis is CCQE, and is tuned to bubble chamber data. Interactions between the incoming neutrino and two nucleons can occur which overlap the CCQE region, their contribution to this region and the higher energy pion production region is considered. The single pion production region is modelled and tuned again using bubble chamber data. Interactions within the nucleus after the primary neutrino interaction, Final State Interactions (FSI), which bias or make impossible neutrino energy reconstruction are modelled using a cascade model. Secondary Interactions (SI) take place after the particles from the interaction leave the nucleus and interact in the detector medium. Both FSI and SI interactions are tuned using external pion nucleus scattering data. At high energies Deep Inelastic Scattering (DIS) processes take place which for T2K are a small contribution.

4.2.1.1 Nuclear Model

Neutrino nucleus interactions at T2K are simulated using the so called "Impulse Approximation" which considers a neutrino interaction as acting on a single nucleon in the nucleus, with the rest of the system spectating, and takes the incoherent sum of these probabilities. Modifications due to: initial nucleon kinematics, extracting the nucleon from the nucleus, re-interactions in the remnant nucleus, and the changes to the cross section due to the nuclear potential are included. However, the nuclear potential is not

included in the ν-nucleon interaction equation, neither is the wave function of the nucleon before interaction and that of the final state. The interaction between the remnant nucleus and the scattered nucleon are not included in the nucleon wave function.

Several effects need to be considered for the simulation of neutrino scattering of bound nucleons and are included in the T2K model. The kinematics of the initial nucleons are described by using a Fermi gas, the momentum distribution being flat up to a maximum Fermi momentum (p_F). The nuclear potential is taken into consideration by subtracting the binding energy (E_b) required to remove a nucleon from the nucleus from the final state. Re-interactions within the struck nucleus by hadrons, FSI, are considered by use of a Monte Carlo cascade model, with Pauli blocking applied. Pauli blocking can also affect the distribution of events observed at low values of Q^2, if the nucleon is not energetic enough to leave the nucleus the creation of the state may be "blocked" due to the Pauli exclusion principle not allowing another particle to occupy the same state. The cascade model treats each collision as independent and conserves energy and momentum, a mean free path calculation takes into account effects from the medium. Tuning of this model is described in section 4.2.2. Modification of the neutrino-nucleus cross-section originating from the nuclear potential is described by the RPA, which is a function of $Q^2 = (\omega, \vec{q})$, the four-momentum transferred to the nucleon. Although RPA effects apply to all particles exiting the nucleus, these are only applied to CCQE events in this analysis, as similar effects for pion production are not yet available.

4.2.1.2 Collective Nuclear Effects (BeRPA)

A relativistic RPA model is used, developed by Nieves et al. in [135] and referred to as Nieves RPA. This is a non-perturbative method that takes into account interactions in complex many body systems. Parameterisations have been made of for Effective RPA (ERPA) models, but unfortunately strong correlations were introduced between parameters. Berstein basis polynomials $b_{i,n}$, of degree n have a functional form where each polynomial is strongly peaked in a particular region of x

$$b_{i,n} = \binom{n}{i} x^i (1-x)^{n-i}, i = 0, \ldots, n. \tag{4.4}$$

The form of the polynomial reduces undesired correlations between parameters [136]. A parameterisation of the Nieves RPA model using Bernstein Polynomials, Bernstein RPA (BeRPA), to allow for the coverage of uncertainties in the model has been developed

$$f(x) = \begin{cases} A(1-x')^3 + 3B(1-x')^2 x' + 3p_1(1-x')x'^2 + Cx'^3, & x < U \\ 1 + p_2 e^{-D(x-U)}, & x > U \end{cases} \tag{4.5}$$

where $x = Q^2$ and $x' = x/U$, and the parameters A, B, C and p_1 are normalisation factors. The parameters $p_{1,2}$ are used for the continuity conditions and are

$$\begin{aligned} p_1 =& C + \frac{UD(C-1)}{3} \\ p_2 =& C - 1. \end{aligned} \tag{4.6}$$

For μ-like samples in FHC mode effects from BeRPA changes event rates by up to 2.5 % and up to 2 % in RHC mode with variations of 1σ around the BANFF tuned values for parameters A, B and D. Similar effects on the event rates are seen for the e-like samples, however the ν_e CC1π^+ sample shows a much smaller effect 0.2 % table B.1 to table B.10.

4.2.1.3 Charged Current Quasielastic (CCQE) and CCQE-like

The CCQE interaction mode, shown in fig. 4.9, is dominant at the peak of the flux used in the T2K experiment. The CCQE-like samples used in the analysis are identified by the requirement of no pion (0π) in the final state, and no attempt is made to reconstruct the outgoing proton. The CC0π mode is the main signal for Super-K. This interaction model is for the vertex before any modification by FSI. Other interactions that have the same final state but where the physics process is different, such as the multi-nucleon 2p2h process, cannot be separated from a true CCQE process. Another process which can result in 0π in the final state is π production followed by absorption of the *pi* within the nucleus. Attempts to better determine the final state using measurements of the outgoing proton are not yet well enough developed to separate the CCQE and 2p2h contributions for an oscillation analysis.

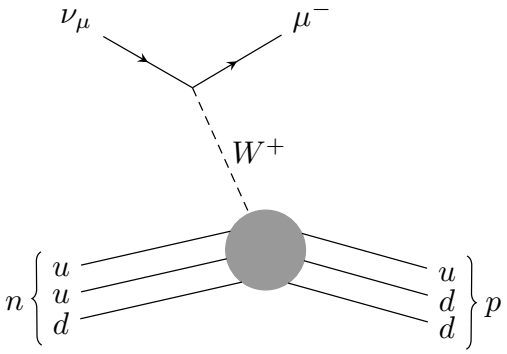

Figure 4.9: Feynman diagram of a muon neutrino charged current quasi-elastic interaction.

The CCQE interaction is implemented using the Llewellyn Smith formalism [137], a

dipole is used for the axial (F_A) form factor with

$$F_A(Q^2) = \frac{g_A}{\left(1 + {Q^2}/{\left(M_A^{QE}\right)^2}\right)^2}. \tag{4.7}$$

where Q^2 is the four-momentum transfer. The axial mass term M_A^{QE} is constrained from neutrino-deuterium scattering experiments, which do not include nuclear effects, although this form has proved effective at describing nuclear parameters. Alternative models for the axial form factor have been studied in order to better describe data at higher values of Q^2. These will be further discussed in section 4.2.1.4 but are not used in this round of analysis.

4.2.1.4 Tuning to Bubble Chamber Data

A joint fit to data that is available from bubble chamber experiments, is made using a sum of the likelihoods for each dataset. The bubble chamber targets were free nucleons in either hydrogen or deuterium. Data is used from Argonne National Laboratory (ANL) [138, 139] and Brookhaven National Laboratory (BNL) [140] in addition to Fermi National Accelerator Laboratory (FNAL) [141] and the Big European Bubble Chamber (BEBC) [142]. The data is presented in a number of different forms, as cross sections $\sigma(E_\nu)$, event rates $R(Q^2)$, and differential cross-sections ${d\sigma}/{dQ^2}$. To avoid biasing the fit and to take into account the information that is available from Q^2 and E_ν the fit is made to both classes of data set simultaneously, fitting the cross sections $\sigma(E_\nu)$ to understand the flux of the experiment and the ${d\sigma}/{dQ^2}$ to gain shape and form factor information. Different treatments are taken for each of the data sets due to overly strong contributions from a particular data sets. Flux uncertainties are taken into account by performing tuning with fixed fluxes from the data sets from ANL and BNL and allowing the flux to vary by 15 %.

The dipole form factor in eq. (4.7) is widely used to model neutrino nucleon quasi-elastic interactions. Available neutrino scattering data from bubble chamber experiments constrains the model at low values of Q^2 but are sparse for $Q^2 > 1\,\mathrm{GeV}^2$.

Two additional models are considered, a "2- and 3-component" model [143], and a model based on QCD sum rules, the "Z-expansion" model [144, 145]. Both these models fit the data from the bubble chamber experiments well but vary in the uncertainty that they predict. Propagation of the additional form factors to ND280 and Super-K shows inflated errors at values of $Q^2 > 1\,\mathrm{GeV}^2$. These models are not used to constrain the parameters for the analysis presented in this thesis but are used to build fake data sets, and will be used in future as the reference model.

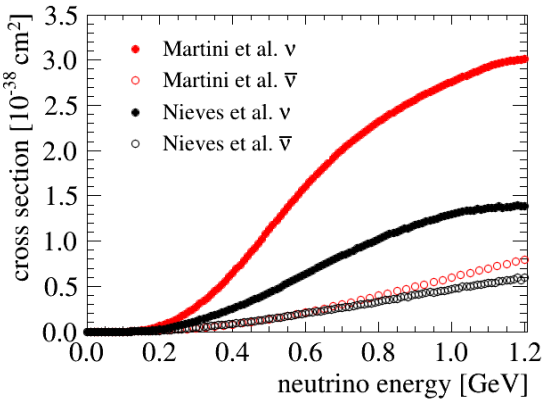

Figure 4.10: Neutrino and antineutrino cross sections for the 2p2h process for the reference T2K model, Nieves et al., and an alternative model, Martini et al. Reproduced from [134].

4.2.1.5 Multi-Nucleon Interactions (2p2h)

The 2p2h interaction process occurs when the incoming neutrino interacts with two nucleons, as shown in fig. 4.11, and this can be decomposed into the following contributions

- Meson Exchange Current (MEC), Δ resonance pion-less decay and other MEC diagrams which include a Δ propagator and contributions due to pions in flight shown in fig. 4.13
- Nucleon-Nucleon (NN) correlations shown in fig. 4.12
- interference between MEC and NN

This class of interactions can account for between 10–20 % of the total CC0π cross section at T2K. The region of phase space $(\omega, \vec{q})$ occupied by 2p2h overlaps that of pion production, whilst NN overlaps with the Quasielastic region. Since these interaction modes have different mappings from true to reconstructed quantities and without knowledge of the contribution from each of these modes the use of the neutrino energy reconstruction formula eq. (4.11) biases the reconstruction to lower energies. Data from electron scattering experiments could potentially be used to constrain this process, however, due to restrictions from the available models this cannot be done directly. A parameter that rescales the 2p2h contribution and a variable which alters the composition of MEC and NN components and alters the differential shape is included in the analysis. There are very different predictions for neutrinos and antineutrinos for the default model [135] and the alternative model [146, 147], and are shown in fig. 4.10. Unfortunately for this analysis there are low antineutrino statistics at ND280 (only data up to Run 6 is used) which makes it impossible to constrain the antineutrino shape uncertainty.

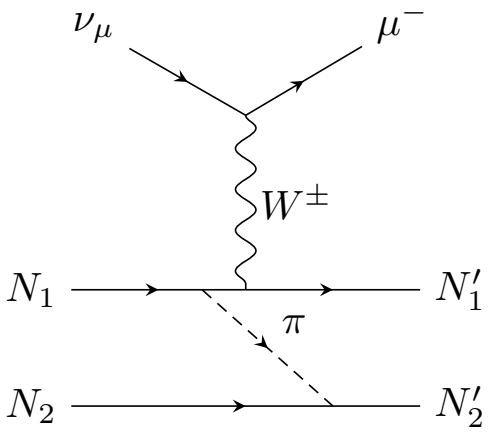

Figure 4.11: Coupling between pairs of nucleons, $N_{1,2}$ via pion exchange in a ν_μ interaction.

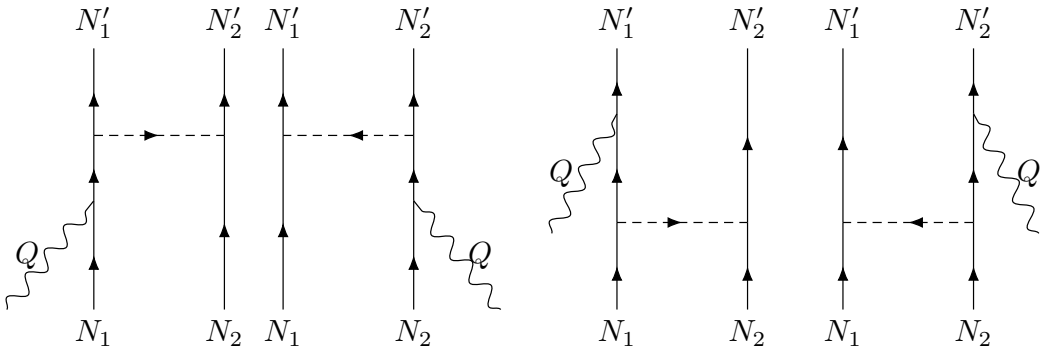

Figure 4.12: Couplings between pairs of nucleons, nucleon-nucleon (NN) interactions.

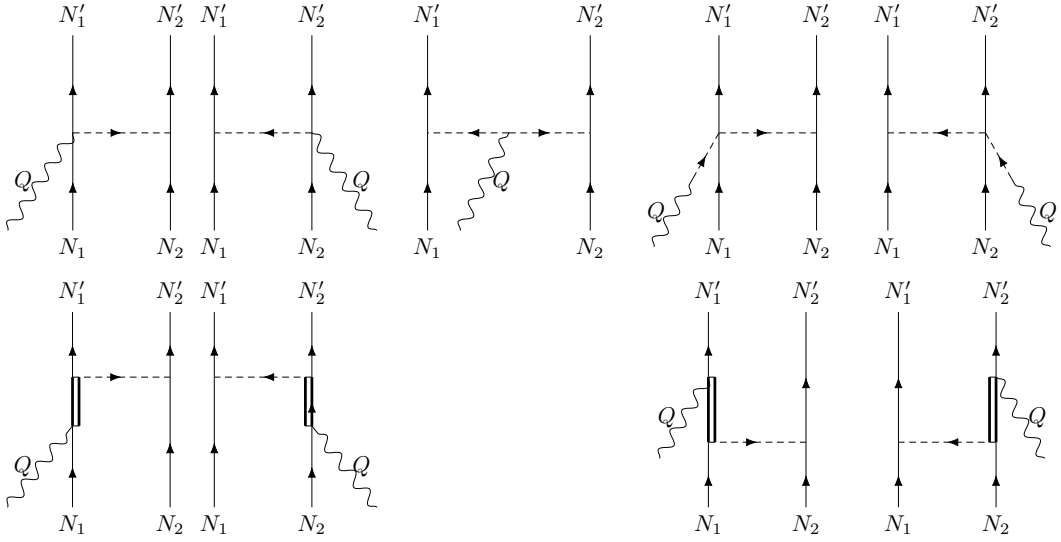

Figure 4.13: Feynman diagrams of the MEC contribution to the two particle two hole interaction. The top line shows the two contact or seagull diagrams, the pion in flight term, and the pion pole term. The second line shows the coupling to a Δ-resonance or Δ-pole

The NEUT Nieves et al. reference model [135] has been developed for isoscalar nuclei, and a study to estimate the uncertainty on the extrapolation from carbon to oxygen has been performed based on data from electron scattering experiments at CLAS [148]. Extrapolation from the phase space of the data and corrections for FSI effects limit the scope of the conclusions from the study, however conservative conclusions are made which motivate the oscillation analysis priors. The parameters for the oscillation analysis are set so that the 2p2h normalisation parameters for ν and $\bar{\nu}$ on carbon have flat prior probability distributions and are uncorrelated. The 2p2h normalisation scaling from carbon to oxygen have 20 % correlation and are fully correlated between ν and $\bar{\nu}$. The 2p2h shape uncertainty is fully correlated between ν and $\bar{\nu}$ and flat within the range $[-1, 1]$, fully NN or not-Δ like to fully MEC or Δ like. The 2p2h shape uncertainty on oxygen behaves in the same manner as the shape uncertainty on carbon and be 30 % correlated with the carbon parameter.

4.2.1.6 Single Pion Production

The previous oscillation analysis of the T2K data included a sample with a single pion in addition to the CCQE-like samples previously included. A final state that includes a single pion can be produced via several different interaction processes. These include: resonance excitations that decay into pions, multi-pion processes, and coherent pion production. The largest contribution comes from resonance production, with a small contribution to this process from a "non-resonant background", in which pion production proceeds without an intermediate resonance state. These are incorporated into the T2K model using Rein-Sehgal model [149], and the hadronic invariant mass, W, of the final state follows the condition $W < 2\,\text{GeV}$ to avoid double counting with the DIS process discussed in section 4.2.1.9. The $\Delta(1232)$ dominates resonance production at T2K beam energies.

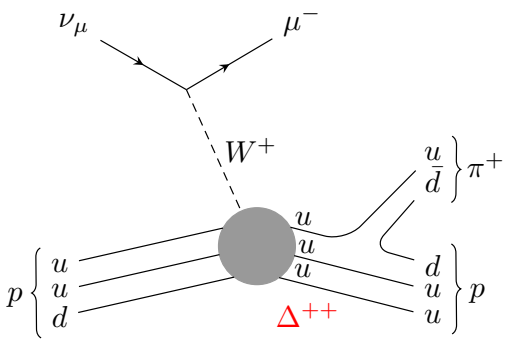

Figure 4.14: A possible Feynman diagram for the production of a charged pion by excitation and subsequent decay of a resonance.

The single pion data was previously tuned to data from nuclear targets, MiniBooNE, K2K, and the data from bubble chambers was not included. This oscillation analysis, bins the

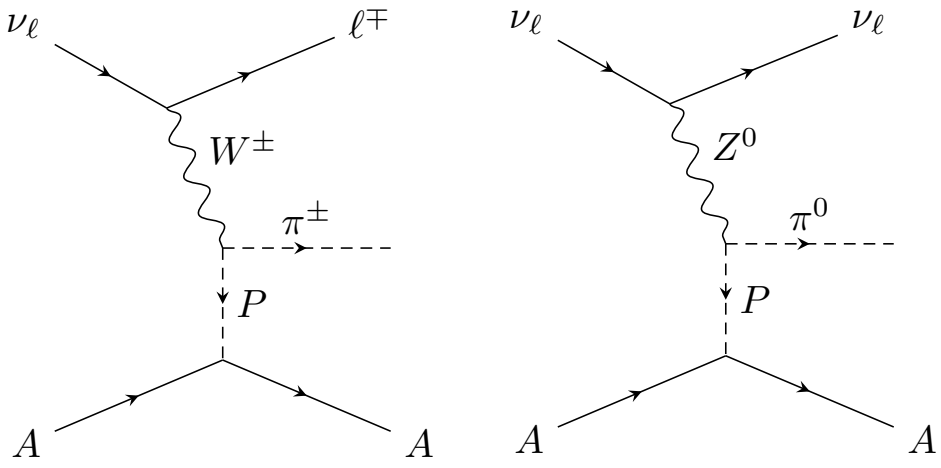

(a) CC process **(b)** NC process

Figure 4.15: Coherent pion production on a nucleus, showing the exchange of a pomeron with the nucleus leaving it in the ground state and the production of charged pion for (a) the CC process, and a neutral pion for (b) the NC process.

events in E_ν and in θ of the outgoing lepton for electron-like events. Lepton kinematics do not undergo the additional final state interactions, and can thecrefore sidestep the pion and nucleon models. The external data from MINERνA and MiniBooNE data which are the most relevant data have associated difficulties which make them unsuitable for the tuning that was performed, and were not used apart from the lepton data available. Bubble chamber data is included by reweighting interactions with single pions on a free nucleon and MiniBooNE $T_\mu \cos\theta_\mu$ data is used to verify the scaling performed to the nuclear environment.

Values extracted from separate fits to different data sets show a wide range of variation, the central values of the parameters and the correlations between the parameters are taken from the ANL+BNL fit with inflated errors in order to cover data on nuclear targets from MiniBooNE.

Coherent pion production produces a pion via interaction with the whole nucleus without exciting the nucleus after neutrino scattering. For this process to take place, there must only be a low energy transfer to the nucleus. Data from MINERνA is lower compared to the prediction from NEUT, and an ad-hoc reweighting has been implemented from the data due to known under prediction from the implemented Rein-Sehgal (RS) model.

4.2.1.7 Tuning to bubble chamber and nuclear data

Previous iterations of the single pion tunes detailed in [150, 151, 152] used the existing scattering data on nuclei from the MiniBooNE [153] and K2K [154] experiments, these experiments reported their results as cross sections as a function of energy rather than

flux integrated differential cross sections which introduces model dependence. The bubble chamber data was not used at all in the previous fits. Lepton ℓ kinematics $p_\ell, \cos\theta_\ell$ are unaffected by subsequent interactions with the nuclear medium which introduce the possibility of misidentifying the interaction topology. This makes leptonic variables ideal for extracting information from the interaction vertex.

Additional functionality was introduced to NEUT in order to generate and reweight single-pion interactions on a free nucleon. This means that the model can fit to the available bubble chamber data using minimisation techniques, rather than the previous eye-balling technique. NEUT tailors its form factor parameterisation for the $\Delta(1232)$ resonance [155], of the 18 that are considered, so tuning is preferably done to $W < 1.4\,\text{GeV}$.

Poisson likelihoods are used for the event distributions $N(\vec{x})$ in the kinematic variable $\vec{x}$ (e.g. p_π, Q^2), and Gaussian likelihoods for cross section distributions $\sigma(E_\nu)$, this leads to the expression

$$\begin{aligned}\chi^2 = &\sum^{N(\vec{x})}\left\{2\sum_{i=1}^{N(\text{bins})}\left(\text{NEUT}_i - \text{Data}_i \ln\left(\frac{\text{Data}_i}{(\text{NEUT}_i}\right)\right)\right\} \\ &+ \sum^{\sigma(E_\nu)}\left\{\sum_{i=1}^{N(\text{bins})}\frac{(\text{Data}_i - \text{NEUT}_i)^2}{\delta_i^2}\right\},\end{aligned} \tag{4.8}$$

where Data_i and NEUT_i are the i^{th} bin contents for either the cross-section or event rate distributions. The $N(\vec{x})$ distributions are fit using shape information only by scaling the generated MC distribution to the data for every fit. Correlations across experiments are not considered and normalisation of the total cross-sections is not performed, shape information only is used. The outer sum for both terms is over the data data sets that are available for that particular category.

This fit does not intend to replicate the fits producing the constraints that are carried out by the ND fitters which will be discussed in section 4.3, but aims to provide ranges within which the model can vary given the input data. Several fits are made to the bubble chamber data, either combined or alone, and the MiniBooNE lepton variable data, setting various conditions in fit, e.g. fixing or allowing the non resonant background parameter $I_{1/2}$ to be free. From these fits which produced a range of best-fit values the central values and uncertainties on the parameters M_A^{RES}, the axial mass for the resonant process analgous to M_A^{QE}, C_A^5, the axial form factor, and $I_{1/2}$ are listed in table 4.4.

4.2.1.8 Final State Interactions (FSI)

Hadrons propagating through the nuclear medium as a result of a neutrino interaction may interact in this medium. These interactions happen before the lepton or hadron

Parameter	Central Value & Uncertainty
M_A^{RES}	1.07 ± 0.15
C_A^5	0.96 ± 0.15
$I_{1/2}$	0.96 ± 0.40

Table 4.4: Central values and uncertainties resulting from the fit to the external data for the pion production parameters from [134].

can be observed, and the probablility of a pion undergoing an additional interaction is significant . To further complicate accessing the underlying physics process, the hadrons which leave the medium can undergo "secondary interactions" (SI) in the detector material before reconstruction. For example when pions are absorbed in the nuclear medium the event reconstruction looks CCQE-like, however the 2-body assumption for CCQE events eq. (4.11), which will be discussed in section 4.4, biases the energy reconstruction. Any FSI and or SI interactions can modify the pion kinematics, which in turn alters the detector particle identification efficiency. Charge exchange processes can modify the observed neutral pion rate, which because of conversion to γ-rays is an important background to understand for ν_e appearance. FSI processes are difficult to constrain because data from well understood hadron beams do not probe the interior of the nucleus and consequently are not subject to the same physical environment as hadrons from neutrino induced interactions.

The FSI interactions are modelled in NEUT by use of a cascade model [132] and constrained using external data [156]. An Intra-Nuclear cascade model is used, in which pions are tracked from their creation at the initial neutrino interaction. The position where the pions are created is chosen based on a nuclear density profile, modelled by a Fermi model, the Woods-Saxon potential [157], using a three parameter model with one set to zero for oxygen. The pion is then stepped through the nucleus in finite steps, where interaction probabilities are calculated till absorption or the pion leaves the nucleus. High and low momentum pions have different treatments, using tables derived from a computational many-body simulation in infinite nuclear matter and scattering data from free protons and deuterons respectively. A mixture of these models is used in the region 400–500 MeV. The model is parameterised by using six factors, one for absorption, two for QE scattering (high and low energies), two for charge exchange (high and low energies) and one for hadron production and are named in table 4.5. Five of the parameters scale the probabilities of π interaction at each step, and the parameter `FEFCX` scales the charge exchange fraction of quasielastic scattering at low momenta.

NEUT Name	ND Fit Name	Momentum Region MeV/c_0	Description
FEFABS	FSI_PI_ABS	<500	Absorption
FEFQE	FSI_INEL_LO	<500	QE scattering (low energy)
FEFCX	FSI_CEX_LO	<500	Single charge exchange (low energy)
FEFQEH	FSI_INEL_HI	>400	QE scattering (high energy)
FEFCXH	FSI_CEX_HI	>400	Single charge exchange (high energy)
FEFINEL	FSI_PI_PROD	>400	Hadron (N+nπ) production

Table 4.5: The NEUT and ND names of the FSI scaling parameters with their associated momentum region. These parameters are also used in the fits to data described in this section and section 4.2.2. The overlapping momentum regions are due to the combination of the scaling parameters in this region.

The uncertainties that are associated with FSI are implemented in the near and far detectors using different methods. Response functions, parameterised using splines, on an event by event basis are used at ND280. The response functions span 1σ, this factorisation of the response functions has been validated and is of order 1 %.

4.2.1.9 Deep inelastic scattering (DIS)

At high neutrino energies, above ∼5 GeV, deep inelastic scattering (DIS) processes dominate, where the interaction of the neutrino is directly with the quark inside the nucleon via one of the weak force bosons, often fragmenting the nucleon in the process and these fragments producing a hadronic shower. These interactions lie in the tail of the T2K flux, and are not part of the signal that is considered for the oscillation analysis.

4.2.2 Final State Interactions and Secondary Interactions Tuning

As previously described in section 4.2.1.8, FSI and SI interactions interactions can mean that the reconstructed energy of an event is biased due to misidentification of the event topology. The NEUT cascade model is tuned to external $\pi^{\pm} - A$ scattering data. The parameters that are used are named in table 4.5, and each of these is used to scale the microscopic probability at each step in the cascade apart from FEFCX which scales the charge fraction in low momentum quasi-elastic scattering. The interaction channels that are used for the analysis are:

- **Absorption (ABS):** No pions in the final state
- **Quasi-elastic Scattering (QE):** Only a single pion in the final state, of the same charge as the incident beam

- **Single Charge Exchange (CX):** Only one π^0 in the final state
- **Absorption + Single Charge Exchange (ABS+CX):** Sum of ABS and CX
- **Reactive:** Sum of ABS + CX + QE, Double Charge Exchange, and Hadron Production. Double charge exchange is final states with one pion with the opposite charge to the incident beam. To be defined as hadron production the final state must contain more than one pion.

The target materials used in the FGDs are plastic scintillator (FGD1), and a combination of water and plastic scintillator (FGD2) as described in section 3.2.1.2, Super-K uses water as its target material described in section 3.3. In principle there is not a need to tune to heavier nuclei but the near detector contains heavier nuclei e.g. the Pb planes in the ECals, on which interactions and FSI/SI interactions can occur. There are also plans to use interaction samples from outside the tracker region in the ND fits to constrain the uncertainties in the oscillation analysis so a variety of targets, Carbon, Oxygen, Aluminium, Iron, Copper and Lead are used to tune the data.

Data comparisons were made to 18 data sets, including measurements from the Dual Use Experiment at TRIUMF (DUET) [158].

A pre-computed grid of pion cross-sections for a grid of the 6 FSI parameters in table 4.5. A best fit for the parameters is then found by minimising a χ^2. A scaling was applied to the χ^2_{FSI} to cover all the external data fits, The scaling Φ is determined by

$$\Phi = \frac{\sigma_j^{\text{Bestfit}}(f_{\text{FSI}}) - \sigma_j^{\text{Data}}}{\Delta\sigma_j^{\text{Bestfit}}(f_{\text{FSI}})}, \tag{4.9}$$

where the, $\sigma_j^{\text{Bestfit}}$ external data are compared with the $\sigma_j^{\text{Bestfit}}$ NEUT values and the 1-σ errors $\Delta\sigma_j^{\text{Bestfit}}(f_{\text{FSI}})$. Even with the inflated errors the post-fit values of the FSI parameters are smaller than those obtained with the previous analysis performed in [152].

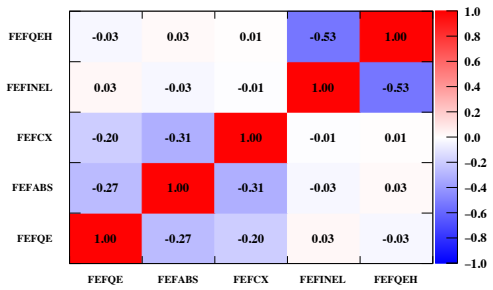

Figure 4.16: Correlation matrix for Final State Interactions parameters obtained from the external data fit, using interpolation and the lower values of correlations retrieved from the two methods used. Reproduced from [156]

Two interpolation methods were used which returned values of minimum χ^2 which agreed, however the covariance matrices that were returned from the two methods differed in the strength of the correlations that they returned. The method with the smaller correlations was used for the final results [156], which are shown in fig. 4.16. The resulting central values and 1σ uncertainties are shown in section 4.2.2. The parameter `FEFCXH` was left fixed in the fits as the data does not cover this region of phase space and the `FEFINEL` `FEFQEH` parameters cover the data sets. fits are shown in fig. 4.17 for a subset of the data considered.

Parameter	Best Fit $\pm$ 1σ
`FEFQE`	1.069 ± 0.313
`FEFABS`	1.404 ± 0.432
`FEFCX`	0.697 ± 0.305
`FEFINEL`	1.002 ± 1.101
`FEFQEH`	1.824 ± 0.859
`FEFCX`	1.8(Fixed)

Table 4.6: The post-fit values of the FSI parameters, with the error scaling described in eq. (4.9).

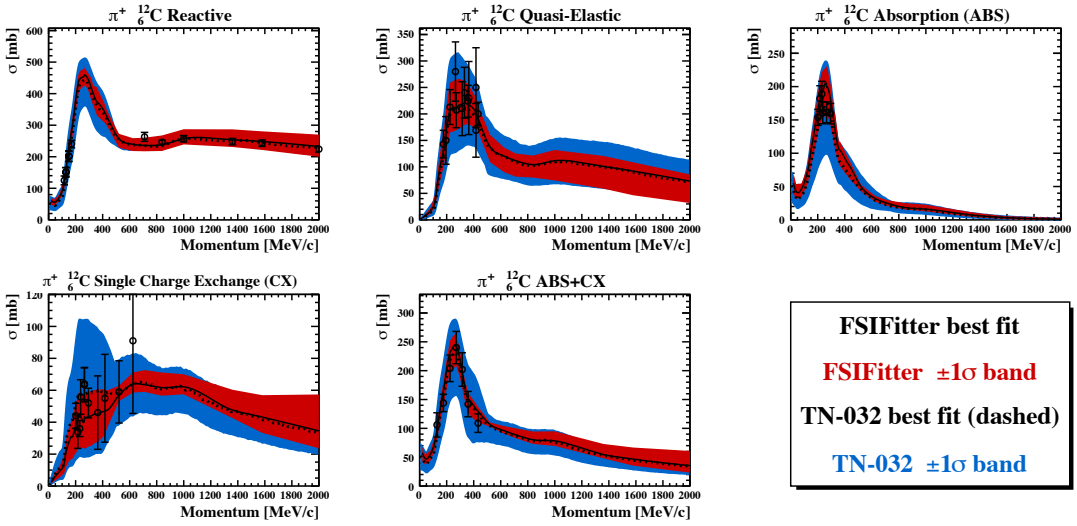

Figure 4.17: Fits to the available π^+-C cross section external data using the FSIFitter developed in [156] compared with earlier fit results and 1-σ error bands from [150].

4.3 Near Detector Flux and Cross-section Model Constraints

The T2K flux and cross section models can be constrained using external and internal measurements, the set of external measurements that constrain the flux and cross section

parameters are described in previous sections. The following section describes how better quantified central values for many systematic parameters are obtained, these form the inputs to the nominal spectra predictions made at Super-K. The uncertainties of each of the systematic parameters are also better quantified and the correlations between them are reported in a covariance matrix, this matrix is used in the bounds of the systematic variations of the Super-K spectra which are used in the oscillation analysis in chapter 5.

The flux and cross section parameters, which are nuisance parameters, are constrained using BANFF [159] and MaCh3 fitters for the T2K experiment. Both analyses fit the near detector data to produce covariance matrices containing the uncertainties on the parameters and separately the associated tuned central values for use as an input to the oscillation analysis. The parameters considered are fitted using ND280 data with the flux parameters for Super-K allowed to vary in the fit according to separately to Super-K, where this constraint is propagated. This analysis uses data whose interaction vertex is in FGD1 or FGD2.

The "Asimov data set" is a statistical technique which is used in the following section and extensively in the analysis in chapter 5. The "Asimov data set" is a single toy experiment generated from MC, without statistical or systematic fluctuations, intended to replace an ensemble of data sets. This set has the property of characterising the sensitivity without the need to generate many MC toy experiments with good accuracy even for small samples [160]. This technique saves computation time by replacing the ensemble of data sets that would otherwise need to be generated.

4.3.1 Sample Selection

Two sets of samples are selected to fit at the near detector, FHC ν_μ and for RHC $\bar{\nu}_\mu\nu_\mu$. For the RHC mode the different production rates of π^+/π^- in the $p-C$ collisions at the T2K target [161] along with the difference in cross section between neutrinos and antineutrinos result in a greater contamination of ν in the $\bar{\nu}$ beam. Without being able to separate neutrino induced events from antineutrino events, this forms an irreducible background at Super-K. For this reason the RHC selection characterises this background by selecting the appropriate sample which are then used in the BANFF and MaCh3 near detector fits. These samples are selected using software which is described in [162, 163, 164].

For the RHC running mode the same criteria were used to select both neutrino and antineutrino events. Three stages are used to select the events: first an event pre-selection takes place for both FGD1 and FGD2, events are then selected to form a CC-inclusive sample, and finally events are separated into CC 1-Track and CC N-Track samples [165,

166]. The CC 1-Track sample is CC-quasielastic enhanced which forms the bulk of the oscillation analysis sample, whilst CC N-Track include hadron production. The event pre-selection for both RHC samples is detailed below:

- **Event Quality:** The event must occur in a defined bunch with good data quality flags
- **Total Multiplicity:** The selected event must have at least one track which crosses TPC2
- **Quality and Fiducial:** The highest momentum positive track (HMPT) in the event must have its vertex in the FV of FGD1 (or FGD2) and >18 TPC nodes
- **Highest Momentum Track:** The HMPT must be the highest momentum track (HMT) in the event
- **TPC1 veto:** Veto on backwards events or events originating from the PØD or Magnet. Additionally for the FGD2 selection no tracks starting in the FGD1 FV are allowed
- **External FGD1 (FGD2):** Rejection of external background from the last two layers of FGD1 (FGD2)
- **Muon PID:** events passing the above cuts are then classified using the TPC by first removing electrons and then removing p and π^+ from CCnonQE interactions.

After the cuts that are outlined above the sample, CC-inclusive, is split into CC 1-Track and CC N-Tracks. Those events with a single matched track reconstructed in the FGD and TPC are CC 1-Track, and those with more tracks are classified as CC N-Track. The CC 1-Track and N-Track samples are separated by the number of matched tracks in the TPC and FGD for an event. Events with a single TPC-FGD matched track are selected for the 1-Track sample, leading to an enhancement in CCQE-like events. Events with more than a single TPC-FGD matched track compose the N-Tracks sample. The efficiency and purity of the of the samples are listed for both the ν_μ and $\bar{\nu}_\mu$ in RHC running mode in FGD1 and FGD2 in table 4.7.

The topologies used in the selections are CC-0π, which is defined as events with a true $\mu^\pm$ and without any $\pi^{\pm,0}$. CC-Nπ are the events remaining from the CC-inclusive sample once the CC-0π events are removed, this includes $\geqslant \pi^{\pm,0}$ and $\mu^\pm$ and also includes K, η. Backgrounds are made up of the (anti)neutrino CC interactions depending on the selection, ν_e and neutral current signal. Events outside the fiducial volume of the FGD, for which the sample is being selected (FGD1 or FGD2), are tagged as external.

Component	Sample	Efficiency(%)		Purity(%)	
		FGD1	FGD2	FGD1	FGD2
ν_μ	CC-Inclusive	55.1	54.6	80.0	79.2
	CC 1-Track	46.3	46.4	50.5	46.2
	CC N-Track	36.5	36.7	66.1	67.4
$\bar{\nu}_\mu$	CC-Inclusive	67	68.5	81.3	80.7
	CC 1-Track	66	68	74.4	74.5
	CC N-Track	29	31	46.4	45.6

Table 4.7: Selection efficiency and purity for the RHC samples selected in FDG1 and FGD2. Data from [165, 166].

The FHC running mode uses similar selection criteria to define the CC-inclusive sample [167]. Although the sample selection names are different they are composed of the same true topologies, with the FHC running mode distinguishing between single and multiple pion production.

- **Event Quality:** The event must occur in a defined bunch with good data quality flags.

- **Total Multiplicity:** The selected event must have at least one track which crosses TPC2

- **Quality and Fiducial:** The event is selected when there is at least one reconstructed track inside the fiducial volumes of FGD1 or FGD2, and must have its vertex inside the FGDs fiducial volume. Short tracks, which are less reliably reconstructed in the TPCs are rejected by requiring > 18 clusters in a vertical or horizontal track.

- **Upstream background veto:** Muon tracks that start upstream but are misreconstructed as originating in the TPC are rejected by vetoing events where the second highest momentum track starts 150 mm upstream of the muon candidate. The FGD2 selection also vetoes events containing a secondary track staring in FDG1 fiducial volume.

- **Broken Track Rejection:** tracks may be split by the reconstruction into two muon candidate tracks a fully contained FGD track and a FDG TPC track. These are rejected by requiring that the start position of the track is < 425 mm from the FGD upstream edge.

- **Muon PID:** events that pass the above cuts are muon candidates, electrons are removed folllowed by protons and pions.

Component	Sample	Efficiency(%)		Purity(%)	
		FGD1	FGD2	FGD1	FGD2
ν_μ	CC0π	47.62	48.45	70.4	67.4
	CC1π	27.49	23.69	54.1	53.5
	CC Other	27.61	28.23	72.9	72.8

Table 4.8: Selection efficiency and purity for the samples selected in FDG1 and FGD2 for FHC running mode, data from [167].

The CC-inclusive data set is subdivided into three sub-samples CC0π, CC1π and CC Other, secondary tracks must start in the same FGD fiducial volume and are identified using a likelihood from the TPC. Three likelihood hypotheses are used for positive tracks, π^+, e^+ and p, negative tracks only consider π^- and e^-. CC0π contains no π^+, e^+ or p using the TPC PID information, and there are no Michel decay electrons or charged pions found in the FGD. CC1π contains events with a single charged pion in the TPC and a single Michel electron, in the absence of a Michel electron the number of π^+ in the TPC and FGD must equal one. CC other contains all events not in either of the previous two classifications. The efficiency and purity of the samples that are selected are listed in table 4.8 for both FGD1 and FGD2.

4.3.2 Near detector binning

Data from both FGD1 and FGD2 are used in the analysis in addition to using data from both positive focussing (PF or FHC) and negative focussing (NF or RHC). Both of the FGDs are expected to have similar number of events so the kinematic binning for the lepton angle and momentum are the same in both.

- FHC ν_μ CC0π bin edges:
  p (MeV): 0, 300, 400, 500, 600, 700, 800, 900, 1000, 1250, 1500, 2000, 3000, 5000, 30000
  $\cos\theta$: -1, 0.6, 0.7, 0.8, 0.85, 0.9, 0.92, 0.94, 0.96, 0.98, 0.99, 1
- FHC ν_μ CC1π bin edges:
  p (MeV): 0, 300, 400, 500, 600, 700, 800, 900, 1000, 1250, 1500, 2000, 5000, 30000
  $\cos\theta$: -1, 0.6, 0.7, 0.8, 0.85, 0.9, 0.92, 0.94, 0.96, 0.98, 0.99, 1
- FHC ν_μ CCOther bin edges:
  p (MeV): 0, 300, 400, 500, 600, 700, 800, 900, 1000, 1250, 1500, 2000, 3000, 5000, 30000
  $\cos\theta$: -1, 0.6, 0.7, 0.8, 0.85, 0.9, 0.92, 0.94, 0.96, 0.98, 0.99, 1
- RHC $\bar{\nu}_\mu$ CC 1-Track bin edges:
  p (MeV): 0, 400, 500, 600, 700, 800, 900, 1100, 1400, 2000, 10000
  $\cos\theta$: -1.0, 0.6, 0.7, 0.8, 0.85, 0.88, 0.91, 0.93, 0.95, 0.96, 0.97, 0.98, 0.99, 1
- RHC $\bar{\nu}_\mu$ CC N-Track bin edges:
  p (MeV): 0, 700, 950, 1200, 1500, 2000, 3000, 10000

$\cos\theta$: -1.0, 0.75, 0.85, 0.88, 0.91, 0.93, 0.95, 0.96, 0.97, 0.98, 0.99, 1

- RHC ν_μ CC 1-Track bin edges:
  p (MeV): 0, 400, 600, 800, 1100, 2000, 10000
  $\cos\theta$: -1.0, 0.7, 0.8, 0.85, 0.9, 0.93, 0.95, 0.96, 0.97, 0.98, 0.99, 1
- RHC ν_μ CC N-Track bin edges:
  p (MeV): 0, 500, 700, 1000, 1500, 2000, 3000, 10000
  $\cos\theta$: -1.0, 0.7, 0.8, 0.85, 0.9, 0.93, 0.95, 0.96, 0.97, 0.98, 0.99, 1.

There are 100 flux parameters considered in the fit broken down into 25 parameters for each of the ND280 FHC and RHC modes and the same for the SK FHC and RHC modes, and is parameterised as presented in table 4.3. For this analysis 25 cross section parameters in addition to 6 FSI parameters are used and are listed in table 4.9. Due to the difference in composition between the near and far detectors the carbon parameters are marginalised to remove them from the covariance matrix. The composition of FDG1 is entirely scintillator, whilst FGD2 has water filled portions, making up 42 % of the target mass, which allow constraints to be set on interactions on oxygen nuclei as described in section 3.2.1.2.

The near detector fit uses bins in leptonic momentum, p and angle θ. The fits are performed by two analysis methods the BANFF and MaCh3. The detector systematics are treated by throwing 2000 variations of the systematics in a framework which allows for event weights and observables to vary and for event migration in samples and different $p-\cos\theta$ bins within a sample. Correlations between FGD1 and FGD2 are accounted for by generating two sets of systematic variations for application to events from the FDGs individually. Bin-to-bin correlations are also applied, a covariance matrix is calculated around the mean values in each $p-\cos\theta$ bin. There are 556 detector systematics considered in the fit.

The cross section matrix, described in section 4.2 contains the parameters which are listed in table 4.9,

ND Fit Name	Description
NC_other_far	NC Other Far
NC_other_near	NC Other Near
NC_1gamma	NC 1 γ
NCCoh	NC Coherent
CC_Coh_O	CC Coherent Oxygen
CC_Coh_C	CC Coherent Carbon
CC_DIS	CC Deep Inelastic Scattering
nuebar_numubar	$\bar{\nu}_e/\bar{\nu}_\mu$
nue_numu	ν_e/ν_μ
ISO_BKG	$I_{1/2}$ non-resonant background
MARES	M_A^{RES}
CA5	C_A^5 axial form factor
BeRPA_U	BeRPA U
BeRPA_E	BeRPA E
BeRPA_D	BeRPA D
BeRPA_B	BeRPA B
BeRPA_A	BeRPA A
2p2h_shape_O	2p2h shape, Oxygen
2p2h_shape_C	2p2h shape, Carbon
2p2h_norm_CtoO	2p2h normalisation, Carbon to Oxygen
2p2h_norm_nubar	2p2h normalisation, $\bar{\nu}$
2p2h_norm_nu	2p2h normalisation,ν
pF_O	Fermi Momentum p_F, Oxygen
pF_C	Fermi Momentum p_F, Carbon
MAQE	M_A^{QE} Axial Mass
FSI_PI_ABS	Absorption
FSI_INEL_LO	QE scattering (low energy)
FSI_CEX_LO	Single charge exchange (low energy)
FSI_INEL_HI	QE scattering (high energy)
FSI_CEX_HI	Single charge exchange (high energy)
FSI_PROD	Hadron (N+nπ) production

Table 4.9: The ND names of the cross-section parameters that are used in the ND280 fit to constrain the uncertainties between near and far detectors. These parameters were described in more detail in section 4.2.

Splines are generated for each event in the ND280 MC, equal interval variations of the cross section parameters are made and weights are calculated at these points. During the fits, each event is then weighted using values interpolated from the previously generated variations.

The fitters are validated using "Asimov" data sets (further described in section 5.3.3.1), where all the values of the parameters from the beam detector and cross section groups are set to their nominal values in a scaled T2K MC. BANFF fit makes throws of the fit

parameters using their prior probability distributions, and statistical throws are made to construct "toy" data. These toy experiments are fitted to understand the behaviour of the fitter.

4.3.3 Analysis Methodology

A binned log likelihood ratio, notated as $\Delta\chi^2_{\text{ND280}}$, is used in both BANFF and MaCh3 on the event samples from ND280. A set of systematic parameters have additional penalty terms applied, both MaCh3 and BANFF treat their systematics in the same way and apply the reweighting for each event . The BANFF framework uses statistical methodology that is Frequentist in nature, whilst MaCh3 uses a Bayesian approach using Markov Chain Monte Carlo to step through the parameter space.

$$\begin{aligned}\Delta\chi^2_{\text{ND280}} =& 2\sum_{i}^{N\,\text{bins}}\left(N_i^p(\vec{b},\vec{x},\vec{d}) - N_i^d + N_i^d\ln[N_i^d/N_i^p(\vec{b},\vec{x},\vec{d})]\right) + \\ & \sum_{i}^{N_b}\sum_{j}^{N_b}\Delta b_i\left(\mathbf{V_b}^{-1}\right)_{i,j}\Delta b_j + \sum_{i}^{N_x}\sum_{j}^{N_x}\Delta x_i\left(\mathbf{V_x}^{-1}\right)_{i,j}\Delta x_j + \\ & \sum_{i}^{N_d}\sum_{j}^{N_d}\Delta d_i\left(\mathbf{V_d}^{-1}\right)_{i,j}\Delta d_j\end{aligned} \tag{4.10}$$

In eq. (4.10), $\Delta\chi^2_{\text{ND280}} \equiv -2\log L$ and N_i^d is the number of data events in the i^{th} bin, N_i^p is the number of predicted events, this term is a function of the flux, $\vec{b}$, cross section, $\vec{x}$, and detector $\vec{d}$ systematic parameters. The first term in the equation captures the difference between the prediction and the data, whilst the remaining terms add penalty terms according to a covariance matrix $\mathbf{V_s}$, where $s = b, x, d$ are the matrices for the flux, cross section and detector effects respectively, and $\Delta b, \Delta x, \Delta d$ are the deviations of those parameters from the prior central values.

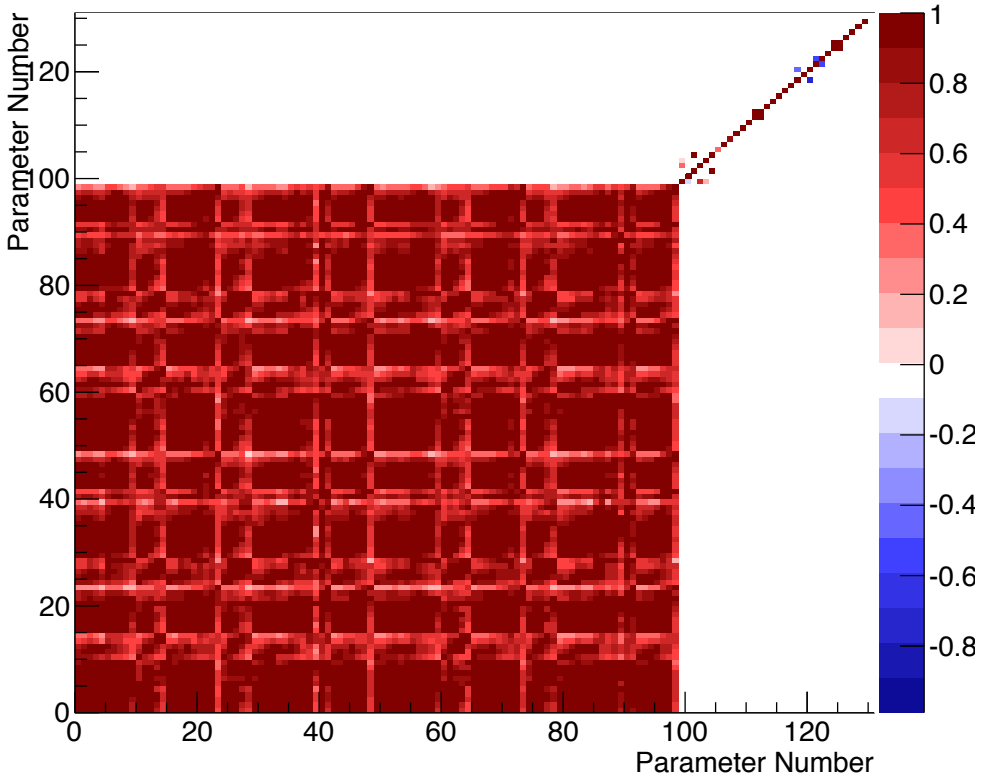

(a) Full prefit correlation matrix for flux and cross section parameters, the flux parameters follow the binning in table 4.3.

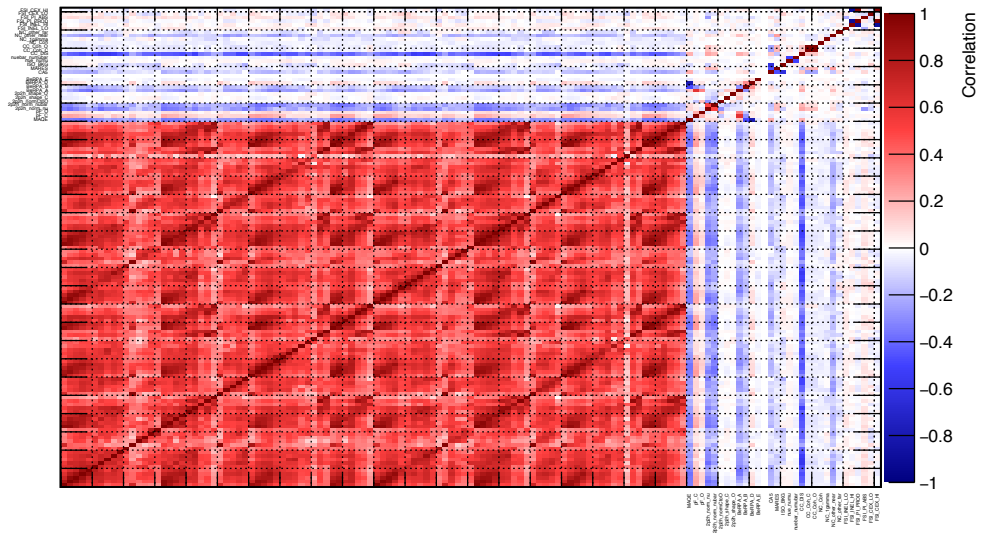

(b) Full postfit correlation matrix for flux and cross section parameters, the flux parameters follow the binning in table 4.3.

Figure 4.18: Prefit (a), and postfit correlation matrix for all flux and cross-section parameters (b) showing the resulting anticorrelation between flux and cross-section parameters. Reproduced from [168].

The correlation matrix resulting from the fit to the flux and cross-section parameter and which is used as a constraint for the oscillation analysis is shown in fig. 4.18. The 2p2h shape parameters caused difficulties in the fit due to hitting the boundary of the

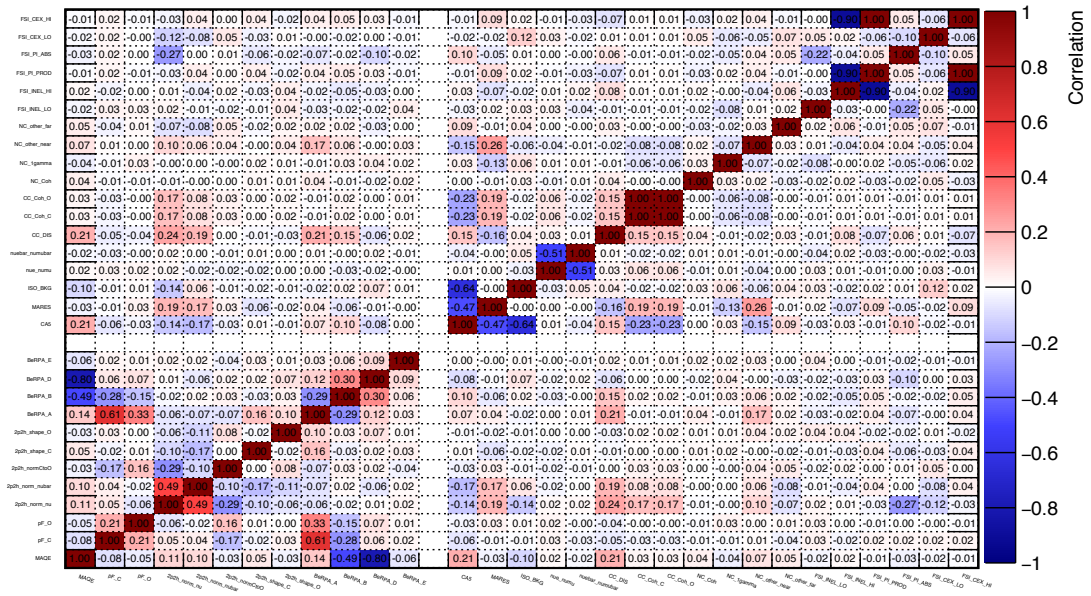

Figure 4.19: Postfit cross section parameters, considered by the near detector fit in the correlation matrix, as described in table 4.9. Reproduced from [168]

parameter values at 1 and not being able to retrieve correlations for those values. In order to retrieve errors and correlations for these values splines whose range is extended by making them symmetric around 1 were used. Studies showed that these splines do not affect the post-fit values of other parameters.

The prefit and postfit central values and uncertainties for the cross-section parameters are shown in table 4.10, along with the values for the flux in both FHC and RHC modes at Super-K in table 4.11. The predicted event rates pre/postfit are shown in table 4.12. The spectra generated with postfit parameter values for FGD1 and FGD2 are shown with data overlaid in figs. 4.20 to 4.26

Parameter	*PreFit*	*PostFit*
FSI_INEL_LO	0.0 ± 0.41	-0.32332 ± 0.081129
FSI_INEL_HI	0.0 ± 0.34	-0.0086159 ± 0.12846
FSI_PI_PROD	0.0 ± 0.5	0.040936 ± 0.18706
FSI_PI_ABS	0.0 ± 0.41	-0.34771 ± 0.14731
FSI_CEX_LO	0.0 ± 0.57	-0.088986 ± 0.30907
FSI_CEX_HI	0.0 ± 0.28	0.022924 ± 0.10475
MAQE(GeV/c^2)	1.2 ± 0.03	1.1314 ± 0.079024
pF_C(MeV/c)	217.0 ± 13.0	224.16 ± 13.295
pF_O(MeV/c)	225.0 ± 13.0	204.98 ± 15.083
2p2h_norm_nu	1.0 ± 1.0	1.5018 ± 0.1955
2p2h_norm_nubar	1.0 ± 1.0	0.726 ± 0.23125
2p2h_normCtoO	1.0 ± 0.2	0.96392 ± 0.16657
2p2h_shape_C(%)	100.0 ± 300.0	200.22 ± 20.606
2p2h_shape_O(%)	100.0 ± 300.0	199.71 ± 34.746
BeRPA_A	0.59 ± 0.118	0.6878 ± 0.057308
BeRPA_B	1.05 ± 0.21	1.5993 ± 0.11727
BeRPA_D	1.13 ± 0.1695	0.96248 ± 0.13445
BeRPA_E	0.88 ± 0.352	0.8749 ± 0.35332
BeRPA_U	1.2 ± 0.1	1.2 ± 0.1
CA5	0.96 ± 0.15	0.97601 ± 0.064304
MARES(GeV/c^2)	1.07 ± 0.15	0.806 ± 0.044916
ISO_BKG	0.96 ± 0.4	1.3147 ± 0.25594
nue_numu	1.0 ± 0.028284	1.0 ± 0.028284
nuebar_numubar	1.0 ± 0.028284	1.0 ± 0.028284
CC_DIS	0.0 ± 0.4	0.38541 ± 0.19726
CC_Coh_C	1.0 ± 0.3	0.87408 ± 0.28178
CC_Coh_O	1.0 ± 0.3	0.87406 ± 0.28179
NC_Coh	1.0 ± 0.3	0.93795 ± 0.29744
NC_1gamma	1.0 ± 1.0	1.0 ± 1.0
NC_other_near	1.0 ± 0.3	1.208 ± 0.25613
NC_other_far	1.0 ± 0.3	1.0 ± 0.3

Table 4.10: Prefit and Postfit values of the cross section parameters that are considered in the near detector fit. Reproduced from [168].

Parameter	*PreFit*	*PostFit*
SKNuModeNumu0	1.0 ± 0.10255	1.012 ± 0.059199
SKNuModeNumu1	1.0 ± 0.10177	1.0333 ± 0.053822
SKNuModeNumu2	1.0 ± 0.092573	1.0164 ± 0.046599
SKNuModeNumu3	1.0 ± 0.084265	0.97575 ± 0.04375
SKNuModeNumu4	1.0 ± 0.10227	0.9291 ± 0.055734
SKNuModeNumu5	1.0 ± 0.084528	0.95065 ± 0.050403
SKNuModeNumu6	1.0 ± 0.066909	1.021 ± 0.04356
SKNuModeNumu7	1.0 ± 0.072355	1.0379 ± 0.045617
SKNuModeNumu8	1.0 ± 0.085299	1.0289 ± 0.043839
SKNuModeNumu9	1.0 ± 0.096725	0.98928 ± 0.044167
SKNuModeNumu10	1.0 ± 0.11411	0.96922 ± 0.053331
SKNuModeNumub0	1.0 ± 0.10313	0.97924 ± 0.07523
SKNuModeNumub1	1.0 ± 0.078327	0.9693 ± 0.049141
SKNuModeNumub2	1.0 ± 0.082367	0.98238 ± 0.058624
SKNuModeNumub3	1.0 ± 0.082121	1.0319 ± 0.063217
SKNuModeNumub4	1.0 ± 0.085123	1.0971 ± 0.066473
SKNuModeNue0	1.0 ± 0.090918	1.0161 ± 0.048301
SKNuModeNue1	1.0 ± 0.087065	1.0171 ± 0.044337
SKNuModeNue2	1.0 ± 0.082527	1.0157 ± 0.043157
SKNuModeNue3	1.0 ± 0.076514	1.0058 ± 0.041025
SKNuModeNue4	1.0 ± 0.075773	1.0245 ± 0.042331
SKNuModeNue5	1.0 ± 0.082078	1.0249 ± 0.044485
SKNuModeNue6	1.0 ± 0.092882	1.0344 ± 0.061478
SKNuModeNueb0	1.0 ± 0.071921	1.0436 ± 0.054925
SKNuModeNueb1	1.0 ± 0.12898	1.0838 ± 0.11501

(a) FHC running mode flux parameters

Parameter	*PreFit*	*PostFit*
SKANuModeNumu0	1.0 ± 0.093954	0.98279 ± 0.067164
SKANuModeNumu1	1.0 ± 0.076369	0.98905 ± 0.050203
SKANuModeNumu2	1.0 ± 0.0749	1.003 ± 0.047121
SKANuModeNumu3	1.0 ± 0.078108	1.0502 ± 0.050704
SKANuModeNumu4	1.0 ± 0.077505	1.0431 ± 0.0465
SKANuModeNumub0	1.0 ± 0.10859	0.99926 ± 0.066429
SKANuModeNumub1	1.0 ± 0.10191	1.0134 ± 0.054275
SKANuModeNumub2	1.0 ± 0.092787	0.99398 ± 0.046643
SKANuModeNumub3	1.0 ± 0.082669	0.97346 ± 0.042743
SKANuModeNumub4	1.0 ± 0.10209	0.97181 ± 0.053869
SKANuModeNumub5	1.0 ± 0.087732	0.98659 ± 0.048507
SKANuModeNumub6	1.0 ± 0.068117	1.029 ± 0.044329
SKANuModeNumub7	1.0 ± 0.069902	1.0583 ± 0.048501
SKANuModeNumub8	1.0 ± 0.091711	1.0633 ± 0.065275
SKANuModeNumub9	1.0 ± 0.084736	1.0388 ± 0.058505
SKANuModeNumub10	1.0 ± 0.11549	0.99739 ± 0.094353
SKANuModeNue0	1.0 ± 0.066204	1.043 ± 0.048071
SKANuModeNue1	1.0 ± 0.082645	1.0378 ± 0.066228
SKANuModeNueb0	1.0 ± 0.095453	1.0052 ± 0.053129
SKANuModeNueb1	1.0 ± 0.088889	1.0042 ± 0.045099
SKANuModeNueb2	1.0 ± 0.085644	1.0025 ± 0.045486
SKANuModeNueb3	1.0 ± 0.078536	1.0068 ± 0.041601
SKANuModeNueb4	1.0 ± 0.075246	1.035 ± 0.05292
SKANuModeNueb5	1.0 ± 0.086384	1.0377 ± 0.065989
SKANuModeNueb6	1.0 ± 0.15251	1.0751 ± 0.13391

(b) RHC running mode flux parameters

Table 4.11: Prefit and postfit values and uncertainties of the Super-K flux parameters for a FHC, and b RHC running modes, the parameterisation of the flux parameters is detailed in table 4.3. Reproduced from [168].

Sample	Data	Postfit	Prefit
FGD1 CC0π	17136.00	17122.22	16723.69
FGD1 CC1π	3954.00	4061.65	4381.48
FGD1 CCOther	4149.00	4095.58	3943.95
FGD1 Anu-CCQE	3527.00	3503.79	3587.65
FGD1 Anu-CCNQE	1054.00	1052.69	1066.91
FGD1 Nu-CCQE	1363.00	1353.44	1272.17
FGD1 Nu-CCNQE	1370.00	1354.02	1357.45
FGD2 CC0π	17443.00	17494.56	16959.19
FGD2 CC1π	3366.00	3416.28	3564.23
FGD2 CCOther	4075.00	3915.36	3570.95
FGD2 Anu-CCQE	3732.00	3685.46	3618.27
FGD2 Anu-CCNQE	1026.00	1097.38	1077.24
FGD2 Nu-CCQE	1320.00	1330.49	1262.63
FGD2 Nu-CCNQE	1253.00	1263.12	1246.71
Total	64768.00	64746.02	63632.53

Table 4.12: Event rates prefit and postfit compared to data, for the samples from both FGD1 and FGD2. Where Nu corresponds to ν Anu corresponds to $\bar{\nu}$. Reproduced from [168].

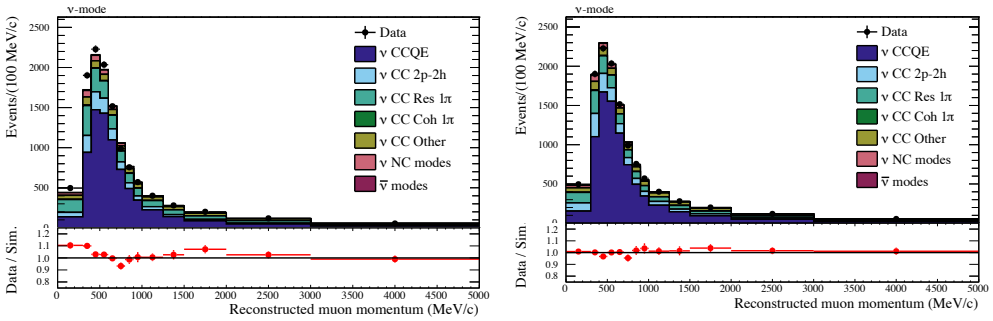

(a) FGD1 ν_μ CC0π prefit

(b) FGD1 ν_μ CC0π postfit

Figure 4.20: FGD1 MC momentum ν_μ CC0π distribution with data overlaid for (a) FGD1 prefit, (b) postfit.

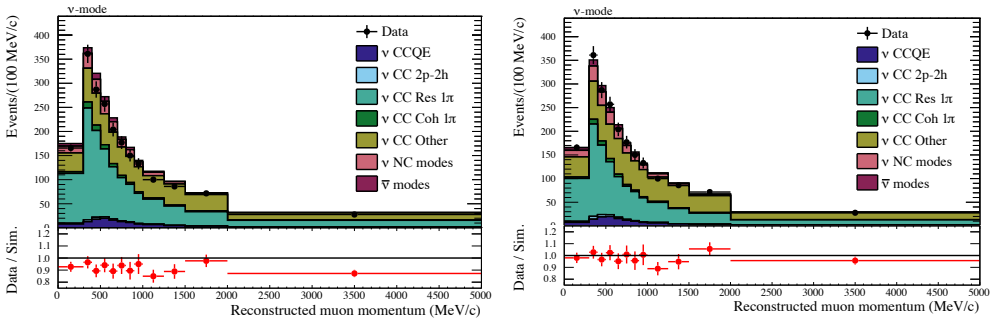

(a) FGD1 ν_μ CC1π prefit

(b) FGD1 ν_μ CC1π postfit

Figure 4.21: FDG1 MC momentum distribution with data overlaid for ν_μ CC1π, (a) prefit, (b) postfit.

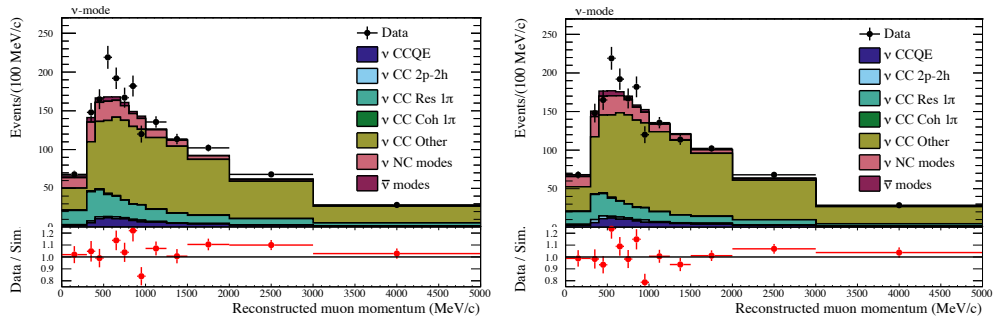

(a) FGD1 ν_μ CC Other prefit

(b) FGD1 ν_μ CC Other postfit

Figure 4.22: FGD1 MC momentum distribution with data overlaid for ν_μ CC Other, (a) prefit, (b) postfit.

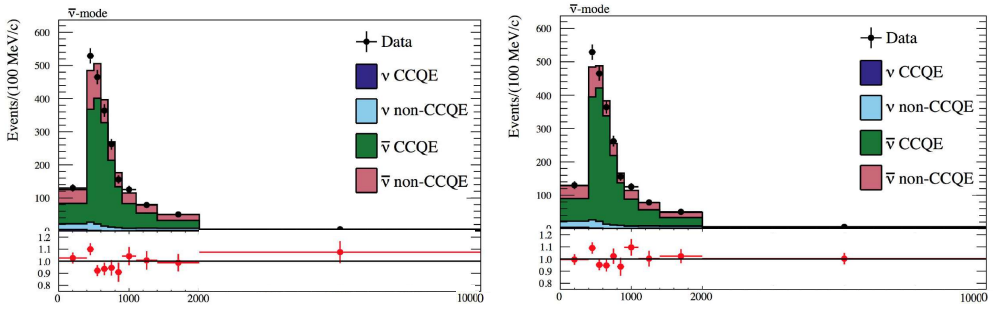

(a) FGD1 $\bar{\nu}_\mu$ 1-Track prefit

(b) FGD1 $\bar{\nu}_\mu$ 1-Track postfit

Figure 4.23: FGD1 MC momentum distribution with data overlaid for $\bar{\nu}_\mu$ 1-Track, (a) prefit, (b) postfit.

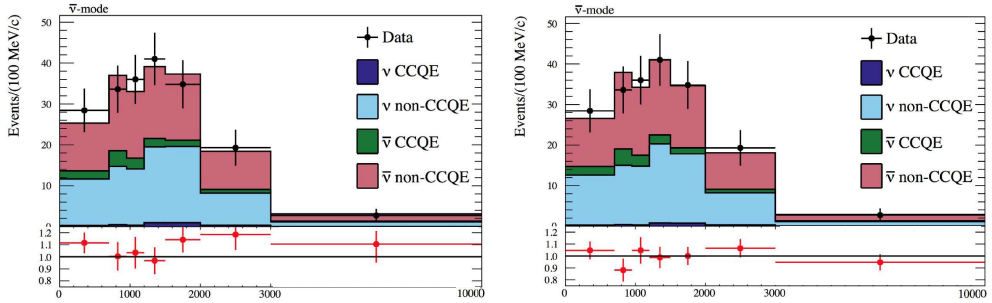

(a) FGD1 $\bar{\nu}_\mu$ N-Track prefit

(b) FGD1 $\bar{\nu}_\mu$ N-Track postfit

Figure 4.24: FGD1 MC momentum distribution with data overlaid for$\bar{\nu}_\mu$ N-Track, (a) prefit, (b) postfit.

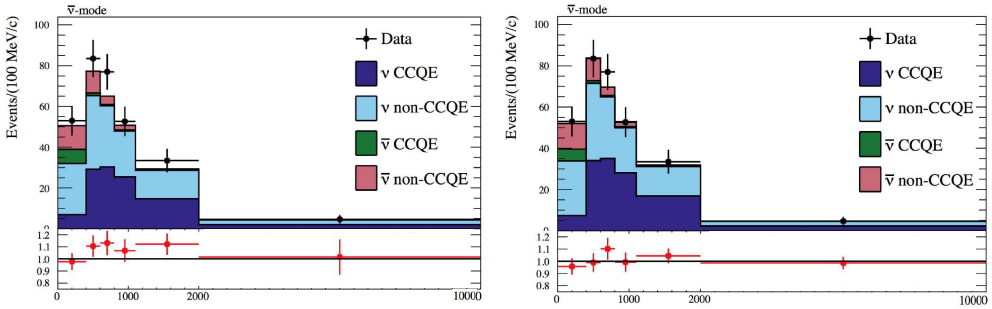

(a) FGD1 ν_μ 1-Track prefit

(b) FGD1 ν_μ 1-Track postfit

Figure 4.25: FGD1 MC momentum distribution with data overlaid for ν_μ 1-Track, (a) prefit, (b) postfit.

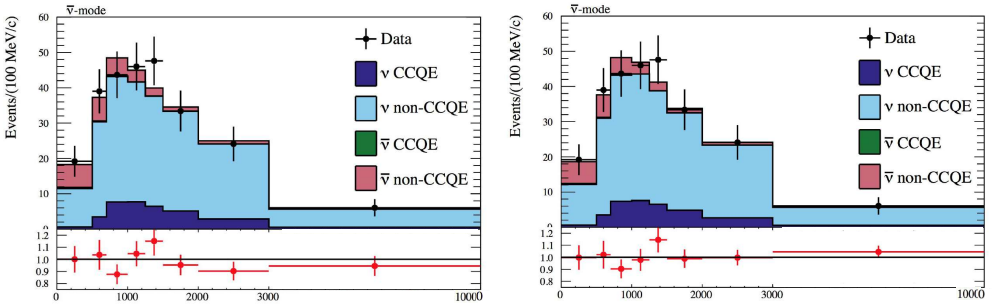

(a) FGD1 ν_μ N-Track prefit

(b) FGD1 ν_μ N-Track postfit

Figure 4.26: FGD1 MC momentum distribution with data overlaid for ν_μ N-Track, (a) prefit, (b) postfit.

4.4 Super-Kamiokande Samples

The data that is selected at Super-K undergoes a series of checks against atmospheric data and additional control samples from cosmic ray muons and their resulting decay Michel electrons. This analysis is the first that makes use of the fiTQun algorithm, introduced in section 3.3.1 to perform the reconstruction of the events, which has been

used to perform a neutral pion background reduction, and is still used in the current analysis. NEUT 5.3.2 and SKDETSIM v13p90 are used in the analysis.

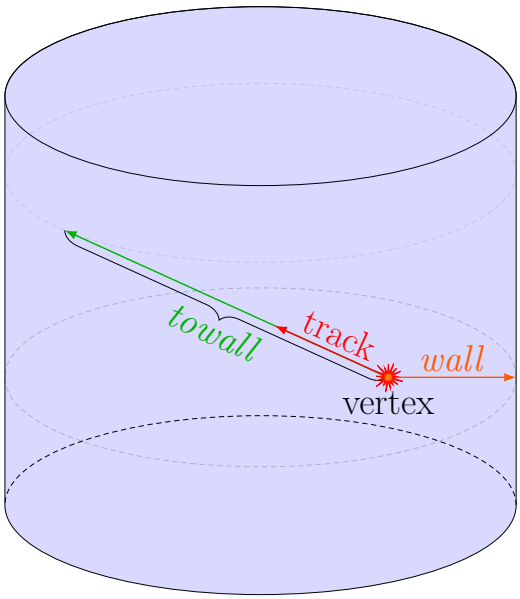

Figure 4.27: FitQun variables *wall* and *towall* which are used in the fiducial volume cuts, the *wall* variable is the minimum distance to the ID PMT wall from the reconstructed vertex, and *towall* is the distance along the particle track to the detector ID wall.

The beam data is first selected on the basis of good beam spills which are determined by the Super-K DAQ. Spills which are rejected by the pre-activity cut are increasing in the Super-K detector due to gain increase in the PMTs resulting in an increase in the low energy events. A timing window $[-2, +10]\,\mu s$ is applied to the beam spill's leading edge. Fully contained (FC) events are selected by requiring the activity in the outer detector (OD), *nhitac* <16, where *nhitac* is the number of hits in the highest charge hit cluster. The fiducial volume (FV) sample is a a sub-sample of the FC sample and is used in this analysis. The selection of FV samples is done by the fiTQun algorithm, and are known as fully contained fiducial volume (FCFV) samples. Two variables,*wall* and *towall*, are used to determine if a sample is FCFV, rather than a single variable, *wall*, as was used by the previous APFit algorithm. The *wall* variable is the distance to the nearest inner detector (ID) wall from the interaction vertex, and *towall* is the distance to the ID wall along the path of the particle direction vector from the vertex, as illustrated in fig. 4.27. Due to differences in the optimum values for the *wall* and *towall* variables for the electron and muon hypotheses, an additional fiducial volume definition $\mathrm{FCFV}_{\mathrm{floor}}$, is made using values of the *wall* and *towall* variables, using the minimum allowed values used in the optimisation study of the FV, which are *wall* >50 cm) and *towall* >150 cm [169], and will be discussed in section 4.5.2. The visible energy condition is, E_{vis}>30 MeV, which is the observed Cherenkov light in an event that would be produced by an electron at that energy.

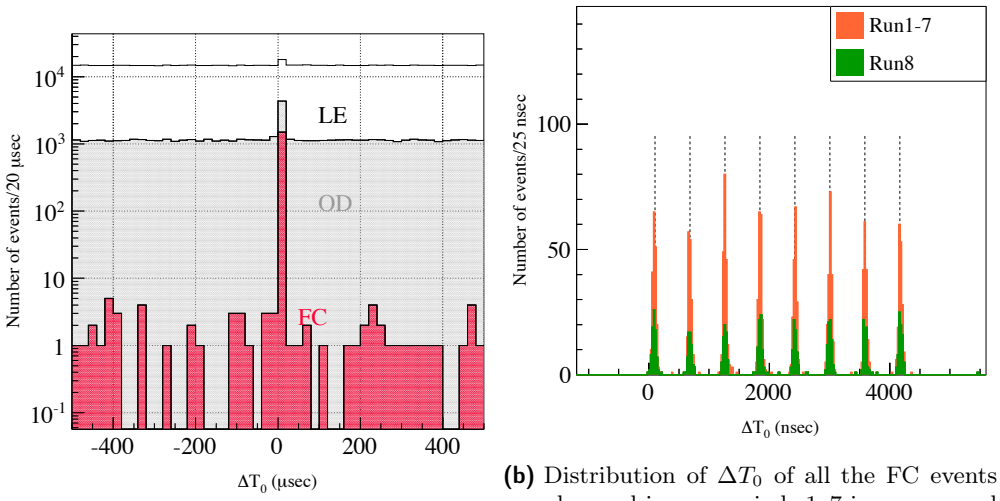

(a) Distribution of all Low Energy (LE), OD and FC events observed in a a window 1 ms around the T2K beam bunch.

(b) Distribution of ΔT_0 of all the FC events observed in run periods 1–7 in orange and 1–8 in green. The dotted vertical lines are spaced according to the bunch spacing of 581 ns and are fitted to the observed FC event times

Figure 4.28: Distributions of ΔT_0 at Super-K. Reproduced from [95]

4.4.1 FiTQun Based Sample Selection

The criteria that are used for the $\nu_e/\bar{\nu}_e$ event selection are

- Fully contained in the SK inner detector (ID) and reconstructed inside the fiducial volume (*wall* >80 cm, *towall* >170 cm)
- The number of rings that are found by the fiTQun multi-ring fitter is one
- The ring is identified as electron-like by fiTQun single-ring fitter
- The visible energy, E_{vis} >100 MeV (use p_e in practice)
- No decay electrons
- The reconstructed neutrino energy (E_ν^{rec}) <1250 MeV
- Neutral pion rejection cut: $\ln(L_{\pi^0}/L_e) < 175 - 0.875 m_{\gamma\gamma}$, L_{π^0} is the likelihood from the dedicated π^0 fit, and m_{π^0} is the the fitted π^0 mass.

The Super-K fiducial volume cut is optimised for sensitivity to δ_{CP}, which is described in greater detail in section 4.4.2. For the ν_e sample an increase of ∼22 % in the $\nu_e + \bar{\nu}_e$ signal and a proportional increase in background is observed by application of the cuts

Sample	Run 8 Data	Run 8 MC $\sin^2\theta_{13}=0.02$	Scaled Runs 1-7 (neutrino-mode) Data	Scaled Runs 1-7 (neutrino-mode) MC $\sin^2\theta_{13}=0.02$
FC	578	591.4	657.8 ± 25.7	596.4
Floor-FCFV	478	484.2	524.0 ± 23.0	488.2
Sample-FCFV	488	495.3	538.1 ± 23.3	499.4
Single Ring	203	207.4	224.3 ± 15.0	209.8
1R μ-like	138	145.7	141.8 ± 11.9	147.5
$p_\mu > 200$ MeV/c	138	145.6	140.8 ± 11.9	147.4
1R e-like	65	61.7	82.5 ± 9.1	62.2
$p_e > 100$ MeV/c	55	54.6	72.4 ± 8.5	55.0
Multi-ring	285	287.9	313.8 ± 17.8	289.6
MR μ-like	147	130.0	142.8 ± 12.0	130.7
MR e-like	123	144.3	153.9 ± 12.4	145.2
FC non-FV	66	66.9	85.5 ± 9.3	67.5

Figure 4.29: Events in Run 8 data (7.170×10^{20} POT) and MC with oscillations applied, compared to the number of events in runs 1-7 (7.565×10^{20} POT) scaled to Run 8 exposure. Reproduced from [95].

compared to the previous set. Similarly for the $\bar{\nu}_e$ sample also see the same $\sim$22 % in the $\nu_e + \bar{\nu}_e$ signal and a $\sim$29 % increase in background.

The neutrino energy reconstruction equation used at Super-K for CCQE events is,

$$E_\nu^{\text{rec}} = \frac{(M_n - V_{nuc}) \cdot E_l - m_l^2/2 + M_n \cdot V_{nuc} - V_{nuc}^2/2 + (M_p^2 - M_n^2)/2}{M_n - V_{nuc} - E_l + P_l \cos(\theta_{\text{beam}})} \tag{4.11}$$

where $M_{n,p}$ are the masses of the neutron and proton, V_{nuc} is the binding energy of the neutron in oxygen, m_l is the energy of the charged lepton, E_l is the total lepton energy, and θ_{beam} is the angle between the outgoing charged lepton and the beam, and P_l is the lepton momentum. Equation (4.11) is based on the assumption of a bound nucleon at rest and two body kinematics for the nucleon and lepton [170].

The criteria that are used for the 1-ring ν_e-CC1π^+ event selection are

- Fully contained in the SK inner detector (ID) and reconstructed inside the fiducial volume (*wall* >50 cm, *towall* >270 cm)
- The number of rings that are found by the fiTQun multi-ring fitter is one
- The ring is identified as electron-like by fiTQun single-ring fitter
- The visible energy, E_{vis} >100 MeV (use p_e in practice)
- The number of decay electrons is one.
- The reconstructed neutrino energy ($E^{\text{rec}}_{\nu_e CC\Delta}$) <1250 MeV

- Neutral pion rejection cut: $\ln(L_{\pi^0}/L_e) < 175 - 0.875\, m_{\gamma\gamma}$, L_{π^0} is the likelihood from the dedicated π^0 fit, and m_{π^0} is the the fitted π^0 mass.

The selection criteria are identical up to the decay electron cut, the neutrino energy reconstruction is determined by

$$E^{\text{rec}}_{\nu_e CC\Delta} = \frac{2M_n E_e + M^2_{\Delta^{++}} - M^2_n - M^2_e}{2(M_n - E_e + p_e \cos\theta_e)}, \tag{4.12}$$

where $M_{\Delta^{++}}$ is the Δ^{++} resonance mass, E_e is the reconstructed electron energy and p_e is the reconstructed momentum for the electron and θ_e is the angle between the beam and outgoing electron. Since the reaction is considered as a two body process with a Δ baryon recoil, the nuclear binding potential is not included in the reconstruction [171]. There is an observed increase in the $\nu_e + \bar{\nu}_e$ signal of ∼33 % and significantly a 70 % reduction of the $\nu_\mu + \bar{\nu}_\mu$ CC background which has a large associated systematic uncertainty.

The criteria that are used for the $\nu_\mu/\bar{\nu}_\mu$ event selection are

1. Fully contained in the SK inner detector (ID), by (OD) classification and reconstructed inside the fiducial volume (*wall* >50 cm, *towall* >250 cm)

2. The number of rings that are found by the fiTQun multi-ring fitter is one

3. The ring is identified as muon-like by fiTQun single-ring fitter: $\ln(L_e/L_\mu) < 0.2p_e$

4. The reconstructed momentum of the single-ring muon-like hypothesis, p_μ >200 MeV

5. The number of decay electrons is one or zero

6. fiTQun π^+ rejection cut: $\ln(L_{\pi^+}/L_\mu) < 0.15p_\mu$, L_{π^+} is the likelihood of the single-ring π^+ hypothesis.

The 6$^{\text{th}}$ cut will be described in more detail in section 4.4.2. The event composition that is reconstructed by fiTQun is different to APFit, namely more multi-ring events are reconstructed, a ∼40 % reduction in CCnonQE, and ∼50 % reduction in NC events remain after the single-ring cut and an ∼13 % increase in the $\nu_\mu + \bar{\nu}_\mu$ signal. For the $\bar{\nu}_\mu$ sample the same improvements are seen. The sample composition after the cuts described are shown with the data in fig. 4.30 for cuts 1–4 and fig. 4.31 shows cuts 5 and 6 along with a summary of the events that pass each of the selection cuts. The momentum cut, shown in fig. 4.30(c) is intended to reduce the number of CC non QE events in the sample.

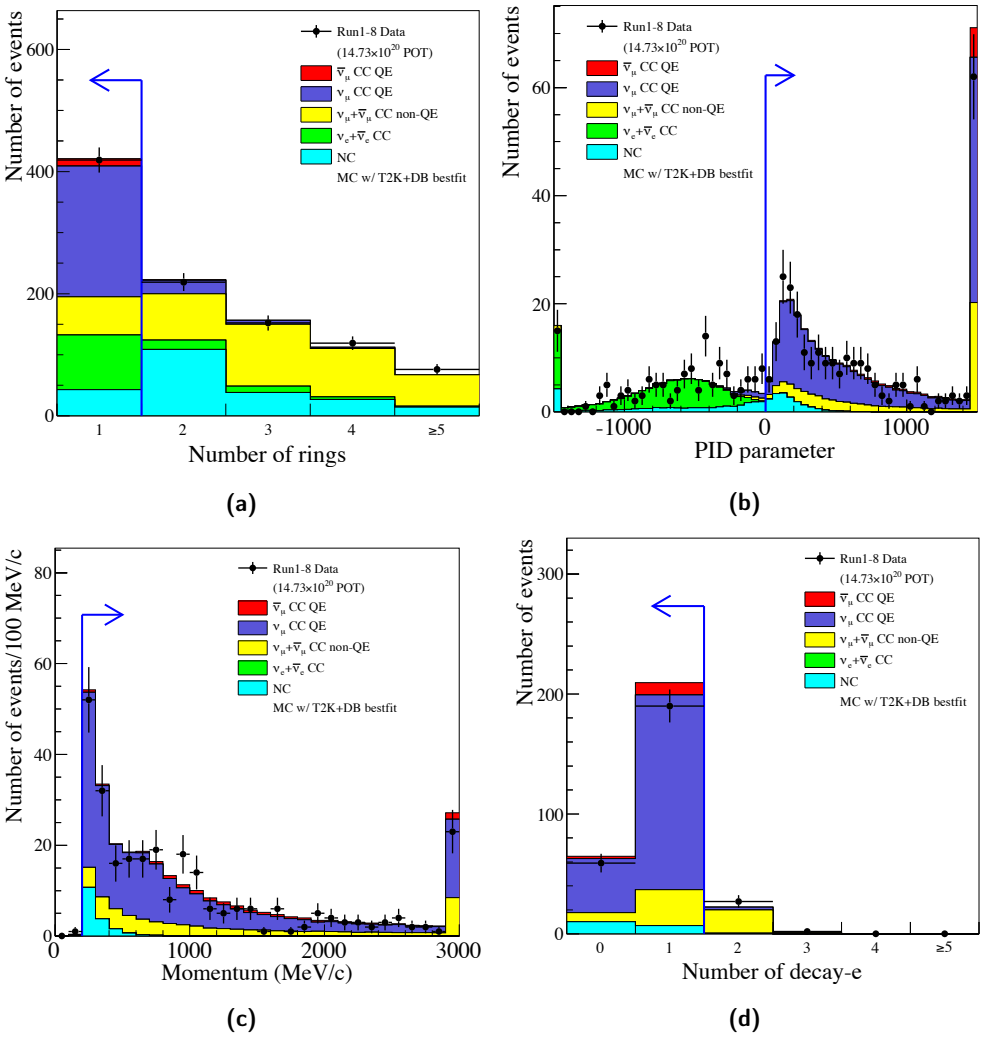

Figure 4.30: Monte Carlo overlaid with data for each of cuts for the 1 Ring μ sample described in section 4.4.1, (a) is the number of rings cut, cut (b) is μ identification, (c) is the momentum cut, and (d) is the cut on the number of decay electrons, reproduced from [95]. The graphical representation of the cuts is continued in fig. 4.31.

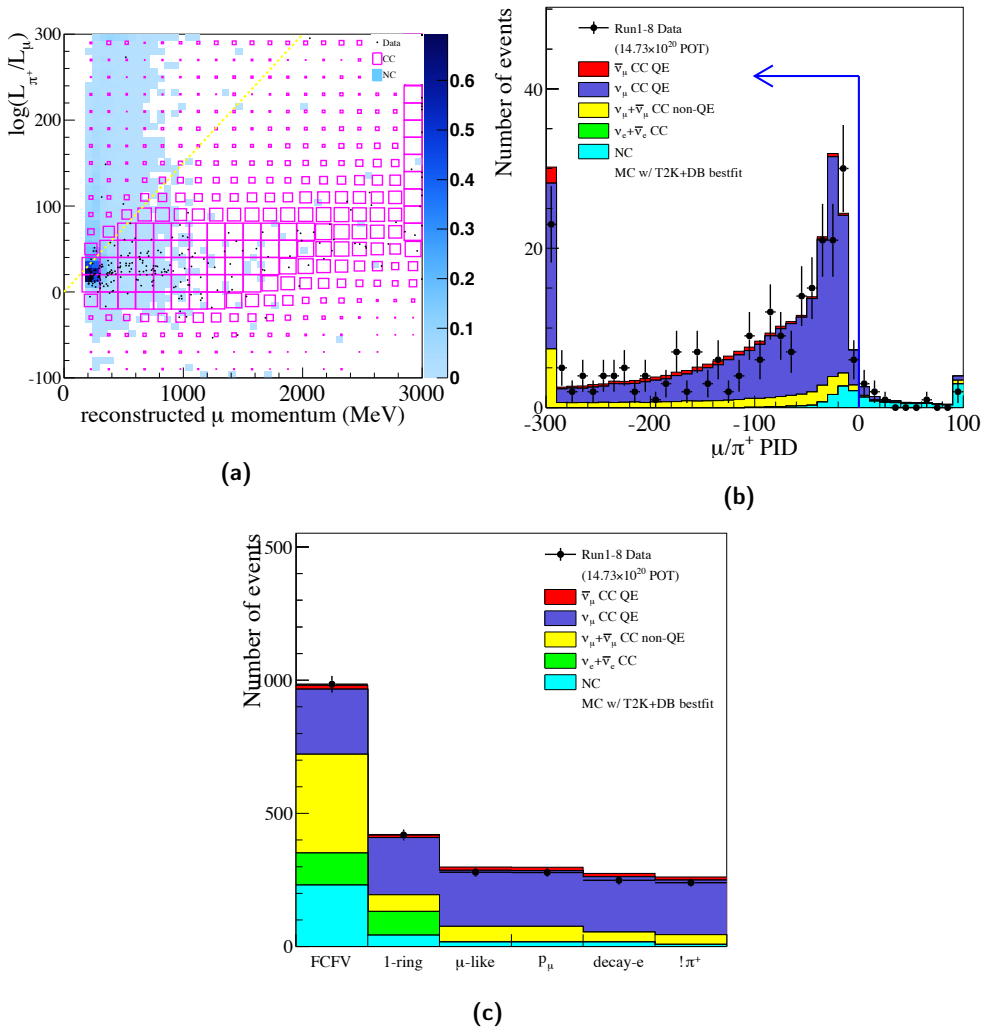

Figure 4.31: Event distributions after each of the cuts described in section 4.4.1, continued from fig. 4.30. The location of the π^+ cut is shown in the likelihood momentum space (a), (b) shows the cut on the MC overlaid with data, and finally the number of events passing each cut is shown in (c). Reproduced from [95]

4.4.2 Event Selection Optimisation

Oscillation analyses at T2K prior to the one described in this thesis, those by the the VALOR (VALOR) group are detailed in section 5.2, have employed a cut which is used to remove the π^0 background which makes up the major background to ν_e appearance. However the location of the cut was not studied in detail and further capabilities within fiTQun are available. These include the reduction of NC1π^+ which is a large background which could not previously be removed for the ν_μ disappearance. The background component and signal components typically have very different systematic uncertainties, e.g. 55 % compared to ∼3 % in NC $1\pi^+$ [172], which complicates the task of preserving signal statistics. For the event selection the sensitivity to the oscillation parameter $\delta_{\mathrm{CP}} \neq 0$ is used to optimise the π^0 cut, and precision of the parameter $\sin^2\theta_{23}$ for the π^+ cut. Systematic parameters are implemented in a different way to the official oscillation analyses, and will be detailed below.

The fits used to determine the sensitivity to the oscillation parameters are determined using the fitter described in [173]. A joint fit of FHC and RHC channels in appearance and disappearance is made. The number of events, N_i for a neutrino type, i, in reconstructed energy, E_r is predicted by

$$N_i(E_r) = \sum_{E_t} \sum_{j} R_{ij}(E_t, E_r) P_{ij}(E_t) \tag{4.13}$$

the neutrino types i, $\nu_\mu \to \nu_\mu$, $\nu_e \to \nu_e$, $\nu_\mu \to \nu_e$ and the same for antineutrinos. The index j runs over the interaction types. The true and reconstructed energies are E_t and E_r respectively. An unoscillated map, $R_{ij}(E_t, E_r)$, is made from T2K events passing all cuts, this contains flux, cross-section and efficiency information. The oscillation probability is $P_{ij}(E_t)$ and is calculated by the Prob3++ [174] package.

In section 5.5 a fuller treatment of the systematic parameters will be given where the systematic parameters which affect both the shape and normalisation of the neutrino energy spectra will be described. For the event selection optimisation a simple treatment is used where the total systematic uncertainties on the reconstructed energy and the correlations on a bin-by-bin basis are used. The matrix resulting from the near detector fit section 4.3 is used to randomly throw 1000 sets of systematic error parameters, weights are generated and saved for each MC event using T2KReWeight if implemented, or are otherwise added manually . Another set of 1000 parameters generated from the Super-K detector and FSI/SI+PN covariance matrix, this matrix is binned in APfit reconstructed energy neutrino flavour and interaction mode, fiTQun SK+FSI/SI+PN errors were not available at the time of the study but are not expected to change significantly when altering the reconstruction algorithm. A total weight is then generated from the product of the BANFF and SK+FSI/SI+PN matrices. Energy distributions are then generated from each of the 1000 parameter sets, and a covariance matrix is generated using the

bin-to-bin correlations of the energy distributions

$$\sigma_{ij}^{E_{\rm rec}} = \frac{1}{1000}\sum_{k=1}^{1000}(N_i^k - N_i^0)(N_j^k - N_j^0) \tag{4.14}$$

where the sum is over k systematic parameter sets for the expected number of events, N_i^k in the $i^{\rm th}$ bin, and N_i^0 is the number of events for the nominal distribution (the parameter set which corresponds to the nominal values from the fits). A fractional covariance matrix is used in the fit which is defined as

$$\sigma_{ij}^{\rm err} = \frac{\sigma_{ij}^{E_{\rm rec}}}{N_i^0 N_j^0}. \tag{4.15}$$

The covariance matrix eq. (4.14), and fractional error matrix eq. (4.15), are re-generated for the fiTQun cut in each iteration. The energy scale uncertainty is not applied as it has a negligible effect [175] and are looking for the relative difference in sensitivities from varying cuts.

In the ν_μ disappearance sample the systematic uncertainty of the NC1π^+ background is 55 % [172], with an expectation for all NC events 13 % of the total sample rate, compared to ∼3 % for the uncertainty on the signal. This is the main background for ν_μ disappearance and can be reduced by use of a single-ring π^+ likelihood. The cuts for the NC1π^+ background are made in $\ln(L_{\pi^+}/L_\mu)$ vs. p_μ space and are parameterised as a straight line ($y = a_\mu x + b_\mu$), the same approach is taken for the π^0 $\ln(L_{\pi^0}/L_e)$ vs. p_e and ($y = a_e x + b_e$). Pairs of a_μ, b_μ variables are iterated over in a grid, where at every point a new systematic uncertainty covariance matrix is generated and a fit to to determine the sensitivity to $\sin^2\theta_{23}$ is made, the optimisation with systematics favours more agressive cuts, sacrificing efficiency for lower background rates, plots of the $\Delta\chi^2$ surface are shown in section 4.4.2 and fig. 4.33. For the π^0 cut the same procedure as previously followed but using pairs of a_e, b_e values the significance of $\delta_{\rm CP} \neq 0$ is evaluated, the optimum value found using this procedure yields only a very small difference in significance so the existing cut was left unaltered. For the one-ring CC π^+ sample no optimisation was run. The results of the optimisation were outlined in section 4.4.1 where the sample selection cuts are described.

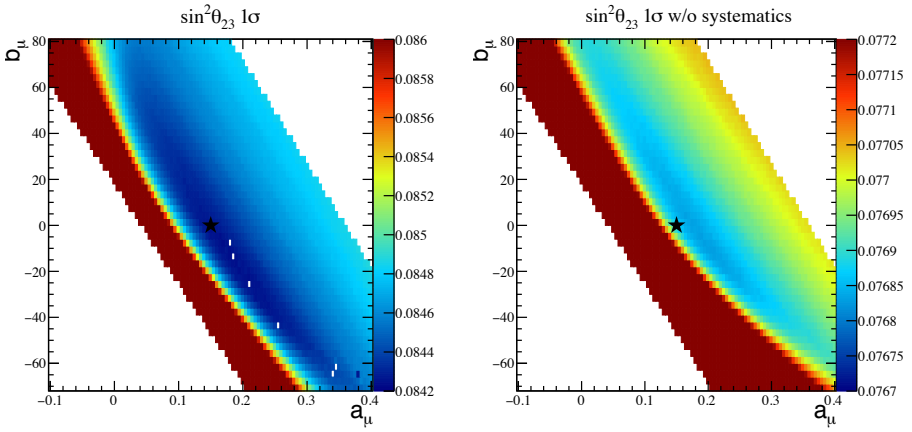

Figure 4.32: 1-σ width of the $\Delta\chi^2$ curve left for the oscillation parameter $\sin^2\theta_{23}$ as a function of the parameters a_μ, b_μ. Systematics are neglected in the plot on the right and included on the left. Reproduced from [176].

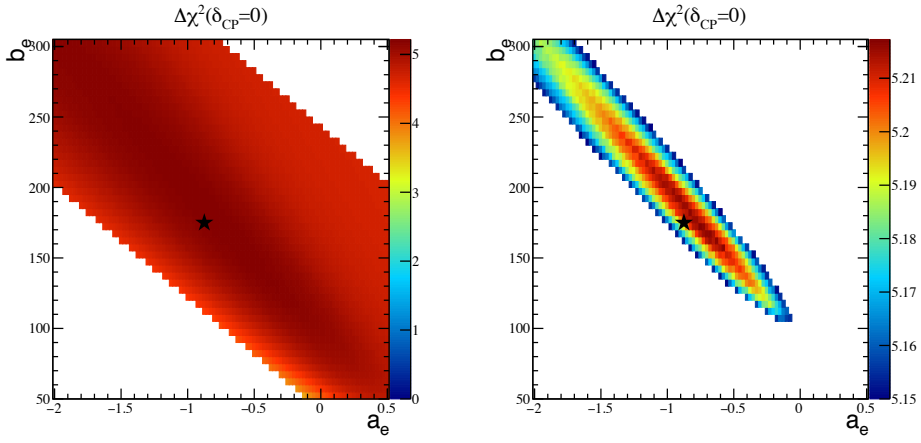

Figure 4.33: Significance to reject $\delta_{\mathrm{CP}} \neq 0$ as a function of the parameters a_e, b_e. The right plot shows part of the $\Delta\chi^2$ surface on the left in a more finely graded scale, the star shows the selected parameter values for the π^0 cut. Reproduced from [176].

4.5 Super Kamiokande Detector and Final State Interactions

Systematic uncertainties that are unique to the Super-K detector can be grouped into three categories: detector selection uncertainties, final state interaction uncertainties and secondary interaction uncertainties. Each of the parameters in these categories takes the form of a normalisation on the content of a particular bin. The contributions from each source are binned in the same way and this means that the contributions from each of the error sources can be combined in an overall covariance matrix.

4.5.1 Super-K FSI and SI Errors

The analysis method that was used to evaluate the FSI and SI errors is presented in section 4.2.2. These are propagated to Super-K by reweighting each parameter set described in table 4.5 and building a covariance matrix with the same binning as the Super-K detector covariance matrix. The covariance matrix that is produced including the photo-nuclear effect (PN) FSI+SI+PN is presented in fig. 4.34. Photo-nuclear interactions occur when a photon from a π^0 decay is absorbed by the nucleus.

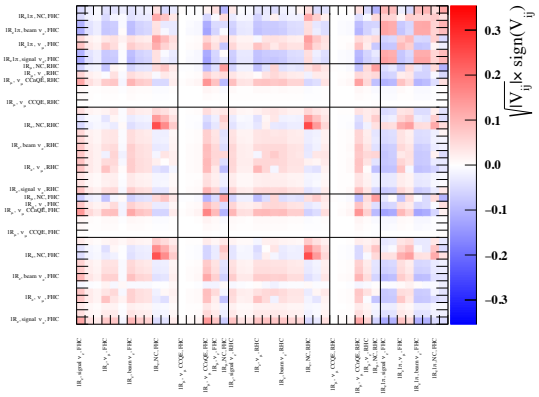

Figure 4.34: The FSI+SI+PN covariance matrix for Super-K, reproduced from [134].

4.5.2 Fiducial Volume Optimisation and Detector Systematic Evaluation

The detector systematics are evaluated with the fiTQun algorithm. Improvements to: decay electron tagging efficiency and false tag rate, mis-PID rate of CC ν_μ interactions, vertex position and, NC pion background, have been made. This analysis was also performed in conjunction with the fiducial volume optimisation which is increased compared to previous analyses.

The cuts defining the fiducial volume from which the sample selection is made for the T2K analysis have remained largely unchanged since the first oscillation analysis. The fiTQun algorithm offers improved resolution of the neutrino interaction vertex, and simulated data studies show parts of the large, ∼30 % of the FV, regions previously rejected by the 200 cm cut can be reconstructed successfully . Since the event selection by fiTQun represents significant change to the event selection the detector systematics need to be re-evaluated. The systematics vary across the detector regions, and areas with similar systematics are selected and evaluated via a fit to the Super-K atmospheric data. This is performed in conjunction with the updated fiTQun event selection which is discussed in section 4.4.1. Finally the detector systematics for the sample selections are evaluated by a toy MC method.

m	fiTQun variable name	Prior Constraint σ_{β_m}
0	e/μ PID	200
1	e/π^0 PID	200
2	μ/π PID	200
3	Ring-Counting	100

Table 4.13: Variables and prior constraints of the fiTQun for the detector systematics evaluation.

The atmospheric neutrino fit is used to extract a set of systematic error parameters, $\vec{d}_{\text{SK}}$ which characterise the fiTQun reconstruction performance, $\vec{d}_{\text{SK}}$ should capture the difference between running on Super-K atmospheric data and MC simulation. Here we assume that the differences are from the mis-modelling of the detector properties. This is done by maximisation (sampling in MCMC terms) of a likelihood described by,

$$L(\vec{a}, \vec{x}_{\text{atm}}, \vec{d}_{\text{SK}} | \vec{M}_{\text{SK}}) = P(\vec{M}_{\text{Atm-SK}} | \vec{a}, \vec{x}_{\text{atm}}, \vec{d}_{\text{SK}}) \cdot \pi(\vec{a}) \cdot \pi(\vec{x}_{\text{atm}}) \cdot \pi(\vec{d}_{\text{SK}}), \tag{4.16}$$

where $\vec{a}$ are atmospheric neutrino flux parameters, $\vec{x}_{\text{atm}}$ the atmospheric cross section parameters, $\vec{M}_{\text{Atm-SK}}$ is the Super-K atmospheric data, and $\pi(\vec{a}), \pi(\vec{x}_{\text{atm}}), \pi(\vec{d}_{\text{SK}})$ are priors on each of the parameters. The choice of $\vec{d}_{\text{SK}}$ is not unique and has varied depending on the particular analysis that was being run, in this case the fiTQun cut variables were modified that define the event selections for ν_e and ν_μ, there are four of these variables, labelled m described in table 4.13 . Each event has the m^{th} cut variable, L_m associated with a parameter β^0 and β^1

$$L'_m = \beta^1 L_m + \beta^0, \tag{4.17}$$

here β^0 shifts the whole distribution whilst β^1 is a multiplicative scaling parameter which gives additional flexibility to the fit.

Precise knowledge of the true distributions for the atmospheric data sample that is used to constrain the Super-K detector errors is not available. This complicates the analysis goal of extracting the detector systematics independently of the T2K flux and cross section systematics. Although the flux is different, in principle the cross section systematics should be captured by the same model, and performing a joint fit is under study. The Super-K detector uncertainties are instead estimated with the available atmospheric neutrino data.

Different event topologies are taken into account by fitting independently for the different likelihoods that are used in fiTQun, 6 different event MC component classes, listed in table 4.14, are taken into account. These components are defined based on topology identification and retaining sufficient statistics to provide a meaningful constraint. Events are then further subdivided by location and the *wall* and *towall* variables see fig. 4.27 for a diagram. Events are better imaged when they hit a larger number of PMTs, this

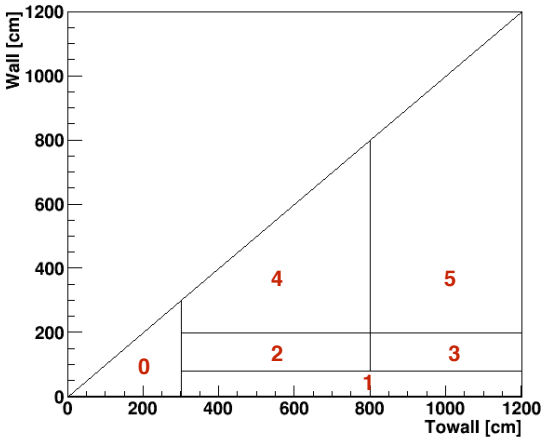

Figure 4.35: Defined detector regions in terms fo the *wall* and *towall* regions, zoomed into the small *wall* and *towall* regions

MC Component k	Name	Definition (from MC truth)
0	Single e	Single visible electron ring
1	Single μ	Single visible muon ring
2	e-like + Other	Visible electron ring with other visible rings
3	μ-like + Other	Visible muon ring with other visible rings
4	Single π^0	Single visible π^0
5	Single Hadron	Single visible proton or pion

Table 4.14: MC component classes that are used in the atmospheric fit, these are based on the true visible topology. Reproduced from [169]

can occur when the event vertex is near the ID wall but points inwards to the detector, and are more poorly imaged when the same vertex points outwards and hits few PMTs. In order to optimise the cuts, the variation of the detector systematics over different *wall* and *towall* regions needs to be known. Bins were made of the detector regions, varying both *wall* and *towall* simultaneously, to produce 6 regions, see fig. 4.35, with each of these bins being parameterised using the same model as eq. (4.17).

Cuts are made that can be applied to both the MC and the atmospheric data, without using the fiTQun cut variables since the study aims to measure their uncertainties. Initial cuts are made on the number of decay electrons table 4.15, this is intended to achieve better resolution of the systematic uncertainties for each component. Any shifts in the likelihood estimations should not depend on the number of sub-events, which is one plus the number of decay electrons seen. A normalisation is introduced instead for each sample in each detector region bin $\gamma_{l,j}$ in eq. (4.18). The decay electron tagging efficiency from cosmic muon tagging is described in [177]. The full model includes

$$\left\{\alpha_n, \beta^i_{j,k,m}, \gamma_{j,l}\right\}, \tag{4.18}$$

the index $i = 0, 1$ represents the multiplicative or additive detector systematic parameters described by eq. (4.17), j is one of 6 detector region bin as shown in fig. 4.35, The index

MC Component l	Definition (from MC truth)
1	`fqnse` $= 1$
2	`fqnse` $= 2$
3	`fqnse` > 2

Table 4.15: Sample cuts applied to both the data and the MC events, for the number of decay electrons `fqnse`. Reproduced from [169]

k is one of 6 the MC components, a full list contained in table 4.14, l, the 3 sample cuts for data and MC as shown in table 4.15, and m the 4 fiTQun variables defined in table 4.13. There are a total of 325 parameters in the fit, broken down into 288 β detector systematic parameters, 19 α_n parameters for atmospheric flux and cross section and 18 $\gamma_{j,l}$ sample normalisations. These parameters are constrained in the fit by fitting to the full fiTQun variables, which provide shape information in the fit which is important for the regions where *wall* and *towall* are small and statistics become the limiting factor. This procedure also makes the detector systematics estimation a separate process from the cut optimisation process .

The negative log likelihood minimised in the fit is

$$-\log\left[L\left(\alpha,\beta,\gamma \mid \vec{h}^{\text{Data}}\right)\right] = -\log\left[P\left\{\vec{h}^{\text{Data}} \mid \vec{h}^{\text{MC}}\left(\alpha,\beta,\gamma\right)\right\}\right] - \log[\pi(\alpha)] - \log[\pi(\beta,\gamma)] \tag{4.19}$$

$\vec{h}^{\text{MC}} \equiv h^{\text{MC}}_{j,l,m}$ is a set of histograms filled from the simulation, likewise the set of histograms $\vec{h}^{\text{Data}} \equiv h^{\text{Data}}_{j,l,m}$ are filled from atmospheric data . The terms on the right hand side of eq. (4.19) can be expanded in terms of the parameters making it up which leads to an expression

$$\begin{aligned}
&-\log\left[L\left(\alpha,\beta,\gamma \mid \vec{h}^{\text{Data}}\right)\right] = \\
&\sum_s \sum_j \sum_l \sum_m \left[\left(\hat{N}_{s,j,l,m}(\alpha,\beta,\gamma) - N_{s,j,l,m}\right) + N_{s,j,l,m}\log\left(\frac{N_{s,j,l,m}}{\hat{N}_{s,j,l,m}(\alpha,\beta,\gamma)}\right)\right. \\
&\left. + \sum_n \frac{1}{2}\left(\frac{(\alpha_n - 1)}{\sigma_{\alpha_n}}\right)^2 + \frac{1}{2}\left(\frac{(\gamma_{j,l} - 1)}{\sigma_{j,l}}\right)^2 + \sum_i \frac{1}{2}\left(\frac{(\beta^i_{j,l,m} - \delta_{i,l})}{\sigma_{\beta_m}}\right)^2\right].
\end{aligned} \tag{4.20}$$

A sum is taken over all the bins, s where N_s are the observed events in the bin and $\hat{N}_s$ is the Poisson mean expectation, the remaining squared terms are priors for the fit parameters. The priors are taken as gaussian with a width σ around a nominal value for the parameter. The procedure used to evaluate eq. (4.20) is to fill histograms for each fiTQun cut variable detector region and sample based on the number of decay electrons, and to do the same for simulated data with the inclusion of the components based on the knowledge of the true visible topology. The sums are then evaluated for the simulation, to remove the true topology dependence, and allow comparison to data and evaluation

of the bin-wise log-likelihood , finally the prior contributions are summed, with the loose priors listed in table 4.13.

In order to find the data favoured regions in the parameter space along with their correlations Markov chain Monte Carlo (MCMC) is used. The Metropolis-Hastings algorithm is used [178], with a modified proposal function to deal with the strongly correlated parameters in the analysis by using ideas from Differential Evolution MCMC (DE-MCMC) [179], which employs a modified sampling of the parameter space to converge more rapidly on the set of parameters which minimise the likelihood.

Ideally the optimum fiducial volume cuts would be determined based on the sensitivity to the oscillation parameters, this approach is taken in section 4.4.2 but does not fully account for the systematic parameters due to computational restrictions. A simplified measure is used instead which takes into account statistics, purity and uncertainty. This "figure of merit" (F.O.M.) is described by

$$\text{F.O.M.} = \frac{\left(\frac{\partial \hat{N}}{\partial \theta}\right)^2}{\hat{N} + \sigma^2_{\text{syst}}} \tag{4.21}$$

where $\hat{N}$ is the MC prediction which approximates the number of events $N(\theta_{\text{true}})$ for an oscillation parameter θ drawn from a Poisson distribution. The eq. (4.21) assumes that the total uncertainty is the sum of the statistical uncertainty and systematic in quadrature $\hat{N}$, and σ^2_{syst} respectively.

The atmospheric fit results previously determined are used as the posterior Markov chain to determine the systematic uncertainties in each detector region. A random set of fit parameters is chosen from the posterior MCMC, a loop over the T2K events is made and for each event the fiTQun cut variables are modified using the parameterisation in eq. (4.17). Then a check is made if the event passes any of the T2K selection cuts and add to count of events passing cut by detector region and category. Repeat the procedure . This generates a set of toy distributions for each region and category in table 4.14 from which two quantities are extracted. The mean of the distribution of toy experiments is compared to the nominal MC value and the fractional difference is extracted, the square root of the variance is also obtained, these are referred to as the "shift error" and the "fit error". The total uncertainty is made up of the the sum of errors in quadrature.

The fitQun energy reconstruction is biased in regions of the detector with $wall \leqslant 50\,\text{cm}$ and $towall \leqslant 150\,\text{cm}$ and so values larger than this are used as a constraint in the figure of merit calculation, this also excludes effects from the PMT structure near the ID wall which are not simulated and assumptions about the PMT geometry.

A total systematic uncertainty weight is assigned which is based on

$$w_{\text{syst}} = w_{\text{detector}} + w_{\text{xsec}} + w_{\text{entering}}, \tag{4.22}$$

w_{detector} is taken from the fractional uncertainty from MC toys, w_{xsec} is drawn from the table , and w_{entering} is applied only to the category of entering events. The FV cut optimisation procedure is to take a particular region in $(towall, wall)$, a loop over all events is made and and $\partial\hat{N}/\partial\theta$ and σ^2_{syst} are calculated, and finally eq. (4.21) is calculated, this is iterated for many $(towall, wall)$ values. The point which maximises the figure of merit lies outside the allowed value for the ν_μ single-ring sample and the ν_e-CC1π^+ samples, in these cases $wall = 50\,\text{cm}$ and the value of $towall$ which maximises the figure of merit is chosen.

The detector regions towards larger values of *wall* and *towall* have higher systematic uncertainties and have lower values for the figure of merit. Backgrounds which have larger systematic uncertainties which are introduced by the increase of the value of the *wall* and *towall* variables mean that those regions of the detector also score lower in the figure of merit. The small *towall* region shows an increase in the background events in the ν_e sample due to difficulty in discriminating between the μ-like and e-like rings and absence of the decay electron ring. The small *wall* region has the previously discussed entering events and NC events as background, with the entering events mostly in the region $wall < 50\,\text{cm}$, and a broader NC events. Similar effects are seen in the ν_e CC1π^+ sample, a larger component of misidentified events is seen but a smaller NC background contribution is seen. The ν_μ sample does not show a sharp peak in the background events and the event distribution in *towall* gradually decreases so the figure of merit is dominated by the uncertainty in the small *towall* regions.

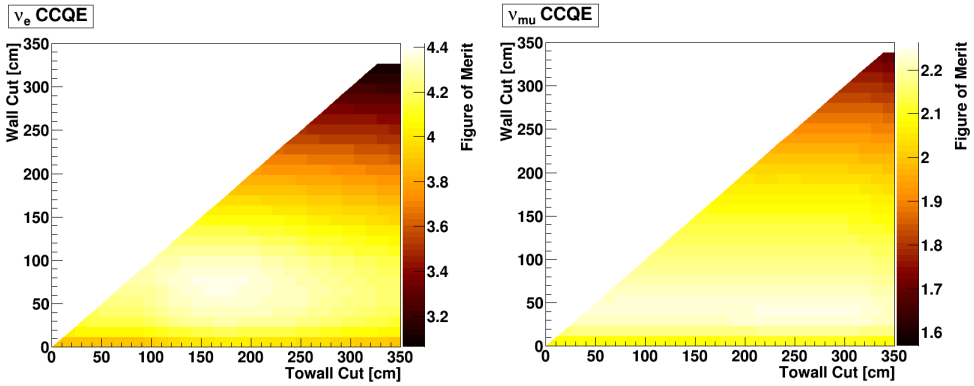

(a) Single ring e-like

(b) Single ring μ-like

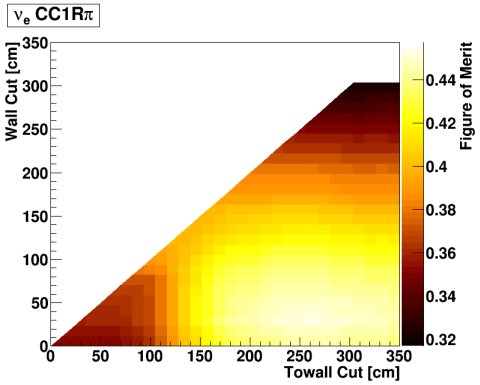

(c) e-like sample with single decay electron ring

Figure 4.36: Figure of merit described in eq. (4.21) as a function of the *wall* and *towall* variables, for (a) the single ring ν_e, and (b) single ring ν_μ sample, and (c) ν_e CC1π^+ samples.

Two categories of detector systematic uncertainties are made, an event selection efficiency and a FV cut efficiency. The event selection efficiency is a result of systematic shifts arising from the underlying detector properties and determined using MC toy study and fit. The FV cut efficiencies, which result from the direction and vertex resolution, also vary due to the detector properties but are not characterised with the atmospheric data and are described in [177].

With the topological cuts for each sample that are defined in section 4.4.2 and the FV cuts that have been obtained with the procedure outlined above, an estimate of the detector systematic uncertainties for each sample can be made. A covariance matrix is generated, containing the uncertainties in the different MC categories and in different energy regions which is used as input to generate the final Super-K uncertainties. An estimate by event category of the fractional efficiency of the "core" cuts applied after the "base" cuts, described in table 4.16, is made and the atmospheric flux, cross section parameters and normalisation parameters are marginalised. The remaining dependence on the fractional change in efficiency $\Delta\epsilon$ is on the shape parameters β,

Category	Base Cuts	Core Cuts
ν_e CC1e	1 e-like ring, $N_{\text{decay}} = 0$, $p_e > 100\,\text{MeV}$	e-like, not π^0-like, 1R-like
ν_e CC Other	e-like + other rings, $N_{\text{decay}} \geq 1$, $p_e > 100\,\text{MeV}$	e-like, not π^0-like, 1R-like
ν_μ CCμ	1 μ-like ring, $N_{\text{decay}} = 1$, $p_e > 30\,\text{MeV}$	μ-like, not π-like, 1R-like
ν_μ CC Other	μ-like + other rings, $N_{\text{decay}} \geq 2$, $p_e > 30\,\text{MeV}$	μ-like, not π-like, 1R-like

Table 4.16: MC categories that are used in the covariance matrix to determine the “core" and “base" cuts

$$\Delta\epsilon = \frac{1}{\epsilon_0}\frac{N_{\text{core}}(\alpha,\beta,\gamma)}{N_{\text{base}}(\alpha,\gamma)}, \tag{4.23}$$

where ϵ_0 is the nominal MC prediction, N_{core} is the number of events that pass the core cuts, and N_{base} is the base number of events. The procedure is almost the same as the previous toy MC fit procedure, and the “core” cuts in table 4.16 are applied. A correlation matrix is generated for each MC category and for each bin in that category which can be seen in fig. 4.37. The constraints reported here cannot be compared directly to the previous analysis that was run in [180] since the shape information is not used which provides a stronger constraint.

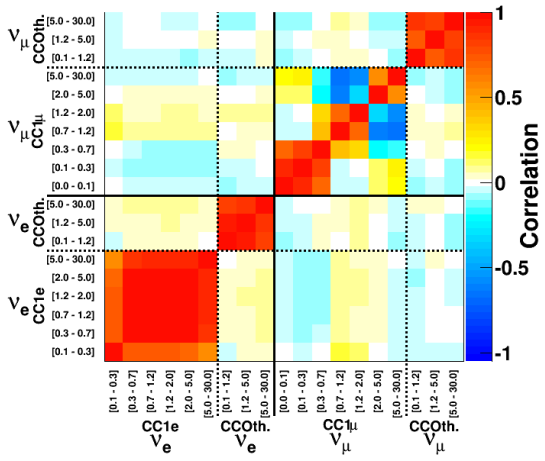

Figure 4.37: Correlation matrix for the efficiencies of the core cuts for each of the energy binned MC categories

Strong correlations in the visible energy bins are observed, the parameters do not include an explicit visible energy dependence and share the same β parameters.

4.5.3 Super-K Energy Scale Uncertainty

Although the rest of Super-K systematics use quantities that are derived from the fiTQun algorithm the determination of the energy scale systematic is made with APFit. Studies

are still ongoing to determine the effect of the increased sensitivity to temporal and spatial anisotropy in the fiTQun algorithm. Four samples are used to evaluate the energy scale uncertainty in order to cover a large range of momenta, 30 MeV to 10 GeV, these samples are

- Decay electrons from stopping cosmic ray muons
- π^0 from atmospheric neutrino interactions
- Sub-GeV stopping cosmic ray muons
- Multi-GeV stopping cosmic ray muons

the previously described samples give the absolute energy scale error, which is selected by taking the uncertainty of the sample with the largest absolute data-MC difference which is the sub-GeV stopping muon sample, and an uncertainty of 2.4 % is used.

5 Joint Fit δ_{CP} Measurement

5.1 Introduction

In this chapter, the results of a 3-flavour $\nu/\bar{\nu}$ joint analysis, on the combined Run 1-8 dataset, using data taken in both neutrino-enhanced forward horn current (FHC) mode (1.4734×10^{21} POT), and antineutrino-enhanced reverse horn current (RHC) mode (7.558×10^{20} POT) are reported.

This analysis updates the previous analyses based on the additional data gathered at Super-K [95], a new cross-section model [134] and a change in the Super-K reconstruction method [91].

Section 5.4 describes the Super-K samples, section 5.5 describes the systematic errors considered and their effects on the extrapolated single-ring event spectra, whilst the sensitivity of the various fits is considered in section 5.6 before presenting the data fit results for Run 1-8 in section 5.7.

The analysis is performed by the VALOR framework which performs an oscillation analysis based on the inputs which were described in chapter 4, and a strategy using those inputs to produce predictions of the far detector, outlined in fig. 4.1. The far detector predictions consist of energy and energy and lepton angle spectra which are compared using a binned likelihood-ratio. Nuisance parameters are marginalised and confidence intervals for δ_{CP} are produced using the Feldman-Cousins method (see section 5.3.3.1), while confidence intervals of the other oscillation parameters are set using the constant $\Delta\chi^2$ method.

As previously discussed in section 3.3.1 and section 4.4, in this analysis we move from the APFit reconstruction algorithm to the fiTQun algorithm [91]. Selection cuts are revisited sections 4.4.1 and 4.4.2 and a significant improvement in statistics is achieved by modifying the fiducial volume cuts to allow for a larger interaction mass section 4.5.2. This analysis includes new cross-section model parameters. A 2p2h shape parameter is added to the 2p2h normalisation parameters already present in the previous analysis. Furthermore, the Random Phase Approximation (RPA) is parameterised by a Bernstein polynomial (BeRPA) [134] and forms a new source of uncertainty. Each of these new parameters will be described in section 5.5.

Finally, a summary is given in section 5.8.

5.2 Analysis Strategy

This analysis builds on our previous analyses in [181, 182] and [183, 184, 185, 186, 187, 188, 189] and for antineutrino [190, 191]. In this analysis we fit Super-K data using a hybrid frequentist-Bayesian method [192], in which nuisance parameters are marginalised according to the priors set by external and Near Detector (ND) data. A description of the method can be found in section 4.2 of [191].

The analysis uses a binned likelihood-ratio method [193] where the estimation of the parameters of interest, $\vec{\theta}$, is obtained by comparing the observed and predicted Super-K spectra for 1-ring events. For the two one-ring μ-like samples the binning of data events is in one-dimensional reconstructed neutrino energy space, whilst the three one-ring e-like samples bin data events in two-dimensional reconstructed neutrino energy and lepton angle space.

The 2D binning scheme used for the e-like samples is to improve the separation of the different reaction / flavour components, in particular $\bar{\nu}_\mu \to \bar{\nu}_e$ and $\nu_\mu \to \nu_e$, which are fundamental in measuring δ_{CP}. The ν_e intrinsic beam and NC components can also be better separated from signal.

μ-like templates have 84 true energy bins and 73 reconstructed energy bins. e-like templates have 84 true energy bins, 25 reconstructed energy bins and 15 reconstructed lepton angle bins.

For all templates the 84 true energy bins of constant width are the following:

- 6 50-MeV bins from 0-0.3 GeV,
- 28 25-MeV bins from 0.3-1 GeV,
- 40 50-MeV bins from 1-3 GeV,
- 5 100-MeV bin from 3-3.5 GeV,
- 1 bin from 3.5-4 GeV,
- 1 bin from 4-5 GeV,
- 1 bin from 5-7 GeV,
- 1 bin from 7-10 GeV and

- 1 bin from 10-30 GeV

For μ-like samples the 73 reconstructed energy bins are the following:

- 60 50-MeV bins from 0-3 GeV,
- 4 250-MeV bins from 3-4 GeV,
- 4 500-MeV bins from 4-6 GeV,
- 4 1000-MeV bins from 6-10 GeV and
- 1 bin from 10-30 GeV.

For e-like samples the 25 reconstructed energy bins with constant width are the following:

- 25 50-MeV bins from 0-1.25 GeV.

The θ binning used for e-like samples is

- 14 10° bins from 0–140°,
- 1 bin for the range 140–180°.

For μ-like samples a single θ bin, that covers the whole range 0° - 180°, is used. The predicted e-like 2-dimensional spectra were studied in detail in [182] for each flavour component and were compared with the 1-dimensional reconstructed energy spectra.

A study was performed to decide the optimum binning scheme for reconstructing neutrino energy, balancing the needs for accuracy and speed. Details are given in Appendix I of Ref. [186].

5.3 Fitter details

5.3.1 Spectra prediction methodology

In this analysis a comparison of the reconstructed energy (E_r) and reconstructed lepton angle (θ) spectrum of single ring events, including the ν_e CC1π^+-like sample, observed at Super-K with the predicted spectrum is used to build the test statistic to quote

confidence intervals for neutrino oscillation parameters. For μ-like samples the templates are built as a function of the reconstructed neutrino energy, as in previous analyses, and a single θ bin is used. The predicted number $N_{SK;r,\theta}$ of single ring and ν_e CC1π^+ events in the r-th and θ-th bin is computed for each selected sample as follows:

$$N_{SK;r,\theta} = \sum_m \sum_t \sum_{r\prime} P_{m;t} \cdot T_{r;r\prime;f^{SK}_{E;r}} \cdot S_{m;t;r\prime,\theta;\vec{f}} \cdot N^{MC}_{SK;m;r\prime,\theta;t} \tag{5.1}$$

In eq. (5.1), $N^{MC}_{SK;m;r\prime,\theta;t}$ is the input Super-K Monte Carlo (MC) template containing the number of events in the single ring MC sample with true reaction mode m in the true energy bin t, the reconstructed energy bin $r\prime$ and reconstructed lepton angle bin θ. $S_{m;t;r\prime,\theta;\vec{f}}$ is an overall, multiplicative, systematic error factor depending on a vector of nuisance (systematic) parameters $\vec{f}$, which is function of the reaction mode m, the true energy bin t, the reconstructed energy bin $r\prime$, and the reconstructed lepton angle bin θ. $T_{r;r\prime;f^{SK}_{E;r}}$ is a transfer function describing the migration of events between the reconstructed energy bins r and $r\prime$ due to uncertainty in the Super-K reconstructed energy scale, expressed here in terms of the nuisance parameter $f^{SK}_{E;r}$. Finally, $P_{m;t}$ is the 3-flavour oscillation probability applied to the true energy bin t of the Super-K MC template which corresponds to mode m; application of the term $P_{m;t}$ is discussed in section 5.3.3.

5.3.2 Construction of the nominal Super-K Monte Carlo templates

The nominal Super-K single ring and ν_e CC1π^+ MC analysis templates $N^{MC}_{SK;m;r\prime,\theta;t}$ are constructed by applying the single e-like ring selection cuts, the ν_e CC1π^+ selection cuts, or the single μ-like ring selection cuts to the official Super-K MC samples [95]. The calculation of the normalisation of each MC sample is described in section 5.3.2.1. The list of MC templates used in this analysis is shown in section 5.3.2.2.

5.3.2.1 Normalisation of Monte Carlo samples

The normalisation (integrated exposure in terms of POT) of each event sample is calculated from the number of events with a MC truth interaction vertex within the 22.5 kt fiducial volume.

$$N = \int dSdIdE \cdot \frac{d^3\Phi_{SK}}{dSdIdE_\nu} \cdot \sigma_{H_2O} \cdot \frac{N_A}{A} \cdot \rho \cdot L \tag{5.2}$$

where $d^3\Phi_{SK}/dSdIdE$ is the number of flux particles for the given neutrino species per neutrino energy bin dE_ν, per unit area dS and per POT, σ_{H_2O} is the total interaction cross section on water for the given neutrino species, I is the beam exposure in terms of POT, N_A is Avogadro's number, A is the mass number for water, ρ is the water density and L is the neutrino path length in the water volume.

The Super-K MC samples are normalised to the Run 1-8 POT. Assuming that all the MC files are used, each sample is first normalised to 10^{21} POT by weighting it with the ratio of the number of events per 22.5 kt per 10^{21} POT to the number of generated events in the true fiducial volume in all the available MC. Then each sample is normalised to 1.4734×10^{21} POT for neutrino and 7.558×10^{20} for antineutrino mode, by weighting the result respectively by 1.4734 and 0.7558 (the Run 1-8 POT in units of 10^{21} POT).

5.3.2.2 List of Monte Carlo templates

For each Super-K MC sample, a number of different MC templates is constructed corresponding to different true reaction modes. The template number depends on the type of oscillation analysis and the specific systematic parameters considered in the analysis. 50 are used for the current analysis, these are the same templates as in our 2016 analysis [181]. The NC templates are built from each true component which exists in the Super-K MC where the flavour of the interacting neutrino is known. In particular

- $\bar{\nu}_\mu$ CCQE,
- $\bar{\nu}_\mu$ CC1π,
- $\bar{\nu}_\mu$ CC coherent,
- $\bar{\nu}_\mu$ CC 2p-2h,
- $\bar{\nu}_\mu$ CC other,
- $\bar{\nu}_\mu$(and $\rightarrow \bar{\nu}_e$, $\bar{\nu}_\tau$) NC1π^0,
- $\bar{\nu}_\mu$(and $\rightarrow \bar{\nu}_e$, $\bar{\nu}_\tau$) NC1$\pi^\pm$,
- $\bar{\nu}_\mu$(and $\rightarrow \bar{\nu}_e$, $\bar{\nu}_\tau$) NC coherent,
- $\bar{\nu}_\mu$(and $\rightarrow \bar{\nu}_e$, $\bar{\nu}_\tau$) NC other,
- $\bar{\nu}_\mu$(and $\rightarrow \bar{\nu}_e$, $\bar{\nu}_\tau$) NC 1γ,
- ν_μ CCQE,
- ν_μ CC1π,
- ν_μ CC coherent,

- ν_μ CC 2p-2h,
- ν_μ CC other,
- ν_μ (and $\rightarrow \nu_e$, ν_τ) NC1π^0,
- ν_μ (and $\rightarrow \nu_e$, ν_τ) NC1$\pi^\pm$,
- ν_μ (and $\rightarrow \nu_e$, ν_τ) NC coherent,
- ν_μ (and $\rightarrow \nu_e$, ν_τ) NC other,
- ν_μ (and $\rightarrow \nu_e$, ν_τ) NC 1γ,
- $\bar{\nu}_e$ CCQE,
- $\bar{\nu}_e$ CC1π,
- $\bar{\nu}_e$ CC coherent,
- $\bar{\nu}_e$ CC 2p-2h,
- $\bar{\nu}_e$ CC other,
- $\bar{\nu}_e$ (and $\rightarrow \bar{\nu}_\mu$, $\bar{\nu}_\tau$) NC1π^0,
- $\bar{\nu}_e$ (and $\rightarrow \bar{\nu}_\mu$, $\bar{\nu}_\tau$) NC1$\pi^\pm$,
- $\bar{\nu}_e$ (and $\rightarrow \bar{\nu}_\mu$, $\bar{\nu}_\tau$) NC coherent,
- $\bar{\nu}_e$ (and $\rightarrow \bar{\nu}_\mu$, $\bar{\nu}_\tau$) NC other,
- $\bar{\nu}_e$ (and $\rightarrow \bar{\nu}_\mu$, $\bar{\nu}_\tau$) NC 1γ,
- ν_e CCQE,
- ν_e CC1π,
- ν_e CC coherent,
- ν_e CC 2p-2h,

- ν_e CC other,
- ν_e (and $\rightarrow \nu_\mu$, ν_τ) NC1π^0,
- ν_e (and $\rightarrow \nu_\mu$, ν_τ) NC1$\pi^\pm$,
- ν_e (and $\rightarrow \nu_\mu$, ν_τ) NC coherent,
- ν_e (and $\rightarrow \nu_\mu$, ν_τ) NC other,
- ν_e (and $\rightarrow \nu_\mu$, ν_τ) NC 1γ,
- oscillated $\nu_\mu \rightarrow \nu_e$ CCQE,
- oscillated $\nu_\mu \rightarrow \nu_e$ CC1π,
- oscillated $\nu_\mu \rightarrow \nu_e$ CC coherent,
- oscillated $\nu_\mu \rightarrow \nu_e$ CC 2p-2h,
- oscillated $\nu_\mu \rightarrow \nu_e$ CC other,
- oscillated $\bar{\nu}_\mu \rightarrow \bar{\nu}_e$ CCQE,
- oscillated $\bar{\nu}_\mu \rightarrow \bar{\nu}_e$ CC1π,
- oscillated $\bar{\nu}_\mu \rightarrow \bar{\nu}_e$ CC coherent,
- oscillated $\bar{\nu}_\mu \rightarrow \bar{\nu}_e$ CC 2p-2h,
- oscillated $\bar{\nu}_\mu \rightarrow \bar{\nu}_e$ CC other.

5.3.3 Applying neutrino oscillations

The MC templates are constructed from the unoscillated MC samples and must be weighted with the appropriate oscillation probability. Oscillations are applied as a function of true energy to the MC templates for all CC interactions.

The MC templates calculated from the $\bar{\nu}_\mu$ MC sample are weighted with $P(\bar{\nu}_\mu \rightarrow \bar{\nu}_\mu)$, with this survival probability being calculated using the oscillation parameters, namely $\sin^2\theta_{23}$, $\sin^2\theta_{12}$, $\sin^2\theta_{13}$, $|\Delta m^2_{32}|$ (normal hierarchy) or $|\Delta m^2_{31}|$ (inverted hierarchy),

Δm^2_{21} and δ_{CP}. The $\bar{\nu}_e$ templates are weighted with $P(\bar{\nu}_e \to \bar{\nu}_e)$, while the oscillated $\bar{\nu}_\mu \to \bar{\nu}_e$ templates are weighted with $P(\bar{\nu}_\mu \to \bar{\nu}_e)$ (the sample was generated assuming 100% of $\bar{\nu}_\mu$ transform to $\bar{\nu}_e$). All these oscillation probabilities are computed in a 3-flavour framework including matter effects in constant-density matter (assuming an Earth crust density of 2.6 g/cm^3). Custom oscillation probability calculation code was developed within the *VALOR* analysis framework. Details and estimates of the numerical accuracy of this code are first presented in [185], and is also shown in Appendix A of [186]. Comparisons between the *VALOR* oscillation probability calculation code and Prob3++ [174], which is typically used by the alternative T2K oscillation analyses, are shown in Appendix B of [186].

In the standard 3-flavour oscillation framework, oscillations of $\bar{\nu}_e$ and $\bar{\nu}_\mu$ can yield $\bar{\nu}_\tau$. In this analysis, we neglect contributions from ν_τ-CC and $\bar{\nu}_\tau$-CC as their energy threshold is around 3.5 GeV and their effect is negligible[1]. Accordingly, this analysis uses no ν_τ-CC and $\bar{\nu}_\tau$-CC MC templates.

It should be emphasized here that the ν_μ NC MC templates for a mode m contain the NC MC templates for the mixture of ν_e+ν_μ+ν_τ resulting from 3-flavour ν_μ oscillations for that mode m. The same applies to the $\bar{\nu}_\mu$, ν_e and $\bar{\nu}_e$ NC MC templates. These NC MC templates are unchanged under standard 3-flavour oscillations.

Also it should be noted that there are no explicit NC MC templates made from the oscillated $\bar{\nu}_e$ and ν_e samples. If they were used, the oscillated $\bar{\nu}_e$ (i.e. $\bar{\nu}_e$ coming from oscillations of $\bar{\nu}_\mu$) would be double counted since they are already included in the $\bar{\nu}_\mu$ NC MC templates. The same applies to oscillated ν_e.

[1] A back-of-the-envelope calculation can be found in the replies to comments and revision history document of [186] that gives $\ll 1\%$ ν_τ contamination in the 1-ring μ-like Super-K sample. A Super-K MC study is required to determine whether the Super-K efficiency assumptions made there are valid.

This analysis uses flux tuning based on NA61/SHINE 2009 data [194][122]. It also uses a model-based extrapolation from ND280 to Super-K, which is implemented via a fit of flux model and cross-section model parameters to ND280 measurements of the muon momentum-angle distributions of $\bar{\nu}_\mu$ and ν_μ charged current interaction candidates for different event topologies with the neutrino interaction vertex either in FGD1 or FGD2 (BANFF fit) [168], which was described in section 4.3.

The log-likelihood function used in the analysis is

$$-2\ \ln\ \lambda(\vec{\theta},\mathbf{a}) = 2\cdot\sum_{i=0}^{N-1}\left(n_i^{obs}\cdot\ln\left(n_i^{obs}/n_i^{exp}\right)+(n_i^{exp}-n_i^{obs})\right) \tag{5.3}$$

where n_i^{obs} is the observed number of events in the i^{th} bin and $n_i^{exp}=n_i^{exp}(\vec{\theta};\mathbf{a})$ is the corresponding expected number of events, N is the number of reconstructed energy and lepton angle bins and $\mathbf{a}$ is a vector of systematic (or nuisance) parameters.

The total likelihood is then given by the sum of $-2\ \ln\ \lambda(\vec{\theta},\mathbf{a})$ from all of the Super-K samples

$$-2\ \ln\ \lambda(\vec{\theta},\mathbf{a}) = \sum_{s=1}^{N_{samples}} -2\ \ln\ \lambda_s(\vec{\theta},\mathbf{a}) \tag{5.4}$$

The procedure for marginalising the nuisance parameters to obtain only the parameters of interest in a marginal likelihood $\lambda_{\text{marg}}(\vec{\theta})$ is

$$\begin{aligned}\lambda_{\text{marg}}(\vec{\theta}) &= \int_A \lambda(\vec{\theta},\mathbf{a})\pi(\mathbf{a})\,d\mathbf{a}\\ &\approx \frac{1}{n}\sum_i^n \lambda(\vec{\theta},\vec{a}_i)\end{aligned} \tag{5.5}$$

where n is the number of toy MC experiments that are used, and $\pi(\mathbf{a})$ is the prior distribution for the nuisance parameters, including correlations between parameters. $\vec{a}_i$ is the set of nuisance parameters generated in the toy MC throw a large number of toys are generated in order to sample the nuisance parameter space A. As the number of events in each bin of the likelihood tends from a Poisson to Gaussian distribution we have

$$\chi^2_{\text{marg}}(\vec{\theta}) = \lambda_{\text{marg}}(\vec{\theta}) \tag{5.6}$$

The postfit covariance matrices which result from the BANFF fit and Super-K fits are used as prior uncertainties. The parameters are thrown using the Cholesky method [195], which allows throws according the parameters' multivariate distribution and existing correlations. Where systematic parameters have physical boundaries, any toy experiment where such a parameter is generated beyond its physical limits is rejected. Furthermore, values of systematic parameters that give a negative predicted number of events in any

reconstructed energy bin in any interaction mode are not allowed. If a systematic throw gives a negative number of events, that toy experiment is rejected. All rejected toys are regenerated.

A single set of oscillation parameters in the 3-flavour framework is used to describe both neutrino and antineutrino data. Nuisance oscillation parameters are marginalised in the fit while the parameters of interest are minimized with respect to the likelihood distribution. Flat priors are used for $\sin^2\theta_{23}$, Δm^2_{32} and δ_{CP} in all fits, whereas $\sin^2\theta_{13}$ uses a flat prior when not applying constraints from reactor experiments and a gaussian prior when using the measurement found in reactor experiments. $\sin^2\theta_{12}$ and Δm^2_{21} use gaussian priors in all fits due to the limited sensitivity of T2K to the solar parameters. Fits are performed for each mass hierarchy and both with and without the constraint for the value of $\sin^2\theta_{13}$ determined from reactor experiments, "the reactor constraint" applied.

Oscillation probabilities include constant-density matter effects, with details of our oscillation probability calculations, estimates of their numerical accuracy and comparisons with calculations used by the alternative T2K oscillation analyses are given in Appendices A and B of Ref. [186].

5.3.3.1 Feldman-Cousins

In the gaussian approximation the constant $\Delta\chi^2$ method can be used to build confidence intervals. However, the oscillation probability is not linear in oscillation parameters and so in some cases the gaussian approximation is not reliable and the Feldman-Cousins method [196] must be used. In this method a different critical value for each point of the $\vec{\theta}$ grid, $\Delta\chi^2(\vec{\theta})_{crit}$, is calculated. Since the most important result of this analysis is the search for CP violation, this method is performed only for the simultaneous fit of δ_{CP} and mass hierarchy. In particular, critical values are calculated for 9 evenly spaced true values of δ_{CP} in the range $[-\pi, +\pi]$ for both normal and inverted mass hierarchy, and linearly interpolated between these points.

In the previous analysis the Feldman-Cousins implementation used the disappearance likelihood surface from the best-fit of the data to generate fake data sets during the procedure. However, this approach causes the critical values to become smaller in the vicinity of the best-fit for δ_{CP} because the generated fake data sets are closer to the real data. The new method [197] instead uses the data best-fit for disappearance parameters, along with the PDG 2016 [198] best-fit values for the remaining oscillation parameters (table 5.1), to perform additional Asimov fits in normal and inverted hierarchy. It is then the likelihood surfaces from these fits that are used to generate the fake data sets during the procedure. The procedure consists of the following steps:

The Asimov data sets are in this case the predicted reconstructed energy spectra with or without the lepton angle dependence. In these spectra all parameters are set to their nominal values, two sets of oscillation parameter central values are used table 5.1, and no statistical fluctuations are applied with scaling to the required POT.

1. At least 1×10^4 fake data sets are produced assuming the oscillation hypothesis of the grid point $\vec{\theta}$ and taking into account both the statistical and systematic uncertainties (i.e. nuisance parameters, including non-fit oscillation parameters, are marginalised);

2. For each fake data set:

   a) $\chi^2(\vec{\theta}_{fix})$ is obtained by computing $\chi^2(\vec{\theta})$ with respect to the marginalisation toys produced for the data fit, with the oscillation parameters $\vec{\theta}$ fixed to the values corresponding to the grid point.

   b) $\chi^2(\vec{\theta}_{bf})$ is obtained by minimizing $\chi^2(\vec{\theta})$ with respect to the marginalisation toys produced for the data fit, leaving the oscillation parameters $\vec{\theta}$ free.

   c) The test statistic is calculated as

$$\Delta\chi^2 = \chi^2(\vec{\theta}_{fix}) - \chi^2(\vec{\theta}_{bf}) \tag{5.7}$$

3. This results in a distribution of $\Delta\chi^2(\vec{\theta})$, $f(\Delta\chi^2)$.

4. Several critical values for $X\%$ CL (e.g. 68%, 90%...), $\Delta\chi^2(\vec{\theta})_{crit}$, can be defined as:

$$\Delta\chi^2_{crit} : \int_0^{\Delta\chi^2_{crit}} f(\Delta\chi^2) d(\Delta\chi^2) = X\% \tag{5.8}$$

   where $f(\Delta\chi^2)$ is the p.d.f. of $\Delta\chi^2$ and $d(\Delta\chi^2)$ is the differential of the integral.

5. This procedure is repeated to produce critical values for all the points of the $\vec{\theta}$ grid.

Once a critical value, $\Delta\chi^2(\vec{\theta})_{crit}$, is computed for each oscillation hypothesis in the $\vec{\theta}$ grid, the confidence intervals are set by the condition

$$\Delta\chi^2(\vec{\theta}) > \Delta\chi^2_{crit} \tag{5.9}$$

with those values of $\Delta\chi^2(\vec{\theta})$ being excluded at the relevant confidence interval.

5.4 Super-K samples used in this analysis

This analysis is comprised of five samples based on the fiTQun selection algorithm, which has improved reconstruction capabilities and can therefore reduce the background components of the selected samples. The five samples are:

- neutrino mode single μ-like ring sample
- antineutrino mode single μ-like ring sample
- neutrino mode single e-like ring sample
- antineutrino mode single e-like ring sample
- neutrino mode single e-like ring sample with one decay electron (referred to as ν_e CC1π^+)

The Super-K MC templates contain events from the ν_μ, $\bar{\nu}_\mu$, ν_e, $\bar{\nu}_e$, oscillated ν_e and oscillated $\bar{\nu}_e$ samples passing the Super-K selection cuts. Details of the selection cuts can be found in [95].

5.4.1 Predicted event rates

Predicted event rates for this analysis are determined for the case of two different sets of oscillation parameters based on previous best fit results from T2K and NOvA. These parameter sets are referred to as Asimov A and B, with their definitions and associated event rates given in the following sections.

5.4.1.1 Definition of Asimov A and B

Table 5.1 shows the definitions used for the Asimov data sets. Asimov A represents parameter values close to the T2K best fit for Run 1-7, whilst Asimov B modifies these parameters such that CP is conserved and changes the $\sin^2\theta_{23}$ octant.

Parameter(s)	Asimov A	Asimov B
$\sin^2\theta_{23}$	0.528	0.450
$\sin^2\theta_{13}$ reactors	0.0219	0.0219
$\sin^2\theta_{12}$	0.304	0.304
$\lvert\Delta m^2_{32}\rvert$ (NH) / $\lvert\Delta m^2_{31}\rvert$ (IH)	2.509×10^{-3} eV^2/c^4	2.509×10^{-3} eV^2/c^4
Δm^2_{21}	7.53×10^{-5} eV^2/c^4	7.53×10^{-5} eV^2/c^4
δ_{CP}	-1.601	0
Mass Hierarchy	Normal	Normal

Table 5.1: Values of oscillation parameters used to compute the event rates, systematic effects and sensitivity studies. Each set of oscillation parameters correspond to a different Asimov data set, which is the MC expected distribution in a certain oscillation hypothesis. In the Asimov data set A the nominal values of $\sin^2 2\theta_{13}$, $\sin^2 2\theta_{12}$ and Δm^2_{21} are from [199], while all the other oscillation parameter values corresponds to the most probable values obtained by the Bayesian analysis on the T2K run 1-4 neutrino mode data [200]. The values for Asimov data set B changes the octant of $\sin^2\theta_{23}$ and conserves δ_{CP}. The mass hierarchy is not marginalised but fixed to either NH or IH.

5.4.1.2 Event rates

Table 5.2 shows the expected event rates for each selected sample at Super-K for the Asimov A data set, but with δ_{CP} varied at $-\pi/2$, 0, $\pi/2$ and π.

	$\delta_{CP}=-\pi/2$	$\delta_{CP}=0$	$\delta_{CP}=\pi/2$	$\delta_{CP}=\pi$
FHC e-like sample	73.47354	61.43388	49.90582	61.94533
FHC μ-like sample	268.40351	268.05327	268.37281	268.81441
FHC ν_e CC1π^+-like sample	6.92243	6.00922	4.86656	5.77983
RHC e-like sample	7.91206	9.02311	10.02989	8.91886
RHC μ-like sample	64.27306	64.12292	64.27392	64.43654

Table 5.2: Predicted total number of events in each sample obtained after applying the BANFF weight for a total exposure of 1.4734×10^{21} POT. The Asimov data set A in 5.1 is used, but with varying δ_{CP}.

Tables 5.3 to 5.7 present the expected event rates for each sample selected Super-K corresponding to the Asimov A data set. Event rates in other oscillation scenarios can be found in appendix A. In each case the normal hierarchy is assumed and all rates are generated for an integrated exposure corresponding to Run 1-8.

	ν_μ	ν_e	$\bar{\nu}_\mu$	$\bar{\nu}_e$	Osc. ν_e	Osc. $\bar{\nu}_e$	Total
CCQE	175.62883	0.00413	11.03473	0.00019	0.02245	0.00015	186.69049
CC1pi	27.69898	0.00199	2.61604	0.00009	0.02406	0.00007	30.34123
CCcoherent	0.28837	0.00000	0.09218	0.00000	0.00000	0.00000	0.38055
2p2h	35.57284	0.00151	1.41213	0.00008	0.02551	0.00004	37.01211
CCother	5.46647	0.00086	0.40615	0.00008	0.00011	0.00001	5.87368
NC1pi0	0.61495	0.01841	0.02120	0.00143	N/A	N/A	0.65599
NC1piPM	4.90783	0.09799	0.17531	0.00975	N/A	N/A	5.19089
NCcoherent	0.00000	0.00000	0.00043	0.00003	N/A	N/A	0.00047
NCother	2.05619	0.07378	0.13055	0.00912	N/A	N/A	2.26963
Total	252.23446	0.19867	15.88872	0.02078	0.07214	0.00027	268.41504

Table 5.3: Predicted number of events in the neutrino mode μ-like sample obtained after applying the BANFF weight for a total exposure of 1.4734×10^{21} POT. The Asimov data set A in 5.1 is used.

	ν_μ	ν_e	$\bar{\nu}_\mu$	$\bar{\nu}_e$	Osc. ν_e	Osc. $\bar{\nu}_e$	Total
CCQE	15.29349	0.00085	29.88622	0.00093	0.00094	0.00137	45.18379
CC1pi	3.95485	0.00033	4.53265	0.00025	0.00060	0.00061	8.48929
CCcoherent	0.04705	0.00000	0.17567	0.00005	0.00000	0.00006	0.22283
2p2h	4.47453	0.00026	2.84291	0.00027	0.00044	0.00021	7.31861
CCother	0.94199	0.00012	0.60584	0.00000	0.00000	0.00000	1.54795
NC1pi0	0.06000	0.00222	0.06147	0.00169	N/A	N/A	0.12538
NC1piPM	0.35950	0.01527	0.46009	0.01235	N/A	N/A	0.84721
NCcoherent	0.00000	0.00000	0.00201	0.00000	N/A	N/A	0.00201
NCother	0.31580	0.01640	0.20064	0.00789	N/A	N/A	0.54073
Total	25.44720	0.03544	38.76749	0.02342	0.00198	0.00226	64.27780

Table 5.4: Predicted number of events in the antineutrino mode μ-like sample obtained after applying the BANFF weight for a total exposure of 7.558×10^{20} POT. The Asimov data set A in 5.1 is used.

	ν_μ	ν_e	$\bar{\nu}_\mu$	$\bar{\nu}_e$	Osc. ν_e	Osc. $\bar{\nu}_e$	Total
CCQE	0.16115	6.30178	0.00634	0.25566	46.25561	0.27811	53.25866
CC1pi	0.04703	0.93168	0.00280	0.06750	4.49505	0.04745	5.59150
CCcoherent	0.00011	0.00830	0.00018	0.00397	0.03445	0.00327	0.05028
2p2h	0.03033	1.59694	0.00117	0.04275	8.68112	0.03893	10.39125
CCother	0.01329	0.12803	0.00034	0.00942	0.08850	0.00326	0.24284
NC1pi0	1.70203	0.03706	0.06012	0.00356	N/A	N/A	1.80278
NC1piPM	0.16854	0.00472	0.01020	0.00057	N/A	N/A	0.18404
NCcoherent	0.52817	0.00715	0.04794	0.00294	N/A	N/A	0.58619
NCother	0.31767	0.01695	0.02120	0.00128	N/A	N/A	0.35711
NC1gamma	0.94222	0.01687	0.04983	0.00233	N/A	N/A	1.01125
Total	3.91054	9.04948	0.20014	0.38998	59.55473	0.37103	73.47589

Table 5.5: Predicted number of events in the neutrino mode e-like sample obtained after applying the BANFF weight for a total exposure of 1.4734×10^{21} POT. The Asimov data set A in 5.1 is used.

	ν_μ	ν_e	$\bar{\nu}_\mu$	$\bar{\nu}_e$	Osc. ν_e	Osc. $\bar{\nu}_e$	Total
CCQE	0.01288	0.50911	0.02388	0.84721	1.02586	2.85198	5.27090
CC1pi	0.00763	0.10111	0.00733	0.14431	0.14337	0.33485	0.73858
CCcoherent	0.00002	0.00099	0.00042	0.01066	0.00114	0.03130	0.04455
2p2h	0.00295	0.14379	0.00219	0.11301	0.23285	0.33042	0.82521
CCother	0.00390	0.02116	0.00120	0.01154	0.01042	0.00668	0.05491
NC1pi0	0.13849	0.00541	0.17659	0.00468	N/A	N/A	0.32516
NC1piPM	0.02475	0.00127	0.02001	0.00080	N/A	N/A	0.04683
NCcoherent	0.04776	0.00221	0.20260	0.00317	N/A	N/A	0.25574
NCother	0.05664	0.00221	0.02672	0.00097	N/A	N/A	0.08654
NC1gamma	0.07943	0.00439	0.17490	0.00383	N/A	N/A	0.26255
Total	0.37445	0.79164	0.63583	1.14019	1.41363	3.55523	7.91097

Table 5.6: Predicted number of events in the antineutrino mode e-like sample obtained after applying the BANFF weight for a total exposure of 1.4734×10^{21} POT. The Asimov data set A in 5.1 is used.

	ν_μ	ν_e	$\bar{\nu}_\mu$	$\bar{\nu}_e$	Osc. ν_e	Osc. $\bar{\nu}_e$	Total
CCQE	0.02857	0.02442	0.00117	0.00174	0.21123	0.00265	0.26979
CC1pi	0.07582	0.76065	0.00257	0.00383	4.85325	0.00227	5.69839
CCcoherent	0.00027	0.01765	0.00008	0.00007	0.11121	0.00011	0.12939
2p2h	0.01012	0.02195	0.00049	0.00095	0.16017	0.00105	0.19473
CCother	0.03770	0.11225	0.00116	0.00279	0.12085	0.00150	0.27625
NC1pi0	0.02049	0.00076	0.00083	0.00008	N/A	N/A	0.02216
NC1piPM	0.06474	0.00165	0.00382	0.00033	N/A	N/A	0.07053
NCother	0.20584	0.00830	0.01304	0.00088	N/A	N/A	0.22807
NC1gamma	0.02844	0.00000	0.00067	0.00007	N/A	N/A	0.02918
Total	0.47199	0.94764	0.02382	0.01075	5.45671	0.00758	6.91850

Table 5.7: Predicted number of events in the neutrino mode ν_e CC1π^+-like sample obtained after applying the BANFF weight for a total exposure of 1.4734×10^{21} POT. The Asimov data set A in 5.1 is used.

5.4.1.3 Predicted and observed spectra

In this section, we present the expected spectra in Super-K for Asimov A and unoscillated scenarios, assuming normal hierarchy. All plots are generated for an integrated exposure corresponding to Run 1-8.

Predicted single ring Super-K spectra are shown in figs. 5.1 and 5.2. By comparing neutrino and antineutrino mode e-like plots it is clear that θ vs E_{reco} distributions are differently populated by $\nu_\mu \to \nu_e$ and $\bar{\nu}_\mu \to \bar{\nu}_e$ events.

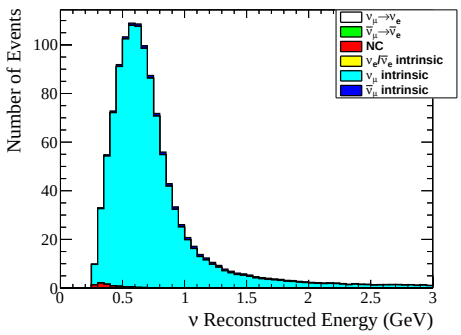

(a) Muon-like, neutrino mode

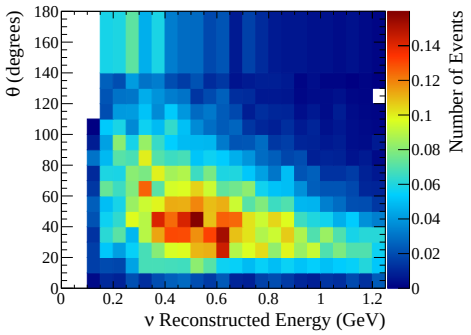

(b) Electron-like, neutrino mode

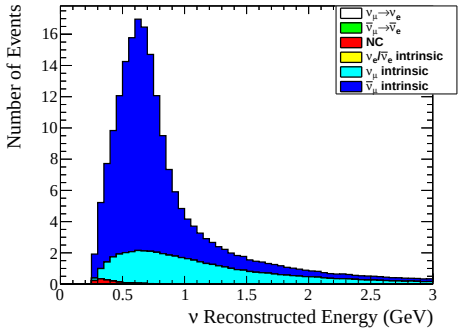

(c) Muon-like, antineutrino mode

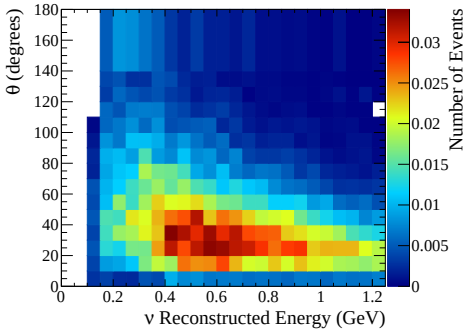

(d) Electron-like antineutrino mode

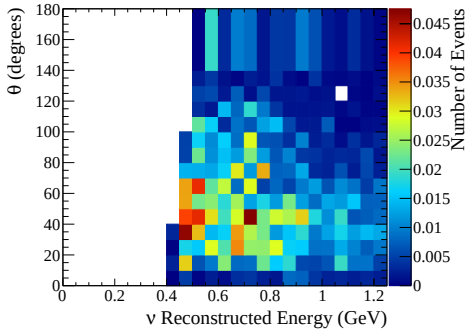

(e) ν_e CC1π^+-like, neutrino mode

Figure 5.1: Predicted unoscillated spectra. μ-like distributions are a function of the reconstructed neutrino energy, while the e-like, including ν_e CC1π^+, distributions are functions of both the reconstructed neutrino energy and the reconstructed angle between the outgoing lepton and the neutrino direction. The distributions correspond to the statistics collected in the full Run 1-8 data set. The spectra are generated with the systematic parameters described in section 5.5.

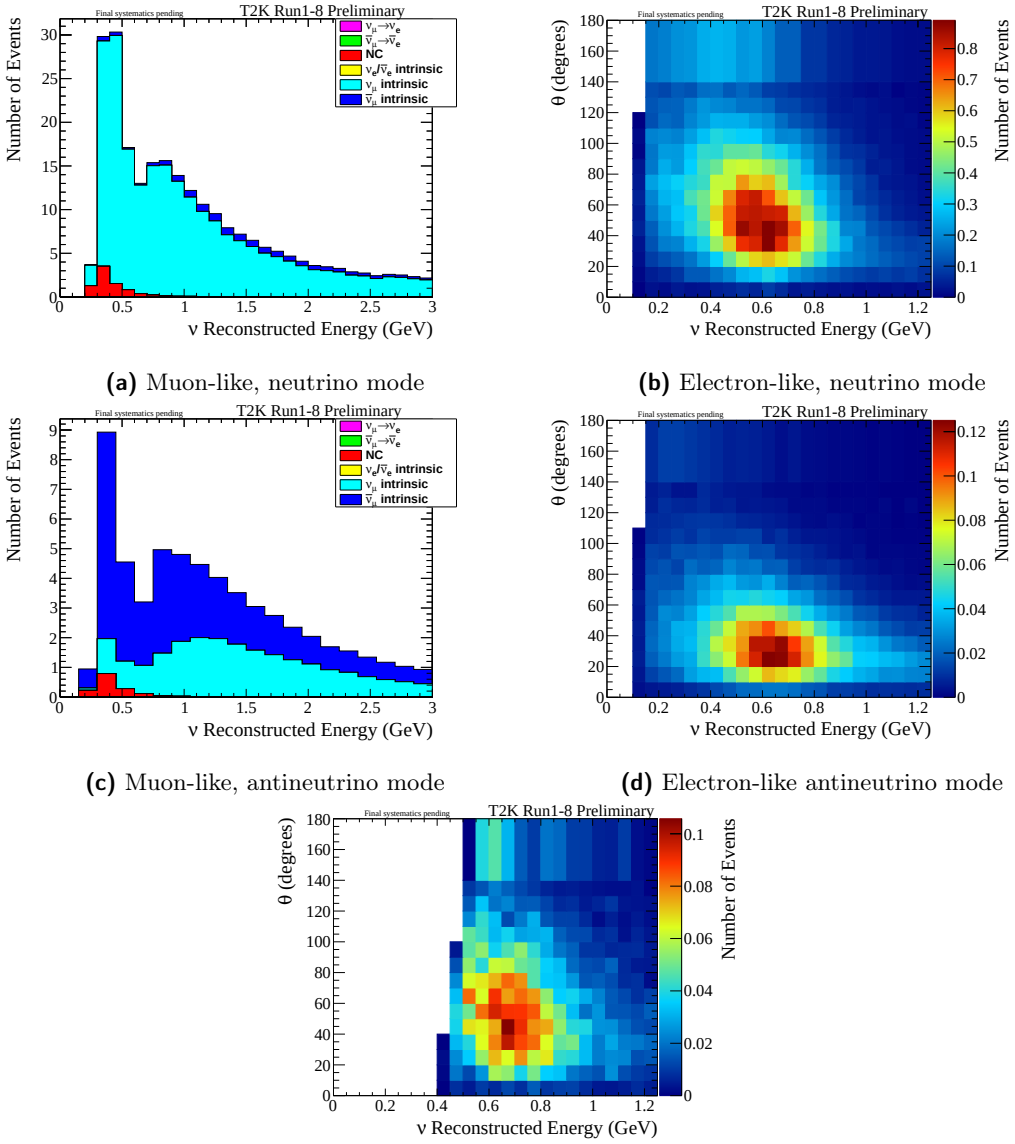

(a) Muon-like, neutrino mode

(b) Electron-like, neutrino mode

(c) Muon-like, antineutrino mode

(d) Electron-like antineutrino mode

(e) ν_e CC1π^+-like, neutrino mode

Figure 5.2: Predicted oscillated Asimov A spectra. μ-like distributions are a function of the reconstructed neutrino energy, while the e-like, including ν_e CC1π^+, distributions are functions of both the reconstructed neutrino energy and the reconstructed angle between the outgoing lepton and the neutrino direction. The distributions correspond to the statistics collected in the full Run 1-8 data set. The spectra are generated with the systematic parameters described in section 5.5 and the oscillation parameters corresponding to the Asimov data set A shown in table 5.1.

5.5 Effects of Systematics in the prediction of the μ and e single ring and ν_e CC$1\pi^+$ - like spectra

This analysis considers 110 flux, cross section and Super-K detector systematic parameters plus 6 oscillation parameters, which can be treated as either nuisance parameters or as parameters of interest, depending on the analysis that is performed.

5.5.1 Flux and cross-section parameters (73 parameters)

In this analysis, all the flux and cross-section systematic parameters are included in the ND280 data (BANFF) fit. However, since the ND fit is not sensitive to the electron neutrino cross section and the NC1γ parameters they remain unconstrained. The parameters fit are 11 ν_μ, 5 $\bar{\nu}_\mu$, 7 ν_e and 2 $\bar{\nu}_e$ neutrino mode (FHC) flux parameters, 5 ν_μ, 11 $\bar{\nu}_\mu$, 2 ν_e and 7 $\bar{\nu}_e$ antineutrino mode (RHC) flux parameters and 23 cross-section parameters. Best-fit values of these parameters and a covariance matrix giving their correlated uncertainties are obtained by the BANFF group from a fit of the $\bar{\nu}_\mu$ and ν_μ ND280 samples as described in Ref [168]. A list of the BANFF parameters, their best-fit values and their prefit and postfit errors can be found in tables 5.8 to 5.10.

The best-fit values are used to reweight the templates as described in Section 5.3, and the postfit errors in the covariance matrix are used as prior uncertainties in this analysis. All the cross section parameters set to 1 correspond to the NEUT nominal value, except "CC other shape" and "2p2h shape O", for which the NEUT nominal value is 0. For all the normalisation parameters, 1 is the nominal pre-BANFF fit value.

The effects of these correlated uncertainties (see fig. 5.3) are evaluated using the Cholesky method, that allows throws of the systematic parameters according to their multivariate distribution taking into account existing correlations.

Many of the cross-section parameters are the same as those used in the previous analysis [181]. However, the binding energy for ^{16}O is no longer included in this analysis and a number of new parameters have been included, see section 5.5.1.1. Five of these new parameters (2p2h, BeRPA A, B, D and E) are implemented using cubic splines, details for which can be found in [181], while one of the new parameters (BeRPA U) is fixed in the analysis.

5.5.1.1 Neutrino-nucleus interaction uncertainties

Overall normalisation uncertainties for 2p2h interactions were included in previous analyses, but this analysis includes a 2p2h shape uncertainty (using best-fit value and

Index	Parameter	Description	Best fit	1σ pre/postfit fractional error
0	$f^{banff}_{0;t,r}$	FHC ν_μ flux normalisation, E = 0.0 - 0.4 GeV	1.026	0.099 / 0.057
1	$f^{banff}_{1;t,r}$	FHC ν_μ flux normalisation, E = 0.4 - 0.5 GeV	1.050	0.103 / 0.052
2	$f^{banff}_{2;t,r}$	FHC ν_μ flux normalisation, E = 0.5 - 0.6 GeV	1.032	0.096 / 0.045
3	$f^{banff}_{3;t,r}$	FHC ν_μ flux normalisation, E = 0.6 - 0.7 GeV	0.991	0.087 / 0.042
4	$f^{banff}_{4;t,r}$	FHC ν_μ flux normalisation, E = 0.7 - 1.0 GeV	0.943	0.113 / 0.054
5	$f^{banff}_{5;t,r}$	FHC ν_μ flux normalisation, E = 1.0 - 1.5 GeV	0.963	0.092 / 0.049
6	$f^{banff}_{6;t,r}$	FHC ν_μ flux normalisation, E = 1.5 - 2.5 GeV	1.030	0.070 / 0.042
7	$f^{banff}_{7;t,r}$	FHC ν_μ flux normalisation, E = 2.5 - 3.5 GeV	1.047	0.074 / 0.044
8	$f^{banff}_{8;t,r}$	FHC ν_μ flux normalisation, E = 3.5 - 5.0 GeV	1.038	0.087 / 0.041
9	$f^{banff}_{9;t,r}$	FHC ν_μ flux normalisation, E = 5.0 - 7.0 GeV	1.003	0.098 / 0.040
10	$f^{banff}_{10;t,r}$	FHC ν_μ flux normalisation, E = 7.0 - 30.0 GeV	0.991	0.114 / 0.048
11	$f^{banff}_{11;t,r}$	FHC $\bar{\nu_\mu}$ flux normalisation, E = 0.0 - 0.7 GeV	0.989	0.103 / 0.074
12	$f^{banff}_{12;t,r}$	FHC $\bar{\nu_\mu}$ flux normalisation, E = 0.7 - 1.0 GeV	0.986	0.079 / 0.048
13	$f^{banff}_{13;t,r}$	FHC $\bar{\nu_\mu}$ flux normalisation, E = 1.0 - 1.5 GeV	0.996	0.084 / 0.057
14	$f^{banff}_{14;t,r}$	FHC $\bar{\nu_\mu}$ flux normalisation, E = 1.5 - 2.5 GeV	1.042	0.086 / 0.062
15	$f^{banff}_{15;t,r}$	FHC $\bar{\nu_\mu}$ flux normalisation, E = 2.5 - 30.0 GeV	1.104	0.086 / 0.065
16	$f^{banff}_{16;t,r}$	FHC ν_e flux normalisation, E = 0.0 - 0.5 GeV	1.030	0.090 / 0.046
17	$f^{banff}_{17;t,r}$	FHC ν_e flux normalisation, E = 0.5 - 0.7 GeV	1.031	0.090 / 0.042
18	$f^{banff}_{18;t,r}$	FHC ν_e flux normalisation, E = 0.7 - 0.8 GeV	1.029	0.086 / 0.041
19	$f^{banff}_{19;t,r}$	FHC ν_e flux normalisation, E = 0.8 - 1.5 GeV	1.017	0.081 / 0.039
20	$f^{banff}_{20;t,r}$	FHC ν_e flux normalisation, E = 1.5 - 2.5 GeV	1.034	0.079 / 0.040
21	$f^{banff}_{21;t,r}$	FHC ν_e flux normalisation, E = 2.5 - 4.0 GeV	1.036	0.084 / 0.041
22	$f^{banff}_{22;t,r}$	FHC ν_e flux normalisation, E = 4.0 - 30.0 GeV	1.050	0.094 / 0.059
23	$f^{banff}_{23;t,r}$	FHC $\bar{\nu_e}$ flux normalisation, E = 0.0 - 2.5 GeV	1.050	0.074 / 0.054
24	$f^{banff}_{24;t,r}$	FHC $\bar{\nu_e}$ flux normalisation, E = 2.5 - 30.0 GeV	1.093	0.128 / 0.114

Table 5.8: Summary of neutrino mode flux systematics included in the VALOR joint fit analysis. A description of how the BANFF fit constrained these systematics can be found in [168].

Index	Parameter	Description	Best fit	1σ pre/postfit fractional error
25	$f^{banff}_{0;t,r}RHC$	RHC ν_μ flux normalisation, E = 0.0 - 0.7 GeV	0.993	0.094 / 0.066
26	$f^{banff}_{1;t,r}RHC$	RHC ν_μ flux normalisation, E = 0.7 - 1.0 GeV	1.003	0.079 / 0.049
27	$f^{banff}_{2;t,r}RHC$	RHC ν_μ flux normalisation, E = 1.0 - 1.5 GeV	1.018	0.077 / 0.045
28	$f^{banff}_{3;t,r}RHC$	RHC ν_μ flux normalisation, E = 1.5 - 2.5 GeV	1.061	0.081 / 0.049
29	$f^{banff}_{4;t,r}RHC$	RHC ν_μ flux normalisation, E = 2.5 - 30.0 GeV	1.051	0.080 / 0.043
30	$f^{banff}_{5;t,r}RHC$	RHC $\bar{\nu_\mu}$ flux normalisation, E = 0.0 - 0.4 GeV	1.012	0.104 / 0.065
31	$f^{banff}_{6;t,r}RHC$	RHC $\bar{\nu_\mu}$ flux normalisation, E = 0.4 - 0.5 GeV	1.028	0.102 / 0.052
32	$f^{banff}_{7;t,r}RHC$	RHC $\bar{\nu_\mu}$ flux normalisation, E = 0.5 - 0.6 GeV	1.008	0.096 / 0.045
33	$f^{banff}_{8;t,r}RHC$	RHC $\bar{\nu_\mu}$ flux normalisation, E = 0.6 - 0.7 GeV	0.988	0.085 / 0.041
34	$f^{banff}_{9;t,r}RHC$	RHC $\bar{\nu_\mu}$ flux normalisation, E = 0.7 - 1.0 GeV	0.986	0.125 / 0.052
35	$f^{banff}_{10;t,r}RHC$	RHC $\bar{\nu_\mu}$ flux normalisation, E = 1.0 - 1.5 GeV	0.997	0.105 / 0.047
36	$f^{banff}_{11;t,r}RHC$	RHC $\bar{\nu_\mu}$ flux normalisation, E = 1.5 - 2.5 GeV	1.036	0.080 / 0.042
37	$f^{banff}_{12;t,r}RHC$	RHC $\bar{\nu_\mu}$ flux normalisation, E = 2.5 - 3.5 GeV	1.063	0.074 / 0.046
38	$f^{banff}_{13;t,r}RHC$	RHC $\bar{\nu_\mu}$ flux normalisation, E = 3.5 - 5.0 GeV	1.069	0.094 / 0.063
39	$f^{banff}_{14;t,r}RHC$	RHC $\bar{\nu_\mu}$ flux normalisation, E = 5.0 - 7.0 GeV	1.044	0.093 / 0.056
40	$f^{banff}_{15;t,r}RHC$	RHC $\bar{\nu_\mu}$ flux normalisation, E = 7.0 - 30.0 GeV	1.007	0.130 / 0.093
41	$f^{banff}_{16;t,r}RHC$	RHC ν_e flux normalisation, E = 0.0 - 2.5 GeV	1.050	0.069 / 0.047
42	$f^{banff}_{17;t,r}RHC$	RHC ν_e flux normalisation, E = 2.5 - 30.0 GeV	1.048	0.085 / 0.065
43	$f^{banff}_{18;t,r}RHC$	RHC $\bar{\nu_e}$ flux normalisation, E = 0.0 - 0.5 GeV	1.018	0.095 / 0.051
44	$f^{banff}_{19;t,r}RHC$	RHC $\bar{\nu_e}$ flux normalisation, E = 0.5 - 0.7 GeV	1.018	0.091 / 0.043
45	$f^{banff}_{20;t,r}RHC$	RHC $\bar{\nu_e}$ flux normalisation, E = 0.7 - 0.8 GeV	1.016	0.091 / 0.044
46	$f^{banff}_{21;t,r}RHC$	RHC $\bar{\nu_e}$ flux normalisation, E = 0.8 - 1.5 GeV	1.018	0.084 / 0.040
47	$f^{banff}_{22;t,r}RHC$	RHC $\bar{\nu_e}$ flux normalisation, E = 1.5 - 2.5 GeV	1.043	0.080 / 0.051
48	$f^{banff}_{23;t,r}RHC$	RHC $\bar{\nu_e}$ flux normalisation, E = 2.5 - 4.0 GeV	1.046	0.089 / 0.064
49	$f^{banff}_{24;t,r}RHC$	RHC $\bar{\nu_e}$ flux normalisation, E = 4.0 - 30.0 GeV	1.083	0.156 / 0.133

Table 5.9: Summary of antineutrino mode flux systematics included in the VALOR joint fit analysis. A description of how the BANFF fit constrained these systematics can be found in [168].

Index	Parameter	Description	Best fit	1σ pre/postfit fractional error
50	$f^{banff}_{Norm_{2p2h}}$	Two particle two hole normalisation for ^{16}O	1.426	1.000 / 0.182
51	$f^{banff}_{C_5^A}$	C_5^A nucleon to Δ transition axial form factor	0.977	0.149 / 0.059
52	$f^{banff}_{Bg_{RES}}$	Scale of isospin 1/2 nonresonant background	0.979	0.308 / 0.190
53	$f^{banff}_{M_A^{QE}}$	CCQE axial-mass scaling factor	0.903	0.025 / 0.057
54	$f^{banff}_{M_A^{RES}}$	Resonance-production axial-mass scaling factor	0.822	0.158 / 0.045
55	f^{banff}_{SCCA}	BANFF; Second current class axial	1.000	- / -
56	f^{banff}_{SCCV}	BANFF; Second current class vector	1.000	- / -
57	$f^{banff}_{p_f}$	Fermi momentum for ^{16}O	0.916	0.058 / 0.072
58	$f^{banff}_{Shape_{CCoth}}$	CC other shape	0.519	0.400 / 0.187
59	$f^{banff}_{Norm_{CCcoh}}$	CC coherent for ^{16}O normalisation	0.906	0.300 / 0.275
60	$f^{banff}_{Norm_{NCcoh}}$	NC coherent normalisation	0.939	0.300 / 0.297
61	$f^{banff}_{Norm_{NCother}}$	NC other normalisation	1.000	- / 0.300
62	$f^{banff}_{Norm_{\nu_e\to\nu_\mu}}$	CC ν_e normalisation	1.000	- / 0.028
63	$f^{banff}_{Norm_{NC1\gamma}}$	NC 1γ normalisation	1.000	- / 1.000
64	$f^{banff}_{Norm_{\bar{\nu}_e\to\bar{\nu}_\mu}}$	CC $\bar{\nu}_e$ normalisation	1.000	- / 0.028
65	$f^{banff}_{Norm_{2p2hBar}}$	Antineutrino two particle two hole normalisation for ^{16}O	0.552	1.000 / 0.201
66	$f^{banff}_{Shape_{BeRPA_A}}$	Bernstein Polynomial coefficient A	0.663	0.118 / 0.056
67	$f^{banff}_{Shape_{BeRPA_B}}$	Bernstein Polynomial coefficient B	1.647	0.210 / 0.117
68	$f^{banff}_{Shape_{BeRPA_D}}$	Bernstein Polynomial coefficient D	0.988	0.170 / 0.128
69	$f^{banff}_{Shape_{BeRPA_E}}$	Bernstein Polynomial coefficient E	0.876	0.352 / 0.355
70	$f^{banff}_{Shape_{BeRPA_U}}$	Bernstein Polynomial coefficient U	1.200	0.100 / 0.100
71	$f^{banff}_{Shape_{2p2h\nu}}$	Neutrino two particle two hole ^{16}O shape	0.997	3.000 / 0.338
72	$f^{banff}_{Norm_{2p2hCtoO}}$	Two particle two hole ^{12}C to ^{16}O normalisation	0.940	0.200 / 0.161

Table 5.10: Summary of cross section systematics included in the VALOR joint fit analysis. Parameters with no prefit error were unconstrained. A description of how the BANFF fit constrained these systematics can be found in [168].

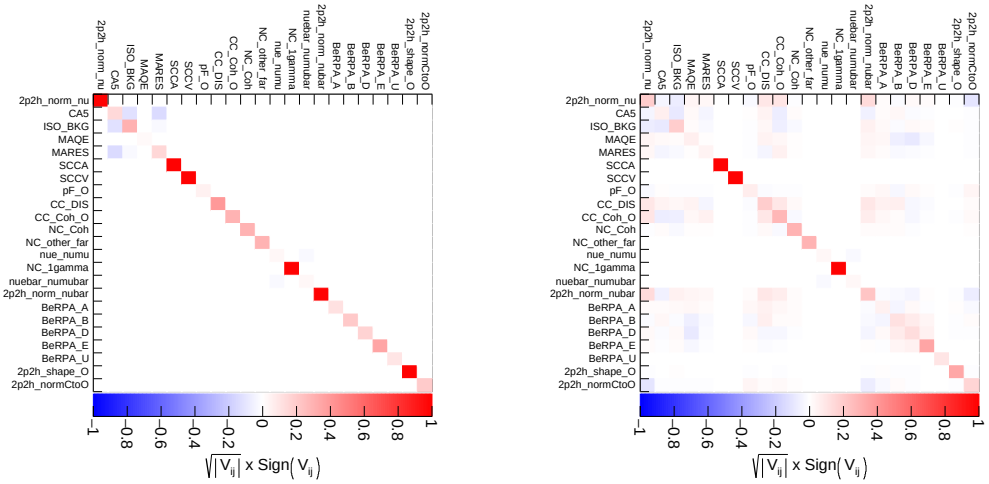

Figure 5.3: The pre-BANFF (left) and post-BANFF (right) cross-section covariance matrix, with the values shown as the sign of the element times the square root of the absolute value of the element.

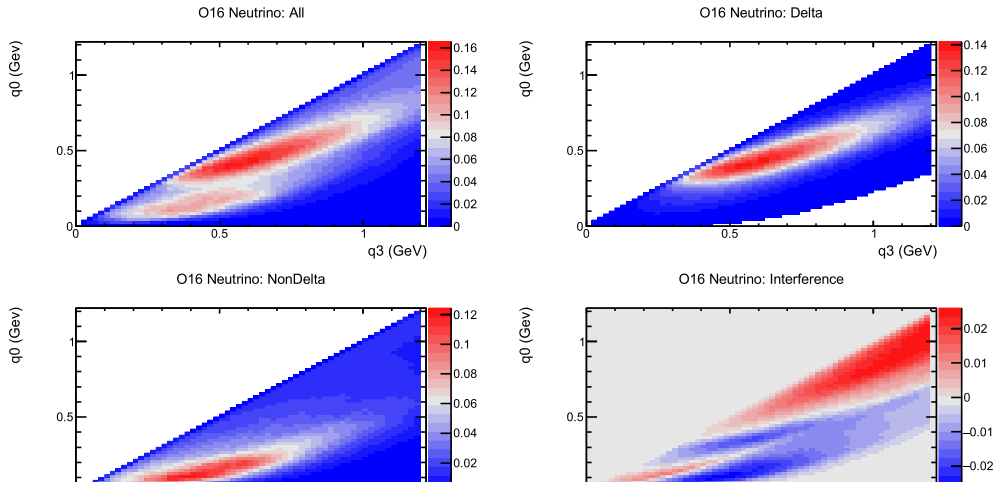

Figure 5.4: Distribution of neutrino events for 2p2h and each 2p2h term in q0-q3 space [201].

errors from the BANFF fit) to describe the uncertainty in the cross-section strength between Delta-like, non-Delta-like and interference terms of the 2p2h model, determined by redistributing the cross-section strength of these terms subject to (approximately) maintaining the total 2p2h event rate (see Section 2 of [201]). In terms of energy transfer (q0) and three-momentum transfer (q3) kinematics, the distribution of events in this space for neutrino and antineutrino interactions on oxygen are shown in figs. 5.4 and 5.5 respectively (see Section 2 of [201]).

This analysis also introduces 5 BeRPA parameters (A, B, D, E and U) to describe the collective effects of interactions between neutrinos and nucleons inside nuclei. These effects modify the Q^2 dependence of the neutrino-nucleus cross-section and in BeRPA are described by a cubic polynomial transitioning to an exponential above a Q^2 threshold, as described in [134]. Neither the 2p2h shape parameter nor the BeRPA parameters apply to interactions on free protons.

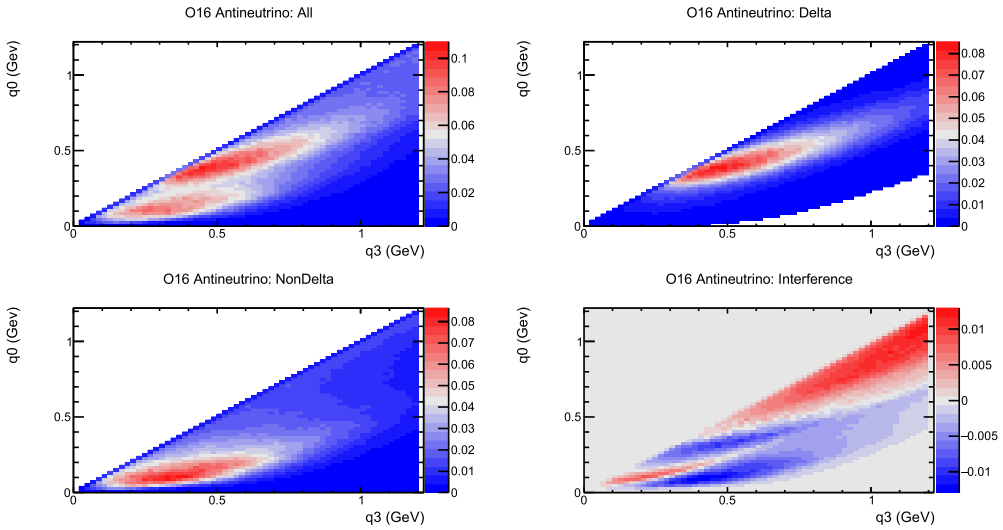

Figure 15: q_0 vs q_3 projection from antineutrinos on oxygen pre-tabulated `TH3D`s.

Figure 5.5: Distribution of antineutrino events for 2p2h and each 2p2h term in q0-q3 space [201].

5.5.2 Super-K efficiencies & effects of intranuclear and secondary re-interactions (44 parameters)

The Super-K detector uncertainties include the efficiencies of the fiducial volume and reduction chain, and the OD, ring-counting, PID, momentum and decay-electron cuts. These uncertainties have been evaluated by comparisons between SK-IV atmospheric data and atmospheric neutrino Monte Carlo. Ring counting errors are evaluated using ν_μ CCQE, ν_μ CCnQE, NC, and ν_e CC-enriched control samples from atmospheric neutrinos. The NC PID error is evaluated using a NC-enriched control sample, obtained by not using the PID information during the selection. All the Monte Carlo control samples are fitted simultaneously to the data with a χ^2 function using the selection efficiencies as fit parameters [172, 202] ad described in section 4.5.

Intranuclear final-state interactions (FSI) have significant effects in the T2K energy range and result in event topologies, for scattering from nuclear targets, which are drastically different from those created in neutrino scattering from free nucleons. Uncertainties due to FSI were estimated by simultaneously varying NEUT parameters that scale interaction probabilities as described in section 2 of [151]. Uncertainties due to secondary pion interactions (SI) were also evaluated by allowing variations in the interaction probabilities. Details of this are given in [203] in addition to the discussion in section 4.2.1.1. Since the same model is used for FSI and SI, it is possible to evaluate the uncertainties in both FSI and SI simultaneously. Details of this procedure are described in section 8 of [204].

Index	Parameter	Description	1σ fractional error
0	$f^{SK+FSI}_{0;t,r}$	SKDet + FSI/SI 0; Ereco range 0.00 - 0.40 GeV; numu/numubar CCQE (1Rmu)	0.009
1	$f^{SK+FSI}_{1;t,r}$	SKDet + FSI/SI 1; Ereco range 0.40 - 1.10 GeV; numu/numubar CCQE (1Rmu)	0.007
2	$f^{SK+FSI}_{2;t,r}$	SKDet + FSI/SI 2; Ereco range 1.10 - 30.00 GeV; numu/numubar CCQE (1Rmu)	0.007
3	$f^{SK+FSI}_{3;t,r}$	SKDet + FSI/SI 3; Ereco range 0.00 - 30.00 GeV; numu/numubar CCnQE (1Rmu)	0.169
4	$f^{SK+FSI}_{4;t,r}$	SKDet + FSI/SI 4; Ereco range 0.00 - 30.00 GeV; nue/nuebar/signue CC (1Rmu)	1.005
5	$f^{SK+FSI}_{5;t,r}$	SKDet + FSI/SI 5; Ereco range 0.00 - 30.00 GeV; all NC (1Rmu)	0.658
6	$f^{SK+FSI}_{6;t,r}$	SKDet + FSI/SI 6; Ereco range 0.00 - 0.35 GeV; oscillated nue CC (1Re)	0.181
7	$f^{SK+FSI}_{7;t,r}$	SKDet + FSI/SI 7; Ereco range 0.35 - 0.80 GeV; oscillated nue CC (1Re)	0.036
8	$f^{SK+FSI}_{8;t,r}$	SKDet + FSI/SI 8; Ereco range 0.80 - 1.25 GeV; oscillated nue CC (1Re)	0.042
9	$f^{SK+FSI}_{9;t,r}$	SKDet + FSI/SI 9; Ereco range 0.00 - 0.35 GeV; numu/numubar CC (1Re)	0.300
10	$f^{SK+FSI}_{10;t,r}$	SKDet + FSI/SI 10; Ereco range 0.35 - 0.80 GeV; numu/numubar CC (1Re)	0.321
11	$f^{SK+FSI}_{11;t,r}$	SKDet + FSI/SI 11; Ereco range 0.80 - 1.25 GeV; numu/numubar CC (1Re)	0.393
12	$f^{SK+FSI}_{12;t,r}$	SKDet + FSI/SI 12; Ereco range 0.00 - 0.35 GeV; nue/nuebar CC (1Re)	0.135
13	$f^{SK+FSI}_{13;t,r}$	SKDet + FSI/SI 13; Ereco range 0.35 - 0.80 GeV; nue/nuebar CC (1Re)	0.070
14	$f^{SK+FSI}_{14;t,r}$	SKDet + FSI/SI 14; Ereco range 0.80 - 1.25 GeV; nue/nuebar CC (1Re)	0.077
15	$f^{SK+FSI}_{15;t,r}$	SKDet + FSI/SI 15; Ereco range 0.00 - 0.35 GeV; all NC (1Re)	0.194
16	$f^{SK+FSI}_{16;t,r}$	SKDet + FSI/SI 16; Ereco range 0.35 - 0.80 GeV; all NC (1Re)	0.181
17	$f^{SK+FSI}_{17;t,r}$	SKDet + FSI/SI 17; Ereco range 0.80 - 1.25 GeV; all NC (1Re)	0.472
18	$f^{SK+FSI}_{0;t,r}RHC$	SKDet + FSI/SI 0; Ereco range 0.00 - 0.40 GeV; numu/numubar CCQE (1Rmu); RHC	0.009
19	$f^{SK+FSI}_{1;t,r}RHC$	SKDet + FSI/SI 1; Ereco range 0.40 - 1.10 GeV; numu/numubar CCQE (1Rmu); RHC	0.007
20	$f^{SK+FSI}_{2;t,r}RHC$	SKDet + FSI/SI 2; Ereco range 1.10 - 30.00 GeV; numu/numubar CCQE (1Rmu); RHC	0.007
21	$f^{SK+FSI}_{3;t,r}RHC$	SKDet + FSI/SI 3; Ereco range 0.00 - 30.00 GeV; numu/numubar CCnQE (1Rmu); RHC	0.130
22	$f^{SK+FSI}_{4;t,r}RHC$	SKDet + FSI/SI 4; Ereco range 0.00 - 30.00 GeV; nue/nuebar/signue CC (1Rmu); RHC	1.005
23	$f^{SK+FSI}_{5;t,r}RHC$	SKDet + FSI/SI 5; Ereco range 0.00 - 30.00 GeV; all NC (1Rmu); RHC	0.657
24	$f^{SK+FSI}_{6;t,r}RHC$	SKDet + FSI/SI 6; Ereco range 0.00 - 0.35 GeV; oscillated nue CC (1Re); RHC	0.108
25	$f^{SK+FSI}_{7;t,r}RHC$	SKDet + FSI/SI 7; Ereco range 0.35 - 0.80 GeV; oscillated nue CC (1Re); RHC	0.036
26	$f^{SK+FSI}_{8;t,r}RHC$	SKDet + FSI/SI 8; Ereco range 0.80 - 1.25 GeV; oscillated nue CC (1Re); RHC	0.057
27	$f^{SK+FSI}_{9;t,r}RHC$	SKDet + FSI/SI 9; Ereco range 0.00 - 0.35 GeV; numu/numubar CC (1Re); RHC	0.349
28	$f^{SK+FSI}_{10;t,r}RHC$	SKDet + FSI/SI 10; Ereco range 0.35 - 0.80 GeV; numu/numubar CC (1Re); RHC	0.342
29	$f^{SK+FSI}_{11;t,r}RHC$	SKDet + FSI/SI 11; Ereco range 0.80 - 1.25 GeV; numu/numubar CC (1Re); RHC	0.417
30	$f^{SK+FSI}_{12;t,r}RHC$	SKDet + FSI/SI 12; Ereco range 0.00 - 0.35 GeV; nue/nuebar CC (1Re); RHC	0.085
31	$f^{SK+FSI}_{13;t,r}RHC$	SKDet + FSI/SI 13; Ereco range 0.35 - 0.80 GeV; nue/nuebar CC (1Re); RHC	0.056
32	$f^{SK+FSI}_{14;t,r}RHC$	SKDet + FSI/SI 14; Ereco range 0.80 - 1.25 GeV; nue/nuebar CC (1Re); RHC	0.078
33	$f^{SK+FSI}_{15;t,r}RHC$	SKDet + FSI/SI 15; Ereco range 0.00 - 0.35 GeV; all NC (1Re); RHC	0.214
34	$f^{SK+FSI}_{16;t,r}RHC$	SKDet + FSI/SI 16; Ereco range 0.35 - 0.80 GeV; all NC (1Re); RHC	0.191
35	$f^{SK+FSI}_{17;t,r}RHC$	SKDet + FSI/SI 17; Ereco range 0.80 - 1.25 GeV; all NC (1Re); RHC	0.465
36	$f^{SK+FSI}_{0;t,r}MultiRing$	SKDet + FSI/SI 0; Ereco range 0.30 - 0.80 GeV; oscillated nue CC (MultiRe); MultiRing	0.249
37	$f^{SK+FSI}_{1;t,r}MultiRing$	SKDet + FSI/SI 1; Ereco range 0.80 - 1.25 GeV; oscillated nue CC (MultiRe); MultiRing	0.215
38	$f^{SK+FSI}_{2;t,r}MultiRing$	SKDet + FSI/SI 2; Ereco range 0.30 - 0.80 GeV; numu/numubar CC (MultiRe); MultiRing	0.507
39	$f^{SK+FSI}_{3;t,r}MultiRing$	SKDet + FSI/SI 3; Ereco range 0.80 - 1.25 GeV; numu/numubar CC (MultiRe); MultiRing	0.236
40	$f^{SK+FSI}_{4;t,r}MultiRing$	SKDet + FSI/SI 4; Ereco range 0.30 - 0.80 GeV; nue/nuebar CC (MultiRe); MultiRing	0.244
41	$f^{SK+FSI}_{5;t,r}MultiRing$	SKDet + FSI/SI 5; Ereco range 0.80 - 1.25 GeV; nue/nuebar CC (MultiRe); MultiRing	0.235
42	$f^{SK+FSI}_{6;t,r}MultiRing$	SKDet + FSI/SI 6; Ereco range 0.30 - 0.80 GeV; all NC (MultiRe); MultiRing	0.983
43	$f^{SK+FSI}_{7;t,r}MultiRing$	SKDet + FSI/SI 7; Ereco range 0.80 - 1.25 GeV; all NC (MultiRe); MultiRing	0.524
44	$f^{SK}_{E;r}$	SK energy scale	0.024

Table 5.11: Summary of SK detector + FSI + SI + PN systematics included in the VALOR joint fit analysis.

A list of the Super-K parameters and their errors can be found in table 5.11. We consider the Super-K detector efficiency and FSI+SI+PN systematics together, adding their covariance matrices linearly and evaluating the effects of these uncertainties using the Cholesky method. Details of all parameters can be found in [181].

5.5.3 Super-K energy scale (1 parameter)

The systematic parameter $f^{SK}_{E;r}$ is included to estimate the effects of uncertainty in the Super-K reconstructed energy scale. This uncertainty is estimated to be 2.4% [205]; its effects are calculated by scaling the bin edges of the MC templates and, assuming uniform distribution of events within the bins, calculating the number of events gained from/lost to other bins (including bins that are not immediately adjacent). This systematic is applied after all other systematics have been applied, because it affects reconstructed rather than true energy, does not commute with spline-based systematics, which are

Parameter(s)	Prior	Range
$\sin^2\theta_{23}$	uniform	$[0.3; 0.7]$
$\sin^2 2\theta_{13}$ ($\sin^2\theta_{13}$) reactors	gaussian	0.0857 ± 0.0046
$\sin^2 2\theta_{13}$ ($\sin^2\theta_{13}$) T2K only	uniform	$[0; 0.4]$
$\sin^2 2\theta_{12}$	gaussian	0.846 ± 0.021
$\lvert\Delta m^2_{32}\rvert$ (NH) / $\lvert\Delta m^2_{13}\rvert$ (IH)	uniform	$[2.3; 2.7] \times 10^{-3}$ eV^2/c^4
Δm^2_{21}	gaussian	$(7.53 \pm 0.18) \times 10^{-5}$ eV^2/c^4
δ_{CP}	uniform	$[-\pi; +\pi]$
Mass Hierarchy	fixed	NH or IH

Table 5.12: Treatment of the oscillation parameters in the $\nu/\bar{\nu}$ joint analysis. All the gaussian priors are from [199]. The parameter $\sin^2 2\theta_{13}$ can be constrained with the measurement of reactor experiments using the gaussian prior, otherwise a uniform prior is used and the measurement relies only on the T2K data. The nominal values of $\sin^2 2\theta_{13}$, $\sin^2 2\theta_{12}$ and Δm^2_{21} are from [199], while all the other oscillation parameter values corresponds to the most probable values obtained by the Bayesian analysis on the T2K run 1-4 neutrino mode data [200]. The mass hierarchy is not marginalised but fixed to either NH or IH.

generated without consideration of energy scale variation and also does not commute with the other Super-K systematics, which are determined from data without any energy scale variation.

5.5.4 Oscillation parameters and mass hierarchy (7 parameters)

The 3-flavour oscillation probability is used. All the nuisance oscillation parameters, i.e. those parameters which are not shown in a given contour, are marginalised except the mass hierarchy which is fixed to either normal or inverted hierarchy.

For $\sin^2\theta_{13}$ two different priors can be used, depending on whether the reactor constraint is applied, denoted as “reactors", when applied and “T2K only" when not applied. The value of the reactor constraint is 0.085 ± 0.005 for $\sin^2 2\theta_{13}$ from [206].

5.5.5 Systematic error on Super-K predictions

The effect of each category of systematic parameter on the expected event rate for Super-K sample is given in tables D.1 to D.5 (details of per-sample event rates for 1σ and 3σ variations of each independent systematic parameter can be found in appendix B). The mean and RMS of 10000 throws of the respective systematics (with correlations taken into account) is computed for each sample and in the case of pre-BANFF and post-BANFF errors. When not measuring the effect of oscillation parameters variations, the oscillation parameters are fixed at Asimov A values (see section 5.4.1.1).

For the measurement of δ_{CP} it is important to understand the effect of the systematic

uncertainties on the ratio of the number of events between neutrino and antineutrino mode samples. If correlations do not reproduce the physics correctly, a fake asymmetry between neutrino and antineutrino oscillations can be seen. Furthermore, if correlations exist but are not taken into account, the measurement of δ_{CP} could be biased. The true value of δ_{CP} determines whether correlations or anti-correlations between systematic parameters have the greatest effect in hiding any oscillation asymmetry. In particular, if true $\delta_{CP} = \pm\pi/2$ then anti-correlation in the e-like samples could hide any oscillation asymmetry. Alternatively, in the case that true $\delta_{CP} \sim 0$ it is uncorrelated parameters that reduce the sensitivity to δ_{CP}. The uncertainties on the ratios between neutrino and antineutrino mode events due to the systematic parameters are shown in table 5.13. The most critical systematic parameters are σ_{ν_e} and $\sigma_{\bar{\nu}_e}$ which are applied respectively to ν_e and $\bar{\nu}_e$ events. Their fractional error from the BANFF covariance matrix is 2.83% (see table 5.10) and they are partially anti-correlated with non-diagonal elements in the covariance matrix of -0.0004.

It can be seen in tables D.1 to D.5 (Appendix D) that the reduction in the error on flux and constrained cross-section systematics achieved through the BANFF fit reduces the fractional error due to all systematics from $\sim 14\%$ to $\sim 4\%$ and $\sim 11\%$ to $\sim 3\%$ in the neutrino- and antineutrino-mode μ-like samples respectively, from $\sim 16\%$ to $\sim 7\%$ and $\sim 13\%$ to $\sim 8\%$ in the neutrino- and antineutrino-mode e-like samples respectively, and from $\sim 25\%$ to $\sim 22\%$ in the ν_e CC$1\pi^+$-like sample. The poor constraint for the ν_e CC$1\pi^+$ sample from the ND fit is due to the systematic uncertainties for this sample being dominated by Super-K detector errors and Super-K FSI+SI+PN errors as can be seen in table 5.13. Only the uncertainty on the parameters $\sin^2\theta_{13}$, $\sin^2\theta_{12}$, Δm^2_{21} is considered which results in the small contribution from the oscillation parameters category for the μ-like samples as can be seen in figs. 5.8 and 5.9.

	1-Ring μ		**1-Ring e**			
Error source	FHC	RHC	FHC	RHC	FHC 1 d.e.	FHC/RHC
SK Detector	1.86	1.51	3.03	4.22	16.69	1.60
SK FSI+SI+PN	2.20	1.98	3.01	2.31	11.43	1.57
Flux + Xsec constrained	3.22	2.72	3.22	2.88	4.05	2.50
$\sigma(\nu_e)/\sigma(\bar{\nu}_e)$	0.00	0.00	2.63	1.46	2.62	3.03
NC1γ	0.00	0.00	1.08	2.59	0.33	1.49
NC Other	0.25	0.25	0.14	0.33	0.98	0.18
Osc	0.04	0.03	3.86	3.60	3.78	0.79
All Systematics	4.40	3.76	6.10	6.51	20.94	4.77
All with osc	4.40	3.76	7.27	7.44	21.24	4.85

Table 5.13: Percentage error on event rate by error source and sample. Final column is the percentage error on the ratio of FHC/RHC events in the one-ring e sample.

The error envelopes corresponding to tables D.1 to D.5 are shown in figs. 5.6 to 5.21.

These error envelopes are determined by performing 1×10^4 correlated throws of the systematic parameter group under consideration and plotting the mean and Gaussian 1σ error resulting.

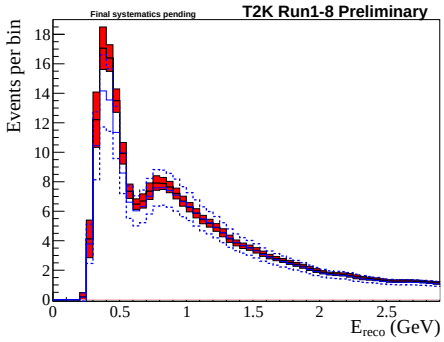

(a) Muon-like, neutrino mode

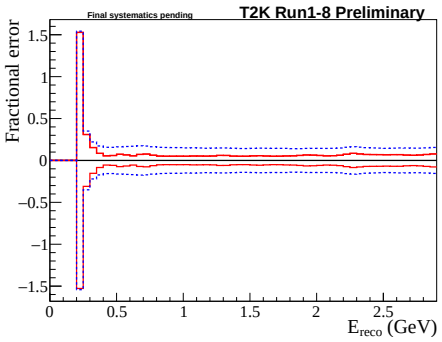

(b) Muon-like, neutrino mode

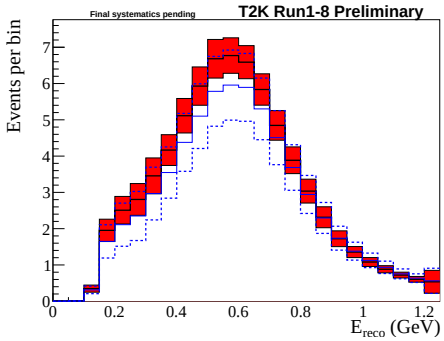

(c) Electron-like, neutrino mode

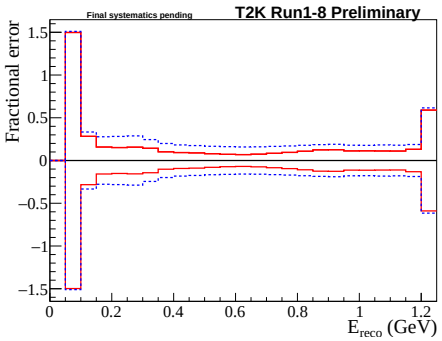

(d) Electron-like, neutrino mode

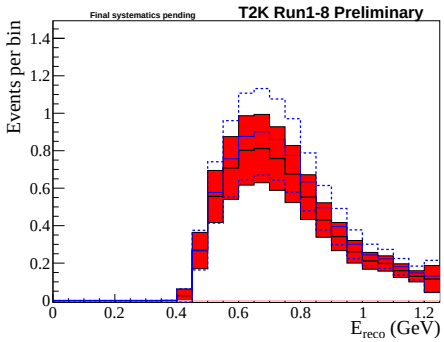

(e) ν_e CC$1\pi^+$-like, neutrino mode

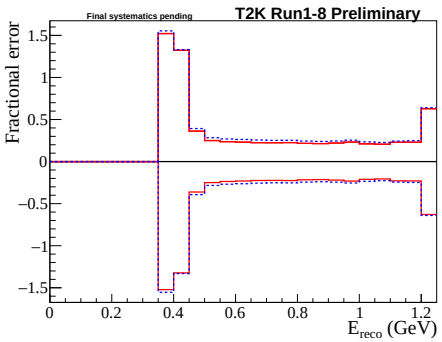

(f) ν_e CC$1\pi^+$-like, neutrino mode

Figure 5.6: Error envelopes (left) and fractional errors (right) for the reconstructed neutrino energy spectrum for all systematic parameters for pre-BANFF (blue) and post-BANFF (red) errors. 1×10^4 toys are generated for the Asimov data set A with randomized systematic parameters with correlations taken into account. Since δ_{CP}, $\sin^2\theta_{23}$, Δm^2_{32} and the mass hierarchy will be measured, only the uncertainty on $\sin^2\theta_{13}$, $\sin^2\theta_{12}$ and Δm^2_{21} are taken into account.

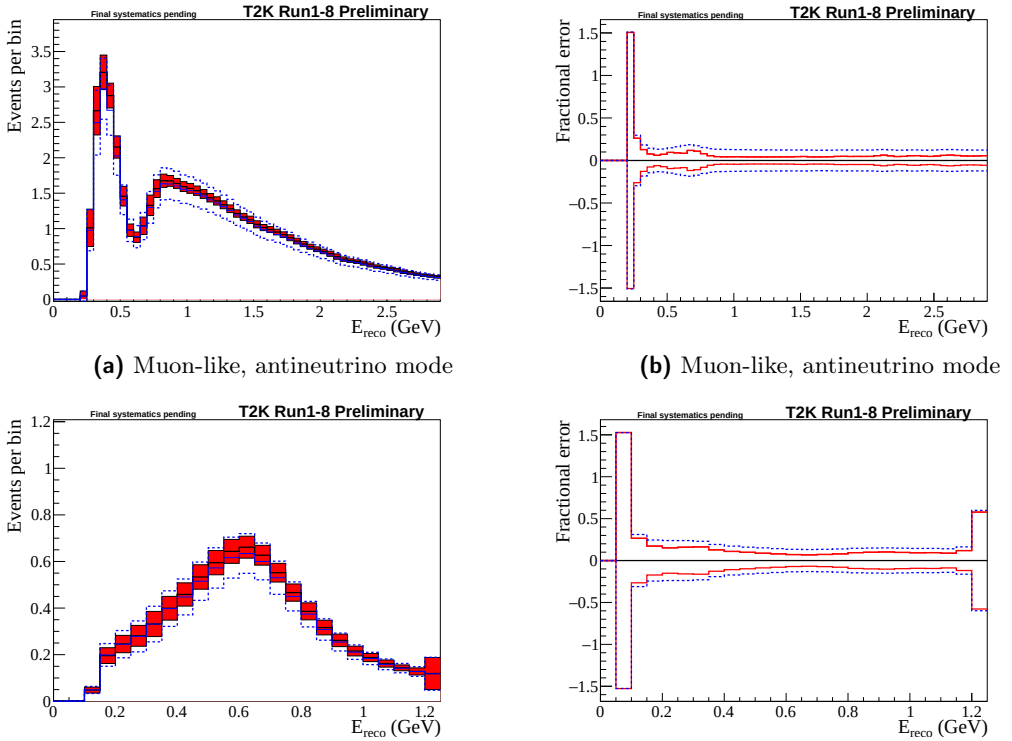

(a) Muon-like, antineutrino mode

(b) Muon-like, antineutrino mode

(c) Electron-like antineutrino mode

(d) Electron-like antineutrino mode

Figure 5.7: Error envelopes (left) and fractional errors (right) for the reconstructed neutrino energy spectrum for all systematic parameters for pre-BANFF (blue) and post-BANFF (red) errors. 1×10^4 toys are generated for the Asimov data set A with randomized systematic parameters with correlations taken into account. Since δ_{CP}, $\sin^2\theta_{23}$, Δm^2_{32} and the mass hierarchy will be measured, only the uncertainty on $\sin^2\theta_{13}$, $\sin^2\theta_{12}$ and Δm^2_{21} are taken into account.

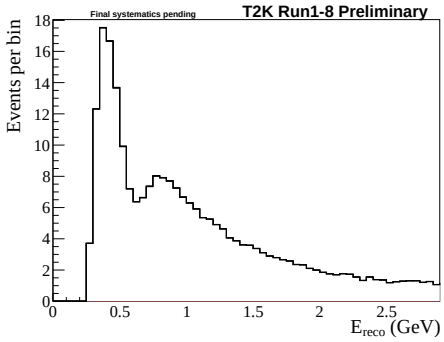

(a) Muon-like, neutrino mode

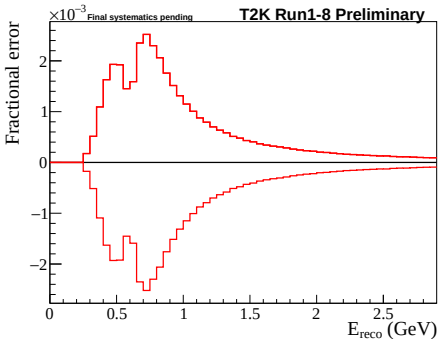

(b) Muon-like, neutrino mode

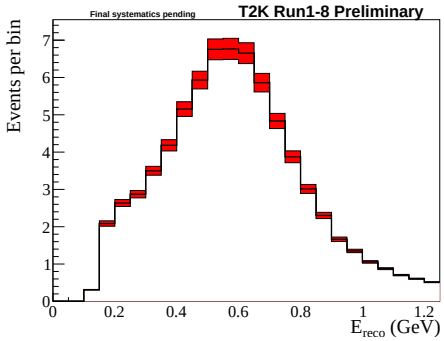

(c) Electron-like, neutrino mode

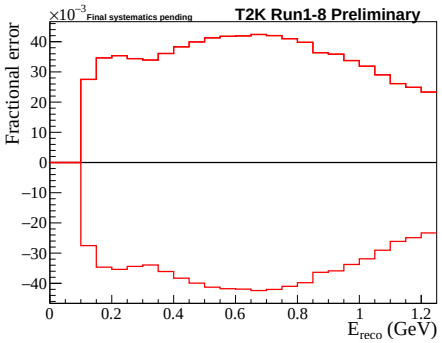

(d) Electron-like, neutrino mode

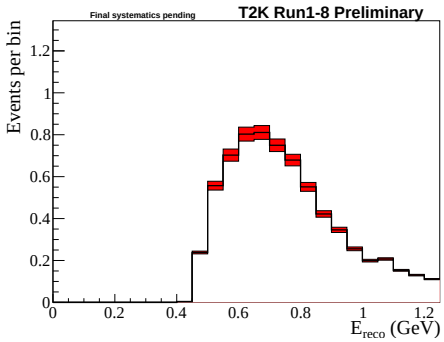

(e) ν_e CC$1\pi^+$-like, neutrino mode

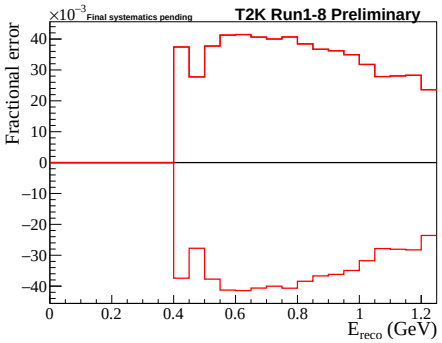

(f) ν_e CC$1\pi^+$-like, neutrino mode

Figure 5.8: Error envelopes (left) and fractional errors (right) for the reconstructed neutrino energy spectrum for all oscillation nuisance parameters. 1×10^4 toys are generated for the Asimov data set A with randomized systematic parameters with correlations taken into account. Since δ_{CP}, $\sin^2\theta_{23}$, Δm^2_{32} and the mass hierarchy will be measured, only the uncertainty on $\sin^2\theta_{13}$, $\sin^2\theta_{12}$ and Δm^2_{21} are taken into account.

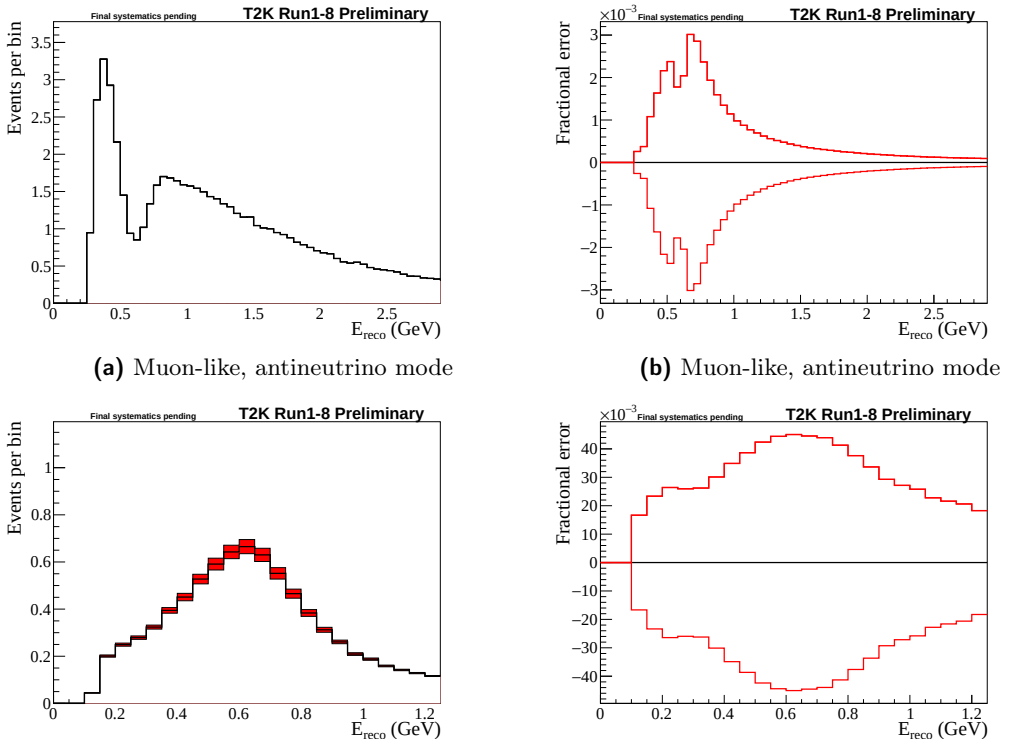

(a) Muon-like, antineutrino mode

(b) Muon-like, antineutrino mode

(c) Electron-like antineutrino mode

(d) Electron-like antineutrino mode

Figure 5.9: Error envelopes (left) and fractional errors (right) for the reconstructed neutrino energy spectrum for all oscillation nuisance parameters. 1×10^4 toys are generated for the Asimov data set A with randomized systematic parameters with correlations taken into account. Since δ_{CP}, $\sin^2\theta_{23}$, Δm^2_{32} and the mass hierarchy will be measured, only the uncertainty on $\sin^2\theta_{13}$, $\sin^2\theta_{12}$ and Δm^2_{21} are taken into account.

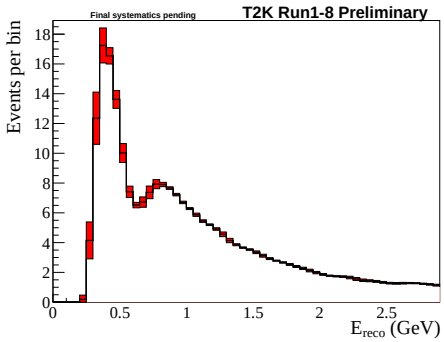

(a) Muon-like, neutrino mode

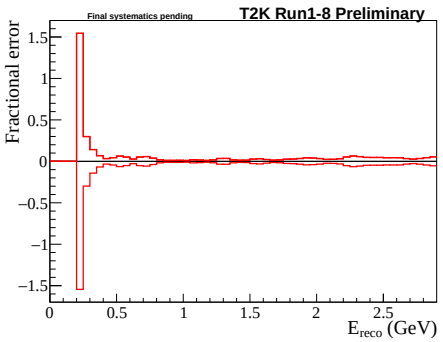

(b) Muon-like, neutrino mode

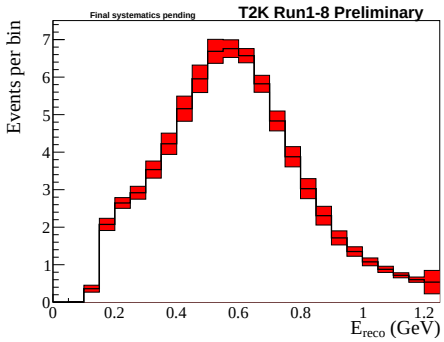

(c) Electron-like, neutrino mode

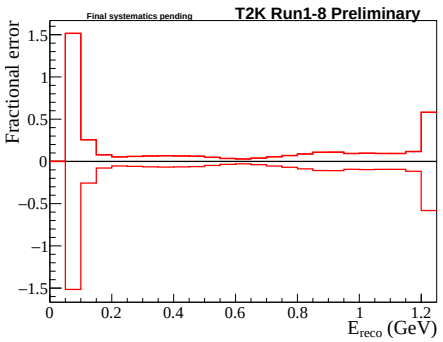

(d) Electron-like, neutrino mode

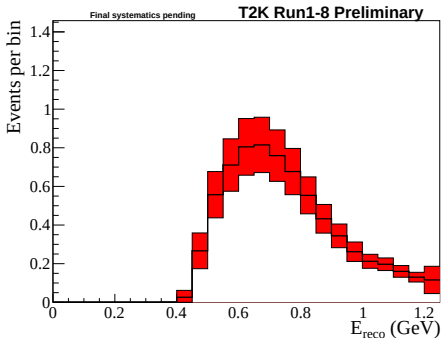

(e) ν_e CC$1\pi^+$-like, neutrino mode

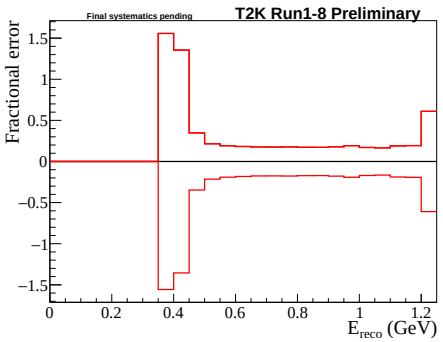

(f) ν_e CC$1\pi^+$-like, neutrino mode

Figure 5.10: Error envelopes (left) and fractional error (right) for the reconstructed neutrino energy spectrum for Super-K detector systematic parameters. 1×10^4 toys are generated for the Asimov data set A with randomized systematic parameters with correlations taken into account.

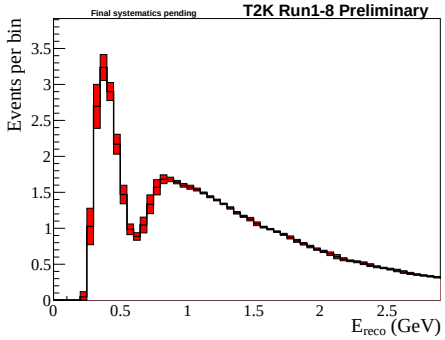

(a) Muon-like, antineutrino mode

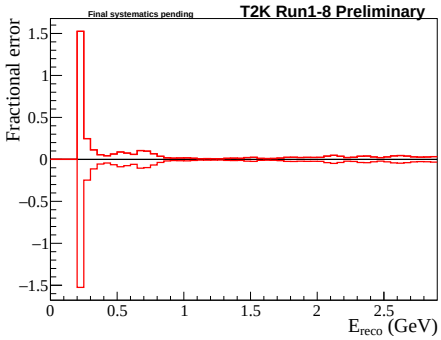

(b) Muon-like, antineutrino mode

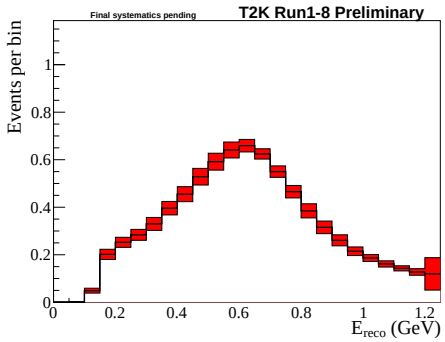

(c) Electron-like antineutrino mode

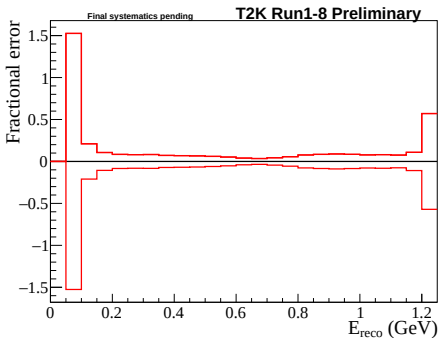

(d) Electron-like antineutrino mode

Figure 5.11: Error envelopes (left) and fractional error (right) for the reconstructed neutrino energy spectrum for Super-K detector systematic parameters. 1×10^4 toys are generated for the Asimov data set A with randomized systematic parameters with correlations taken into account.

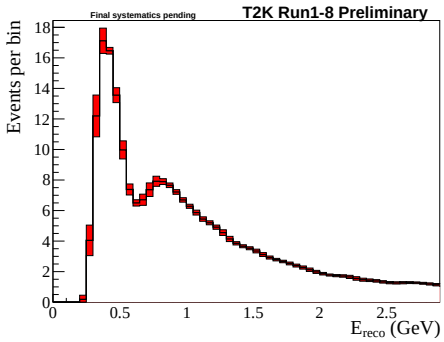

(a) Muon-like, neutrino mode

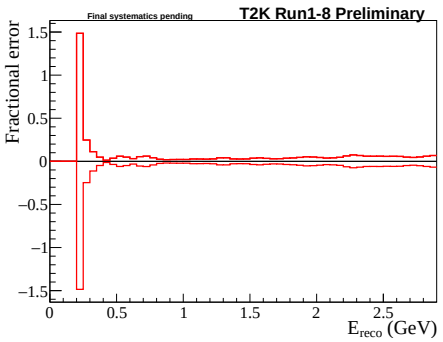

(b) Muon-like, neutrino mode

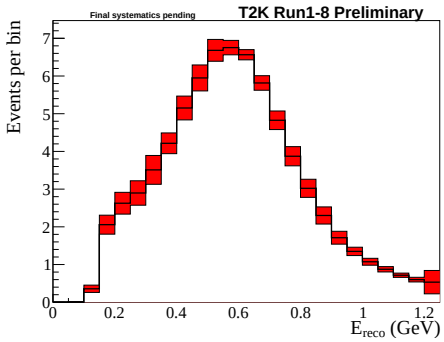

(c) Electron-like, neutrino mode

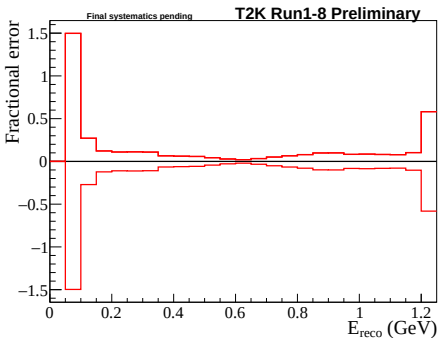

(d) Electron-like, neutrino mode

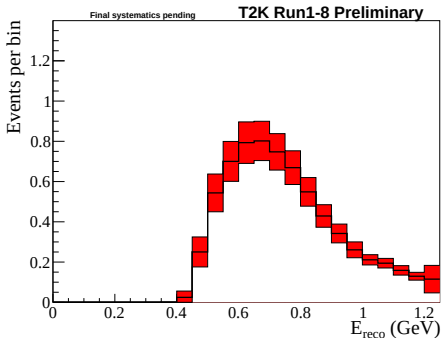

(e) ν_e CC$1\pi^+$-like, neutrino mode

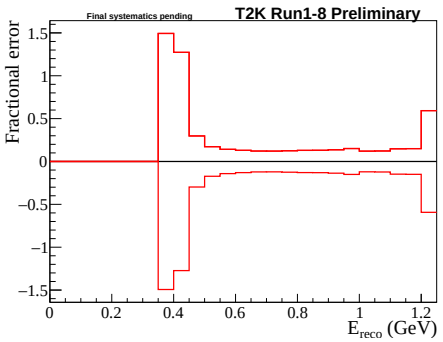

(f) ν_e CC$1\pi^+$-like, neutrino mode

Figure 5.12: Error envelopes (left) and fractional error (right) for the reconstructed neutrino energy spectrum for Super-K FSI+SI+PN systematic parameters. 1×10^4 toys are generated for the Asimov data set A with randomized systematic parameters with correlations taken into account.

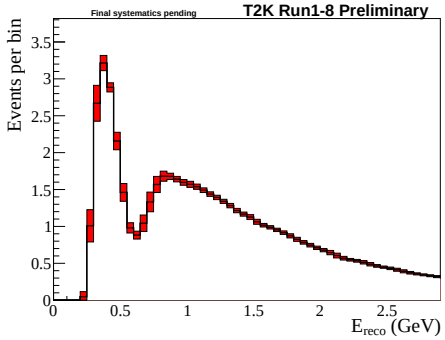

(a) Muon-like, antineutrino mode

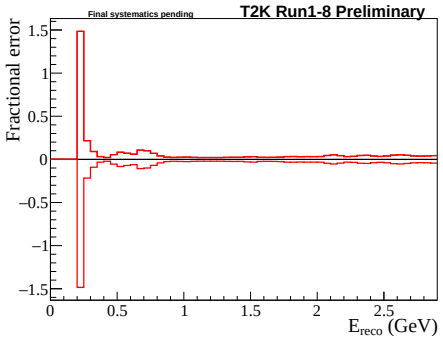

(b) Muon-like, antineutrino mode

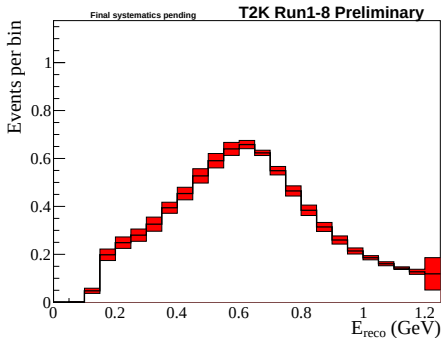

(c) Electron-like antineutrino mode

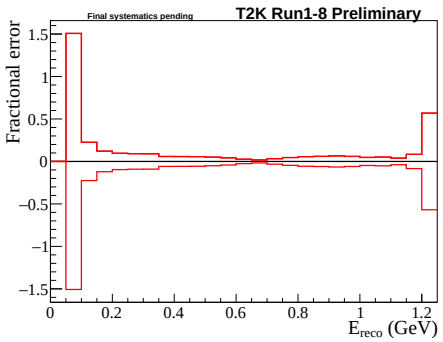

(d) Electron-like antineutrino mode

Figure 5.13: Error envelopes (left) and fractional errors (right) for the reconstructed neutrino energy spectrum for Super-K FSI+SI+PN systematic parameters. 1×10^4 toys are generated for the Asimov data set A with randomized systematic parameters with correlations taken into account.

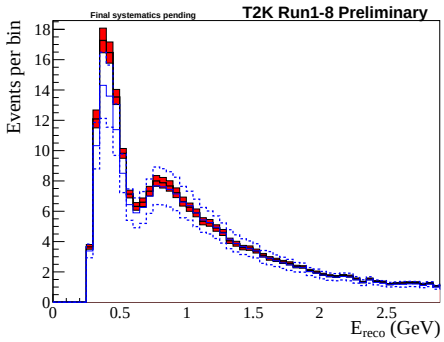

(a) Muon-like, neutrino mode

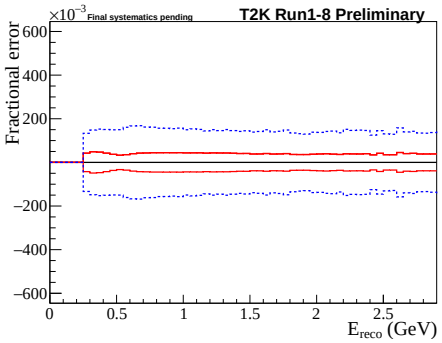

(b) Muon-like, neutrino mode

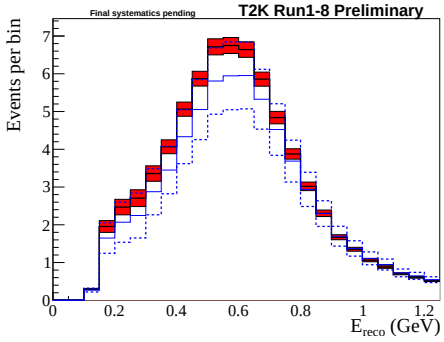

(c) Electron-like, neutrino mode

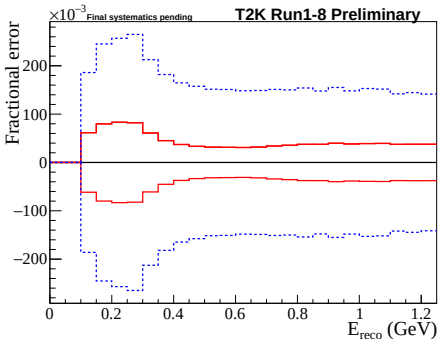

(d) Electron-like, neutrino mode

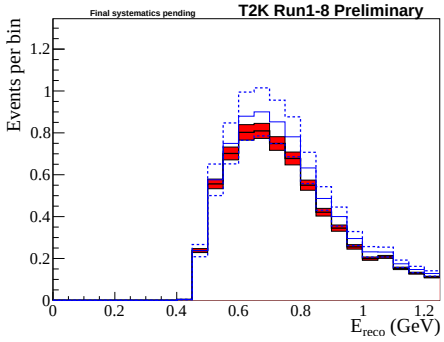

(e) ν_e CC$1\pi^+$-like, neutrino mode

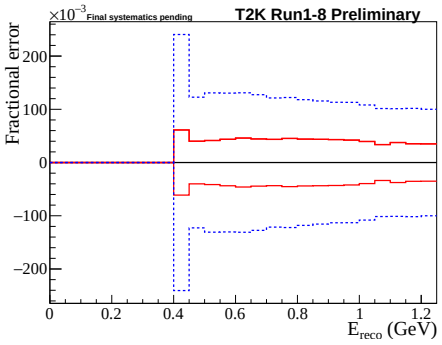

(f) ν_e CC$1\pi^+$-like, neutrino mode

Figure 5.14: Error envelopes (left) and fractional errors (right) for the reconstructed neutrino energy spectrum for the flux and constrained cross-section systematic parameters for pre-BANFF (blue) and post-BANFF (red) errors. 1×10^4 toys are generated for the Asimov data set A with randomized systematic parameters with correlations taken into account.

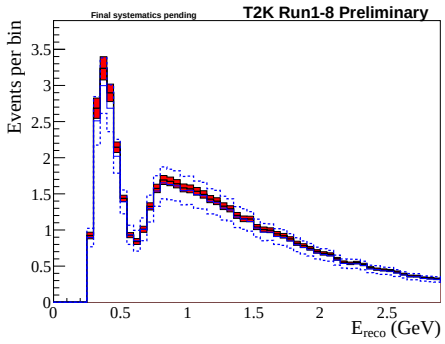

(a) Muon-like, antineutrino mode

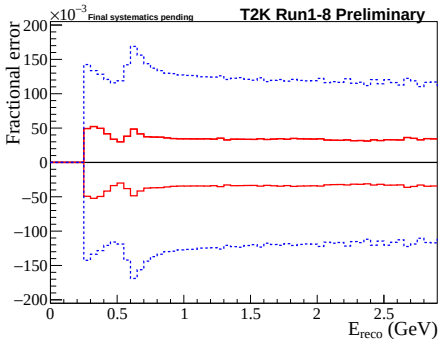

(b) Muon-like, antineutrino mode

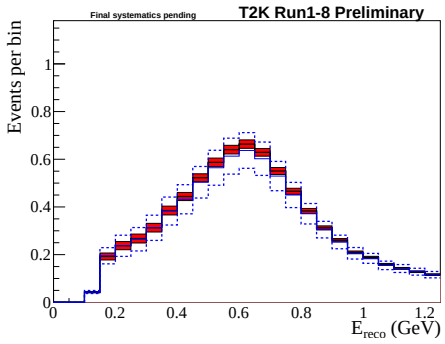

(c) Electron-like antineutrino mode

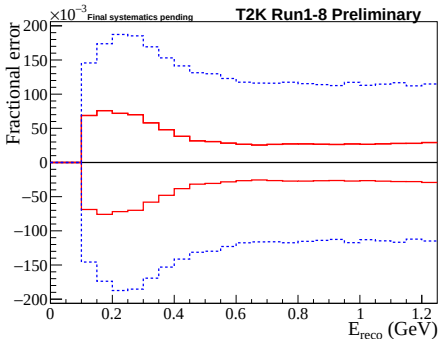

(d) Electron-like antineutrino mode

Figure 5.15: Error envelopes (left) and fractional error (right) for the reconstructed neutrino energy spectrum for the flux and constrained cross-section systematic parameters for pre-BANFF (blue) and post-BANFF (red) errors. 1×10^4 toys are generated for the Asimov data set A with randomized systematic parameters with correlations taken into account.

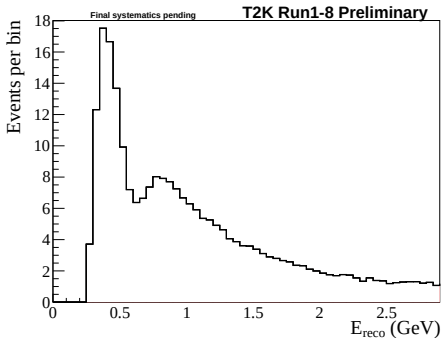

(a) Muon-like, neutrino mode

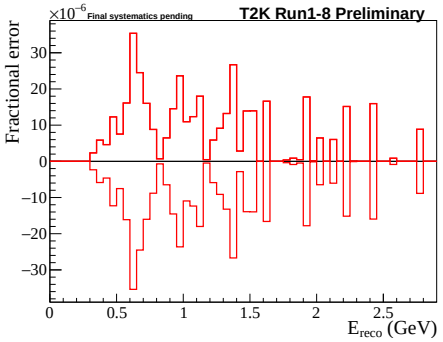

(b) Muon-like, neutrino mode

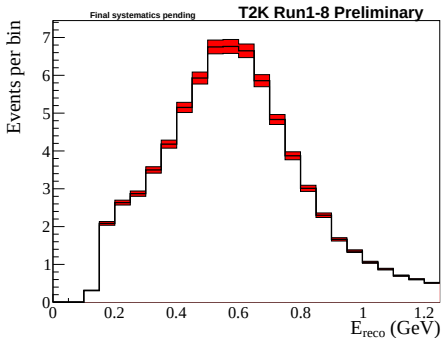

(c) Electron-like, neutrino mode

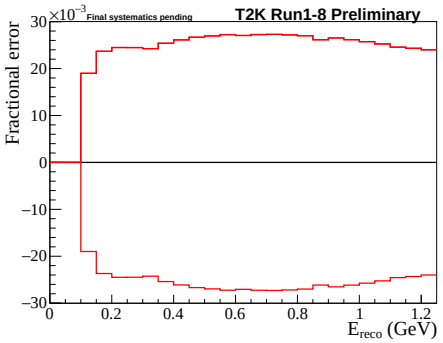

(d) Electron-like, neutrino mode

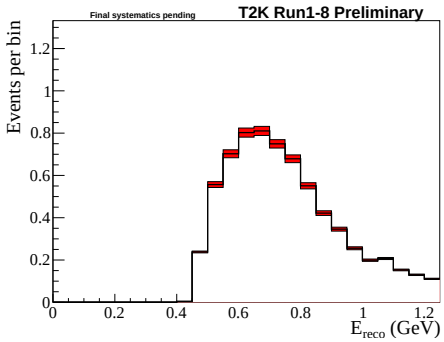

(e) ν_e CC$1\pi^+$-like, neutrino mode

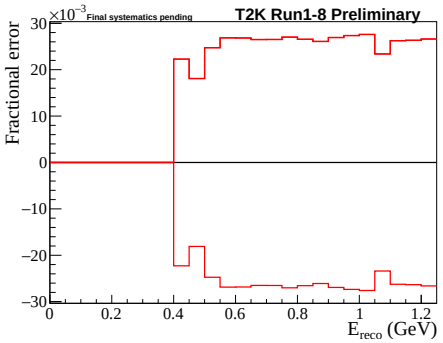

(f) ν_e CC$1\pi^+$-like, neutrino mode

Figure 5.16: Error envelopes (left) and fractional errors (right) for the reconstructed neutrino energy spectrum for the unconstrained electron neutrino cross-section systematic parameters. 1×10^4 toys are generated for the Asimov data set A with randomized systematic parameters with correlations taken into account.

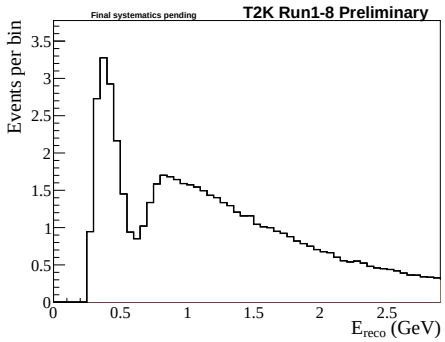

(a) Muon-like, antineutrino mode

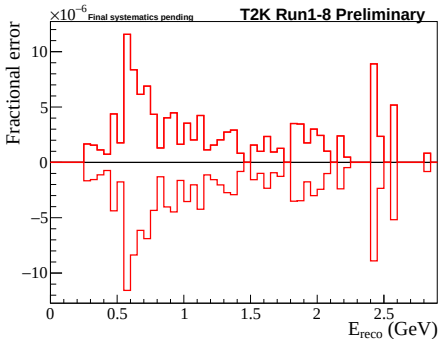

(b) Muon-like, antineutrino mode

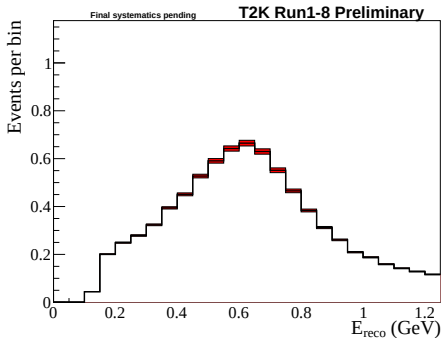

(c) Electron-like antineutrino mode

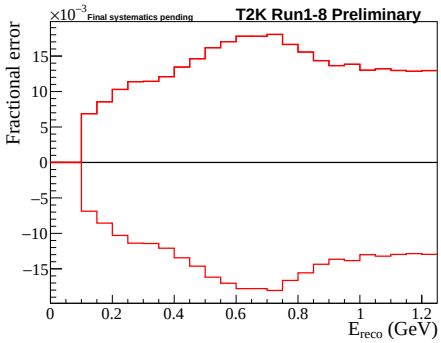

(d) Electron-like antineutrino mode

Figure 5.17: Error envelopes (left) and fractional errors (right) for the reconstructed neutrino energy spectrum for the unconstrained electron neutrino cross-section systematic parameters. 1×10^4 toys are generated for the Asimov data set A with randomized systematic parameters with correlations taken into account.

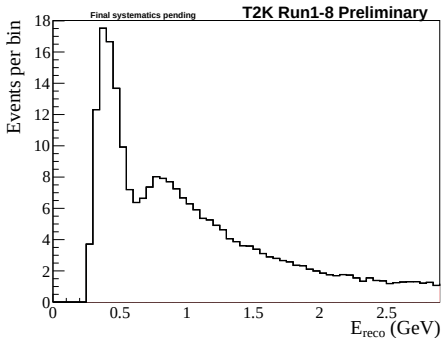

(a) Muon-like, neutrino mode

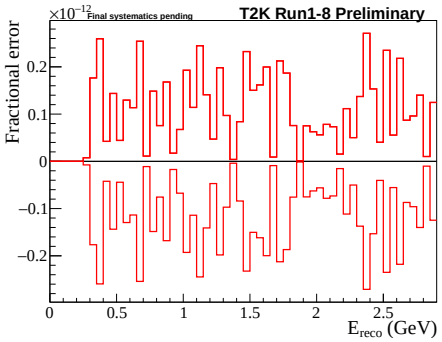

(b) Muon-like, neutrino mode

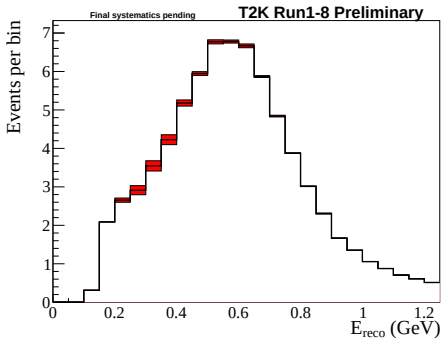

(c) Electron-like, neutrino mode

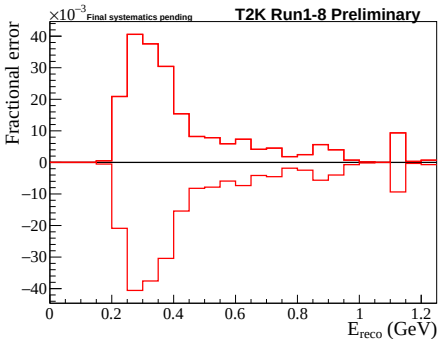

(d) Electron-like, neutrino mode

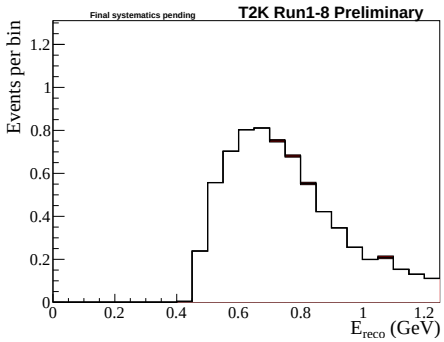

(e) ν_e CC$1\pi^+$-like, neutrino mode

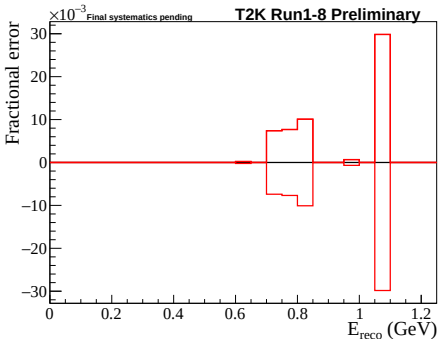

(f) ν_e CC$1\pi^+$-like, neutrino mode

Figure 5.18: Error envelopes (left) and fractional error (right) for the reconstructed neutrino energy spectrum for the unconstrained NC1γ systematic parameters. 1×10^4 toys are generated for the Asimov data set A with randomized systematic parameters with correlations taken into account.

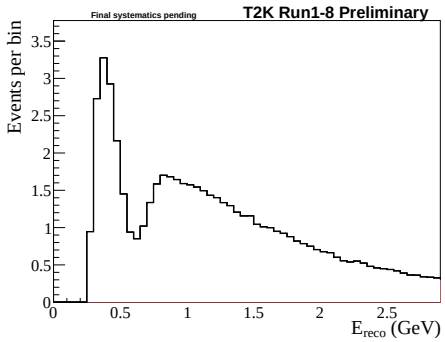

(a) Muon-like, antineutrino mode

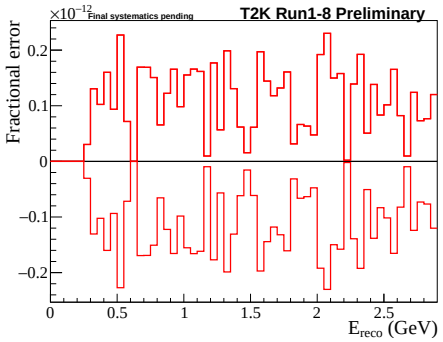

(b) Muon-like, antineutrino mode

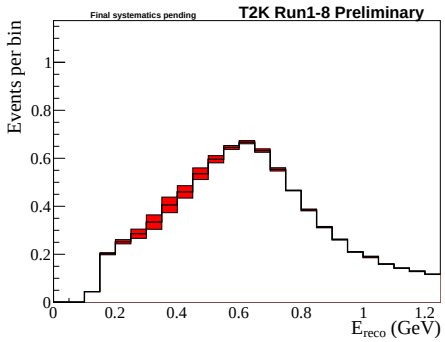

(c) Electron-like antineutrino mode

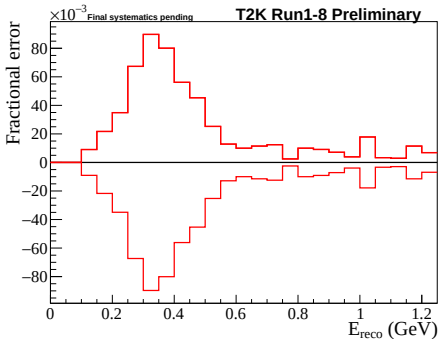

(d) Electron-like antineutrino mode

Figure 5.19: Error envelopes (left) and fractional errors (right) for the reconstructed neutrino energy spectrum for the unconstrained NC1γ systematic parameters. 1×10^4 toys are generated for the Asimov data set A with randomized systematic parameters with correlations taken into account.

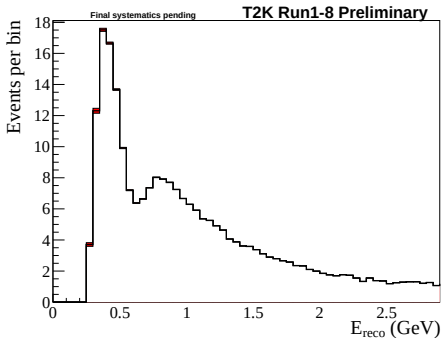

(a) Muon-like, neutrino mode

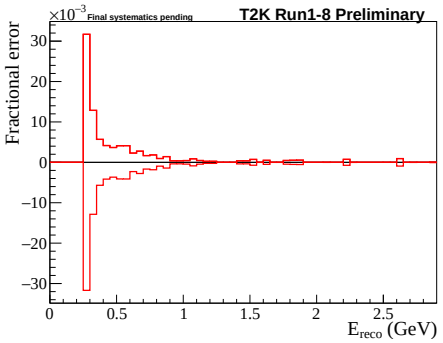

(b) Muon-like, neutrino mode

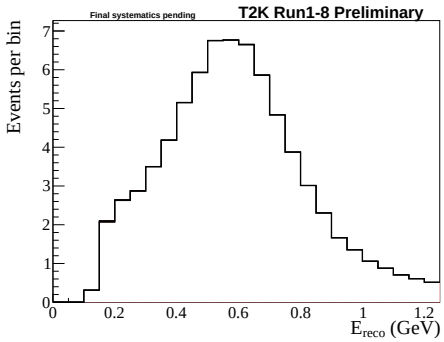

(c) Electron-like, neutrino mode

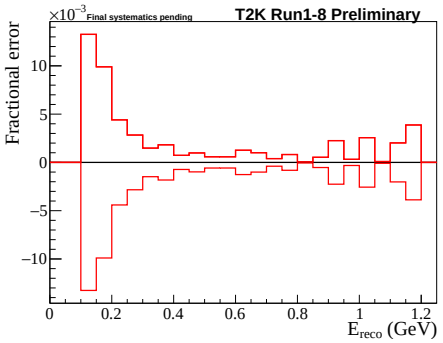

(d) Electron-like, neutrino mode

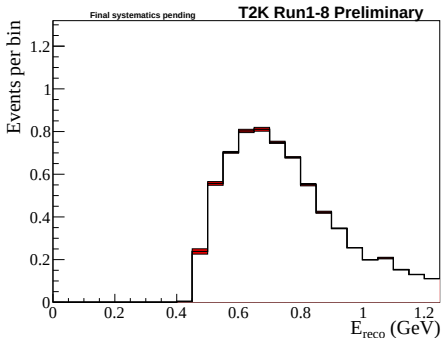

(e) ν_e CC$1\pi^+$-like, neutrino mode

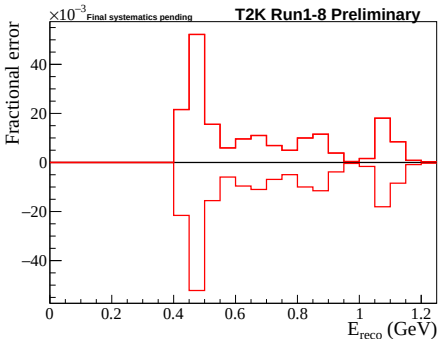

(f) ν_e CC$1\pi^+$-like, neutrino mode

Figure 5.20: Error envelopes (left) and fractional errors (right) for the reconstructed neutrino energy spectrum for the unconstrained NCother systematic parameters. 1×10^4 toys are generated for the Asimov data set A with randomized systematic parameters with correlations taken into account.

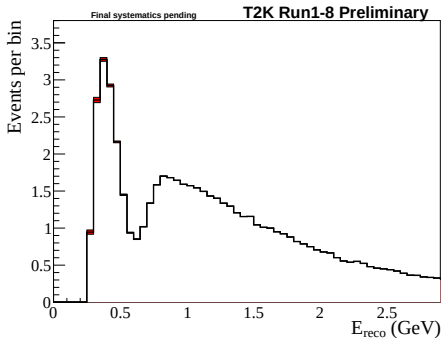

(a) Muon-like, antineutrino mode

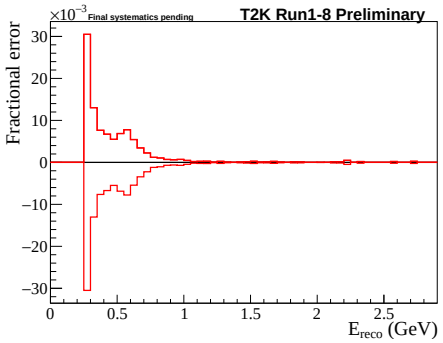

(b) Muon-like, antineutrino mode

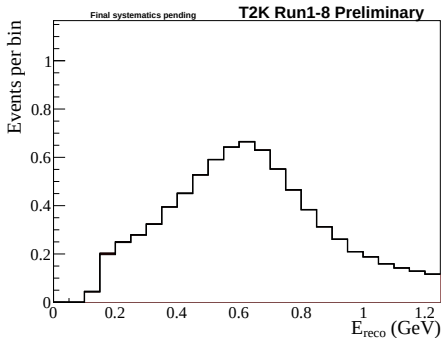

(c) Electron-like antineutrino mode

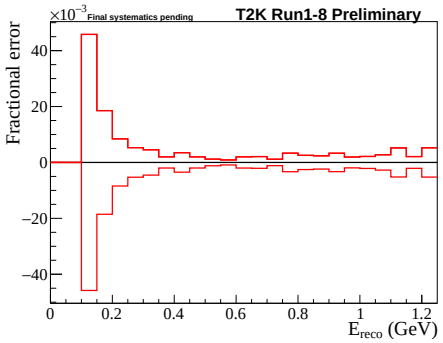

(d) Electron-like antineutrino mode

Figure 5.21: Error envelopes (left) and fractional errors (right) for the reconstructed neutrino energy spectrum for the unconstrained NCother systematic parameters. 1×10^4 toys are generated for the Asimov data set A with randomized systematic parameters with correlations taken into account.

5.6 Expected Sensitivity studies

To determine the sensitivity of the analysis a number of fits were performed using Asimov data set A and B, the contours for which indicate the ability of the analysis to measure the oscillation parameters in the absence of statistical fluctuations and under the assumption that their true values correspond to the Asimov A (or B) values. Fits of single parameters are performed for each of $\sin^2\theta_{13}$, δ_{CP}, $\sin^2\theta_{23}$ and Δm^2_{32}, with two-dimensional fits being performed for δ_{CP} vs $\sin^2\theta_{13}$ and Δm^2_{32} vs $\sin^2\theta_{23}$. Fits are performed for each of normal and inverted hierarchy, and also with and without the reactor constraint on $\sin^2\theta_{13}$.

5.6.1 Results for Asimov sets A and B

5.6.1.1 Results for δ_{CP} vs $\sin^2\theta_{13}$

In fig. 5.22 the sensitivity to δ_{CP} vs $\sin^2\theta_{13}$ with reactor constraint and T2K only is shown for the Asimov data sets A and B. Note that in the Asimov B case it can be seen that the best-fit point is shifted away from the true δ_{CP} value of zero towards $-\pi$. In addition to best-fit points being moved from the true value due to marginalisation of oscillation and systematic parameters there are additional contributing effects. There is a lack of sensitivity to distinguish $\delta_{CP} = 0$ and $\delta_{CP} = \pi$ due to the spectra for $\delta_{CP} = 0$ in inverted hierarchy being similar to the spectra for $\delta_{CP} = \pi$ in normal hierarchy and vice versa (see fig. G.1 in appendix G), leading to similar $\Delta\chi^2$ values for the two points. This can be seen in fig. 5.24(c) and fig. 5.24(d), with the difference in $\Delta\chi^2_{true}$ and $\Delta\chi^2_{best-fit}$ being only ~ 0.2. Furthermore, degeneracy between δ_{CP} and mass hierarchy can cause $\delta_{CP} = 0$ to behave more like $\delta_{CP} = \pi/2$ in inverted hierarchy, and more like $\delta_{CP} = -\pi/2$ in normal hierarchy, shifting the best-fit for inverted hierarchy away from zero to a value between $-\pi$ and $-\pi/2$.

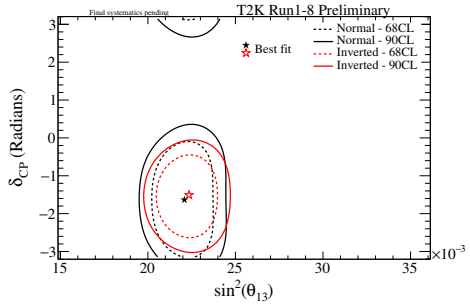

(a) Asimov A δ_{CP} vs $\sin^2\theta_{13}$ with reactor constraint

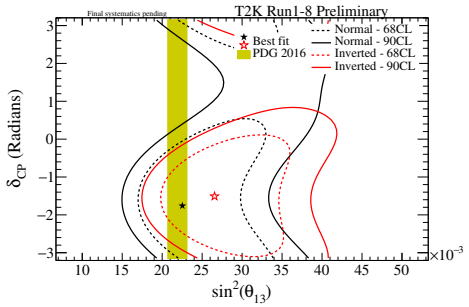

(b) Asimov A δ_{CP} vs $\sin^2\theta_{13}$ T2K only

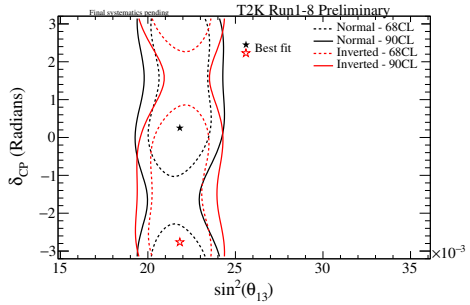

(c) Asimov B δ_{CP} vs $\sin^2\theta_{13}$ with reactor constraint

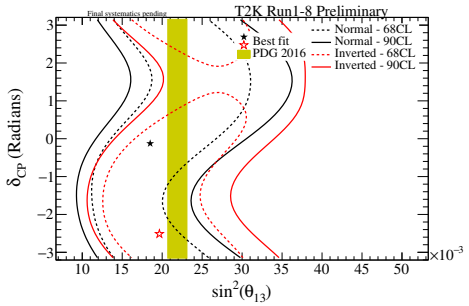

(d) Asimov B δ_{CP} vs $\sin^2\theta_{13}$ T2K only

Figure 5.22: Contours at 68% and 90% CL for δ_{CP} vs $\sin^2\theta_{13}$ with and without reactor constraint for Asimov data sets A and B. Normal and inverted hierarchy contours are independent. All 5 samples were used to produce these fits.

5.6.1.2 Results for Δm^2_{32} vs $\sin^2\theta_{23}$

The sensitivity to Δm^2_{32} vs $\sin^2\theta_{23}$ with reactor constraint and T2K only is shown for the Asimov data sets A and B in fig. 5.23.

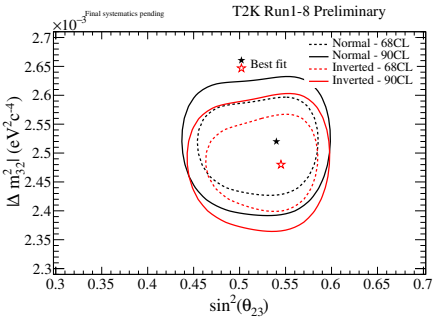

(a) Asimov A Δm^2_{32} vs $\sin^2\theta_{23}$ with reactor constraint

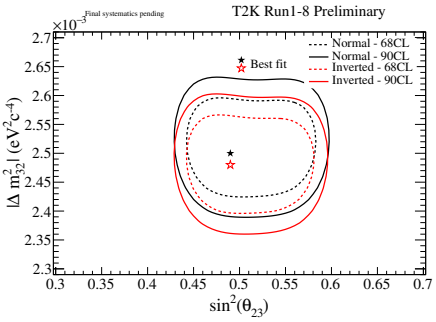

(b) Asimov A Δm^2_{32} vs $\sin^2\theta_{23}$ T2K only

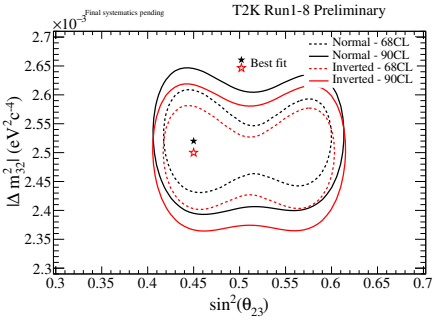

(c) Asimov B Δm^2_{32} vs $\sin^2\theta_{23}$ with reactor constraint

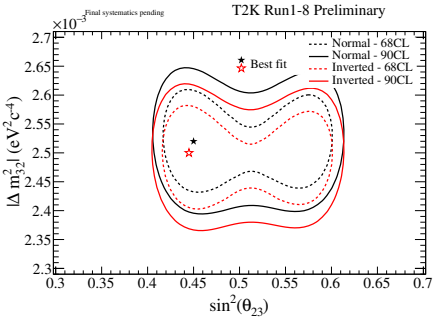

(d) Asimov B Δm^2_{32} vs $\sin^2\theta_{23}$ T2K only

Figure 5.23: Contours at 68% and 90% CL for Δm^2_{32} vs $\sin^2\theta_{23}$ with and without reactor constraint for Asimov data sets A and B. Normal and inverted hierarchy contours are independent. All 5 samples were used to produce these fits.

5.6.1.3 Results for δ_{CP}

The sensitivity to δ_{CP} with reactor constraint and T2K only is shown for the Asimov data sets A and B in fig. 5.24.

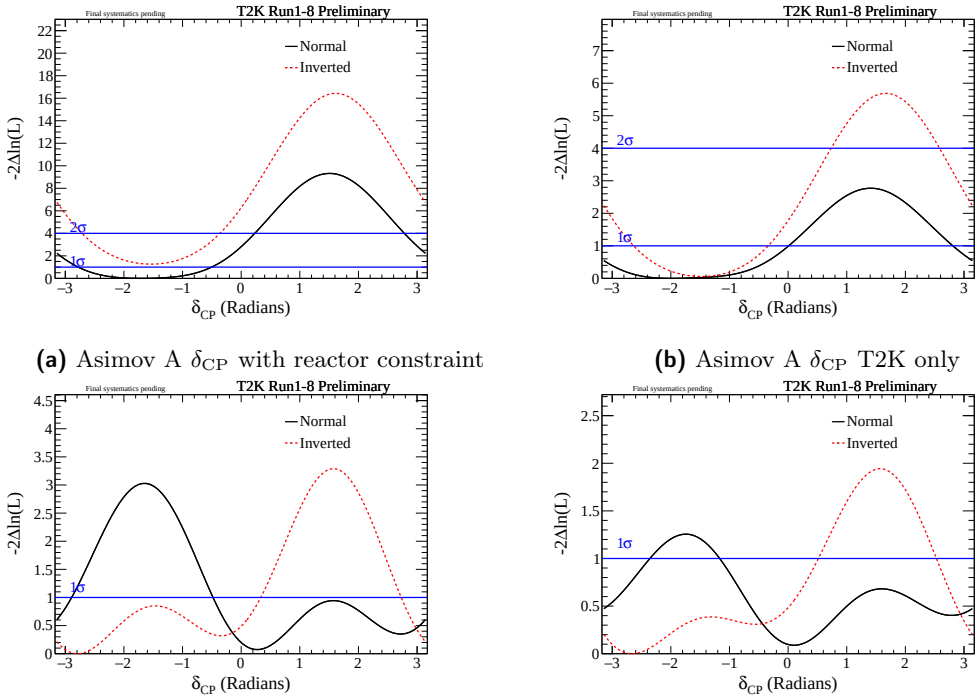

(a) Asimov A δ_{CP} with reactor constraint

(b) Asimov A δ_{CP} T2K only

(c) Asimov B δ_{CP} with reactor constraint

(d) Asimov B δ_{CP} T2K only

Figure 5.24: The expected $\Delta\chi^2$ distribution as a function of δ_{CP} with and without reactor constraint for Asimov data sets A and B. The mass hierarchy is minimized, with normal and inverted hierarchy $\Delta\chi^2$ distributions shifted to the same global best-fit χ^2 value, which is taken to be the minimum between normal and inverted hierarchy. All 5 samples were used to produce these fits.

5.6.1.4 Results for $\sin^2\theta_{13}$

The sensitivity to $\sin^2\theta_{13}$ (without reactor constraint) is shown for the Asimov data sets A and B in fig. 5.25.

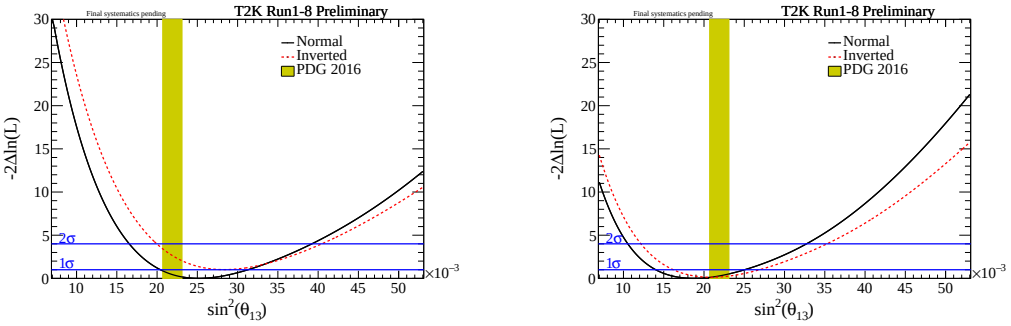

(a) Asimov A $\sin^2\theta_{13}$ T2K only

(b) Asimov B $\sin^2\theta_{13}$ T2K only

Figure 5.25: The expected $\Delta\chi^2$ distribution as a function of $\sin^2\theta_{13}$ without reactor constraint for Asimov data sets A and B. The mass hierarchy is minimized, with normal and inverted hierarchy $\Delta\chi^2$ distributions shifted to the same global best-fit χ^2 value, which is taken to be the minimum between normal and inverted hierarchy. All 5 samples were used to produce these fits.

5.6.1.5 Results for $\sin^2\theta_{23}$

The sensitivity to $\sin^2\theta_{23}$ with reactor constraint and T2K only is shown for the Asimov data sets A and B in fig. 5.26.

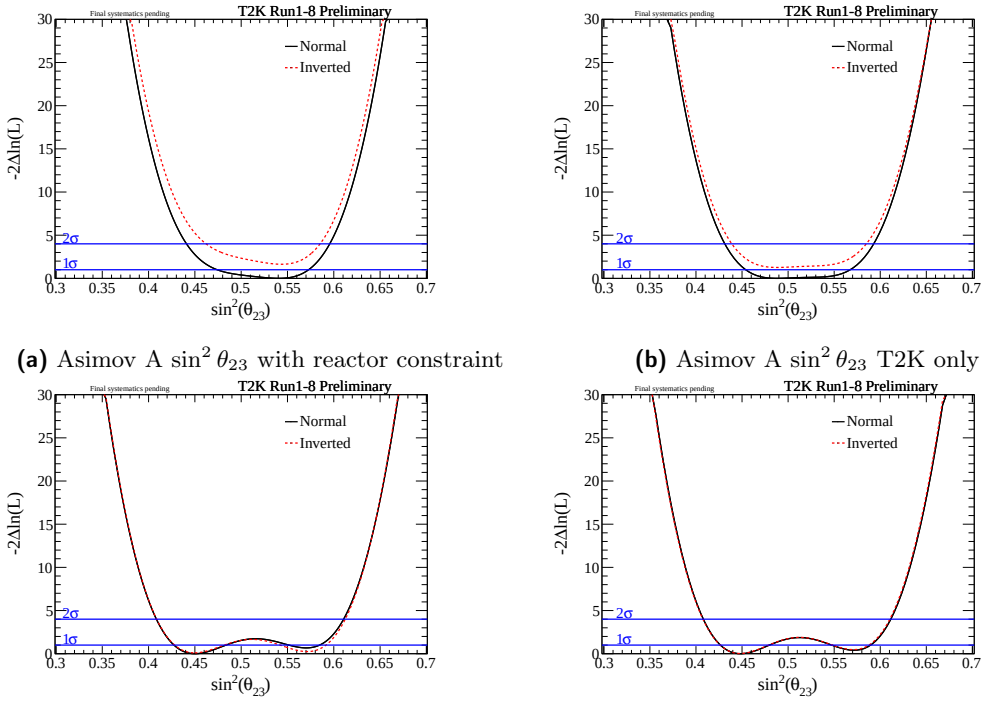

(a) Asimov A $\sin^2\theta_{23}$ with reactor constraint

(b) Asimov A $\sin^2\theta_{23}$ T2K only

(c) Asimov B $\sin^2\theta_{23}$ with reactor constraint

(d) Asimov B $\sin^2\theta_{23}$ T2K only

Figure 5.26: The expected $\Delta\chi^2$ distribution as a function of $\sin^2\theta_{23}$ with and without reactor constraint for Asimov data sets A and B. The mass hierarchy is minimized, with normal and inverted hierarchy $\Delta\chi^2$ distributions shifted to the same global best-fit χ^2 value, which is taken to be the minimum between normal and inverted hierarchy. All 5 samples were used to produce these fits.

5.6.1.6 Results for Δm^2_{32}

The sensitivity to Δm^2_{32} with reactor constraint and T2K only is shown for the Asimov data sets A and B in fig. 5.27.

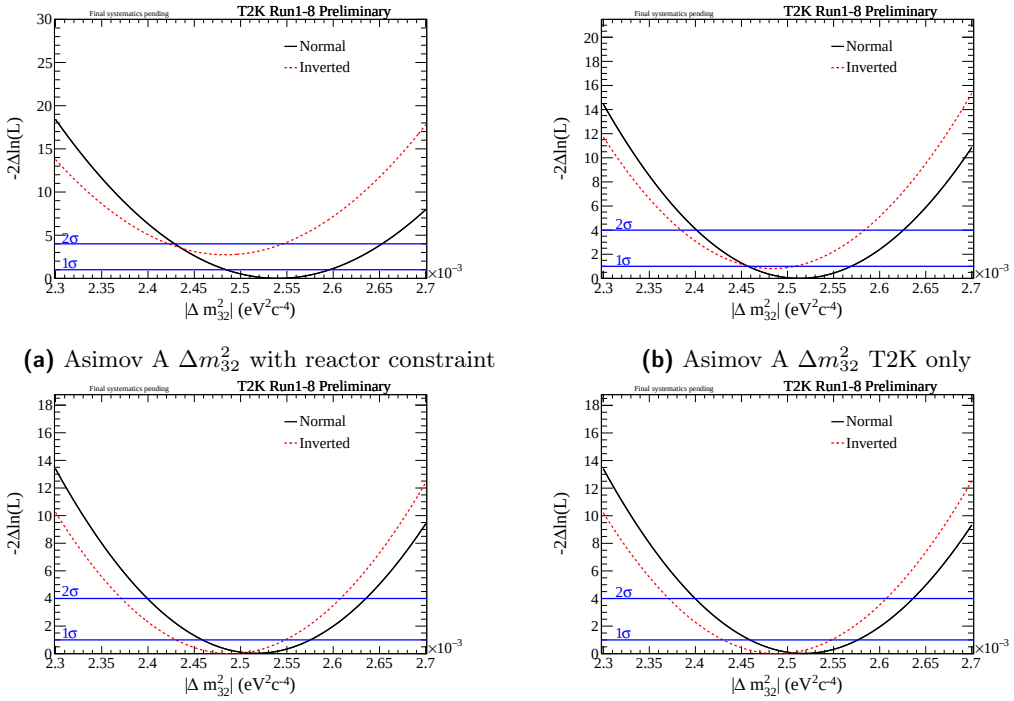

(a) Asimov A Δm^2_{32} with reactor constraint

(b) Asimov A Δm^2_{32} T2K only

(c) Asimov B Δm^2_{32} with reactor constraint

(d) Asimov B Δm^2_{32} T2K only

Figure 5.27: The expected $\Delta\chi^2$ distribution as a function of Δm^2_{32} with and without reactor constraint for Asimov data sets A and B. The mass hierarchy is minimized, with normal and inverted hierarchy $\Delta\chi^2$ distributions shifted to the same global best-fit χ^2 value, which is taken to be the minimum between normal and inverted hierarchy. All 5 samples were used to produce these fits.

5.7 Results of the $\nu\bar{\nu}$ joint analysis with the Run 1-8 dataset

The results of the Run 1-8 data set fit, for an exposure of 1.4734×10^{21}POT in neutrino mode and of 7.558×10^{20}POT in antineutrino mode, are shown in this chapter. In fig. 5.28 the predicted spectra of μ-like and e-like samples are compared to the observed data. In table 5.14 the expected and observed number of events in Run 1-8 data set are shown. The predicted number of events are shown for the oscillation parameters of Asimov data sets A and B. The comparison of the confidence intervals obtained by the fit of the Run 1-8 data set among all the oscillation analysis groups is shown in [207].

The predicted and observed spectra are shown for each of the samples in fig. 5.28. The e-like samples are broken down into E_{rec} and θ projections in fig. 5.29.

Beam mode	Sample	Exp. Asimov A	Exp. Asimov A ($\delta_{CP} = 0$)	Exp. Asimov B	Exp. Not Osc	Observed
ν	μ-like	268.415	268.053	280.994	1209.918	240
ν	e-like	73.476	61.434	54.684	15.356	74
$\bar{\nu}$	μ-like	64.278	64.123	66.010	211.548	68
$\bar{\nu}$	e-like	7.911	9.023	8.187	3.243	7
ν	ν_e CC1π^+-like	6.919	6.009	5.389	2.543	15

Table 5.14: The observed, expected and best-fit number of events in Run 1-8 data set for an exposure ofx 1.4734×10^{21} POT in neutrino mode and of 7.558×10^{20} POT in antineutrino mode are shown for each selected sample. The prediction is produced using the BANFF tuning and the oscillation parameters shown in table 5.1.

Beam mode	Sample	Exp. Best-fit ($\delta_{CP} = -1.883$)	Exp. Best-fit ($\delta_{CP} = -\pi/2$)	Exp. Best-Fit ($\delta_{CP} = 0$)	Exp. Best-Fit ($\delta_{CP} = \pi/2$)	Exp. Best-Fit ($\delta_{CP} = \pi$)	Observed
ν	μ-like	270.824	270.634	269.953	270.60058	271.396	240
ν	e-like	86.513	86.962	73.734	60.527	73.754	74
$\bar{\nu}$	μ-like	64.996	64.940	64.739	64.941	65.159	68
$\bar{\nu}$	e-like	9.309	9.2918	10.576	11.678	10.394	7
ν	ν_e CC1π^+-like	8.045	8.125	7.137	5.838	6.826	15

Table 5.15: The observed and number of events for the NH best fit values of the oscillation parameters in Run 1-8 data set for an exposure of 1.4734×10^{21} POT in neutrino mode and of 7.558×10^{20} POT in antineutrino mode are shown for each selected sample. The prediction is produced using the BANFF tuning and the oscillation parameters shown in table 5.16.

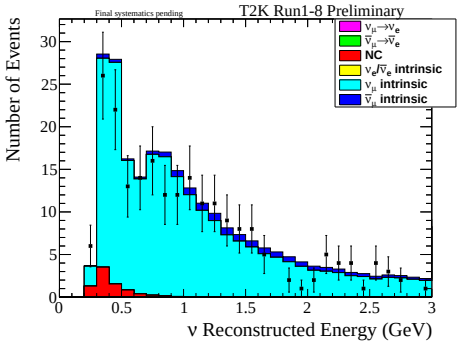

(a) Muon-like, neutrino mode

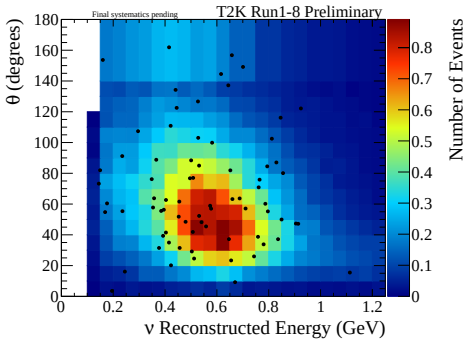

(b) Electron-like, neutrino mode

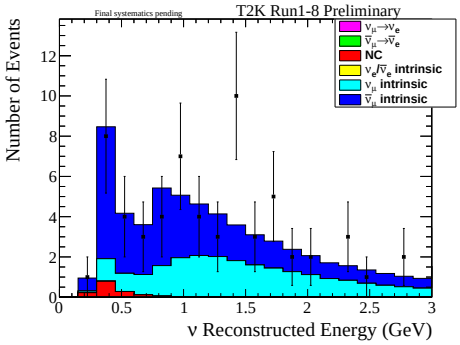

(c) Muon-like, antineutrino mode

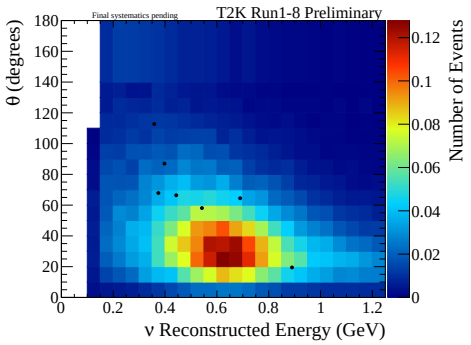

(d) Electron-like antineutrino mode

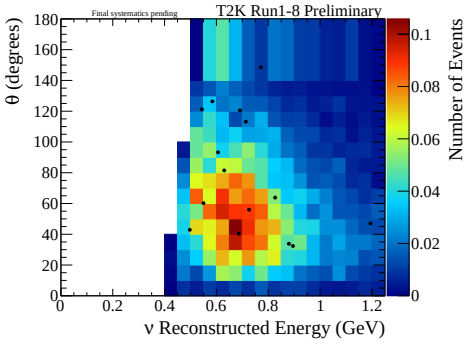

(e) ν_e CC1π^+-like, neutrino mode

Figure 5.28: Predicted spectra and observed events (points). μ-like distributions are a function of the reconstructed neutrino energy, while the e-like, including ν_e CC1π^+, distributions are functions of both the reconstructed neutrino energy and the reconstructed angle between the outgoing lepton and the neutrino direction. The distributions correspond to the statistics collected in the full Run 1-8 data set. The spectra are generated with the systematic parameters described in section 5.5 and the oscillation parameters corresponding to the best-fit values from the data fit (solar parameters at PDG 2016).

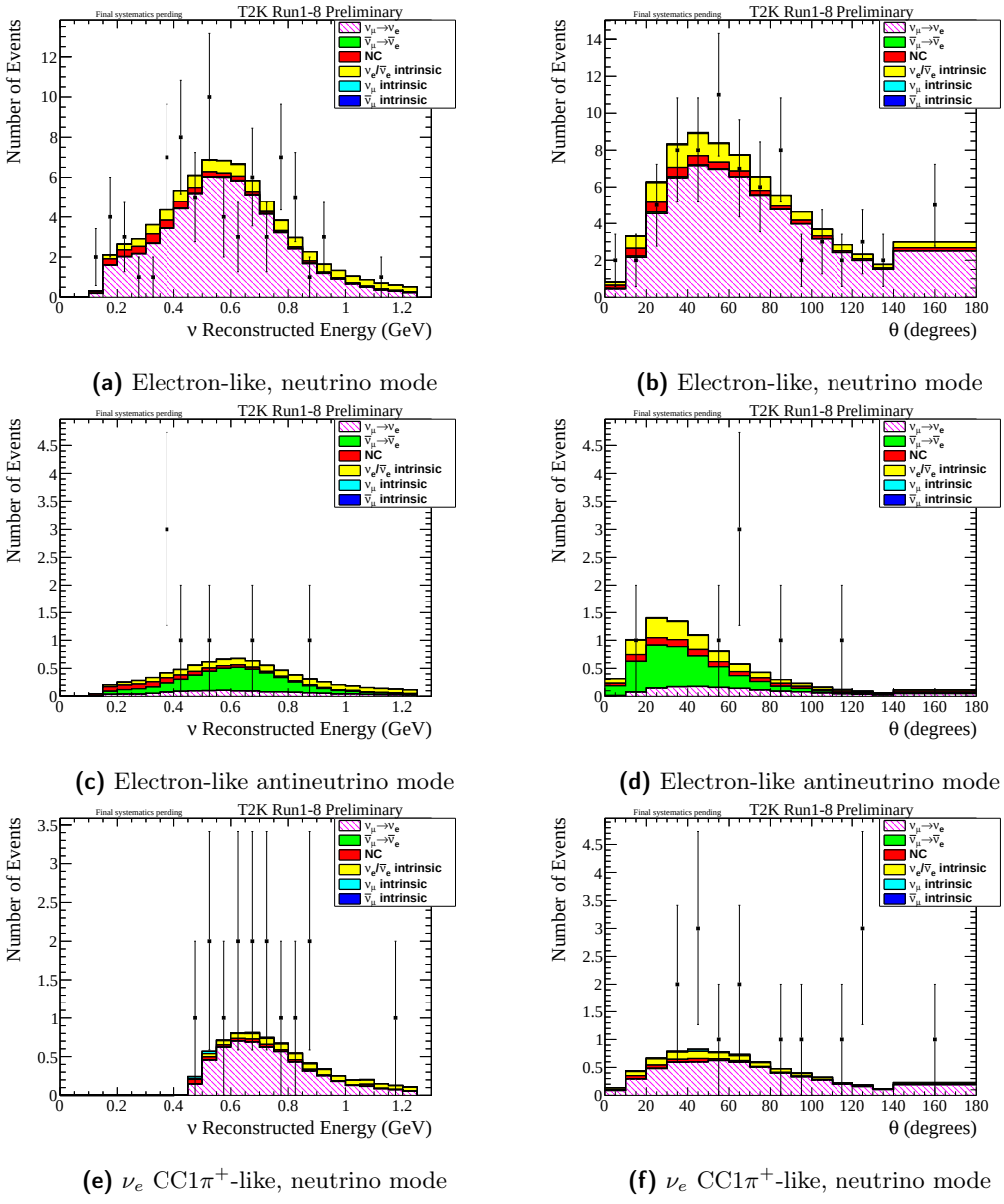

(a) Electron-like, neutrino mode

(b) Electron-like, neutrino mode

(c) Electron-like antineutrino mode

(d) Electron-like antineutrino mode

(e) ν_e CC1π^+-like, neutrino mode

(f) ν_e CC1π^+-like, neutrino mode

Figure 5.29: Predicted spectra and observed events (points). The e-like, including ν_e CC1π^+, distributions are functions of both the reconstructed neutrino energy and the reconstructed angle between the outgoing lepton and the neutrino direction, with the projections in each variable shown here. The distributions correspond to the statistics collected in the full Run 1-8 data set. The spectra are generated with the systematic parameters described in section 5.5 and the oscillation parameters corresponding to the best-fit values from the data fit (solar parameters at PDG 2016).

Parameter	Reactor	Best-fit (NH)	$\pm1\sigma$ (NH)	Best-fit (IH)	$\pm1\sigma$ (IH)
δ_{CP}	Yes	-1.833	[-2.476,-1.151]	-1.374	[-1.947,-0.886]
δ_{CP}	No	-2.083	[-2.972,-1.151]	-1.157	[-1.965,-0.403]
$\sin^2\theta_{13}$	No	0.0277	[0.0230,0.0331]	0.0331	[0.0265,0.0378]
$\sin^2\theta_{23}$	Yes	0.530	[0.493,0.561]	0.530	[0.496,0.559]
Δm^2_{32} or Δm^2_{13} (10^{-3} eV^2/c^4)	Yes	2.462	[2.407,2.519]	2.436	[2.383,2.491]

Table 5.16: The Run 1-8 measured oscillation parameter best-fit and the $\pm1\sigma$ intervals are shown for normal and inverted hierarchies with respect to the hierarchy best-fit. The $\pm1\sigma$ interval is obtained by using the constant $\Delta\chi^2$ method. For each parameter normal hierarchy is the global best-fit.

The best-fit values and 1σ ranges for each oscillation parameter are shown in table 5.16 for normal hierarchy (which is preferred in all data fits). The 1σ ranges are extracted for each oscillation parameter from the 1-dimensional $\Delta\chi^2$ distributions shown in figs. 5.32 to 5.35.

The 1-dimensional contours are plotted with respect to the global minimum from normal and inverted hierarchies, while the 2-dimensional confidence intervals are shown drawing the normal and inverted hierarchy contours independently, i.e. each contour is produced with respect to the global minimum under that hierarchy hypothesis.

5.7.1 Results for δ_{CP} vs $\sin^2\theta_{13}$

In fig. 5.30 the result for δ_{CP} vs $\sin^2\theta_{13}$ with reactor constraint and T2K only is shown. The fit shows agreement with the reactor constraint with further discussion in section 5.7.8. The 1D projection of $\sin^2\theta_{13}$ is shown in section 5.7.4 and for δ_{CP} in section 5.7.3.

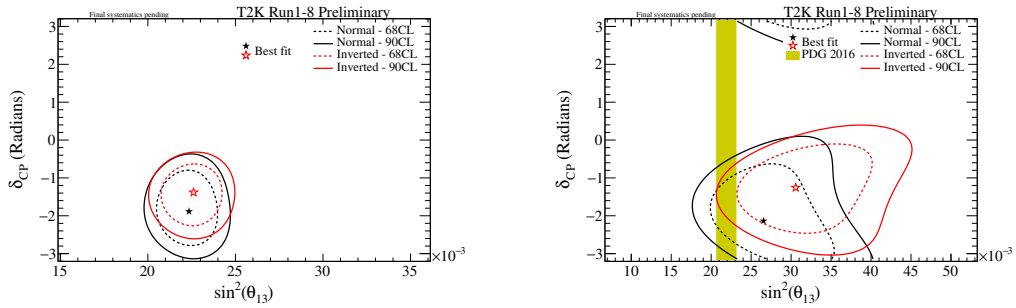

(a) δ_{CP} vs $\sin^2\theta_{13}$ with reactor constraint

(b) δ_{CP} vs $\sin^2\theta_{13}$ T2K only

Figure 5.30: Contours at 68% and 90% CL for δ_{CP} vs $\sin^2\theta_{13}$ with and without reactor constraint. Normal and inverted hierarchy contours are independent. All 5 samples were used to produce these fits.

5.7.2 Results for Δm^2_{32} vs $\sin^2\theta_{23}$

The result for Δm^2_{32} vs $\sin^2\theta_{23}$ with reactor constraint and T2K only is shown in fig. 5.31. The parameter $\sin^2\theta_{23}$ is shown in section 5.7.5, and Δm^2_{32} in section 5.7.6. Results are further discussed in section 5.7.8

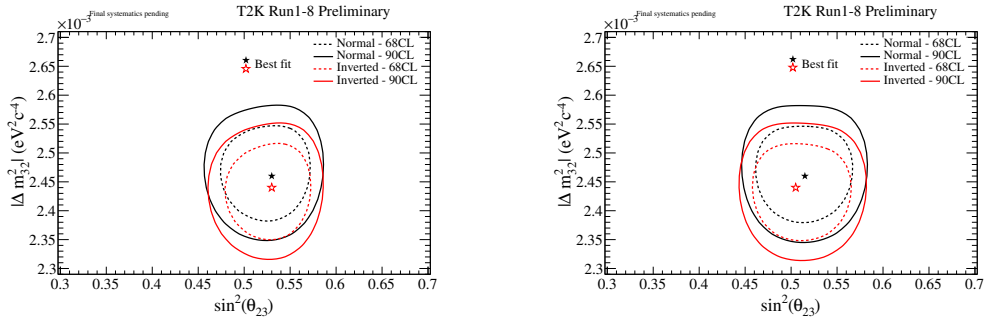

(a) Δm^2_{32} vs $\sin^2\theta_{23}$ with reactor constraint

(b) Δm^2_{32} vs $\sin^2\theta_{23}$ T2K only

Figure 5.31: Contours at 68% and 90% CL for Δm^2_{32} vs $\sin^2\theta_{23}$ with and without reactor constraint. Normal and inverted hierarchy contours are independent. All 5 samples were used to produce these fits.

5.7.3 Results for δ_{CP}

The result for δ_{CP} with reactor constraint and T2K only is shown in fig. 5.32. A stronger than expected constraint is observed based on the Asimov A data set, this is further discussed in section 5.7.8, and studies performed to understand the sensitivity in section 5.7.9.

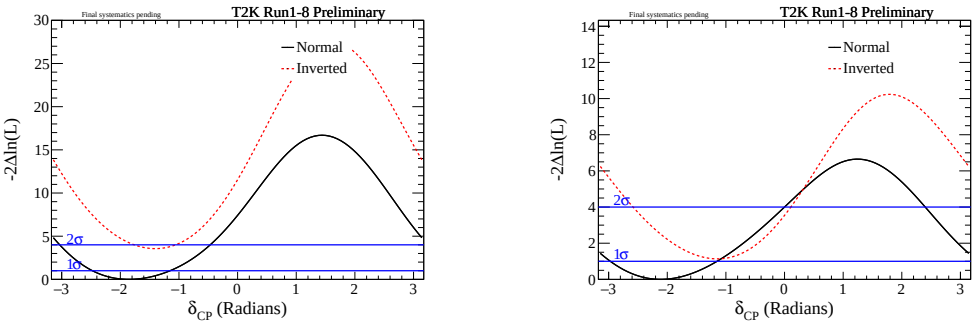

(a) δ_{CP} with reactor constraint

(b) δ_{CP} T2K only

Figure 5.32: The expected $\Delta\chi^2$ distribution as a function of δ_{CP} with and without reactor constraint. The mass hierarchy is minimized, with normal and inverted hierarchy $\Delta\chi^2$ distributions shifted to the same global best-fit χ^2 value, which is taken to be the minimum between normal and inverted hierarchy. All 5 samples were used to produce these fits.

5.7.4 Results for $\sin^2\theta_{13}$

The result for $\sin^2\theta_{13}$ (without reactor constraint) is shown in fig. 5.33.

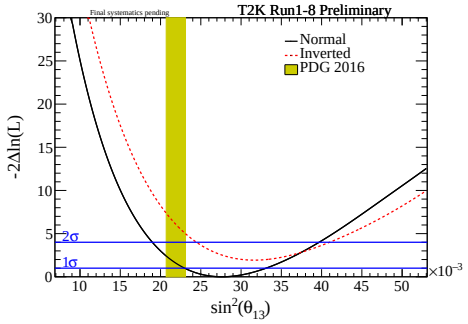

(a) $\sin^2\theta_{13}$ T2K only

Figure 5.33: The expected $\Delta\chi^2$ distribution as a function of $\sin^2\theta_{13}$ without reactor constraint. The mass hierarchy is minimized, with normal and inverted hierarchy $\Delta\chi^2$ distributions shifted to the same global best-fit χ^2 value, which is taken to be the minimum between normal and inverted hierarchy. All 5 samples were used to produce these fits.

5.7.5 Results for $\sin^2\theta_{23}$

The result for $\sin^2\theta_{23}$ with reactor constraint and T2K only is shown in fig. 5.34. To understand the stronger than expected constraint from the data fit studies described in section 5.7.10 were carried out.

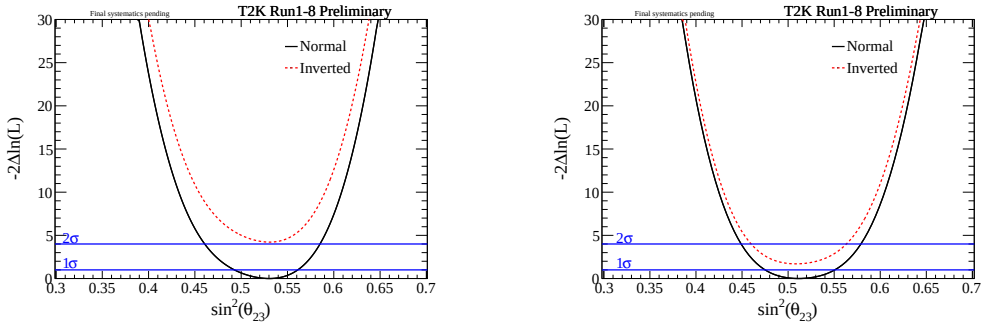

(a) $\sin^2\theta_{23}$ with reactor constraint

(b) $\sin^2\theta_{23}$ T2K only

Figure 5.34: The expected $\Delta\chi^2$ distribution as a function of $\sin^2\theta_{23}$ with and without reactor constraint. The mass hierarchy is minimized, with normal and inverted hierarchy $\Delta\chi^2$ distributions shifted to the same global best-fit χ^2 value, which is taken to be the minimum between normal and inverted hierarchy. All 5 samples were used to produce these fits.

5.7.6 Results for Δm^2_{32}

The result for Δm^2_{32} with reactor constraint and T2K only is shown in fig. 5.35. To understand the constraint compared with the data fit studies described in section 5.7.10 were carried out.

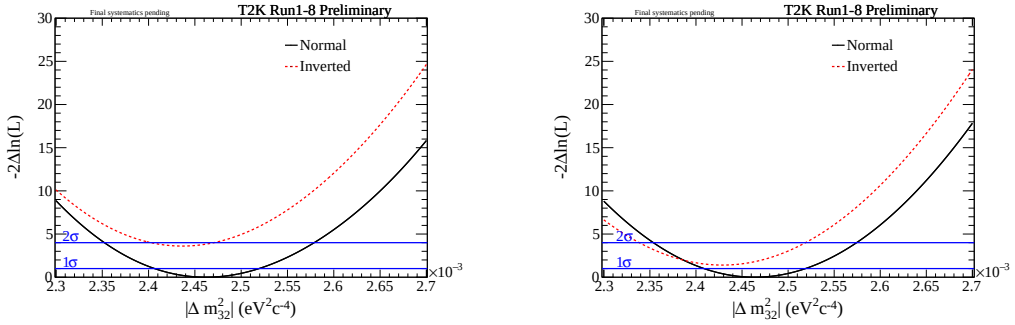

(a) Δm^2_{32} with reactor constraint

(b) Δm^2_{32} T2K only

Figure 5.35: The expected $\Delta\chi^2$ distribution as a function of Δm^2_{32} with and without reactor constraint. The mass hierarchy is minimized, with normal and inverted hierarchy $\Delta\chi^2$ distributions shifted to the same global best-fit χ^2 value, which is taken to be the minimum between normal and inverted hierarchy. All 5 samples were used to produce these fits.

5.7.7 Feldman-Cousins simultaneous fit of δ_{CP} and mass hierarchy

This section presents the results of the Feldman-Cousins fit of δ_{CP} and mass hierarchy. Throws of oscillation parameters are made according to PDG 2016 best-fit values and errors for $\sin^2\theta_{13}$, $\sin^2\theta_{12}$ and Δm^2_{21}, whilst $\sin^2\theta_{23}$ and Δm^2_{32} are thrown according to the likelihood distribution produced by an Asimov fit using the best-fit values from data for these parameters, this is an updated method from the previous analysis and the proposal is given in [197]. δ_{CP} is fixed at one of 9 evenly specified values in the range $[-\pi, \pi]$.

5.7.7.1 Input oscillation parameters

The distributions of oscillation parameters (for normal hierarchy) are shown in fig. 5.36. Note that whilst the distributions of the atmospheric parameters are shown independently they are generated jointly from the likelihood distribution shown in fig. 5.37.

5.7.7.2 Feldman-Cousins critical values and confidence intervals

In fig. 5.38 the confidence intervals obtained with the 'Feldman-Cousins' method are shown for δ_{CP} and mass hierarchy with reactor constraint for the Run 1-8 data set. The critical values at 90%, 2σ and 3σ CL are computed for both the mass hierarchies at the following true values of δ_{CP}; $-\pi$, $-3\pi/4$, $-\pi/2$, $-\pi/4$, 0, $+\pi/4$, $+\pi/2$, $+3\pi/4$, and $+\pi$. Inverted hierarchy is almost excluded at 2σ, except for a small interval around $\delta_{CP} = -\pi/2$. Both $\delta_{CP} = 0$ and $\delta_{CP} = \pi$ are excluded at 2σ. In table 5.17 the 2σ CL intervals for δ_{CP} versus mass hierarchy, obtained with the Feldman-Cousins method, are shown.

Parameter	Reactor	CL	Normal hierarchy	Inverted hierarchy
δ_{CP}	Yes	90%	$[-2.805, -0.830]$	-
δ_{CP}	Yes	2σ	$[-2.981, -0.600]$	$[-1.531, -1.184]$

Table 5.17: The confidence intervals at 2σ CL obtained with the Feldman-Cousins method for the Run 1-8 data set is shown for the measurement of δ_{CP} versus mass hierarchy.

In fig. 5.38 the confidence intervals obtained with the "Feldman-Cousins" method are shown for δ_{CP} and mass hierarchy with reactor constraint for the Run 1-8 data set. The critical values at 90%, 2σ and 3σ CL are computed for both the mass hierarchies and the following true values of δ_{CP}: $-\pi$, $-3\pi/4$, $-\pi/2$, $-\pi/4$, 0, $+\pi/4$, $+\pi/2$, $+3\pi/4$, $+\pi$. The procedure described in section 5.3.3.1 is used.

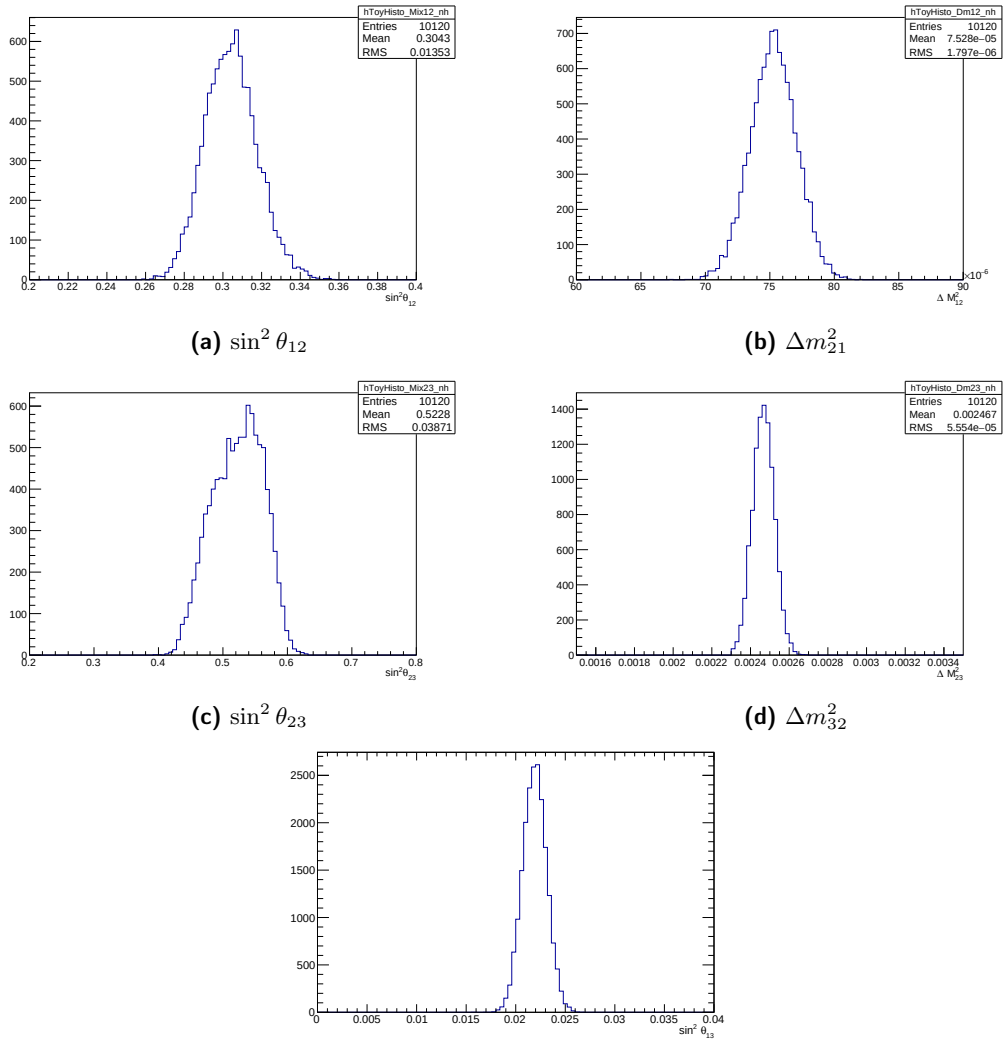

(a) $\sin^2\theta_{12}$ **(b)** Δm^2_{21}

(c) $\sin^2\theta_{23}$ **(d)** Δm^2_{32}

(e) $\sin^2\theta_{13}$

Figure 5.36: Distribution of oscillation parameter throws for Feldman-Cousins fits.

5.7.8 Discussion of the Run 1-8 data fit results

The ν_e CC1π^+data set shows an excess in the number of observed appearance events, observing 15 events compared to an Asimov A expectation of 7. Unlike in our previous analysis, an excess is not observed in the neutrino mode one ring e-like sample, rather in this analysis we see a deficit in the number of observed events in neutrino mode one ring μ-like sample, observing 240 against an Asimov A expectation of 268.

The value of δ_{CP} favoured by the joint fit analysis, when the reactor constraint is applied, is -1.833 and corresponds to normal hierarchy. If the reactor constraint is not applied, the best-fit value of δ_{CP} is -2.083 and $\delta_{CP} = 0$ is still excluded at 2σ CL.

When considering the constant $\Delta\chi^2$ method, we see that the constraint on δ_{CP} is stronger than expected. To investigate the source of this difference a number of fits were

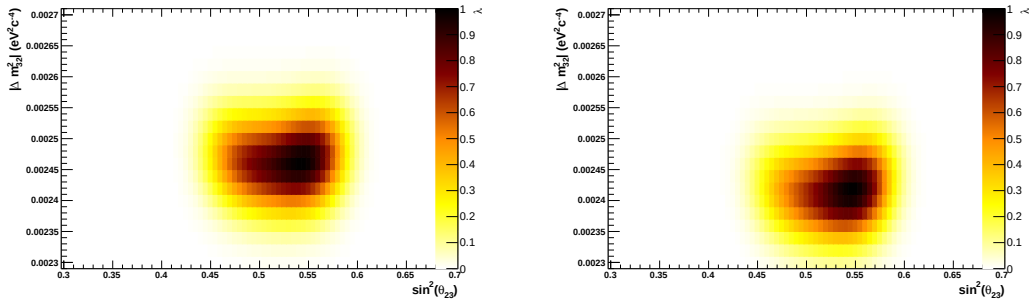

(a) Normal hierarchy **(b)** Inverted hierarchy

Figure 5.37: Likelihood surfaces for throws of the disappearance parameter, obtained from an Asimov fit using the best-fit values from data.

undertaken using hybrids of data and MC. In particular fig. 5.39 shows the expected sensitivity from the Asimov A data set (dashed), the data fit (solid black) and then a number of additional fits where one of the data samples was replaced by the corresponding Asimov A sample (e.g. Data x1Rmu indicates a fit of 4 data samples, with the one-ring μ-like sample being replaced by the Asimov A prediction). From this one can see that the largest contribution to the stronger constraint comes from the upward fluctuation observed in the ν_e CC1π^+ sample, but contributions are also evident from the FHC one-ring μ-like sample, where a deficit in events is seen, and from the two one-ring e-like samples. This results in the exclusion of CP-conservation at more than 2σ with the reactor constraint applied and the inverted hierarchy is disfavoured at 90%CL. The effect is also apparent in the appearance contour.

A stronger than expected constraint is also evident in the disappearance contour, with greater exclusion in $\sin^2\theta_{23}$. Similarly to the δ_{CP} hybrid fits above, fig. 5.40 shows the expected sensitivity from the Asimov A data set (red), the data fit (black) and then a number of additional fits where one of the data samples was replaced by the corresponding Asimov A sample. From this one can see that the stronger constraint can be explained by the deficit in the observed number of events in the one-ring μ-like sample.

The value of $\sin^2\theta_{13}$ favoured by the analysis is 0.0277 and corresponds to normal hierarchy, with the 1D contours in agreement with the PDG 2016 reactor constraint (0.0219 ± 0.0012) at $\sim 1.2\sigma$ (see table 5.16).

The value of $\sin^2\theta_{23}$ favoured by the analysis is 0.530 (0.510) with (without) the reactor constraint and corresponds to normal hierarchy, with the 1D contours in agreement with and without the reactor constraint at 1σ, favouring maximal mixing as seen in our previous analyses.

The value of Δm^2_{32} favoured by the analysis is 2.462 $\times 10^{-3}$ eV^2/c^4 (2.466 $\times 10^{-3}$ eV^2/c^4)

with (without) the reactor constraint and corresponds to normal hierarchy, with the 1D contours in agreement with and without the reactor constraint at 1σ.

5.7.9 Comparison of δ_{CP} versus mass hierarchy result with sensitivity

In order to provide a better understanding of the results of the Run 1-8 data fit, the result has been compared with the expected sensitivity obtained from a large number (1×10^4) of toy experiments for different true values of δ_{CP} ($\delta_{CP} = -\pi/2, -1.833$) and the mass hierarchy.

5.7.9.1 Expected sensitivity method

This section outlines the procedure to produce the expected sensitivity comparison plots. The example given is for true normal hierarchy and $\delta_{CP} = -\pi/2$.

- 1×10^4 fake data sets are generated following the Feldman-Cousins method for a true value of δ_{CP} and mass hierarchy, in this case $\delta_{CP} = -\pi/2$ and normal hierarchy.

- A χ^2 distribution is computed with respect to the marginalisation toys as a function of δ_{CP} and mass hierarchy.

- For each fake data set, the minimum value of χ^2 for each bin of δ_{CP}, $\chi^2_{bin,min}$ is found with respect to both normal and inverted hierarchy.

- The test statistic is then computed as $\Delta\chi^2_{bin} = \chi^2_{bin} - \chi^2_{bin,min}$, which is slightly different to the Feldman-Cousins method, where $\Delta\chi^2_{FC} = \chi^2_{true} - \chi^2_{best-fit}$. The distributions of $\Delta\chi^2_{bin}$ and $\Delta\chi^2_{FC}$ coincide if the bin is $\delta_{CP} = -\pi/2$ and normal hierarchy, i.e. the true point used to generate the toy experiments.

- This results in a $\Delta\chi^2$ distribution from which we can draw conclusions about the expected $\Delta\chi^2$ for each value of δ_{CP} given a hypothesised true value and hierarchy.

- The spread of the $\Delta\chi^2$ distribution for each point of δ_{CP} and mass hierarchy is obtained as the range of the $\Delta\chi^2_{bin}$ distribution that contains respectively the 68.27% and 95.45% of the toy experiments on its left side. The test statistic $\Delta\chi^2_{bin}$ is assumed ot be 1-sided because by construction $\chi^2_{bin,min} \leq \chi^2_{bin}$.

- An alternative to the one-sided distribution is also produced, for which values of $\Delta\chi^2$ of each bin of δ_{CP} are themselves binned (100 evenly-spaced bins on the

range $[\Delta\chi^2_{bin,min}, \Delta\chi^2_{bin,max}]$) and then toys are added to the expected sensitivity bands starting from the bin of $\Delta\chi^2$ that contains the most toys, until 68.27% and 95.45% of the toy experiments have been included, thereby producing two-sided distributions.

- A plot is also produced, fig. 5.41(c) to show the fraction of toy experiments which exclude each value of δ_{CP} to greater than 2σ significance in the Feldman-Cousins corrected critical values along with the probabilities to exclude $\delta_{CP} = 0$ and $\delta_{CP} = \pi$ for a given true value of δ_{CP}.

5.7.9.2 $\delta_{CP} = -\pi/2$ - normal hierarchy

In fig. 5.41 the Run 1-8 data result for δ_{CP} versus mass hierarchy is compared to the 1σ and 2σ uncertainties on the $\Delta\chi^2$ distributions corresponding to $\delta_{CP} = -\pi/2$ and (a) normal hierarchy and (b) inverted hierarchy. We see that the data contour is contained within the 2σ band for inverted hierarchy, whilst the data contour falls just outside the 2σ band for normal hierarchy in the region around $\delta_{CP} = 0$. This suggests that the data constraint is consistent with the PMNS matrix at around the 2σ level.

We also see an interesting feature near $\delta_{CP} = -\pi/2$ where the $\Delta\chi^2$ values have a wider distribution. This is due to the boundary at $\delta_{CP} = -\pi/2$ which causes a wider distribution when the parameter δ_{CP} would like to be pushed beyond the boundary in the fit.

Finally from fig. 5.41(c) we see that $\delta_{CP} = 0$ and $\delta_{CP} = \pi$ are excluded at 90% confidence level in around 40% (see table 5.18) of the toy experiments and excluded at 2σ confidence level in between 25% and 30% of the toy experiments, with $\delta_{CP} = \pi$ excluded in slightly fewer toy experiments in each case.

δ_{CP}	Hierarchy	90%	2σ
0	NH	0.430	0.300
π	NH	0.383	0.250
0	IH	0.760	0.656
π	IH	0.769	0.667

Table 5.18: The fraction of toy experiments for which $\delta_{CP} = 0, \pi$ and normal and inverted hierarchy are excluded at 90% and 2σ CL is shown. 10k toy experiments are used.

5.7.9.3 $\delta_{CP} = -1.833$ - normal hierarchy

In fig. 5.42 the Run 1-8 data result for δ_{CP} versus mass hierarchy is compared to the 1σ and 2σ uncertainties on the $\Delta\chi^2$ distributions corresponding to $\delta_{CP} = -1.833$ and (a)

normal hierarchy and (b) inverted hierarchy. We see that the data contour is consistent with the PMNS matrix at around the 2σ level.

5.7.9.4 Sample-by-sample expected sensitivity

An extension to the two-sided method described above was applied in order to assess the effect of each sample on the δ_{CP} contour obtained. There key difference to the two-sided method described in section 5.7.9.1 is that the generation of the 1×10^4 fake data sets is undertaken for a single sample of interest, with the remaining 4 samples being fixed at the observed spectra.

It can be seen from fig. 5.43 that for normal hierarchy the observed contour resides within the 1σ band of expected sensitivities for 4 of the samples and thus while three of these contours are contributing to a stronger constraint than expected, the additional strength of the constraint in these samples is by no means surprising.

The contribution from the ν_e CC1π^+sample is rather extreme, as might be expected given the excess events observed in this sample, with the observed contour falling outside the 2σ band of expected sensitivities for this sample. Nonetheless, with all 5 samples considered together, as in fig. 5.41(a), the observed constraint resides approximately within the 2σ expected sensitivity.

For the case of inverted hierarchy (fig. 5.44) a similar scenario is observed, the principal difference being that the FHC one-ring μ-like sample has an observed contour contained with the 2σ band of expected sensitivities, though the full 5 sample contour remains within the 2σ expected sensitivity (fig. 5.41).

5.7.10 Comparison of $\sin^2\theta_{23}$ versus mass hierarchy result with sensitivity

This section provides a comparison of the Run 1-8 data fit with the expected sensitivity for $\sin^2\theta_{23}$.

The procedure used is the one outlined in section 5.7.9.1 for the two-sided distribution, with the appropriate change in oscillation parameter. Furthermore, whereas the expected sensitivity method for δ_{CP} throws the atmospheric parameters from a 2D likelihood distribution from on an Asimov fake data set, whose oscillation parameter values are those from the disappearance data fit, in this case the Δm^2_{32} parameter is thrown from the 1D projection of this likelihood distribution.

5.7.10.1 $\sin^2\theta_{23} = 0.530$ - normal hierarchy

In fig. 5.45 the Run 1-8 data result for $\sin^2\theta_{23}$ versus mass hierarchy is compared to the 1σ and 2σ uncertainties on the $\Delta\chi^2$ distributions corresponding to $\sin^2\theta_{23} = 0.530$ for (a) normal hierarchy and (b) inverted hierarchy.

5.7.11 Comparison of Δm^2_{32} versus mass hierarchy result with sensitivity

This section provides a comparison of the Run 1-8 data fit with the expected sensitivity for Δm^2_{32}.

The procedure used is the one outlined in section 5.7.9.1 for the two-sided distribution, with the appropriate change in oscillation parameter. Furthermore, whereas the expected sensitivity method for δ_{CP} throws the atmospheric parameters from a 2D likelihood distribution from on an Asimov fake data set, whose oscillation parameter values are those from the disappearance data fit, in this case the $\sin^2\theta_{23}$ parameter is thrown from the 1D projection of this likelihood distribution.

5.7.11.1 $\Delta m^2_{32} = -2.462 \times 10^{-3}\text{eV}^2\ \text{c}^{-4}$ - normal hierarchy

In fig. 5.46 the Run 1-8 data result for Δm^2_{32} versus mass hierarchy is compared to the 1σ and 2σ uncertainties on the $\Delta\chi^2$ distributions corresponding to $\Delta m^2_{32} = -2.462 \times 10^{-3}\text{eV}^2\ \text{c}^{-4}$ for (a) normal hierarchy and (b) inverted hierarchy.

5.7.12 Comparison of e-like event rates with expectation

It is valuable to see how different values of δ_{CP}, $\sin^2\theta_{23}$ and hierarchy affect the predicted event rates. Figure 5.47 shows the predicted $\bar{\nu}_e$ event rate vs ν_e event rate for best-fit values of oscillation parameters where δ_{CP} is varied between CP conserving and maximally CP violating values, and $\sin^2\theta_{23}$ is varied around its best-fit, for both hierarchies. Event rates for a given value of $\sin^2\theta_{23}$ and mass hierarchy are linearly interpolated between those computed for 9 evenly-spaced values of δ_{CP} from $-\pi$ to $+\pi$ to indicate the behaviour produced by varying δ_{CP}. The observed event rates with 1σ errors are also shown. Figure 5.47(a) shows e-like event rates where the FHC sample includes the ν_e CC1π^+sample, while fig. 5.47(b) shows e-like event rates where the FHC sample does not include the ν_e CC1π^+sample.

5.8 Summary

The results of the 3-flavour $\bar{\nu}/\nu$ joint analysis performed by the *VALOR* group, on the combined Run 1-8 data set. The goal of the analysis was to search for CP violation in the leptonic sector and determine limits on δ_{CP} as well as measure all the other oscillation parameters to which T2K is sensitive: $\sin^2\theta_{13}$, $\sin^2\theta_{23}$, Δm^2_{32} (Δm^2_{13}) and partially mass hierarchy, to which T2K has little sensitivity.

This analysis predicts 268.4 ± 11.8 (syst) for neutrino μ-like, 64.3 ± 2.4 (syst) for antineutrino μ-like, 73.5 ± 5.3 (syst) for neutrino e-like, 7.9 ± 0.6 (syst) for antineutrino e-like and 6.9 ± 1.5 (syst) for neutrino ν_e CC1π^+ events in Super K and observes respectively 240 for neutrino μ-like, 68 for antineutrino μ-like, 74 for neutrino e-like, 7 for antineutrino e-like and 15 for neutrino ν_e CC1π^+.

The $\bar{\nu}/\nu$ analysis was performed in a framework of 3-flavour oscillations including matter effects in constant-density matter. The observed reconstructed energy spectrum of single μ-like ring events and reconstructed energy versus lepton angle of single e-like ring events in addition to e-like events with an additional decay electron were used to compute the confidence intervals. All 110 systematic parameters as well as the oscillation parameters which were not parameters of interest considered in this analysis were marginalised.

From the fit of the Run 1-8 data using the reactor constraint we can see that the favoured value of δ_{CP} is -1.833, close to $-\pi/2$. The Feldman-Cousins method is used to construct confidence intervals with neither over or under coverage from which the significance to exclude the hypothesis of CP conservation is greater than 2 standard deviations.

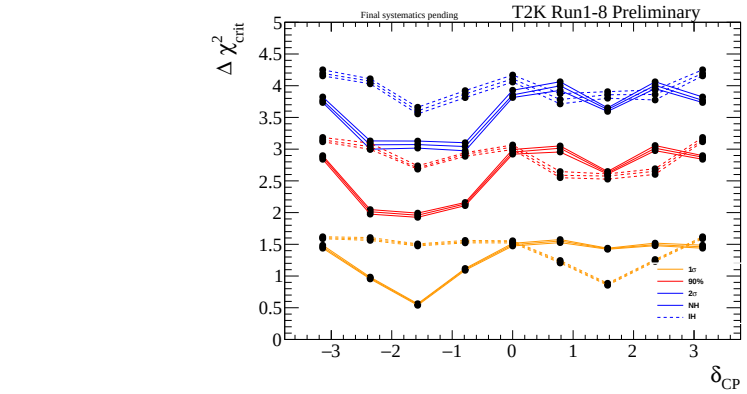

(a) Critical $\Delta\chi^2$ values

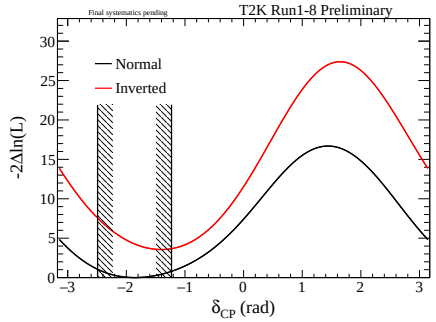

(b) 1σ CL exclusion region

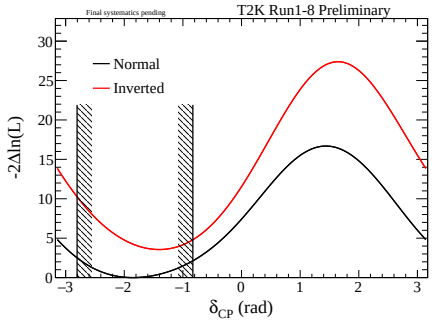

(c) 90% CL exclusion region

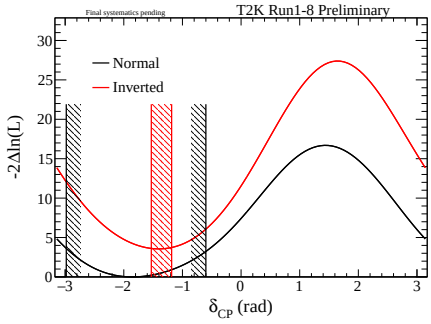

(d) 2σ CL exclusion region

Figure 5.38: $\Delta\chi^2$ critical values and confidence intervals for the measured $\Delta\chi^2$ distributions for Run 1-8. Critical values obtained with the Feldman-Cousins method for Run 1-8 for 9 evenly spaced values on the range $[-\pi, \pi]$. Critical values are shown for $1\sigma, 2\sigma$ and 90% CL for normal (solid lines) and inverted (dashed lines) hierarchies. At least 1×10^4 toy experiments are performed for each point. The three bands of lines show the $\pm 1\sigma$ uncertainty on the critical values. Also shown are the measured $\Delta\chi^2$ distributions shifted with respect to the same global minium and the 1σ, 90% and 2σ exclusion regions for both mass hierarchies.

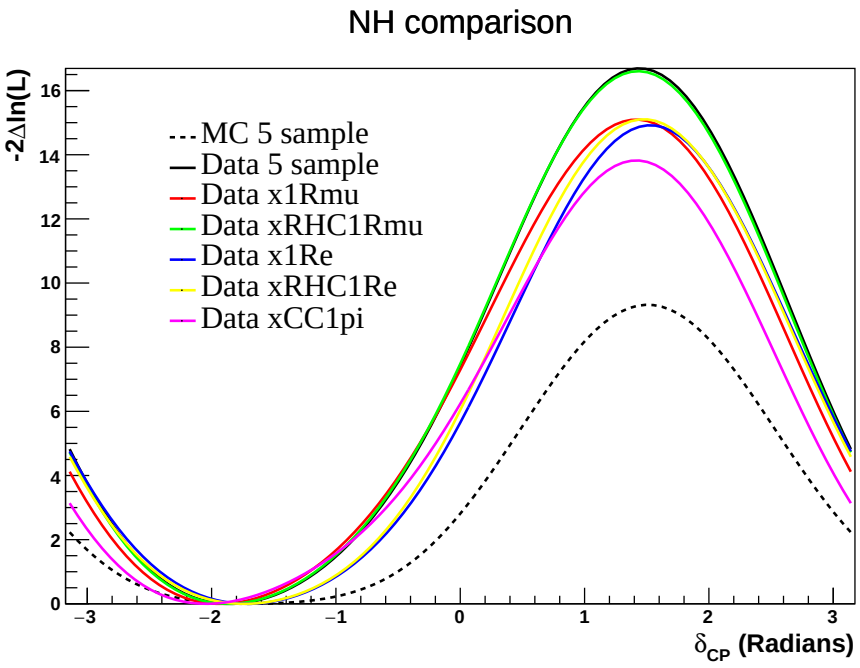

Figure 5.39: The expected $\Delta\chi^2$ distribution as a function of δ_{CP} with reactor constraint for MC, data and data/MC hybrid data sets.

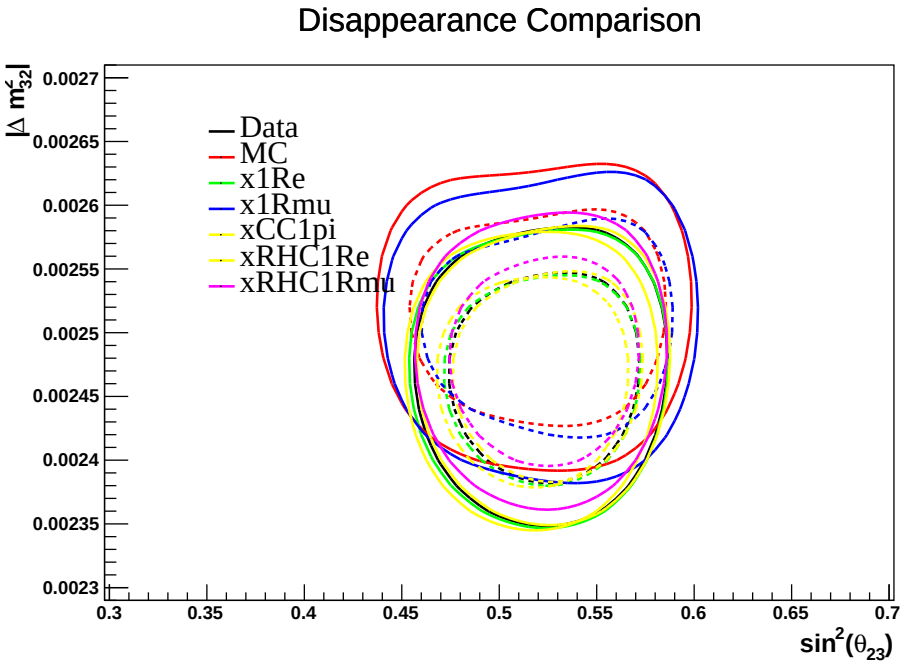

Figure 5.40: The expected disappearance contours with reactor constraint for normal hierarchy for MC, data and data/MC hybrid data sets.

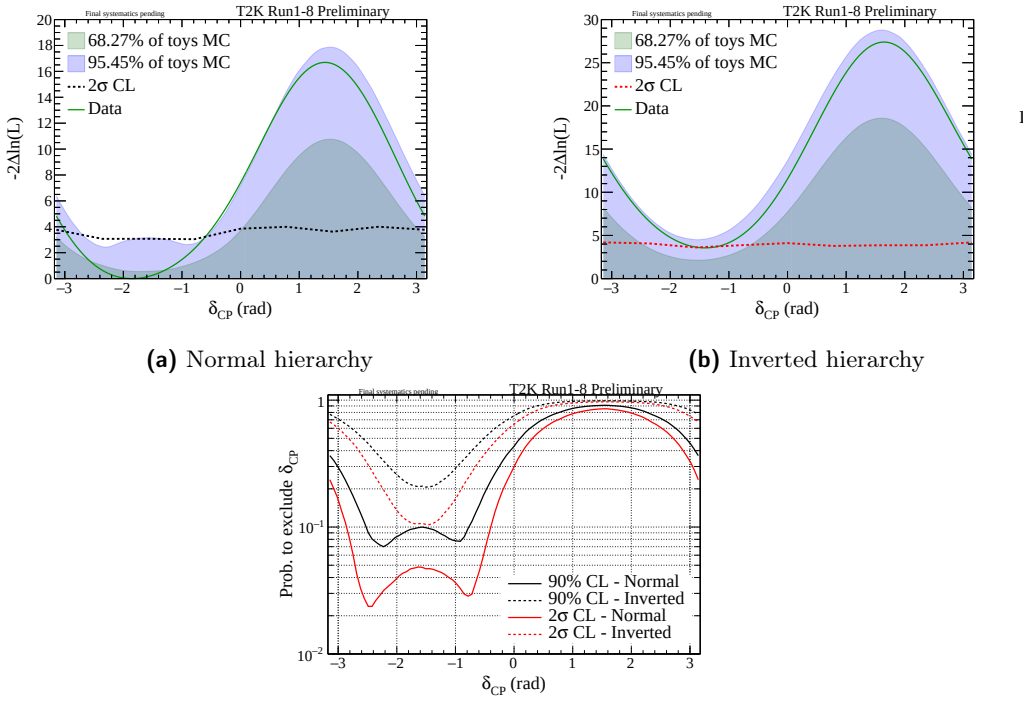

(a) Normal hierarchy

(b) Inverted hierarchy

(c) Data $\Delta\chi^2$ probablility

Figure 5.41: The distribution of $\Delta\chi^2$ vs δ_{CP} obtained with 1×10^4 toy experiments generated with $\delta_{CP} = -\pi/2$ and normal hierarchy is shown. The $\Delta\chi^2$ distributions obtained by fixing the mass hierarchy to normal (left) and inverted (right) are shown, along with the $\Delta\chi^2$ values corresponding to 68.27% and 95.45% of the toy experiments and the average $\Delta\chi^2$ values from all experiments. Also shown are the fractions of toys which exclude each value of δ_{CP} to 90% and 2σ using the Feldman-Cousins corrected critical values (bottom).

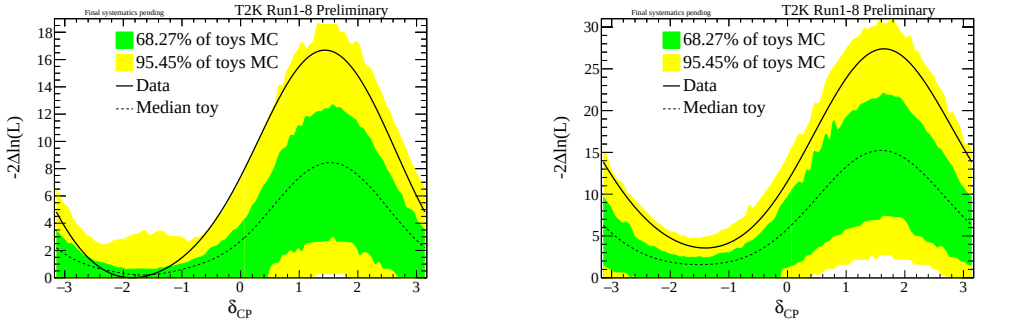

(a) Normal hierarchy

(b) Inverted hierarchy

Figure 5.42: The distribution of $\Delta\chi^2$ vs δ_{CP} obtained with 1×10^4 toy experiments generated with $\delta_{CP} = -1,833$ and normal hierarchy is shown. The $\Delta\chi^2$ distributions obtained by fixing the mass hierarchy to normal (left) and inverted (right) are shown, along with the $\Delta\chi^2$ values corresponding to 68.27% and 95.45% of the toy experiments, the median toy and the data contour.

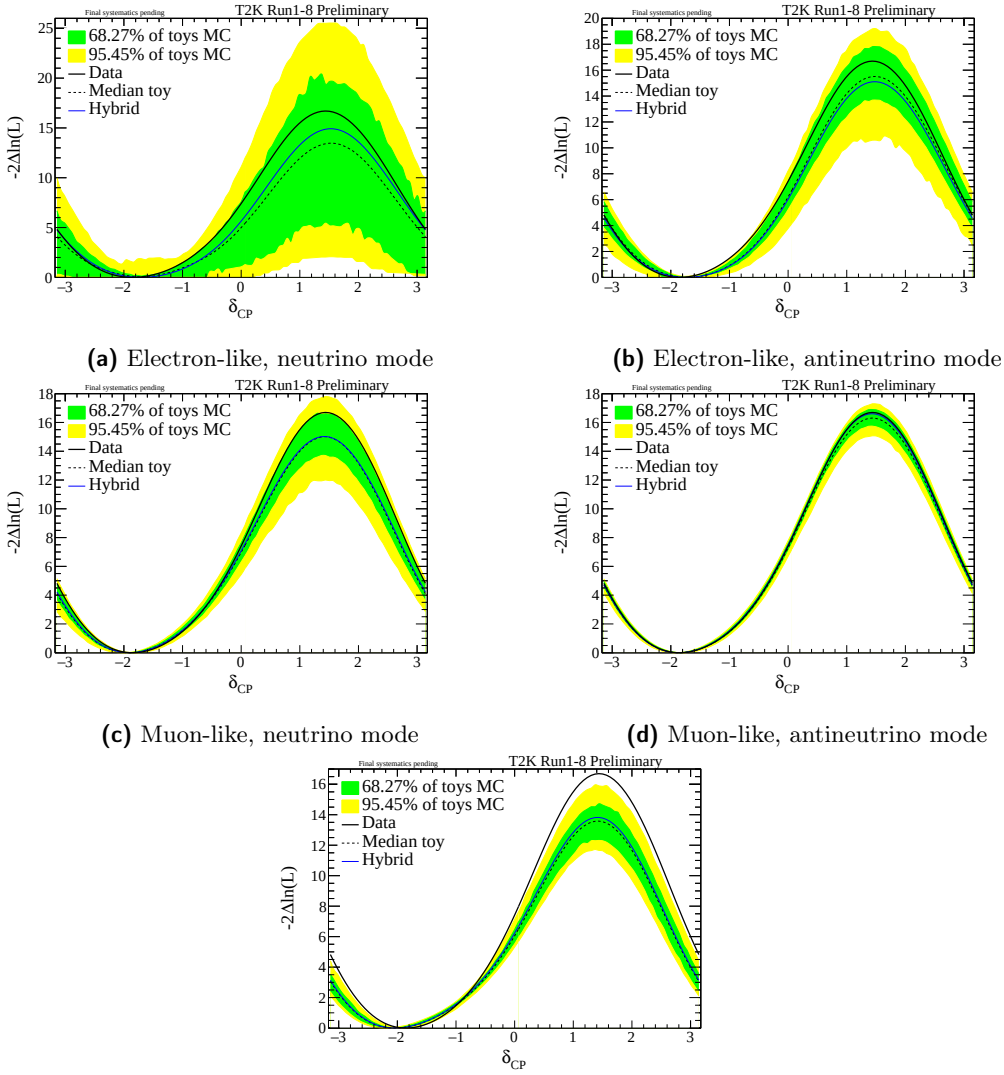

(a) Electron-like, neutrino mode

(b) Electron-like, antineutrino mode

(c) Muon-like, neutrino mode

(d) Muon-like, antineutrino mode

(e) ν_e CC1π^+-like, neutrino mode

Figure 5.43: The distribution of $\Delta\chi^2$ vs δ_{CP} obtained with 1×10^4 toy experiments generated with $\delta_{CP} = -1.833$ and normal hierarchy is shown. The $\Delta\chi^2$ distribution obtained from the full 5-sample fit, obtained by fixing the mass hierarchy to normal, is shown, along with the $\Delta\chi^2$ values corresponding to 68.27% and 95.45% of the toy experiments for the indicated sample, with all other samples fixed at their observed spectra.

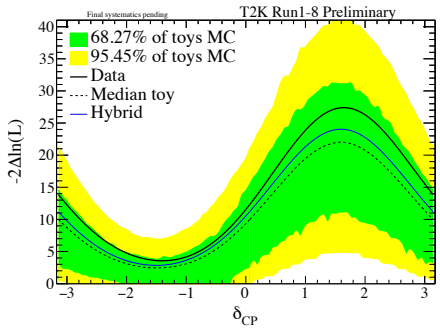

(a) Electron-like, neutrino mode

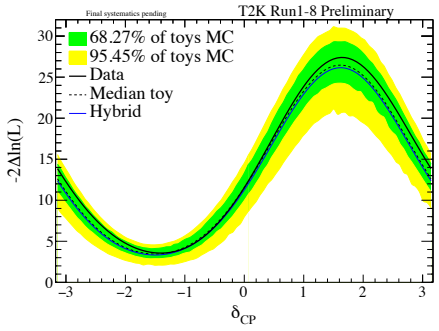

(b) Electron-like, antineutrino mode

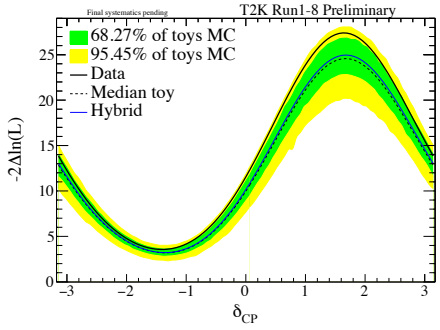

(c) Muon-like, neutrino mode

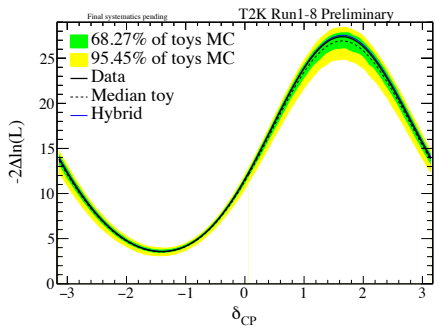

(d) Muon-like, antineutrino mode

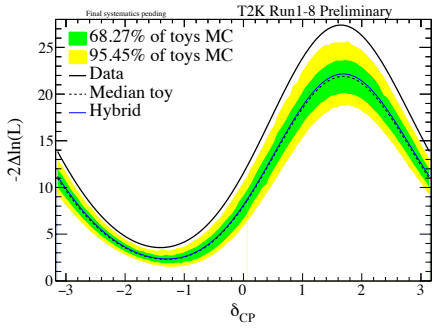

(e) ν_e CC1π^+-like, neutrino mode

Figure 5.44: The distribution of $\Delta\chi^2$ vs δ_{CP} obtained with 1×10^4 toy experiments generated with $\delta_{CP} = -1.833$ and normal hierarchy is shown. The $\Delta\chi^2$ distribution obtained from the full 5-sample fit, obtained by fixing the mass hierarchy to inverted, is shown, along with the $\Delta\chi^2$ values corresponding to 68.27% and 95.45% of the toy experiments for the indicated sample, with all other samples fixed at their observed spectra.

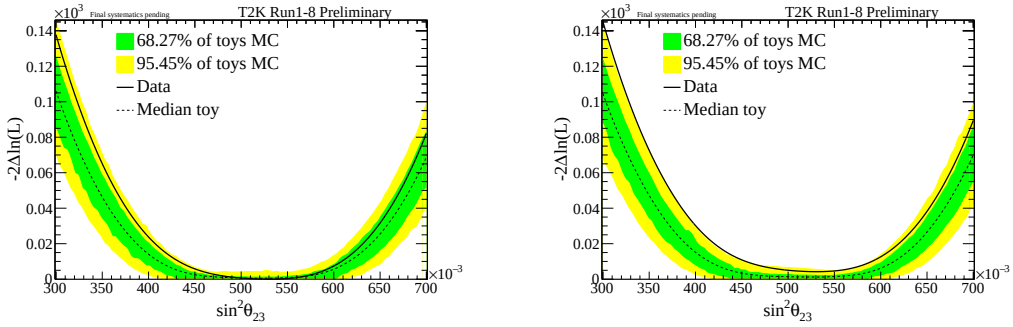

(a) Normal hierarchy **(b)** Inverted hierarchy

Figure 5.45: The distribution of $\Delta\chi^2$ vs $\sin^2\theta_{23}$ obtained with 1×10^4 toy experiments generated with $\sin^2\theta_{23} = 0.530$ and normal hierarchy is shown. The $\Delta\chi^2$ distributions obtained by fixing the mass hierarchy to normal (left) and inverted (right) are shown, along with the $\Delta\chi^2$ values corresponding to 68.27% and 95.45% of the toy experiments, the median toy and the data contour.

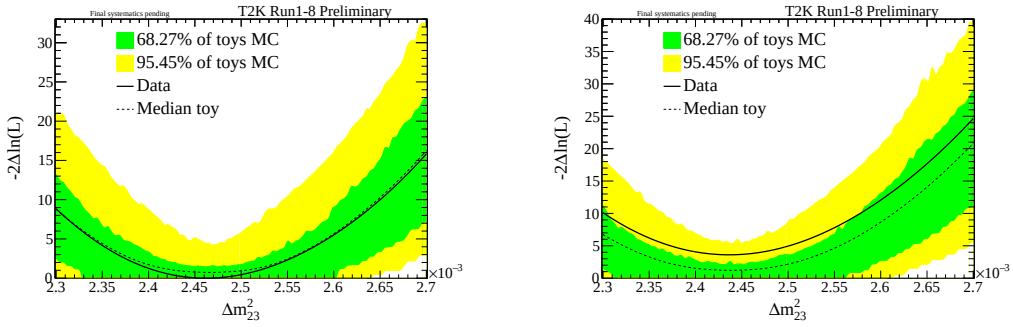

(a) Normal hierarchy **(b)** Inverted hierarchy

Figure 5.46: The distribution of $\Delta\chi^2$ vs Δm^2_{32} obtained with 1×10^4 toy experiments generated with $\Delta m^2_{32} = -2.462 \times 10^{-3}\text{eV}^2\ \text{c}^{-4}$ and normal hierarchy is shown. The $\Delta\chi^2$ distributions obtained by fixing the mass hierarchy to normal (left) and inverted (right) are shown, along with the $\Delta\chi^2$ values corresponding to 68.27% and 95.45% of the toy experiments, the median toy and the data contour.

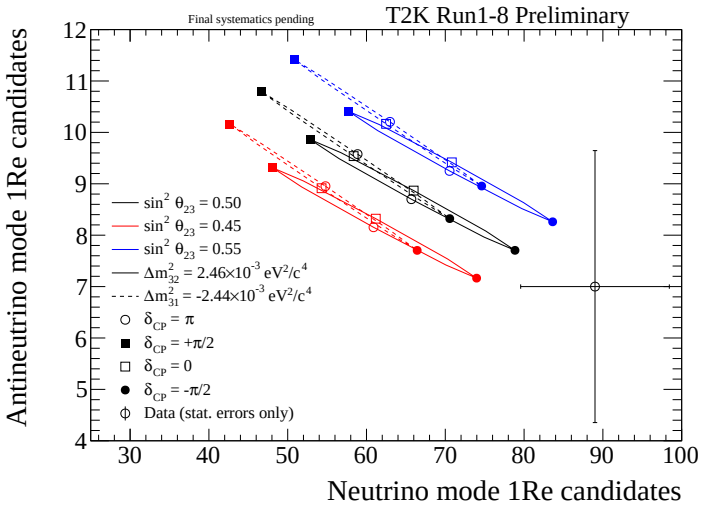

Figure 5.47: This plot shows the candidate RHC one-ring e-like event rate vs the candidate FHC one-ring e-like event rate for a variety of different oscillation parameter values. Predictions are generated for best-fit values of oscillation parameters for different values of δ_{CP}, $\sin^2\theta_{23}$ and mass hierarchy. In particular the FHC and RHC event rates are plotted for the CP conserving and maximally CP violating values of δ_{CP}, with $\sin^2\theta_{23}$ set at the best-fit value and $\pm 1\sigma$ values in both normal and inverted hierarchy. The observed rates with statistical error shown are also included.

6 Conclusions and Outlook

A joint analysis of the transitions $\overset{(-)}{\nu}_\mu \to \overset{(-)}{\nu}_\mu$ and $\overset{(-)}{\nu}_e \to \overset{(-)}{\nu}_e$ was performed assuming PMNS neutrino oscillations in constant density matter. The analysis used data from the T2K experiment Run 1-8 with 1.4734×10^{21} POT in FHC mode and 7.558×10^{20} POT in RHC mode. Fits were made to reconstructed neutrino energy for μ-like events and energy and lepton angle for e-like events with separate fits for the normal and inverted hierarchies. The results of collaboration's analysis in are presented in [208]. The 110 systematic parameters are marginalised to construct a marginal likelihood from which the oscillation parameters of interest are extracted. The exclusion of the $\mathcal{CP}$ conserving values 0 and π, determined using the Feldman-Cousins method and using available measurements, $[3\sigma]$ range, of $\sin^2\theta_{13} = 0.0215\,[0.0190{-}0.0240]$ $(0.0216\,[0.0190{-}0.0242])$, determined by reactor experiments

$$\begin{aligned} &[-2.805, -0.830] \quad 90\,\%\text{CL} \\ &[-2.981, -0.600]\,([-1.531, -1.184]) \quad 2\sigma. \end{aligned}$$

for normal (inverted) hierarchies. The oscillation parameters measured in this analysis, with the confidence intervals for δ_{CP} extracted using the constant $\Delta\chi^2$ method and T2K data only were

$$\begin{aligned} \delta_{\text{CP}} &= -2.083\ ^{+0.932}_{-0.889} \quad (-1.157\ ^{+0.754}_{-0.808}) \\ \sin^2\theta_{13} &= 0.0277\ ^{+0.0053}_{-0.0047} \quad (0.0331\ ^{+0.0047}_{-0.0065}) \\ \sin^2\theta_{23} &= 0.530\ ^{+0.031}_{-0.037} \quad (0.530\ ^{+0.029}_{-0.034}) \\ \left|\Delta m^2_{32}\right|(\Delta m^2_{13}) &= [2.462\ ^{+0.057}_{-0.055} \quad (2.436\ ^{+0.055}_{-0.053})] \times 10^{-3}\,\text{eV}^2. \end{aligned}$$

Addition of Gd, to tag neutrons at the level of 90 % with 0.2 % Gd by mass to the water detection medium at Super-K has been approved, and upgrades to the detector are underway. Improvements by tagging neutrons in the final state are under study, with 78 % of $\nu/\bar{\nu}$ correctly identified, in the T2K beam energy range [209]. Separation of the NC and CC components of e-like interactions at Super-K via neutron multiplicity allows for the correct classification of 80 % of true NC and DIS interactions, this region contains information to determine the mass hierarchy. Neutrons that are produced as a result of FSI from neutral hadrons in the nuclear medium can be used to correct for the neutrino energy that is not seen by the Super-K detector. Sensitivity studies using the General Long Baseline Experiment Simulator (GLoBES) package [210] have been performed, considering only statistical uncertainty for an exposure of 3.9×10^{21} POT, and show an increase in sensitivity with the inclusion of neutron tagging.

T2K will continue to collect beam data for appearance and disappearance in neutrino and

antineutrino modes towards an approved 7.8×10^{21} POT and a potential 20×10^{21} POT for T2K-II with a potential constraint on the value of δ_{CP} at 3σ and a 1σ precision on the value of $\sin^2\theta_{23}$ of 1.7° and Δm^2_{32} at the 1 % level assuming equal running in ν and $\bar{\nu}$ modes[211]. A joint analysis of T2K and NOνA data is approved in principle, with discussions underway by the two collaborations on understanding commonalities in the analyses and using common interaction modelling. The future Hyper-Kamiokande (Hyper-K) experiment [212] will use the experience from the T2K experiment to resolve the still open questions of the phase of δ_{CP} and the neutrino mass hierarchy. In order to achieve these goals it will use the same water Cherenkov technology with a single tank containing 258 kt of water (in one possible scenario), with the same 295 km baseline and 0.6 GeV beam peak energy as T2K [213]. The future DUNE experiment also seeks to address these questions as part of its physics goals but is designed with a 1300 km baseline for the far detector and 575 m for the near detector both using liquid Argon TPCs technology. The far detector will have a fiducial mass of 40 kt and the experiment will operate with a high intensity (reaching 2.4 MW) [214] wide-band beam with flux in the region 1–4 GeV [215].

Appendix A

Event rates

Tables table A.1-table A.5 present unoscillated rates.

	ν_μ	ν_e	$\bar{\nu}_\mu$	$\bar{\nu}_e$	Osc. ν_e	Osc. $\bar{\nu}_e$	Total
CCQE	953.15505	0.00429	23.18824	0.00020	0.00000	0.00000	976.34778
CC1pi	76.40088	0.00211	4.12922	0.00010	0.00000	0.00000	80.53230
CCcoherent	0.75678	0.00000	0.17387	0.00000	0.00000	0.00000	0.93065
2p2h	134.02475	0.00161	2.51636	0.00008	0.00000	0.00000	136.54280
CCother	6.94520	0.00090	0.50167	0.00008	0.00000	0.00000	7.44785
NC1pi0	0.61495	0.01841	0.02120	0.00143	N/A	N/A	0.65599
NC1piPM	4.90783	0.09799	0.17531	0.00975	N/A	N/A	5.19089
NCcoherent	0.00000	0.00000	0.00043	0.00003	N/A	N/A	0.00047
NCother	2.05619	0.07378	0.13055	0.00912	N/A	N/A	2.26963
Total	1178.86162	0.19909	30.83686	0.02080	0.00000	0.00000	1209.91837

Table A.1: Predicted number of events in the neutrino mode μ-like sample obtained after applying the BANFF weight for a total exposure of 1.4734×10^{21} POT. Oscillations are not applied.

	ν_μ	ν_e	$\bar{\nu}_\mu$	$\bar{\nu}_e$	Osc. ν_e	Osc. $\bar{\nu}_e$	Total
CCQE	36.21445	0.00089	133.92633	0.00096	0.00000	0.00000	170.14262
CC1pi	6.51012	0.00035	11.57229	0.00027	0.00000	0.00000	18.08303
CCcoherent	0.06956	0.00000	0.75838	0.00005	0.00000	0.00000	0.82799
2p2h	8.28538	0.00028	10.73613	0.00028	0.00000	0.00000	19.02208
CCother	1.18677	0.00012	0.77049	0.00000	0.00000	0.00000	1.95738
NC1pi0	0.06000	0.00222	0.06147	0.00169	N/A	N/A	0.12538
NC1piPM	0.35950	0.01527	0.46009	0.01235	N/A	N/A	0.84721
NCcoherent	0.00000	0.00000	0.00201	0.00000	N/A	N/A	0.00201
NCother	0.31580	0.01640	0.20064	0.00789	N/A	N/A	0.54073
Total	53.00159	0.03552	158.48783	0.02349	0.00000	0.00000	211.54843

Table A.2: Predicted number of events in the antineutrino mode μ-like sample obtained after applying the BANFF weight for a total exposure of 7.558×10^{20}POT. Oscillations are not applied.

	ν_μ	ν_e	$\bar{\nu}_\mu$	$\bar{\nu}_e$	Osc. ν_e	Osc. $\bar{\nu}_e$	Total
CCQE	0.99622	6.79206	0.02082	0.27180	0.00000	0.00000	8.08090
CC1pi	0.18090	0.99514	0.00514	0.07082	0.00000	0.00000	1.25199
CCcoherent	0.00076	0.00885	0.00031	0.00419	0.00000	0.00000	0.01412
2p2h	0.13667	1.71219	0.00236	0.04511	0.00000	0.00000	1.89633
CCother	0.02827	0.13255	0.00057	0.00971	0.00000	0.00000	0.17111
NC1pi0	1.70203	0.03706	0.06012	0.00356	N/A	N/A	1.80278
NC1piPM	0.16854	0.00472	0.01020	0.00057	N/A	N/A	0.18404
NCcoherent	0.52817	0.00715	0.04794	0.00294	N/A	N/A	0.58619
NCother	0.31767	0.01695	0.02120	0.00128	N/A	N/A	0.35711
NC1gamma	0.94222	0.01687	0.04983	0.00233	N/A	N/A	1.01125
Total	5.00145	9.72355	0.21850	0.41231	0.00000	0.00000	15.35581

Table A.3: Predicted number of events in the neutrino mode e-like sample obtained after applying the BANFF weight for a total exposure of 1.4734×10^{21} POT. Oscillations are not applied.

	ν_μ	ν_e	$\bar{\nu}_\mu$	$\bar{\nu}_e$	Osc. ν_e	Osc. $\bar{\nu}_e$	Total
CCQE	0.04096	0.54758	0.13906	0.90195	0.00000	0.00000	1.62955
CC1pi	0.01660	0.10715	0.01787	0.15254	0.00000	0.00000	0.29415
CCcoherent	0.00006	0.00105	0.00143	0.01133	0.00000	0.00000	0.01388
2p2h	0.00652	0.15324	0.00694	0.11994	0.00000	0.00000	0.28664
CCother	0.00568	0.02184	0.00232	0.01193	0.00000	0.00000	0.04177
NC1pi0	0.13849	0.00541	0.17659	0.00468	N/A	N/A	0.32516
NC1piPM	0.02475	0.00127	0.02001	0.00080	N/A	N/A	0.04683
NCcoherent	0.04776	0.00221	0.20260	0.00317	N/A	N/A	0.25574
NCother	0.05664	0.00221	0.02672	0.00097	N/A	N/A	0.08654
NC1gamma	0.07943	0.00439	0.17490	0.00383	N/A	N/A	0.26255
Total	0.41688	0.84635	0.76842	1.21115	0.00000	0.00000	3.24280

Table A.4: Predicted number of events in the antineutrino mode e-like sample obtained after applying the BANFF weight for a total exposure of 7.558×10^{20} POT. Oscillations are not applied.

	ν_μ	ν_e	$\bar{\nu}_\mu$	$\bar{\nu}_e$	Osc. ν_e	Osc. $\bar{\nu}_e$	Total
CCQE	0.34542	0.02646	0.00615	0.00187	0.00000	0.00000	0.37990
CC1pi	0.54696	0.82041	0.00710	0.00403	0.00000	0.00000	1.37850
CCcoherent	0.00364	0.01905	0.00021	0.00008	0.00000	0.00000	0.02298
2p2h	0.08323	0.02355	0.00176	0.00100	0.00000	0.00000	0.10953
CCother	0.17904	0.11704	0.00287	0.00289	0.00000	0.00000	0.30184
NC1pi0	0.02049	0.00076	0.00083	0.00008	N/A	N/A	0.02216
NC1piPM	0.06474	0.00165	0.00382	0.00033	N/A	N/A	0.07053
NCother	0.20584	0.00830	0.01304	0.00088	N/A	N/A	0.22807
NC1gamma	0.02844	0.00000	0.00067	0.00007	N/A	N/A	0.02918
Total	1.47780	1.01722	0.03645	0.01122	0.00000	0.00000	2.54269

Table A.5: Predicted number of events in the neutrino mode e-like sample obtained after applying the BANFF weight for a total exposure of 1.4734×10^{21} POT. Oscillations are not applied.

Tables table A.6-table A.10 present oscillated rates corresponding to the Asimov B data set.

	ν_μ	ν_e	$\bar{\nu}_\mu$	$\bar{\nu}_e$	Osc. ν_e	Osc. $\bar{\nu}_e$	Total
CCQE	186.41514	0.00413	11.15862	0.00019	0.01514	0.00018	197.59340
CC1pi	28.20533	0.00199	2.62809	0.00009	0.01651	0.00009	30.85209
CCcoherent	0.29385	0.00000	0.09293	0.00000	0.00000	0.00001	0.38678
2p2h	36.71916	0.00151	1.42161	0.00008	0.01693	0.00005	38.15934
CCother	5.47728	0.00086	0.40680	0.00008	0.00011	0.00001	5.88513
NC1pi0	0.61495	0.01841	0.02120	0.00143	N/A	N/A	0.65599
NC1piPM	4.90783	0.09799	0.17531	0.00975	N/A	N/A	5.19089
NCcoherent	0.00000	0.00000	0.00043	0.00003	N/A	N/A	0.00047
NCother	2.05619	0.07378	0.13055	0.00912	N/A	N/A	2.26963
Total	264.68973	0.19867	16.03554	0.02078	0.04868	0.00032	280.99373

Table A.6: Predicted number of events in the neutrino mode μ-like sample obtained after applying the BANFF weight for a total exposure of 1.4734×10^{21} POT. The Asimov data set B in 5.1 is used.

	ν_μ	ν_e	$\bar{\nu}_\mu$	$\bar{\nu}_e$	Osc. ν_e	Osc. $\bar{\nu}_e$	Total
CCQE	15.53910	0.00085	31.15342	0.00093	0.00068	0.00181	46.69679
CC1pi	3.97662	0.00033	4.60026	0.00025	0.00043	0.00073	8.57862
CCcoherent	0.04724	0.00000	0.18223	0.00005	0.00000	0.00007	0.22959
2p2h	4.50940	0.00026	2.92853	0.00027	0.00030	0.00025	7.43900
CCother	0.94370	0.00012	0.60700	0.00000	0.00000	0.00000	1.55082
NC1pi0	0.06000	0.00222	0.06147	0.00169	N/A	N/A	0.12538
NC1piPM	0.35950	0.01527	0.46009	0.01235	N/A	N/A	0.84721
NCcoherent	0.00000	0.00000	0.00201	0.00000	N/A	N/A	0.00201
NCother	0.31580	0.01640	0.20064	0.00789	N/A	N/A	0.54073
Total	25.75135	0.03544	40.19565	0.02342	0.00142	0.00286	66.01015

Table A.7: Predicted number of events in the antineutrino mode μ-like sample obtained after applying the BANFF weight for a total exposure of 7.558×10^{20} POT. The Asimov data set B in 5.1 is used.

	ν_μ	ν_e	$\bar{\nu}_\mu$	$\bar{\nu}_e$	Osc. ν_e	Osc. $\bar{\nu}_e$	Total
CCQE	0.17174	6.30178	0.00647	0.25566	31.20630	0.33860	38.28056
CC1pi	0.04847	0.93168	0.00282	0.06750	3.28336	0.05561	4.38943
CCcoherent	0.00012	0.00830	0.00018	0.00397	0.02515	0.00382	0.04154
2p2h	0.03143	1.59694	0.00118	0.04275	6.08289	0.04642	7.80162
CCother	0.01346	0.12803	0.00034	0.00942	0.07482	0.00374	0.22981
NC1pi0	1.70203	0.03706	0.06012	0.00356	N/A	N/A	1.80278
NC1piPM	0.16854	0.00472	0.01020	0.00057	N/A	N/A	0.18404
NCcoherent	0.52817	0.00715	0.04794	0.00294	N/A	N/A	0.58619
NCother	0.31767	0.01695	0.02120	0.00128	N/A	N/A	0.35711
NC1gamma	0.94222	0.01687	0.04983	0.00233	N/A	N/A	1.01125
Total	3.92386	9.04948	0.20030	0.38998	40.67252	0.44819	54.68432

Table A.8: Predicted number of events in the neutrino mode e-like sample obtained after applying the BANFF weight for a total exposure of 1.4734×10^{21} POT. The Asimov data set B in 5.1 is used.

	ν_μ	ν_e	$\bar{\nu}_\mu$	$\bar{\nu}_e$	Osc. ν_e	Osc. $\bar{\nu}_e$	Total
CCQE	0.01318	0.50911	0.02513	0.84721	0.72476	3.38779	5.50718
CC1pi	0.00771	0.10111	0.00742	0.14431	0.11344	0.39683	0.77081
CCcoherent	0.00002	0.00099	0.00043	0.01066	0.00090	0.03680	0.04981
2p2h	0.00298	0.14379	0.00224	0.11301	0.17444	0.39087	0.82733
CCother	0.00392	0.02116	0.00121	0.01154	0.00920	0.00777	0.05480
NC1pi0	0.13849	0.00541	0.17659	0.00468	N/A	N/A	0.32516
NC1piPM	0.02475	0.00127	0.02001	0.00080	N/A	N/A	0.04683
NCcoherent	0.04776	0.00221	0.20260	0.00317	N/A	N/A	0.25574
NCother	0.05664	0.00221	0.02672	0.00097	N/A	N/A	0.08654
NC1gamma	0.07943	0.00439	0.17490	0.00383	N/A	N/A	0.26255
Total	0.37487	0.79164	0.63724	1.14019	1.02275	4.22006	8.18675

Table A.9: Predicted number of events in the antineutrino mode μ-like sample obtained after applying the BANFF weight for a total exposure of 7.558×10^{20} POT. The Asimov data set B in 5.1 is used.

	ν_μ	ν_e	$\bar{\nu}_\mu$	$\bar{\nu}_e$	Osc. ν_e	Osc. $\bar{\nu}_e$	Total
CCQE	0.03298	0.02442	0.00123	0.00174	0.14531	0.00339	0.20908
CC1pi	0.08149	0.76065	0.00261	0.00383	3.47649	0.00267	4.32774
CCcoherent	0.00031	0.01765	0.00008	0.00007	0.07633	0.00013	0.09457
2p2h	0.01100	0.02195	0.00050	0.00095	0.11660	0.00125	0.15225
CCother	0.03947	0.11225	0.00117	0.00279	0.09788	0.00174	0.25531
NC1pi0	0.02049	0.00076	0.00083	0.00008	N/A	N/A	0.02216
NC1piPM	0.06474	0.00165	0.00382	0.00033	N/A	N/A	0.07053
NCother	0.20584	0.00830	0.01304	0.00088	N/A	N/A	0.22807
NC1gamma	0.02844	0.00000	0.00067	0.00007	N/A	N/A	0.02918
Total	0.48477	0.94764	0.02396	0.01075	3.91261	0.00917	5.38890

Table A.10: Predicted number of events in the neutrino mode e-like sample obtained after applying the BANFF weight for a total exposure of 1.4734×10^{21} POT. The Asimov data set B in 5.1 is used.

Appendix B

Systematic variations

Table B.1 through table B.10 show the effect of systematic variations on the event rates for pre-BANFF and post-BANFF errors.

Parameter	1 σ value	BANFF tuned -3σ		BANFF tuned -1σ		BANFF tuned +1σ		BANFF tuned +3σ	
All syst		61.9761	−74.2947(%)	143.921	−40.307 (%)	385.63	59.945(%)	900.64	273.551(%)
BANFF 0, SK numu flux, 0.0 - 0.4 GeV	0.098 732 3	234.448	−2.760 12	238.884	−0.920 04	243.321	0.920 04	247.757	2.760 12
BANFF 1, SK numu flux, 0.4 - 0.5 GeV	0.103 488	234.367	−2.793 41	238.857	−0.931 14	243.347	0.931 14	247.837	2.793 41
BANFF 2, SK numu flux, 0.5 - 0.6 GeV	0.096 444	239.435	−0.691 534	240.547	−0.230 51	241.658	0.230 51	242.77	0.691 534
BANFF 3, SK numu flux, 0.6 - 0.7 GeV	0.086 695 8	239.741	−0.564 733	240.648	−0.188 24	241.556	0.188 24	242.464	0.564 733
BANFF 4, SK numu flux, 0.7 - 1.0 GeV	0.113 052	224.426	−6.916 84	235.543	−2.3056	246.661	2.3056	257.779	6.916 84
BANFF 5, SK numu flux, 1.0 - 1.5 GeV	0.091 747 6	228.616	−5.178 78	236.94	−1.7263	245.264	1.7263	253.588	5.178 78
BANFF 6, SK numu flux, 1.5 - 2.5 GeV	0.070 174 2	233.261	−3.252 25	238.489	−1.0841	243.716	1.0841	248.944	3.252 25
BANFF 7, SK numu flux, 2.5 - 3.5 GeV	0.073 680 5	237.002	−1.700 83	239.735	−0.566 94	242.469	0.566 94	245.203	1.700 83
BANFF 8, SK numu flux, 3.5 - 5.0 GeV	0.087 373 3	236.859	−1.760 11	239.688	−0.5867	242.517	0.5867	245.346	1.760 11
BANFF 9, SK numu flux, 5.0 - 7.0 GeV	0.097 936 9	239.83	−0.527 644	240.678	−0.175 88	241.526	0.175 88	242.374	0.527 644
BANFF 10, SK numu flux, 7.0 - 30.0 GeV	0.114 36	240.982	−0.049 815 7	241.062	−0.016 605	241.142	0.016 605	241.222	0.049 815 7
BANFF 11, SK numubar flux, 0.0 - 0.7 GeV	0.102 576	240.821	−0.116 474	241.009	−0.038 825	241.196	0.038 825	241.383	0.116 474
BANFF 12, SK numubar flux, 0.7 - 1.0 GeV	0.078 533 1	240.849	−0.105 028	241.018	−0.035 009	241.187	0.035 009	241.356	0.105 028
BANFF 13, SK numubar flux, 1.0 - 1.5 GeV	0.084 453 6	240.163	−0.389 64	240.789	−0.129 88	241.415	0.129 88	242.042	0.389 64
BANFF 14, SK numubar flux, 1.5 - 2.5 GeV	0.085 568 3	239.779	−0.548 919	240.661	−0.182 97	241.543	0.182 97	242.426	0.548 919
BANFF 15, SK numubar flux, 2.5 - 30.0 GeV	0.086 428 4	240.158	−0.391 625	240.788	−0.130 54	241.417	0.130 54	242.046	0.391 625
BANFF 16, SK nue flux, 0.0 - 0.5 GeV	0.089 698 3	241.101	−0.000 449 436	241.102	−0.000 149 81	241.103	0.000 149 81	241.103	0.000 449 436
BANFF 17, SK nue flux, 0.5 - 0.7 GeV	0.089 952	241.1	−0.001 126 08	241.101	−0.000 375 36	241.103	0.000 375 36	241.105	0.001 126 08
BANFF 18, SK nue flux, 0.7 - 0.8 GeV	0.085 964 8	241.1	−0.000 823 573	241.102	−0.000 274 52	241.103	0.000 274 52	241.104	0.000 823 573
BANFF 19, SK nue flux, 0.8 - 1.5 GeV	0.080 918 2	241.088	−0.005 849 91	241.098	−0.001 95	241.107	0.001 95	241.116	0.005 849 91
BANFF 20, SK nue flux, 1.5 - 2.5 GeV	0.078 971 9	241.085	−0.007 055 64	241.097	−0.002 351 9	241.108	0.002 351 9	241.119	0.007 055 64
BANFF 21, SK nue flux, 2.5 - 4.0 GeV	0.083 85	241.09	−0.005 217 14	241.098	−0.001 739	241.106	0.001 739	241.115	0.005 217 14
BANFF 22, SK nue flux, 4.0 - 30.0 GeV	0.093 894 3	241.096	−0.002 758 5	241.1	−0.000 919 5	241.104	0.000 919 5	241.109	0.002 758 5
BANFF 23, SK nuebar flux, 0.0 - 2.5 GeV	0.074 027 9	241.1	−0.000 885 825	241.102	−0.000 295 28	241.103	0.000 295 28	241.104	0.000 885 825
BANFF 24, SK nuebar flux, 2.5 - 30.0 GeV	0.128 416	241.097	−0.002 092 35	241.101	−0.000 697 45	241.104	0.000 697 45	241.107	0.002 092 35
BANFF; Norm; 2p2h	1	214.649	−10.972	214.649	−10.972	267.556	10.972	320.463	32.9159
BANFF; CA5 RES	0.148 515	223.261	−7.399 78	234.198	−2.8636	248.963	3.2605	267.557	10.9725
BANFF; Norm; BgRES Isospin 1/2	0.307 692	237.768	−1.3831	238.756	−0.973 28	244.684	1.4855	255.552	5.993 38
BANFF, Ma QE	0.025	231.751	−3.878 74	238.038	−1.2711	244.113	1.2487	249.969	3.677 67
BANFF, Ma RES	0.157 895	223.458	−7.318 19	235.185	−2.4544	246.811	2.3678	257.26	6.701 57
BANFF; Fermi Momentum	0.057 777 8	246.226	2.125 31	243.832	1.1323	238.262	−1.1782	232.278	−3.659 93
BANFF; Shape; CC Oth	0.4	238.696	−0.998 015	240.292	−0.336 17	241.913	0.336 17	243.534	1.008 52
BANFF; Norm, CC Coh	0.3	240.713	−0.161 511	240.972	−0.053 837	241.232	0.053 837	241.492	0.161 511
BANFF; Norm, NC Coh	0.3	241.102	−0.000 187 994	241.102	-6.2665×10^{-5}	241.102	6.2665×10^{-5}	241.103	0.000 187 994
BANFF; Norm, NC Oth	0.3	239.074	−0.841 32	240.426	−0.280 44	241.778	0.280 44	243.131	0.841 32
BANFF; Norm, ν_e To ν_μ	0.028 284 3	241.097	−0.002 326 35	241.1	−0.000 775 45	241.104	0.000 775 45	241.108	0.002 326 35
BANFF; Norm, $\bar{\nu}_e$ To $\bar{\nu}_\mu$	0.028 284 3	241.102	$-2.252\,73 \times 10^{-5}$	241.102	-7.5091×10^{-6}	241.102	7.5091×10^{-6}	241.102	$2.252\,73 \times 10^{-5}$
BANFF; Norm; 2p2hBar	1	239.969	−0.470 064	239.969	−0.470 06	242.236	0.470 06	244.502	1.410 19
BANFF; BeRPA A	0.118	207.044	−14.1262	229.749	−4.7088	252.455	4.7088	275.161	14.1263
BANFF; BeRPA B	0.21	208.023	−13.72	230.076	−4.5734	252.129	4.5734	274.182	13.7201
BANFF; BeRPA D	0.1695	216.789	−10.0843	232.998	−3.3614	249.207	3.3615	265.416	10.0843
BANFF; BeRPA E	0.352	240.035	−0.442 852	240.672	−0.178 53	241.537	0.180 37	242.416	0.545 028
BANFF; Shape; 2p2h	3	242.411	0.542 684	241.756	0.271 34	240.37	−0.303 51	239.639	−0.607 028
BANFF; Norm; 2p2h C to O	0.2	224.55	−6.865 22	235.585	−2.2884	246.62	2.2884	257.654	6.865 22
SKDet + FSI/SI 0; E_{reco}(0.00 - 0.40)GeV; $\nu_\mu/\bar{\nu}_\mu$ CCQE ($1R_\mu$)	0.008 785 93	240.569	−0.221 14	240.925	−0.073 713	241.28	0.073 713	241.635	0.221 14
SKDet + FSI/SI 1; E_{reco}(0.40 - 1.10)GeV; $\nu_\mu/\bar{\nu}_\mu$ CCQE ($1R_\mu$)	0.007 403 28	239.211	−0.784 536	240.472	−0.261 51	241.733	0.261 51	242.994	0.784 536
SKDet + FSI/SI 2; E_{reco}(1.10 - 30.00)GeV; $\nu_\mu/\bar{\nu}_\mu$ CCQE ($1R_\mu$)	0.007 204 4	239.287	−0.752 812	240.497	−0.250 94	241.707	0.250 94	242.917	0.752 812
SKDet + FSI/SI 3; E_{reco}(0.00 - 30.00)GeV; $\nu_\mu/\bar{\nu}_\mu$ CCnQE ($1R_\mu$)	0.169 035	219.654	−8.895 93	233.953	−2.9653	248.252	2.9653	262.551	8.895 93
SKDet + FSI/SI 4; E_{reco}(0.00 - 30.00)GeV; $\nu_e/\bar{\nu}_e$/sigν_e CC ($1R_\mu$)	1.005 48	240.901	−0.083 500 7	241.035	−0.027 834	241.169	0.027 834	241.304	0.083 500 7
SKDet + FSI/SI 5; E_{reco}(0.00 - 30.00)GeV; all NC ($1R_\mu$)	0.658 101	222.61	−7.669 98	234.938	−2.5567	247.266	2.5567	259.595	7.669 98
SK energy scale	0.024	241.102	$-2.357\,65 \times 10^{-14}$	241.102	-3.5365×10^{-14}	241.102	-1.1788×10^{-14}	241.102	4.7153×10^{-14}

Table B.1: $\pm1\sigma$ and $\pm3\sigma$ effect of the systematic parameters on the total number of μ-like Super-K events with Run 1-8 POT for neutrino mode pre-BANFF Asimov data set A. Only the systematic parameters which affect this sample are shown.

Parameter	1 σ value	BANFF tuned -3σ		BANFF tuned -1σ		BANFF tuned +1σ		BANFF tuned +3σ	
All syst		19.3721	−66.6249(%)	37.6935	−35.06 (%)	88.523	52.511(%)	201.123	246.503(%)
BANFF 0, SK numu flux, 0.0 - 0.7 GeV; RHC	0.093 682 2	57.6767	−0.632 032	57.9213	−0.210 68	58.1658	0.210 68	58.4104	0.632 032
BANFF 1, SK numu flux, 0.7 - 1.0 GeV; RHC	0.079 343	57.5584	−0.835 793	57.8819	−0.2786	58.2053	0.2786	58.5287	0.835 793
BANFF 2, SK numu flux, 1.0 - 1.5 GeV; RHC	0.076 727 1	56.6231	−2.447 23	57.5701	−0.815 74	58.5171	0.815 74	59.464	2.447 23
BANFF 3, SK numu flux, 1.5 - 2.5 GeV; RHC	0.080 558 7	56.1916	−3.190 67	57.4262	−1.0636	58.6609	1.0636	59.8955	3.190 67
BANFF 4, SK numu flux, 2.5 - 30.0 GeV; RHC	0.080 289 6	56.7027	−2.310 12	57.5966	−0.770 04	58.4905	0.770 04	59.3844	2.310 12
BANFF 5, SK numubar flux, 0.0 - 0.4 GeV; RHC	0.104 476	56.5378	−2.594 24	57.5416	−0.864 75	58.5455	0.864 75	59.5494	2.594 24
BANFF 6, SK numubar flux, 0.4 - 0.5 GeV; RHC	0.101 533	57.067	−1.682 51	57.718	−0.560 84	58.3691	0.560 84	59.0202	1.682 51
BANFF 7, SK numubar flux, 0.5 - 0.6 GeV; RHC	0.096 167 3	57.8301	−0.367 714	57.9724	−0.122 57	58.1147	0.122 57	58.257	0.367 714
BANFF 8, SK numubar flux, 0.6 - 0.7 GeV; RHC	0.084 636 6	57.8844	−0.274 248	57.9905	−0.091 416	58.0966	0.091 416	58.2027	0.274 248
BANFF 9, SK numubar flux, 0.7 - 1.0 GeV; RHC	0.125 091	55.6825	−4.067 81	57.2565	−1.3559	58.8306	1.3559	60.4047	4.067 81
BANFF 10, SK numubar flux, 1.0 - 1.5 GeV; RHC	0.105 291	55.8659	−3.751 76	57.3177	−1.2506	58.7695	1.2506	60.2212	3.751 76
BANFF 11, SK numubar flux, 1.5 - 2.5 GeV; RHC	0.079 987	56.4133	−2.808 66	57.5001	−0.936 22	58.587	0.936 22	59.6738	2.808 66
BANFF 12, SK numubar flux, 2.5 - 3.5 GeV; RHC	0.073 938 4	57.3425	−1.207 82	57.8099	−0.402 61	58.2773	0.402 61	58.7446	1.207 82
BANFF 13, SK numubar flux, 3.5 - 5.0 GeV; RHC	0.093 992 3	57.4113	−1.089 34	57.8328	−0.363 11	58.2543	0.363 11	58.6759	1.089 34
BANFF 14, SK numubar flux, 5.0 - 7.0 GeV; RHC	0.092 512 6	57.9201	−0.212 685	58.0024	−0.070 895	58.0847	0.070 895	58.167	0.212 685
BANFF 15, SK numubar flux, 7.0 - 30.0 GeV; RHC	0.130 312	58.032	−0.019 895 6	58.0397	−0.006 631 9	58.0474	0.006 631 9	58.0551	0.019 895 6
BANFF 16, SK nue flux, 0.0 - 2.5 GeV; RHC	0.068 881 3	58.0397	−0.006 697 58	58.0423	−0.002 232 5	58.0449	0.002 232 5	58.0475	0.006 697 58
BANFF 17, SK nue flux, 2.5 - 30.0 GeV; RHC	0.084 944 6	58.0384	−0.008 949 23	58.0418	−0.002 983 1	58.0453	0.002 983 1	58.0488	0.008 949 23
BANFF 18, SK nuebar flux, 0.0 - 0.5 GeV; RHC	0.094 695 4	58.0435	−0.000 168 308	58.0435	-5.6103×10^{-5}	58.0436	5.6103×10^{-5}	58.0437	0.000 168 308
BANFF 19, SK nuebar flux, 0.5 - 0.7 GeV; RHC	0.091 039 3	58.0432	−0.000 576 142	58.0435	−0.000 192 05	58.0437	0.000 192 05	58.0439	0.000 576 142
BANFF 20, SK nuebar flux, 0.7 - 0.8 GeV; RHC	0.091 012 4	58.0434	−0.000 288 631	58.0435	-9.621×10^{-5}	58.0436	9.621×10^{-5}	58.0437	0.000 288 631
BANFF 21, SK nuebar flux, 0.8 - 1.5 GeV; RHC	0.083 856 5	58.042	−0.002 779 29	58.043	−0.000 926 43	58.0441	0.000 926 43	58.0452	0.002 779 29
BANFF 22, SK nuebar flux, 1.5 - 2.5 GeV; RHC	0.079 577 6	58.042	−0.002 617 59	58.0431	−0.000 872 53	58.0441	0.000 872 53	58.0451	0.002 617 59
BANFF 23, SK nuebar flux, 2.5 - 4.0 GeV; RHC	0.089 007 5	58.0416	−0.003 421 41	58.0429	−0.001 140 5	58.0442	0.001 140 5	58.0456	0.003 421 41
BANFF 24, SK nuebar flux, 4.0 - 30.0 GeV; RHC	0.155 813	58.0419	−0.002 941 6	58.043	−0.000 980 53	58.0441	0.000 980 53	58.0453	0.002 941 6
BANFF; Norm; 2p2h	1	55.0471	−5.162 51	55.0471	−5.1625	61.0401	5.1625	67.0331	15.4875
BANFF; CA5 RES	0.148 515	54.0272	−6.919 63	56.3167	−2.9751	60.1584	3.6436	65.5523	12.9363
BANFF; Norm; BgRES Isospin 1/2	0.307 692	57.1647	−1.514 08	57.4252	−1.0654	58.9874	1.6261	61.8515	6.560 39
BANFF, Ma QE	0.025	56.3858	−2.856 11	57.4906	−0.952 62	58.5957	0.951 22	59.6946	2.844 45
BANFF, Ma RES	0.157 895	54.3275	−6.402 21	56.6448	−2.4099	59.5013	2.5114	62.3804	7.471 77
BANFF; Fermi Momentum	0.057 777 8	59.1725	1.944 97	58.637	1.0224	57.4477	−1.0265	56.2466	−3.095 93
BANFF; Shape; CC Oth	0.4	57.4048	−1.100 53	57.8291	−0.369 55	58.2581	0.369 55	58.6871	1.108 64
BANFF; Norm, CC Coh	0.3	57.8175	−0.389 455	57.9682	−0.129 82	58.1189	0.129 82	58.2696	0.389 455
BANFF; Norm, NC Coh	0.3	58.0416	−0.003 404 46	58.0429	−0.001 134 8	58.0442	0.001 134 8	58.0455	0.003 404 46
BANFF; Norm, NC Oth	0.3	57.5743	−0.808 423	57.8872	−0.269 47	58.2	0.269 47	58.5128	0.808 423
BANFF; Norm, ν_e To ν_μ	0.028 284 3	58.0433	−0.000 419 022	58.0435	−0.000 139 67	58.0436	0.000 139 67	58.0438	0.000 419 022
BANFF; Norm, $\bar{\nu}_e$ To $\bar{\nu}_\mu$	0.028 284 3	58.0433	−0.000 467 005	58.0435	−0.000 155 67	58.0437	0.000 155 67	58.0438	0.000 467 005
BANFF; Norm; 2p2hBar	1	55.5746	−4.253 65	55.5746	−4.2536	60.5125	4.2536	65.4505	12.7609
BANFF; BeRPA A	0.118	51.1456	−11.8841	55.7443	−3.9613	60.3428	3.9613	64.9414	11.8839
BANFF; BeRPA B	0.21	52.501	−9.549 05	56.196	−3.183	59.8911	3.183	63.5862	9.549 09
BANFF; BeRPA D	0.1695	54.0755	−6.836 36	56.7209	−2.2788	59.3663	2.2788	62.0118	6.836 64
BANFF; BeRPA E	0.352	57.8798	−0.282 06	57.9772	−0.114 38	58.111	0.116 18	58.2481	0.352 391
BANFF; Shape; 2p2h	3	58.1578	0.196 836	58.1007	0.098 417	57.9753	−0.117 56	57.9071	−0.235 113
BANFF; Norm; 2p2h C to O	0.2	54.7643	−5.649 69	56.9505	−1.8832	59.1367	1.8832	61.3228	5.649 69
SKDet + FSI/SI 0; E_{reco}(0.00 - 0.40)GeV; $\nu_\mu/\bar{\nu}_\mu$ CCQE ($1R_\mu$); RHC	0.008 512 49	57.9186	−0.215 368	58.0019	−0.071 789	58.0852	0.071 789	58.1686	0.215 368
SKDet + FSI/SI 1; E_{reco}(0.40 - 1.10)GeV; $\nu_\mu/\bar{\nu}_\mu$ CCQE ($1R_\mu$); RHC	0.007 050 99	57.7186	−0.559 823	57.9353	−0.186 61	58.1519	0.186 61	58.3685	0.559 823
SKDet + FSI/SI 2; E_{reco}(1.10 - 30.00)GeV; $\nu_\mu/\bar{\nu}_\mu$ CCQE ($1R_\mu$); RHC	0.006 784	57.5365	−0.873 521	57.8746	−0.291 17	58.2126	0.291 17	58.5506	0.873 521
SKDet + FSI/SI 3; E_{reco}(0.00 - 30.00)GeV; $\nu_\mu/\bar{\nu}_\mu$ CCnQE ($1R_\mu$); RHC	0.129 646	53.7137	−7.4596	56.6003	−2.4865	59.4868	2.4865	62.3734	7.4596
SKDet + FSI/SI 4; E_{reco}(0.00 - 30.00)GeV; $\nu_e/\bar{\nu}_e$/sigν_e CC ($1R_\mu$); RHC	1.004 54	58.0253	−0.031 468	58.0375	−0.010 489	58.0497	0.010 489	58.0618	0.031 468
SKDet + FSI/SI 5; E_{reco}(0.00 - 30.00)GeV; all NC ($1R_\mu$); RHC	0.657 251	54.6208	−5.896 82	56.9027	−1.9656	59.1845	1.9656	61.4663	5.896 82
SK energy scale	0.024	58.0436	$-2.448\,31 \times 10^{-14}$	58.0436	-8.5691×10^{-14}	58.0436	-1.2242×10^{-13}	58.0436	$-6.120\,77 \times 10^{-14}$

Table B.2: $\pm 1\sigma$ and $\pm 3\sigma$ effect of the systematic parameters on the total number of μ-like Super-K events with Run 1-8 POT for antineutrino mode pre-BANFF Asimov data set A. Only the systematic parameters which affect this sample are shown.

Parameter	T2K value	BANFF tuned -3σ		BANFF tuned -1σ		BANFF tuned +1σ		BANFF tuned +3σ	
All syst		13.4912	−79.0516(%)	36.0858	−43.968 (%)	109.17	69.507(%)	276.4	329.178(%)
BANFF 0, SK numu flux, 0.0 - 0.4 GeV	0.098 732 3	64.0102	−0.608 829	64.2716	−0.202 94	64.533	0.202 94	64.7944	0.608 829
BANFF 1, SK numu flux, 0.4 - 0.5 GeV	0.103 488	62.682	−2.671 26	63.8289	−0.890 42	64.9758	0.890 42	66.1227	2.671 26
BANFF 2, SK numu flux, 0.5 - 0.6 GeV	0.096 444	60.6675	−5.799 23	63.1574	−1.9331	65.6473	1.9331	68.1372	5.799 23
BANFF 3, SK numu flux, 0.6 - 0.7 GeV	0.086 695 8	60.3974	−6.218 64	63.0673	−2.0729	65.7373	2.0729	68.4073	6.218 64
BANFF 4, SK numu flux, 0.7 - 1.0 GeV	0.113 052	58.8035	−8.693 53	62.536	−2.8978	66.2686	2.8978	70.0011	8.693 53
BANFF 5, SK numu flux, 1.0 - 1.5 GeV	0.091 747 6	63.687	−1.110 72	64.1639	−0.370 24	64.6408	0.370 24	65.1176	1.110 72
BANFF 6, SK numu flux, 1.5 - 2.5 GeV	0.070 174 2	64.2733	−0.200 259	64.3593	−0.066 753	64.4453	0.066 753	64.5313	0.200 259
BANFF 7, SK numu flux, 2.5 - 3.5 GeV	0.073 680 5	64.3235	−0.122 345	64.376	−0.040 782	64.4286	0.040 782	64.4811	0.122 345
BANFF 8, SK numu flux, 3.5 - 5.0 GeV	0.087 373 3	64.2921	−0.171 13	64.3656	−0.057 043	64.439	0.057 043	64.5125	0.171 13
BANFF 9, SK numu flux, 5.0 - 7.0 GeV	0.097 936 9	64.3488	−0.083 04	64.3845	−0.027 68	64.4201	0.027 68	64.4558	0.083 04
BANFF 10, SK numu flux, 7.0 - 30.0 GeV	0.114 36	64.3732	−0.045 278 9	64.3926	−0.015 093	64.412	0.015 093	64.4315	0.045 278 9
BANFF 11, SK numubar flux, 0.0 - 0.7 GeV	0.102 576	64.3597	−0.066 141 9	64.3881	−0.022 047	64.4165	0.022 047	64.4449	0.066 141 9
BANFF 12, SK numubar flux, 0.7 - 1.0 GeV	0.078 533 1	64.3627	−0.061 523 9	64.3891	−0.020 508	64.4155	0.020 508	64.4419	0.061 523 9
BANFF 13, SK numubar flux, 1.0 - 1.5 GeV	0.084 453 6	64.3682	−0.053 012 6	64.3909	−0.017 671	64.4137	0.017 671	64.4365	0.053 012 6
BANFF 14, SK numubar flux, 1.5 - 2.5 GeV	0.085 568 3	64.3811	−0.033 001 7	64.3952	−0.011 001	64.4094	0.011 001	64.4236	0.033 001 7
BANFF 15, SK numubar flux, 2.5 - 30.0 GeV	0.086 428 4	64.3817	−0.031 934 7	64.3955	−0.010 645	64.4092	0.010 645	64.4229	0.031 934 7
BANFF 16, SK nue flux, 0.0 - 0.5 GeV	0.089 698 3	64.0426	−0.558 585	64.2824	−0.1862	64.5222	0.1862	64.7621	0.558 585
BANFF 17, SK nue flux, 0.5 - 0.7 GeV	0.089 952	63.9068	−0.769 331	64.2372	−0.256 44	64.5675	0.256 44	64.8978	0.769 331
BANFF 18, SK nue flux, 0.7 - 0.8 GeV	0.085 964 8	64.1548	−0.384 367	64.3198	−0.128 12	64.4848	0.128 12	64.6499	0.384 367
BANFF 19, SK nue flux, 0.8 - 1.5 GeV	0.080 918 2	63.6486	−1.170 31	64.1511	−0.3901	64.6535	0.3901	65.156	1.170 31
BANFF 20, SK nue flux, 1.5 - 2.5 GeV	0.078 971 9	64.3446	−0.089 644 1	64.3831	−0.029 881	64.4216	0.029 881	64.46	0.089 644 1
BANFF 21, SK nue flux, 2.5 - 4.0 GeV	0.083 85	64.3936	−0.013 484 5	64.3994	−0.004 494 8	64.4052	0.004 494 8	64.411	0.013 484 5
BANFF 22, SK nue flux, 4.0 - 30.0 GeV	0.093 894 3	64.3987	−0.005 670 38	64.4011	−0.001 890 1	64.4035	0.001 890 1	64.406	0.005 670 38
BANFF 23, SK nuebar flux, 0.0 - 2.5 GeV	0.074 027 9	64.3297	−0.112 81	64.3781	−0.037 603	64.4265	0.037 603	64.475	0.112 81
BANFF 24, SK nuebar flux, 2.5 - 30.0 GeV	0.128 416	64.3995	−0.004 383 1	64.4014	−0.001 461	64.4033	0.001 461	64.4051	0.004 383 1
BANFF; Norm; 2p2h	1	57.5264	−10.6765	57.5264	−10.677	71.2782	10.677	85.0301	32.0295
BANFF; CA5 RES	0.148 515	60.5772	−5.939 36	62.946	−2.2612	66.0398	2.5426	69.8586	8.472 18
BANFF; Norm; BgRES Isospin 1/2	0.307 692	63.9148	−0.756 971	64.0593	−0.532 67	64.9259	0.813 02	66.5148	3.280 13
BANFF, Ma QE	0.025	61.7753	−4.078 99	63.5516	−1.3209	65.2283	1.2825	66.8074	3.734 46
BANFF, Ma RES	0.157 895	61.1503	−5.0496	63.4044	−1.5494	65.3124	1.4132	66.9029	3.882 76
BANFF; Fermi Momentum	0.057 777 8	65.765	2.115 87	65.128	1.1268	63.6315	−1.1968	61.9681	−3.779 65
BANFF; Shape; CC Oth	0.4	64.2479	−0.239 744	64.3445	−0.089 736	64.4601	0.089 736	64.5757	0.269 208
BANFF; Norm, CC Coh	0.3	64.3496	−0.081 866 2	64.3847	−0.027 289	64.4199	0.027 289	64.455	0.081 866 2
BANFF; Norm, NC Coh	0.3	63.8321	−0.885 326	64.2123	−0.295 11	64.5924	0.295 11	64.9725	0.885 326
BANFF; Norm, NC Oth	0.3	64.0843	−0.493 823	64.2963	−0.164 61	64.5083	0.164 61	64.7203	0.493 823
BANFF; Norm, ν_e To ν_μ	0.028 284 3	59.4949	−7.619 97	62.7665	−2.54	66.0381	2.54	69.3097	7.619 97
BANFF; Norm; NC 1 γ	1	62.3329	−3.213 31	62.3329	−3.2133	66.4718	3.2133	70.6107	9.639 94
BANFF; Norm, $\bar{\nu}_e$ To $\bar{\nu}_\mu$	0.028 284 3	64.347	−0.085 852 9	64.3839	−0.028 618	64.4207	0.028 618	64.4576	0.085 852 9
BANFF; Norm; 2p2hBar	1	64.3424	−0.093 002 2	64.3424	−0.093 002	64.4622	0.093 002	64.582	0.279 007
BANFF; BeRPA A	0.118	55.2091	−14.2747	61.3379	−4.7582	67.4667	4.7582	73.5956	14.2747
BANFF; BeRPA B	0.21	53.464	−16.9843	60.7562	−5.6614	68.0484	5.6614	75.3406	16.9843
BANFF; BeRPA D	0.1695	58.0806	−9.815 99	62.2951	−3.272	66.5096	3.272	70.724	9.815 97
BANFF; BeRPA E	0.352	64.0489	−0.548 743	64.2615	−0.2187	64.5432	0.218 73	64.8249	0.656 212
BANFF; Shape; 2p2h	3	63.9869	−0.644 983	64.1946	−0.322 49	64.603	0.311 56	64.8036	0.623 127
BANFF; Norm; 2p2h C to O	0.2	60.2408	−6.4617	63.0152	−2.1539	65.7895	2.1539	68.5638	6.4617
SKDet + FSI/SI 6; E_{reco}(0.00 - 0.35)GeV; Osc. ν_e CC ($1R_e$)	0.181 271	61.2702	−4.863 41	63.3583	−1.6211	65.4464	1.6211	67.5345	4.863 41
SKDet + FSI/SI 7; E_{reco}(0.35 - 0.80)GeV; Osc. ν_e CC ($1R_e$)	0.036 083	60.4597	−6.1219	63.0881	−2.0406	65.7165	2.0406	68.345	6.1219
SKDet + FSI/SI 8; E_{reco}(0.80 - 1.25)GeV; Osc. ν_e CC ($1R_e$)	0.041 663 6	63.3311	−1.663 28	64.0452	−0.554 43	64.7594	0.554 43	65.4735	1.663 28
SKDet + FSI/SI 9; E_{reco}(0.00 - 0.35)GeV; $\nu_\mu/\bar{\nu}_\mu$ CC ($1R_e$)	0.300 431	64.3482	−0.083 951 1	64.3843	−0.027 984	64.4203	0.027 984	64.4564	0.083 951 1
SKDet + FSI/SI 10; E_{reco}(0.35 - 0.80)GeV; $\nu_\mu/\bar{\nu}_\mu$ CC ($1R_e$)	0.321 346	64.2457	−0.243 223	64.3501	−0.081 074	64.4545	0.081 074	64.559	0.243 223
SKDet + FSI/SI 11; E_{reco}(0.80 - 1.25)GeV; $\nu_\mu/\bar{\nu}_\mu$ CC ($1R_e$)	0.392 969	64.3731	−0.045 282 3	64.3926	−0.015 094	64.412	0.015 094	64.4315	0.045 282 3
SKDet + FSI/SI 12; E_{reco}(0.00 - 0.35)GeV; $\nu_e/\bar{\nu}_e$ CC ($1R_e$)	0.135 399	64.0289	−0.579 849	64.2778	−0.193 28	64.5268	0.193 28	64.7757	0.579 849
SKDet + FSI/SI 13; E_{reco}(0.35 - 0.80)GeV; $\nu_e/\bar{\nu}_e$ CC ($1R_e$)	0.069 892 8	63.5422	−1.335 58	64.1156	−0.445 19	64.689	0.445 19	65.2625	1.335 58
SKDet + FSI/SI 14; E_{reco}(0.80 - 1.25)GeV; $\nu_e/\bar{\nu}_e$ CC ($1R_e$)	0.077 136 1	63.7745	−0.974 818	64.193	−0.324 94	64.6116	0.324 94	65.0301	0.974 818
SKDet + FSI/SI 15; E_{reco}(0.00 - 0.35)GeV; all NC ($1R_e$)	0.194 453	63.1388	−1.961 83	63.9812	−0.653 94	64.8235	0.653 94	65.6658	1.961 83
SKDet + FSI/SI 16; E_{reco}(0.35 - 0.80)GeV; all NC ($1R_e$)	0.181 015	62.8486	−2.412 51	63.8844	−0.804 17	64.9202	0.804 17	65.956	2.412 51
SKDet + FSI/SI 17; E_{reco}(0.80 - 1.25)GeV; all NC ($1R_e$)	0.472 078	63.4933	−1.4115	64.0993	−0.4705	64.7053	0.4705	65.3113	1.4115
SK energy scale	0.024	64.4023	0	64.4023	-2.2066×10^{-14}	64.4023	0	64.4023	0

Table B.3: $\pm1\sigma$ and $\pm3\sigma$ effect of the systematic parameters on the total number of e-like Super-K events with Run 1-8 POT for neutrino mode pre-BANFF Asimov data set A. Only the systematic parameters which affect this sample are shown.

Parameter	1 σ value	BANFF tuned -3σ		BANFF tuned -1σ		BANFF tuned +1σ		BANFF tuned +3σ	
All syst		1.979 92	−73.1627(%)	4.194 57	−43.144 (%)	12.51	69.576(%)	32.2025	336.497(%)
BANFF 0, SK numu flux, 0.0 - 0.7 GeV; RHC	0.093 682 2	7.219 18	−2.145 75	7.324 71	−0.715 25	7.430 25	0.715 25	7.535 78	2.145 75
BANFF 1, SK numu flux, 0.7 - 1.0 GeV; RHC	0.079 343	7.256 37	−1.641 56	7.337 11	−0.547 19	7.417 85	0.547 19	7.498 59	1.641 56
BANFF 2, SK numu flux, 1.0 - 1.5 GeV; RHC	0.076 727 1	7.304 03	−0.995 621	7.353	−0.331 87	7.401 96	0.331 87	7.450 93	0.995 621
BANFF 3, SK numu flux, 1.5 - 2.5 GeV; RHC	0.080 558 7	7.341 56	−0.486 92	7.365 51	−0.162 31	7.389 46	0.162 31	7.4134	0.486 92
BANFF 4, SK numu flux, 2.5 - 30.0 GeV; RHC	0.080 289 6	7.337 62	−0.540 283	7.364 19	−0.180 09	7.390 77	0.180 09	7.417 34	0.540 283
BANFF 5, SK numubar flux, 0.0 - 0.4 GeV; RHC	0.104 476	7.353 38	−0.326 617	7.369 45	−0.108 87	7.385 51	0.108 87	7.401 58	0.326 617
BANFF 6, SK numubar flux, 0.4 - 0.5 GeV; RHC	0.101 533	7.290 96	−1.172 75	7.348 64	−0.390 92	7.406 32	0.390 92	7.464	1.172 75
BANFF 7, SK numubar flux, 0.5 - 0.6 GeV; RHC	0.096 167 3	7.156 96	−2.989 11	7.303 97	−0.996 37	7.450 99	0.996 37	7.598	2.989 11
BANFF 8, SK numubar flux, 0.6 - 0.7 GeV; RHC	0.084 636 6	7.110 41	−3.620 06	7.288 46	−1.2067	7.4665	1.2067	7.644 55	3.620 06
BANFF 9, SK numubar flux, 0.7 - 1.0 GeV; RHC	0.125 091	6.877 86	−6.772 27	7.210 94	−2.2574	7.544 02	2.2574	7.8771	6.772 27
BANFF 10, SK numubar flux, 1.0 - 1.5 GeV; RHC	0.105 291	7.285 18	−1.251 17	7.346 71	−0.417 06	7.408 25	0.417 06	7.469 79	1.251 17
BANFF 11, SK numubar flux, 1.5 - 2.5 GeV; RHC	0.079 987	7.353 22	−0.328 861	7.369 39	−0.109 62	7.385 57	0.109 62	7.401 74	0.328 861
BANFF 12, SK numubar flux, 2.5 - 3.5 GeV; RHC	0.073 938 4	7.3661	−0.154 206	7.373 69	−0.051 402	7.381 27	0.051 402	7.388 86	0.154 206
BANFF 13, SK numubar flux, 3.5 - 5.0 GeV; RHC	0.093 992 3	7.364 21	−0.179 93	7.373 06	−0.059 977	7.381 91	0.059 977	7.390 76	0.179 93
BANFF 14, SK numubar flux, 5.0 - 7.0 GeV; RHC	0.092 512 6	7.373 16	−0.058 575 7	7.376 04	−0.019 525	7.378 92	0.019 525	7.3818	0.058 575 7
BANFF 15, SK numubar flux, 7.0 - 30.0 GeV; RHC	0.130 312	7.374 81	−0.036 139	7.376 59	−0.012 046	7.378 37	0.012 046	7.380 15	0.036 139
BANFF 16, SK nue flux, 0.0 - 2.5 GeV; RHC	0.068 881 3	7.243 97	−1.809 73	7.332 98	−0.603 24	7.421 99	0.603 24	7.510 99	1.809 73
BANFF 17, SK nue flux, 2.5 - 30.0 GeV; RHC	0.084 944 6	7.375 09	−0.032 427 5	7.376 68	−0.010 809	7.378 28	0.010 809	7.379 87	0.032 427 5
BANFF 18, SK nuebar flux, 0.0 - 0.5 GeV; RHC	0.094 695 4	7.325 35	−0.706 645	7.3601	−0.235 55	7.394 86	0.235 55	7.429 61	0.706 645
BANFF 19, SK nuebar flux, 0.5 - 0.7 GeV; RHC	0.091 039 3	7.317 31	−0.815 59	7.357 42	−0.271 86	7.397 54	0.271 86	7.437 65	0.815 59
BANFF 20, SK nuebar flux, 0.7 - 0.8 GeV; RHC	0.091 012 4	7.344 44	−0.447 891	7.366 47	−0.1493	7.3885	0.1493	7.410 52	0.447 891
BANFF 21, SK nuebar flux, 0.8 - 1.5 GeV; RHC	0.083 856 5	7.268 36	−1.4791	7.341 11	−0.493 03	7.413 85	0.493 03	7.4866	1.4791
BANFF 22, SK nuebar flux, 1.5 - 2.5 GeV; RHC	0.079 577 6	7.370 79	−0.090 695 5	7.375 25	−0.030 232	7.379 71	0.030 232	7.384 17	0.090 695 5
BANFF 23, SK nuebar flux, 2.5 - 4.0 GeV; RHC	0.089 007 5	7.376 11	−0.018 546 3	7.377 02	−0.006 182 1	7.377 94	0.006 182 1	7.378 85	0.018 546 3
BANFF 24, SK nuebar flux, 4.0 - 30.0 GeV; RHC	0.155 813	7.376 35	−0.015 332 2	7.3771	−0.005 110 7	7.377 86	0.005 110 7	7.378 61	0.015 332 2
BANFF; Norm; 2p2h	1	7.132 28	−3.323 58	7.132 28	−3.3236	7.622 68	3.3236	8.113 07	9.970 75
BANFF; CA5 RES	0.148 515	6.848 93	−7.164 38	7.1284	−3.3762	7.699 46	4.3644	8.562 12	16.0575
BANFF; Norm; BgRES Isospin 1/2	0.307 692	7.286 15	−1.237 96	7.313 21	−0.871 15	7.475 58	1.3297	7.773 24	5.364 46
BANFF, Ma QE	0.025	7.198 64	−2.424 09	7.318 05	−0.805 61	7.436 54	0.800 56	7.553 11	2.380 56
BANFF, Ma RES	0.157 895	6.986 82	−5.295 35	7.221 81	−2.1101	7.540 13	2.2047	7.857 05	6.500 38
BANFF; Fermi Momentum	0.057 777 8	7.530 15	2.069 35	7.458 34	1.0961	7.295 45	−1.1119	7.127 52	−3.3882
BANFF; Shape; CC Oth	0.4	7.344 09	−0.452 601	7.365 67	−0.160 04	7.389 29	0.160 04	7.4129	0.480 121
BANFF; Norm, CC Coh	0.3	7.3311	−0.628 631	7.362 02	−0.209 54	7.392 94	0.209 54	7.423 86	0.628 631
BANFF; Norm, NC Coh	0.3	7.131 97	−3.327 78	7.295 65	−1.1093	7.459 32	1.1093	7.622 99	3.327 78
BANFF; Norm, NC Oth	0.3	7.302 47	−1.016 77	7.352 48	−0.338 92	7.402 48	0.338 92	7.452 49	1.016 77
BANFF; Norm, ν_e To ν_μ	0.028 284 3	7.221 29	−2.117 13	7.325 42	−0.705 71	7.429 54	0.705 71	7.533 67	2.117 13
BANFF; Norm; NC 1 γ	1	6.853 36	−7.1043	6.853 36	−7.1043	7.9016	7.1043	8.949 84	21.3129
BANFF; Norm, $\bar{\nu}_e$ To $\bar{\nu}_\mu$	0.028 284 3	7.0285	−4.730 33	7.261 15	−1.5768	7.493 81	1.5768	7.726 46	4.730 33
BANFF; Norm; 2p2hBar	1	7.054 87	−4.372 86	7.054 87	−4.3729	7.700 09	4.3729	8.3453	13.1186
BANFF; BeRPA A	0.118	6.480 99	−12.1517	7.078 65	−4.0506	7.676 31	4.0506	8.273 97	12.1517
BANFF; BeRPA B	0.21	6.6711	−9.574 82	7.142 02	−3.1916	7.612 94	3.1916	8.083 86	9.574 79
BANFF; BeRPA D	0.1695	7.055 99	−4.357 67	7.270 32	−1.4526	7.484 64	1.4526	7.698 97	4.357 65
BANFF; BeRPA E	0.352	7.359 57	−0.242 812	7.370 34	−0.096 784	7.384 62	0.096 802	7.398 91	0.290 453
BANFF; Shape; 2p2h	3	7.337 46	−0.542 431	7.357 47	−0.271 22	7.409 66	0.436 17	7.441 84	0.872 345
BANFF; Norm; 2p2h C to O	0.2	7.0368	−4.617 87	7.263 92	−1.5393	7.491 04	1.5393	7.718 16	4.617 87
SKDet + FSI/SI 6; E_{reco}(0.00 - 0.35)GeV; Osc. ν_e CC ($1R_e$); RHC	0.108 165	7.263 51	−1.544 86	7.339 49	−0.514 95	7.415 47	0.514 95	7.491 45	1.544 86
SKDet + FSI/SI 7; E_{reco}(0.35 - 0.80)GeV; Osc. ν_e CC ($1R_e$); RHC	0.036 303 9	7.0458	−4.4959	7.266 92	−1.4986	7.488 04	1.4986	7.709 17	4.4959
SKDet + FSI/SI 8; E_{reco}(0.80 - 1.25)GeV; Osc. ν_e CC ($1R_e$); RHC	0.056 731 5	7.216 19	−2.186 26	7.323 72	−0.728 75	7.431 24	0.728 75	7.538 77	2.186 26
SKDet + FSI/SI 9; E_{reco}(0.00 - 0.35)GeV; $\nu_\mu/\bar{\nu}_\mu$ CC ($1R_e$); RHC	0.348 644	7.367 59	−0.134 016	7.374 19	−0.044 672	7.380 78	0.044 672	7.387 37	0.134 016
SKDet + FSI/SI 10; E_{reco}(0.35 - 0.80)GeV; $\nu_\mu/\bar{\nu}_\mu$ CC ($1R_e$); RHC	0.341 647	7.340 54	−0.500 721	7.365 17	−0.166 91	7.389 79	0.166 91	7.414 42	0.500 721
SKDet + FSI/SI 11; E_{reco}(0.80 - 1.25)GeV; $\nu_\mu/\bar{\nu}_\mu$ CC ($1R_e$); RHC	0.417 164	7.360 76	−0.226 635	7.371 91	−0.075 545	7.383 05	0.075 545	7.3942	0.226 635
SKDet + FSI/SI 12; E_{reco}(0.00 - 0.35)GeV; $\nu_e/\bar{\nu}_e$ CC ($1R_e$); RHC	0.084 556 3	7.336 87	−0.550 513	7.363 94	−0.1835	7.391 02	0.1835	7.418 09	0.550 513
SKDet + FSI/SI 13; E_{reco}(0.35 - 0.80)GeV; $\nu_e/\bar{\nu}_e$ CC ($1R_e$); RHC	0.056 069 7	7.2436	−1.814 67	7.332 86	−0.604 89	7.422 11	0.604 89	7.511 36	1.814 67
SKDet + FSI/SI 14; E_{reco}(0.80 - 1.25)GeV; $\nu_e/\bar{\nu}_e$ CC ($1R_e$); RHC	0.078 024 1	7.2246	−2.072 23	7.326 52	−0.690 74	7.428 44	0.690 74	7.530 36	2.072 23
SKDet + FSI/SI 15; E_{reco}(0.00 - 0.35)GeV; all NC ($1R_e$); RHC	0.214 066	7.064 69	−4.239 82	7.273 22	−1.4133	7.481 74	1.4133	7.690 27	4.239 82
SKDet + FSI/SI 16; E_{reco}(0.35 - 0.80)GeV; all NC ($1R_e$); RHC	0.190 575	6.973 98	−5.469 32	7.242 98	−1.8231	7.511 98	1.8231	7.780 98	5.469 32
SKDet + FSI/SI 17; E_{reco}(0.80 - 1.25)GeV; all NC ($1R_e$); RHC	0.464 86	7.137 17	−3.2574	7.297 38	−1.0858	7.457 59	1.0858	7.617 79	3.2574
SK energy scale	0.024	7.377 48	0	7.377 48	-1.2039×10^{-14}	7.377 48	-2.4078×10^{-14}	7.377 48	0

Table B.4: $\pm1\sigma$ and $\pm3\sigma$ effect of the systematic parameters on the total number of e-like Super-K events with Run 1-8 POT for antineutrino mode pre-BANFF Asimov data set A. Only the systematic parameters which affect this sample are shown.

Parameter	1 σ value	BANFF tuned -3σ		BANFF tuned -1σ		BANFF tuned +1σ		BANFF tuned +3σ	
All syst		0.424 293	−94.5073(%)	3.6093	−53.276 (%)	14.919	93.127(%)	45.8854	494.009(%)
BANFF 0, SK numu flux, 0.0 - 0.4 GeV	0.098 732 3	7.721 82	−0.037 355 8	7.723 75	−0.012 452	7.725 67	0.012 452	7.727 59	0.037 355 8
BANFF 1, SK numu flux, 0.4 - 0.5 GeV	0.103 488	7.633 42	−1.181 75	7.694 28	−0.393 92	7.755 14	0.393 92	7.815 99	1.181 75
BANFF 2, SK numu flux, 0.5 - 0.6 GeV	0.096 444	7.359 53	−4.727 45	7.602 98	−1.5758	7.846 43	1.5758	8.089 89	4.727 45
BANFF 3, SK numu flux, 0.6 - 0.7 GeV	0.086 695 8	7.204 13	−6.739 09	7.551 18	−2.2464	7.898 23	2.2464	8.245 28	6.739 09
BANFF 4, SK numu flux, 0.7 - 1.0 GeV	0.113 052	6.907 02	−10.5853	7.452 15	−3.5284	7.997 27	3.5284	8.542 39	10.5853
BANFF 5, SK numu flux, 1.0 - 1.5 GeV	0.091 747 6	7.623 55	−1.309 51	7.690 99	−0.4365	7.758 43	0.4365	7.825 86	1.309 51
BANFF 6, SK numu flux, 1.5 - 2.5 GeV	0.070 174 2	7.702 59	−0.286 339	7.717 33	−0.095 446	7.732 08	0.095 446	7.746 83	0.286 339
BANFF 7, SK numu flux, 2.5 - 3.5 GeV	0.073 680 5	7.710 56	−0.183 134	7.719 99	−0.061 045	7.729 42	0.061 045	7.738 85	0.183 134
BANFF 8, SK numu flux, 3.5 - 5.0 GeV	0.087 373 3	7.6978	−0.348 282	7.715 74	−0.116 09	7.733 68	0.116 09	7.751 61	0.348 282
BANFF 9, SK numu flux, 5.0 - 7.0 GeV	0.097 936 9	7.713 17	−0.149 381	7.720 86	−0.049 794	7.728 55	0.049 794	7.736 25	0.149 381
BANFF 10, SK numu flux, 7.0 - 30.0 GeV	0.114 36	7.7233	−0.018 241	7.724 24	−0.006 080 3	7.725 18	0.006 080 3	7.726 12	0.018 241
BANFF 11, SK numubar flux, 0.0 - 0.7 GeV	0.102 576	7.723 85	−0.011 103 3	7.724 42	−0.003 701 1	7.724 99	0.003 701 1	7.725 56	0.011 103 3
BANFF 12, SK numubar flux, 0.7 - 1.0 GeV	0.078 533 1	7.723 78	−0.012 024	7.7244	−0.004 008	7.725 02	0.004 008	7.725 64	0.012 024
BANFF 13, SK numubar flux, 1.0 - 1.5 GeV	0.084 453 6	7.723 26	−0.018 690 7	7.724 23	−0.006 230 2	7.725 19	0.006 230 2	7.726 15	0.018 690 7
BANFF 14, SK numubar flux, 1.5 - 2.5 GeV	0.085 568 3	7.722 55	−0.027 962 6	7.723 99	−0.009 320 9	7.725 43	0.009 320 9	7.726 87	0.027 962 6
BANFF 15, SK numubar flux, 2.5 - 30.0 GeV	0.086 428 4	7.7221	−0.033 754 7	7.723 84	−0.011 252	7.725 58	0.011 252	7.727 31	0.033 754 7
BANFF 16, SK nue flux, 0.0 - 0.5 GeV	0.089 698 3	7.714 48	−0.132 379	7.7213	−0.044 126	7.728 12	0.044 126	7.734 93	0.132 379
BANFF 17, SK nue flux, 0.5 - 0.7 GeV	0.089 952	7.668 23	−0.731 188	7.705 88	−0.243 73	7.743 53	0.243 73	7.781 19	0.731 188
BANFF 18, SK nue flux, 0.7 - 0.8 GeV	0.085 964 8	7.6858	−0.503 612	7.711 74	−0.167 87	7.737 67	0.167 87	7.763 61	0.503 612
BANFF 19, SK nue flux, 0.8 - 1.5 GeV	0.080 918 2	7.585 96	−1.796 18	7.678 46	−0.598 73	7.770 96	0.598 73	7.863 46	1.796 18
BANFF 20, SK nue flux, 1.5 - 2.5 GeV	0.078 971 9	7.713 81	−0.141 038	7.721 08	−0.047 013	7.728 34	0.047 013	7.7356	0.141 038
BANFF 21, SK nue flux, 2.5 - 4.0 GeV	0.083 85	7.723 24	−0.018 965 5	7.724 22	−0.006 321 8	7.7252	0.006 321 8	7.726 17	0.018 965 5
BANFF 22, SK nue flux, 4.0 - 30.0 GeV	0.093 894 3	7.724 12	−0.007 605 52	7.724 51	−0.002 535 2	7.7249	0.002 535 2	7.725 29	0.007 605 52
BANFF 23, SK nuebar flux, 0.0 - 2.5 GeV	0.074 027 9	7.722 91	−0.023 243	7.724 11	−0.007 747 7	7.725 31	0.007 747 7	7.7265	0.023 243
BANFF 24, SK nuebar flux, 2.5 - 30.0 GeV	0.128 416	7.724 28	−0.005 480 76	7.724 57	−0.001 826 9	7.724 85	0.001 826 9	7.725 13	0.005 480 76
BANFF; Norm; 2p2h	1	7.621 98	−1.329 85	7.621 98	−1.3298	7.827 43	1.3298	8.032 89	3.989 54
BANFF; CA5 RES	0.148 515	4.948 98	−35.9331	6.684 39	−13.467	8.880 11	14.957	11.5362	49.3409
BANFF; Norm; BgRES Isospin 1/2	0.307 692	7.420 76	−3.934 73	7.510 82	−2.7689	8.051 17	4.2262	9.041 81	17.0505
BANFF, Ma QE	0.025	7.709 58	−0.195 853	7.7198	−0.063 538	7.729 48	0.061 781	7.738 62	0.180 117
BANFF, Ma RES	0.157 895	5.557 65	−28.0536	7.121 25	−7.8121	8.227 51	6.509	9.004 84	16.5719
BANFF; Fermi Momentum	0.057 777 8	7.730 57	0.075 903 9	7.727 76	0.039 489	7.721 22	−0.045 097	7.713 41	−0.146 216
BANFF; Shape; CC Oth	0.4	7.537 21	−2.427 24	7.648 13	−0.991 37	7.801 29	0.991 37	7.954 45	2.974 11
BANFF; Norm, CC Coh	0.3	7.589 06	−1.755 98	7.679 49	−0.585 33	7.769 92	0.585 33	7.860 35	1.755 98
BANFF; Norm, NC Oth	0.3	7.522 66	−2.615 63	7.657 36	−0.871 88	7.792 06	0.871 88	7.926 76	2.615 63
BANFF; Norm, ν_e To ν_μ	0.028 284 3	7.118 46	−7.848 14	7.522 63	−2.616	7.926 79	2.616	8.330 95	7.848 14
BANFF; Norm; NC 1 γ	1	7.666 15	−0.758 101	7.666 15	−0.7581	7.783 27	0.7581	7.900 39	2.2743
BANFF; Norm, $\bar{\nu}_e$ To $\bar{\nu}_\mu$	0.028 284 3	7.7235	−0.015 681 4	7.7243	−0.005 227 1	7.725 11	0.005 227 1	7.725 92	0.015 681 4
BANFF; Norm; 2p2hBar	1	7.723 12	−0.020 606 6	7.723 12	−0.020 607	7.7263	0.020 607	7.729 48	0.061 819 8
BANFF; BeRPA A	0.118	7.6872	−0.485 527	7.712 21	−0.161 84	7.737 21	0.161 84	7.762 21	0.485 527
BANFF; BeRPA B	0.21	7.663 89	−0.787 311	7.704 43	−0.262 44	7.744 98	0.262 44	7.785 52	0.787 31
BANFF; BeRPA D	0.1695	7.686 58	−0.493 568	7.712	−0.164 52	7.737 42	0.164 52	7.762 83	0.493 568
BANFF; BeRPA E	0.352	7.722 55	−0.027 970 1	7.723 85	−0.011 147	7.725 57	0.011 148	7.727 29	0.033 442 8
BANFF; Shape; 2p2h	3	7.6796	−0.583 888	7.702 16	−0.291 94	7.742 43	0.229 37	7.760 14	0.458 739
BANFF; Norm; 2p2h C to O	0.2	7.662 12	−0.810 272	7.703 84	−0.270 09	7.745 57	0.270 09	7.7873	0.810 272
SKDet + FSI/SI 0; E_{reco}(0.30 - 0.80)GeV; Osc. ν_e CC ($MultiR_e$); MultiRing	0.248 951	4.603 12	−40.4104	6.684 18	−13.47	8.765 24	13.47	10.8463	40.4104
SKDet + FSI/SI 1; E_{reco}(0.80 - 1.25)GeV; Osc. ν_e CC ($MultiR_e$); MultiRing	0.214 994	6.460 97	−16.3597	7.303 46	−5.4532	8.145 95	5.4532	8.988 45	16.3597
SKDet + FSI/SI 2; E_{reco}(0.30 - 0.80)GeV; $\nu_\mu/\bar{\nu}_\mu$ CC ($MultiR_e$); MultiRing	0.507 403	7.569 86	−2.004 53	7.673 09	−0.668 18	7.776 32	0.668 18	7.879 55	2.004 53
SKDet + FSI/SI 3; E_{reco}(0.80 - 1.25)GeV; $\nu_\mu/\bar{\nu}_\mu$ CC ($MultiR_e$); MultiRing	0.236 118	7.687 85	−0.477 076	7.712 42	−0.159 03	7.736 99	0.159 03	7.761 56	0.477 076
SKDet + FSI/SI 4; E_{reco}(0.30 - 0.80)GeV; $\nu_e/\bar{\nu}_e$ CC ($MultiR_e$); MultiRing	0.244 289	7.426 86	−3.855 77	7.625 42	−1.2853	7.823 99	1.2853	8.022 55	3.855 77
SKDet + FSI/SI 5; E_{reco}(0.80 - 1.25)GeV; $\nu_e/\bar{\nu}_e$ CC ($MultiR_e$); MultiRing	0.234 55	7.292 99	−5.588 77	7.5808	−1.8629	7.868 61	1.8629	8.156 42	5.588 77
SKDet + FSI/SI 6; E_{reco}(0.30 - 0.80)GeV; all NC ($MultiR_e$); MultiRing	0.983 178	6.846 41	−11.37	7.431 94	−3.79	8.017 47	3.79	8.603 01	11.37
SKDet + FSI/SI 7; E_{reco}(0.80 - 1.25)GeV; all NC ($MultiR_e$); MultiRing	0.523 609	7.545 27	−2.3229	7.664 89	−0.7743	7.784 52	0.7743	7.904 14	2.3229
SK energy scale	0.024	7.724 71	0	7.724 71	2.2996×10^{-14}	7.724 71	0	7.724 71	$1.149 79 \times 10^{-14}$

Table B.5: $\pm 1\sigma$ and $\pm 3\sigma$ effect of the systematic parameters on the total number of e-like Super-K events with one decay electron with Run 1-8 POT for neutrino mode pre-BANFF Asimov data set A. Only the systematic parameters which affect this sample are shown.

Parameter	1 σ value	BANFF tuned -3σ		BANFF tuned -1σ		BANFF tuned +1σ		BANFF tuned +3σ	
All syst		107.89	−58.8929(%)	200.066	−23.773 (%)	337.7	28.666(%)	550.51	109.75 (%)
BANFF 0, SK numu flux, 0.0 - 0.4 GeV	0.057 496 7	257.64	−1.836 31	260.853	−0.6121	264.066	0.6121	267.28	1.836 31
BANFF 1, SK numu flux, 0.4 - 0.5 GeV	0.051 936 3	258.407	−1.544 03	261.109	−0.514 68	263.811	0.514 68	266.512	1.544 03
BANFF 2, SK numu flux, 0.5 - 0.6 GeV	0.044 568 2	261.573	−0.337 759	262.164	−0.112 59	262.755	0.112 59	263.346	0.337 759
BANFF 3, SK numu flux, 0.6 - 0.7 GeV	0.041 886 1	261.743	−0.273 275	262.221	−0.091 092	262.699	0.091 092	263.177	0.273 275
BANFF 4, SK numu flux, 0.7 - 1.0 GeV	0.054 16	253.774	−3.309 58	259.565	−1.1032	265.355	1.1032	271.146	3.309 58
BANFF 5, SK numu flux, 1.0 - 1.5 GeV	0.049 026 1	255.414	−2.684 71	260.111	−0.8949	264.809	0.8949	269.506	2.684 71
BANFF 6, SK numu flux, 1.5 - 2.5 GeV	0.041 778 9	257.572	−1.862 32	260.831	−0.620 77	264.089	0.620 77	267.348	1.862 32
BANFF 7, SK numu flux, 2.5 - 3.5 GeV	0.043 606 9	259.942	−0.959 321	261.621	−0.319 77	263.299	0.319 77	264.978	0.959 321
BANFF 8, SK numu flux, 3.5 - 5.0 GeV	0.040 772	260.44	−0.769 586	261.787	−0.256 53	263.133	0.256 53	264.48	0.769 586
BANFF 9, SK numu flux, 5.0 - 7.0 GeV	0.040 095 8	261.934	−0.200 252	262.285	−0.066 751	262.635	0.066 751	262.986	0.200 252
BANFF 10, SK numu flux, 7.0 - 30.0 GeV	0.048 214	262.415	−0.017 173 8	262.445	−0.005 724 6	262.475	0.005 724 6	262.505	0.017 173 8
BANFF 11, SK numubar flux, 0.0 - 0.7 GeV	0.073 717	262.238	−0.084 566 9	262.386	−0.028 189	262.534	0.028 189	262.682	0.084 566 9
BANFF 12, SK numubar flux, 0.7 - 1.0 GeV	0.0477	262.299	−0.061 424 1	262.406	−0.020 475	262.514	0.020 475	262.621	0.061 424 1
BANFF 13, SK numubar flux, 1.0 - 1.5 GeV	0.057 472 1	261.806	−0.249 264	262.242	−0.083 088	262.678	0.083 088	263.114	0.249 264
BANFF 14, SK numubar flux, 1.5 - 2.5 GeV	0.061 890 7	261.514	−0.360 463	262.145	−0.120 15	262.775	0.120 15	263.406	0.360 463
BANFF 15, SK numubar flux, 2.5 - 30.0 GeV	0.064 676 3	261.784	−0.257 58	262.235	−0.085 86	262.685	0.085 86	263.136	0.257 58
BANFF 16, SK nue flux, 0.0 - 0.5 GeV	0.046 471 9	262.459	−0.000 248 152	262.46	-8.2717×10^{-5}	262.46	8.2717×10^{-5}	262.461	0.000 248 152
BANFF 17, SK nue flux, 0.5 - 0.7 GeV	0.042 400 3	262.459	−0.000 425 298	262.46	−0.000 141 77	262.46	0.000 141 77	262.461	0.000 425 298
BANFF 18, SK nue flux, 0.7 - 0.8 GeV	0.041 175	262.459	−0.000 313 178	262.46	−0.000 104 39	262.46	0.000 104 39	262.461	0.000 313 178
BANFF 19, SK nue flux, 0.8 - 1.5 GeV	0.039 056 6	262.454	−0.002 205 89	262.458	−0.000 735 3	262.462	0.000 735 3	262.466	0.002 205 89
BANFF 20, SK nue flux, 1.5 - 2.5 GeV	0.040 055 2	262.453	−0.002 770 52	262.458	−0.000 923 51	262.462	0.000 923 51	262.467	0.002 770 52
BANFF 21, SK nue flux, 2.5 - 4.0 GeV	0.041 468 5	262.455	−0.001 941 69	262.458	−0.000 647 23	262.462	0.000 647 23	262.465	0.001 941 69
BANFF 22, SK nue flux, 4.0 - 30.0 GeV	0.058 681 4	262.457	−0.001 271 22	262.459	−0.000 423 74	262.461	0.000 423 74	262.463	0.001 271 22
BANFF 23, SK nuebar flux, 0.0 - 2.5 GeV	0.053 829 3	262.459	−0.000 493 865	262.46	−0.000 164 62	262.46	0.000 164 62	262.461	0.000 493 865
BANFF 24, SK nuebar flux, 2.5 - 30.0 GeV	0.114 234	262.456	−0.001 434 86	262.459	−0.000 478 29	262.461	0.000 478 29	262.464	0.001 434 86
BANFF; Norm; 2p2h	0.182 443	249.661	−4.876 37	258.194	−1.6255	266.726	1.6255	275.258	4.876 37
BANFF; CA5 RES	0.059 470 4	255.895	−2.501 22	260.15	−0.880 07	264.891	0.9264	270.119	2.918 18
BANFF; Norm; BgRES Isospin 1/2	0.189 77	258.529	−1.497 55	260.792	−0.635 64	264.486	0.7721	269.614	2.725 68
BANFF, Ma QE	0.056 648 3	234.686	−10.5823	253.493	−3.4164	271.097	3.2909	287.323	9.472 98
BANFF, Ma RES	0.045 292 1	256.99	−2.084 16	260.608	−0.705 68	264.33	0.712 44	268.095	2.146 89
BANFF; Fermi Momentum	0.071 668 1	260.153	−0.878 886	263.803	0.511 59	258.576	−1.4798	250.147	−4.691 34
BANFF; Shape; CC Oth	0.186 63	261.304	−0.440 596	262.074	−0.146 87	262.845	0.146 87	263.616	0.440 596
BANFF; Norm, CC Coh	0.274 896	262.097	−0.138 277	262.339	−0.046 092	262.581	0.046 092	262.823	0.138 277
BANFF; Norm, NC Coh	0.297 426	262.46	−0.000 172 198	262.46	-5.7399×10^{-5}	262.46	5.7399×10^{-5}	262.46	0.000 172 198
BANFF; Norm, NC Oth	0.3	260.395	−0.786 683	261.772	−0.262 23	263.148	0.262 23	264.525	0.786 683
BANFF; Norm, ν_e To ν_μ	0.028 284 3	262.453	−0.002 545 52	262.458	−0.000 848 51	262.462	0.000 848 51	262.467	0.002 545 52
BANFF; Norm, $\bar{\nu}_e$ To $\bar{\nu}_\mu$	0.028 284 3	262.46	-2.093×10^{-5}	262.46	-6.9767×10^{-6}	262.46	6.9767×10^{-6}	262.46	2.093×10^{-5}
BANFF; Norm; 2p2hBar	0.201 069	261.848	−0.233 015	262.237	−0.084 844	262.683	0.084 844	263.128	0.254 533
BANFF; BeRPA A	0.055 826 7	244.308	−6.916 12	256.409	−2.3054	268.511	2.3054	280.612	6.916 13
BANFF; BeRPA B	0.117 434	244.85	−6.709 68	256.59	−2.2366	268.33	2.2365	280.07	6.709 66
BANFF; BeRPA D	0.127 806	241.706	−7.907 32	255.542	−2.6358	269.378	2.6358	283.214	7.907 35
BANFF; BeRPA E	0.354 515	261.309	−0.438 695	261.985	−0.180 78	262.939	0.182 51	263.907	0.551 209
BANFF; Shape; 2p2h	0.338 124	264.48	0.769 509	263.47	0.384 76	262.061	−0.151 97	264.505	0.779 109
BANFF; Norm; 2p2h C to O	0.161 427	244.958	−6.668 47	256.626	−2.2228	268.294	2.2228	279.962	6.668 47
SKDet + FSI/SI 0; E_{reco}(0.00 - 0.40)GeV; $\nu_\mu/\bar{\nu}_\mu$ CCQE ($1R_\mu$)	0.008 785 93	261.76	−0.266 69	262.227	−0.088 897	262.693	0.088 897	263.16	0.266 69
SKDet + FSI/SI 1; E_{reco}(0.40 - 1.10)GeV; $\nu_\mu/\bar{\nu}_\mu$ CCQE ($1R_\mu$)	0.007 403 28	260.255	−0.840 095	261.725	−0.280 03	263.195	0.280 03	264.665	0.840 095
SKDet + FSI/SI 2; E_{reco}(1.10 - 30.00)GeV; $\nu_\mu/\bar{\nu}_\mu$ CCQE ($1R_\mu$)	0.007 204 4	260.47	−0.758 196	261.797	−0.252 73	263.123	0.252 73	264.45	0.758 196
SKDet + FSI/SI 3; E_{reco}(0.00 - 30.00)GeV; $\nu_\mu/\bar{\nu}_\mu$ CCnQE ($1R_\mu$)	0.169 035	243.977	−7.042 31	256.299	−2.3474	268.621	2.3474	280.943	7.042 31
SKDet + FSI/SI 4; E_{reco}(0.00 - 30.00)GeV; $\nu_e/\bar{\nu}_e$/sigν_e CC ($1R_\mu$)	1.005 48	262.22	−0.091 235 1	262.38	−0.030 412	262.54	0.030 412	262.699	0.091 235 1
SKDet + FSI/SI 5; E_{reco}(0.00 - 30.00)GeV; all NC ($1R_\mu$)	0.658 101	246.61	−6.039 01	257.177	−2.013	267.743	2.013	278.31	6.039 01
SK energy scale	0.024	262.46	$-4.331\,59 \times 10^{-14}$	262.46	-2.1658×10^{-14}	262.46	-4.3316×10^{-14}	262.46	$-2.165\,79 \times 10^{-14}$

Table B.6: $\pm1\sigma$ and $\pm3\sigma$ effect of the systematic parameters on the total number of μ-like Super-K events with Run 1-8 POT for neutrino mode post-BANFF Asimov data set A. Only the systematic parameters which affect this sample are shown.

Parameter	1 σ value	BANFF tuned -3σ		BANFF tuned -1σ		BANFF tuned +1σ		BANFF tuned +3σ	
All syst		30.5141	−50.7005(%)	49.2477	−20.434 (%)	77.269	24.839(%)	121.097	95.6478(%)
BANFF 0, SK numu flux, 0.0 - 0.7 GeV; RHC	0.065 643 2	61.5824	−0.505 456	61.791	−0.168 49	61.9995	0.168 49	62.2081	0.505 456
BANFF 1, SK numu flux, 0.7 - 1.0 GeV; RHC	0.048 611 9	61.5733	−0.520 155	61.7879	−0.173 38	62.0026	0.173 38	62.2172	0.520 155
BANFF 2, SK numu flux, 1.0 - 1.5 GeV; RHC	0.045 404 8	61.0082	−1.4332	61.5996	−0.477 73	62.1909	0.477 73	62.7823	1.4332
BANFF 3, SK numu flux, 1.5 - 2.5 GeV; RHC	0.048 620 6	60.7269	−1.887 59	61.5058	−0.6292	62.2847	0.6292	63.0636	1.887 59
BANFF 4, SK numu flux, 2.5 - 30.0 GeV; RHC	0.043 062 7	61.1628	−1.183 34	61.6511	−0.394 45	62.1394	0.394 45	62.6277	1.183 34
BANFF 5, SK numubar flux, 0.0 - 0.4 GeV; RHC	0.064 779 5	60.8622	−1.669 06	61.5509	−0.556 35	62.2396	0.556 35	62.9283	1.669 06
BANFF 6, SK numubar flux, 0.4 - 0.5 GeV; RHC	0.052 486 4	61.34	−0.897 129	61.7102	−0.299 04	62.0803	0.299 04	62.4505	0.897 129
BANFF 7, SK numubar flux, 0.5 - 0.6 GeV; RHC	0.044 828 8	61.7886	−0.172 346	61.8597	−0.057 449	61.9308	0.057 449	62.0019	0.172 346
BANFF 8, SK numubar flux, 0.6 - 0.7 GeV; RHC	0.040 954 3	61.8144	−0.130 581	61.8683	−0.043 527	61.9222	0.043 527	61.9761	0.130 581
BANFF 9, SK numubar flux, 0.7 - 1.0 GeV; RHC	0.052 165 1	60.8576	−1.676 54	61.5494	−0.558 85	62.2411	0.558 85	62.9329	1.676 54
BANFF 10, SK numubar flux, 1.0 - 1.5 GeV; RHC	0.047 032 3	60.8991	−1.609 36	61.5632	−0.536 45	62.2273	0.536 45	62.8914	1.609 36
BANFF 11, SK numubar flux, 1.5 - 2.5 GeV; RHC	0.042 404 3	61.0423	−1.377 99	61.6109	−0.459 33	62.1796	0.459 33	62.7482	1.377 99
BANFF 12, SK numubar flux, 2.5 - 3.5 GeV; RHC	0.046 242 6	61.4714	−0.684 739	61.754	−0.228 25	62.0365	0.228 25	62.3191	0.684 739
BANFF 13, SK numubar flux, 3.5 - 5.0 GeV; RHC	0.062 880 7	61.4938	−0.648 57	61.7614	−0.216 19	62.0291	0.216 19	62.2967	0.648 57
BANFF 14, SK numubar flux, 5.0 - 7.0 GeV; RHC	0.055 519 7	61.8265	−0.111 012	61.8723	−0.037 004	61.9182	0.037 004	61.964	0.111 012
BANFF 15, SK numubar flux, 7.0 - 30.0 GeV; RHC	0.092 647 5	61.8878	−0.011 987 5	61.8928	−0.003 995 8	61.8977	0.003 995 8	61.9027	0.011 987 5
BANFF 16, SK nue flux, 0.0 - 2.5 GeV; RHC	0.046 545 2	61.893	−0.003 660 41	61.8945	−0.001 220 1	61.896	0.001 220 1	61.8975	0.003 660 41
BANFF 17, SK nue flux, 2.5 - 30.0 GeV; RHC	0.064 639	61.8919	−0.005 333 91	61.8941	−0.001 778	61.8963	0.001 778	61.8986	0.005 333 91
BANFF 18, SK nuebar flux, 0.0 - 0.5 GeV; RHC	0.051 375 5	61.8952	-9.4396×10^{-5}	61.8952	-3.1465×10^{-5}	61.8953	3.1465×10^{-5}	61.8953	9.4396×10^{-5}
BANFF 19, SK nuebar flux, 0.5 - 0.7 GeV; RHC	0.043 268	61.8951	−0.000 240 04	61.8952	-8.0013×10^{-5}	61.8953	8.0013×10^{-5}	61.8954	0.000 240 04
BANFF 20, SK nuebar flux, 0.7 - 0.8 GeV; RHC	0.043 836 5	61.8952	−0.000 123 246	61.8952	-4.1082×10^{-5}	61.8953	4.1082×10^{-5}	61.8953	0.000 123 246
BANFF 21, SK nuebar flux, 0.8 - 1.5 GeV; RHC	0.039 880 6	61.8946	−0.000 993 981	61.895	−0.000 331 33	61.8955	0.000 331 33	61.8959	0.000 993 981
BANFF 22, SK nuebar flux, 1.5 - 2.5 GeV; RHC	0.051 444 5	61.8944	−0.001 328 37	61.895	−0.000 442 79	61.8955	0.000 442 79	61.8961	0.001 328 37
BANFF 23, SK nuebar flux, 2.5 - 4.0 GeV; RHC	0.064 480 7	61.894	−0.002 020 42	61.8948	−0.000 673 47	61.8957	0.000 673 47	61.8965	0.002 020 42
BANFF 24, SK nuebar flux, 4.0 - 30.0 GeV; RHC	0.132 852	61.894	−0.001 945 78	61.8948	−0.000 648 59	61.8957	0.000 648 59	61.8965	0.001 945 78
BANFF; Norm; 2p2h	0.182 443	60.2874	−2.597 71	61.3593	−0.8659	62.4312	0.8659	63.5031	2.597 71
BANFF; CA5 RES	0.059 470 4	60.1443	−2.828 81	61.2586	−1.0287	62.585	1.1144	64.1236	3.600 24
BANFF; Norm; BgRES Isospin 1/2	0.189 77	60.7952	−1.777 35	61.4283	−0.754 41	62.4624	0.916 36	63.8975	3.234 95
BANFF, Ma QE	0.056 648 3	57.5502	−7.019 95	60.4125	−2.3956	63.3914	2.4172	66.3733	7.234 88
BANFF, Ma RES	0.045 292 1	60.824	−1.730 71	61.5157	−0.613 17	62.2944	0.6448	63.1423	2.014 83
BANFF; Fermi Momentum	0.071 668 1	61.3847	−0.824 911	62.1854	0.468 83	61.0781	−1.3202	59.4091	−4.016 69
BANFF; Shape; CC Oth	0.186 63	61.5816	−0.506 818	61.7907	−0.168 94	61.9998	0.168 94	62.2089	0.506 818
BANFF; Norm, CC Coh	0.274 896	61.683	−0.342 957	61.8245	−0.114 32	61.966	0.114 32	62.1075	0.342 957
BANFF; Norm, NC Coh	0.297 426	61.8933	−0.003 141 37	61.8946	−0.001 047 1	61.8959	0.001 047 1	61.8972	0.003 141 37
BANFF; Norm, NC Oth	0.3	61.4044	−0.792 965	61.7316	−0.264 32	62.0589	0.264 32	62.3861	0.792 965
BANFF; Norm, ν_e To ν_μ	0.028 284 3	61.895	−0.000 474 143	61.8952	−0.000 158 05	61.8953	0.000 158 05	61.8955	0.000 474 143
BANFF; Norm, $\bar{\nu}_e$ To $\bar{\nu}_\mu$	0.028 284 3	61.895	−0.000 475 571	61.8952	−0.000 158 52	61.8953	0.000 158 52	61.8955	0.000 475 571
BANFF; Norm; 2p2hBar	0.201 069	60.6651	−1.987 46	61.4473	−0.723 67	62.3432	0.723 67	63.239	2.171
BANFF; BeRPA A	0.055 826 7	58.3023	−5.804 84	60.6976	−1.935	63.0929	1.9349	65.4882	5.804 85
BANFF; BeRPA B	0.117 434	58.8486	−4.922 25	60.8797	−1.6407	62.9108	1.6408	64.9419	4.922 26
BANFF; BeRPA D	0.127 806	58.4343	−5.591 62	60.7416	−1.8639	63.0489	1.8639	65.3562	5.591 61
BANFF; BeRPA E	0.354 515	61.7148	−0.291 494	61.8205	−0.1208	61.9711	0.122 62	62.1253	0.371 737
BANFF; Shape; 2p2h	0.338 124	61.957	0.099 688 3	61.9261	0.049 839	62.0044	0.176 38	62.5317	1.028 21
BANFF; Norm; 2p2h C to O	0.161 427	59.1021	−4.512 71	60.9642	−1.5042	62.8263	1.5042	64.6884	4.512 71
SKDet + FSI/SI 0; E_{reco}(0.00 - 0.40)GeV; $\nu_\mu/\bar{\nu}_\mu$ CCQE ($1R_\mu$); RHC	0.008 512 49	61.7509	−0.233 153	61.8471	−0.077 718	61.9434	0.077 718	62.0396	0.233 153
SKDet + FSI/SI 1; E_{reco}(0.40 - 1.10)GeV; $\nu_\mu/\bar{\nu}_\mu$ CCQE ($1R_\mu$); RHC	0.007 050 99	61.5329	−0.585 454	61.7745	−0.195 15	62.016	0.195 15	62.2576	0.585 454
SKDet + FSI/SI 2; E_{reco}(1.10 - 30.00)GeV; $\nu_\mu/\bar{\nu}_\mu$ CCQE ($1R_\mu$); RHC	0.006 784	61.3387	−0.899 18	61.7097	−0.299 73	62.0808	0.299 73	62.4518	0.899 18
SKDet + FSI/SI 3; E_{reco}(0.00 - 30.00)GeV; $\nu_\mu/\bar{\nu}_\mu$ CCnQE ($1R_\mu$); RHC	0.129 646	57.9032	−6.449 68	60.5646	−2.1499	63.2259	2.1499	65.8873	6.449 68
SKDet + FSI/SI 4; E_{reco}(0.00 - 30.00)GeV; $\nu_e/\bar{\nu}_e$/sigν_e CC ($1R_\mu$); RHC	1.004 54	61.8744	−0.033 729 9	61.8883	−0.011 243	61.9022	0.011 243	61.9161	0.033 729 9
SKDet + FSI/SI 5; E_{reco}(0.00 - 30.00)GeV; all NC ($1R_\mu$); RHC	0.657 251	58.9447	−4.766 96	60.9117	−1.589	62.8788	1.589	64.8458	4.766 96
SK energy scale	0.024	61.8952	1.14798×10^{-14}	61.8952	-5.7399×10^{-14}	61.8952	0	61.8952	-4.5919×10^{-14}

Table B.7: $\pm1\sigma$ and $\pm3\sigma$ effect of the systematic parameters on the total number of μ-like Super-K events with Run 1-8 POT for antineutrino mode post-BANFF Asimov data set A. Only the systematic parameters which affect this sample are shown.

Parameter	1 σ value	BANFF tuned -3σ		BANFF tuned -1σ		BANFF tuned +1σ		BANFF tuned +3σ	
All syst		24.922	−65.9618(%)	51.4515	−29.728 (%)	102.19	39.569(%)	190.164	159.724(%)
BANFF 0, SK numu flux, 0.0 - 0.4 GeV	0.057 496 7	72.9223	−0.403 375	73.1192	−0.134 46	73.3161	0.134 46	73.513	0.403 375
BANFF 1, SK numu flux, 0.4 - 0.5 GeV	0.051 936 3	72.1503	−1.457 78	72.8619	−0.485 93	73.5734	0.485 93	74.285	1.457 78
BANFF 2, SK numu flux, 0.5 - 0.6 GeV	0.044 568 2	71.1561	−2.815 69	72.5305	−0.938 56	73.9049	0.938 56	75.2792	2.815 69
BANFF 3, SK numu flux, 0.6 - 0.7 GeV	0.041 886 1	70.9918	−3.040 09	72.4757	−1.0134	73.9596	1.0134	75.4435	3.040 09
BANFF 4, SK numu flux, 0.7 - 1.0 GeV	0.054 16	70.287	−4.002 65	72.2408	−1.3342	74.1945	1.3342	76.1483	4.002 65
BANFF 5, SK numu flux, 1.0 - 1.5 GeV	0.049 026 1	72.8314	−0.527 495	73.0889	−0.175 83	73.3464	0.175 83	73.6039	0.527 495
BANFF 6, SK numu flux, 1.5 - 2.5 GeV	0.041 778 9	73.1531	−0.088 139 6	73.1962	−0.029 38	73.2392	0.029 38	73.2822	0.088 139 6
BANFF 7, SK numu flux, 2.5 - 3.5 GeV	0.043 606 9	73.1782	−0.053 842 2	73.2045	−0.017 947	73.2308	0.017 947	73.2571	0.053 842 2
BANFF 8, SK numu flux, 3.5 - 5.0 GeV	0.040 772	73.1759	−0.056 987 9	73.2038	−0.018 996	73.2316	0.018 996	73.2594	0.056 987 9
BANFF 9, SK numu flux, 5.0 - 7.0 GeV	0.040 095 8	73.2002	−0.023 894 1	73.2118	−0.007 964 7	73.2235	0.007 964 7	73.2352	0.023 894 1
BANFF 10, SK numu flux, 7.0 - 30.0 GeV	0.048 214	73.208	−0.013 257 5	73.2144	−0.004 419 2	73.2209	0.004 419 2	73.2274	0.013 257 5
BANFF 11, SK numubar flux, 0.0 - 0.7 GeV	0.073 717	73.1847	−0.044 983 2	73.2067	−0.014 994	73.2286	0.014 994	73.2506	0.044 983 2
BANFF 12, SK numubar flux, 0.7 - 1.0 GeV	0.0477	73.1928	−0.033 892 6	73.2094	−0.011 298	73.2259	0.011 298	73.2425	0.033 892 6
BANFF 13, SK numubar flux, 1.0 - 1.5 GeV	0.057 472 1	73.1952	−0.030 620 8	73.2102	−0.010 207	73.2251	0.010 207	73.2401	0.030 620 8
BANFF 14, SK numubar flux, 1.5 - 2.5 GeV	0.061 890 7	73.2042	−0.018 418 1	73.2132	−0.006 139 4	73.2222	0.006 139 4	73.2311	0.018 418 1
BANFF 15, SK numubar flux, 2.5 - 30.0 GeV	0.064 676 3	73.2046	−0.017 792 4	73.2133	−0.005 930 8	73.222	0.005 930 8	73.2307	0.017 792 4
BANFF 16, SK nue flux, 0.0 - 0.5 GeV	0.046 471 9	72.9814	−0.322 666	73.1389	−0.107 56	73.2964	0.107 56	73.4539	0.322 666
BANFF 17, SK nue flux, 0.5 - 0.7 GeV	0.042 400 3	72.9412	−0.377 611	73.1255	−0.125 87	73.3098	0.125 87	73.4941	0.377 611
BANFF 18, SK nue flux, 0.7 - 0.8 GeV	0.041 175	73.0844	−0.182 013	73.1732	−0.060 671	73.2621	0.060 671	73.3509	0.182 013
BANFF 19, SK nue flux, 0.8 - 1.5 GeV	0.039 056 6	72.8167	−0.547 63	73.084	−0.182 54	73.3513	0.182 54	73.6186	0.547 63
BANFF 20, SK nue flux, 1.5 - 2.5 GeV	0.040 055 2	73.1876	−0.041 083	73.2076	−0.013 694	73.2277	0.013 694	73.2477	0.041 083
BANFF 21, SK nue flux, 2.5 - 4.0 GeV	0.041 468 5	73.2139	−0.005 123 28	73.2164	−0.001 707 8	73.2189	0.001 707 8	73.2214	0.005 123 28
BANFF 22, SK nue flux, 4.0 - 30.0 GeV	0.058 681 4	73.216	−0.002 314 32	73.2171	−0.000 771 44	73.2182	0.000 771 44	73.2194	0.002 314 32
BANFF 23, SK nuebar flux, 0.0 - 2.5 GeV	0.053 829 3	73.1626	−0.075 266 1	73.1993	−0.025 089	73.236	0.025 089	73.2728	0.075 266 1
BANFF 24, SK nuebar flux, 2.5 - 30.0 GeV	0.114 234	73.2155	−0.003 008 59	73.2169	−0.001 002 9	73.2184	0.001 002 9	73.2199	0.003 008 59
BANFF; Norm; 2p2h	0.182 443	69.5006	−5.076 71	71.9786	−1.6922	74.4567	1.6922	76.9347	5.076 71
BANFF; CA5 RES	0.059 470 4	71.8118	−1.920 13	72.7247	−0.673 29	73.735	0.706 54	74.8426	2.219 38
BANFF; Norm; BgRES Isospin 1/2	0.189 77	72.627	−0.806 784	72.9669	−0.342 44	73.5222	0.415 96	74.2928	1.468 42
BANFF, Ma QE	0.056 648 3	64.696	−11.6388	70.5376	−3.6604	75.731	3.4327	80.2664	9.6271
BANFF, Ma RES	0.045 292 1	72.1583	−1.4469	72.8705	−0.474 12	73.5578	0.464 58	74.2156	1.362 97
BANFF; Fermi Momentum	0.071 668 1	72.6124	−0.826 631	73.5743	0.487 05	72.1652	−1.4375	69.8285	−4.628 86
BANFF; Shape; CC Oth	0.186 63	73.137	−0.110 225	73.1908	−0.036 741	73.2446	0.036 741	73.2984	0.110 222
BANFF; Norm, CC Coh	0.274 896	73.1696	−0.065 688	73.2016	−0.021 896	73.2337	0.021 896	73.2658	0.065 688
BANFF; Norm, NC Coh	0.297 426	72.6524	−0.772 032	73.0292	−0.257 34	73.4061	0.257 34	73.7829	0.772 032
BANFF; Norm, NC Oth	0.3	72.8927	−0.443 771	73.1094	−0.147 92	73.326	0.147 92	73.5426	0.443 771
BANFF; Norm, ν_e To ν_μ	0.028 284 3	67.5071	−7.799 41	71.3141	−2.5998	75.1212	2.5998	78.9282	7.799 41
BANFF; Norm; NC 1 γ	1	71.1672	−2.800 47	71.1672	−2.8005	75.2681	2.8005	79.369	8.401 41
BANFF; Norm, $\bar{\nu}_e$ To $\bar{\nu}_\mu$	0.028 284 3	73.1582	−0.081 196 6	73.1978	−0.027 066	73.2375	0.027 066	73.2771	0.081 196 6
BANFF; Norm; 2p2hBar	0.201 069	73.1818	−0.048 996 4	73.2046	−0.017 84	73.2307	0.017 84	73.2568	0.053 521 1
BANFF; BeRPA A	0.055 826 7	68.1306	−6.9479	71.522	−2.316	74.9134	2.316	78.3048	6.9479
BANFF; BeRPA B	0.117 434	67.4635	−7.858 98	71.2996	−2.6197	75.1357	2.6197	78.9718	7.858 98
BANFF; BeRPA D	0.127 806	67.8054	−7.392 04	71.4136	−2.464	75.0218	2.464	78.6299	7.392 04
BANFF; BeRPA E	0.354 515	72.8409	−0.514 573	73.064	−0.209 88	73.3713	0.209 88	73.6787	0.629 665
BANFF; Shape; 2p2h	0.338 124	72.6822	−0.731 326	72.9499	−0.365 66	73.9761	1.0359	75.739	3.443 59
BANFF; Norm; 2p2h C to O	0.161 427	68.2076	−6.842 65	71.5477	−2.2809	74.8877	2.2809	78.2277	6.842 65
SKDet + FSI/SI 6; E_{reco}(0.00 - 0.35)GeV; Osc. ν_e CC ($1R_e$)	0.181 271	68.7493	−6.1029	71.7282	−2.0343	74.7071	2.0343	77.6861	6.1029
SKDet + FSI/SI 7; E_{reco}(0.35 - 0.80)GeV; Osc. ν_e CC ($1R_e$)	0.036 083	68.6468	−6.242 86	71.694	−2.081	74.7413	2.081	77.7885	6.242 86
SKDet + FSI/SI 8; E_{reco}(0.80 - 1.25)GeV; Osc. ν_e CC ($1R_e$)	0.041 663 6	72.1642	−1.438 86	72.8665	−0.479 62	73.5688	0.479 62	74.2712	1.438 86
SKDet + FSI/SI 9; E_{reco}(0.00 - 0.35)GeV; $\nu_\mu/\bar{\nu}_\mu$ CC ($1R_e$)	0.300 431	73.1543	−0.086 531 7	73.1965	−0.028 844	73.2388	0.028 844	73.281	0.086 531 7
SKDet + FSI/SI 10; E_{reco}(0.35 - 0.80)GeV; $\nu_\mu/\bar{\nu}_\mu$ CC ($1R_e$)	0.321 346	73.0587	−0.217 089	73.1647	−0.072 363	73.2706	0.072 363	73.3766	0.217 089
SKDet + FSI/SI 11; E_{reco}(0.80 - 1.25)GeV; $\nu_\mu/\bar{\nu}_\mu$ CC ($1R_e$)	0.392 969	73.1904	−0.037 232 2	73.2086	−0.012 411	73.2267	0.012 411	73.2449	0.037 232 2
SKDet + FSI/SI 12; E_{reco}(0.00 - 0.35)GeV; $\nu_e/\bar{\nu}_e$ CC ($1R_e$)	0.135 399	72.7003	−0.706 59	73.0452	−0.235 53	73.3901	0.235 53	73.735	0.706 59
SKDet + FSI/SI 13; E_{reco}(0.35 - 0.80)GeV; $\nu_e/\bar{\nu}_e$ CC ($1R_e$)	0.069 892 8	72.1921	−1.400 77	72.8758	−0.466 92	73.5595	0.466 92	74.2433	1.400 77
SKDet + FSI/SI 14; E_{reco}(0.80 - 1.25)GeV; $\nu_e/\bar{\nu}_e$ CC ($1R_e$)	0.077 136 1	72.5317	−0.936 824	72.989	−0.312 27	73.4463	0.312 27	73.9036	0.936 824
SKDet + FSI/SI 15; E_{reco}(0.00 - 0.35)GeV; all NC ($1R_e$)	0.194 453	72.0874	−1.543 71	72.8409	−0.514 57	73.5944	0.514 57	74.3479	1.543 71
SKDet + FSI/SI 16; E_{reco}(0.35 - 0.80)GeV; all NC ($1R_e$)	0.181 015	71.849	−1.869 26	72.7615	−0.623 09	73.6739	0.623 09	74.5863	1.869 26
SKDet + FSI/SI 17; E_{reco}(0.80 - 1.25)GeV; all NC ($1R_e$)	0.472 078	72.5075	−0.969 968	72.9809	−0.323 32	73.4544	0.323 32	73.9279	0.969 968
SK energy scale	0.024	73.2177	$1.940\,91 \times 10^{-14}$	73.2177	1.9409×10^{-14}	73.2177	1.9409×10^{-14}	73.2177	0

Table B.8: $\pm1\sigma$ and $\pm3\sigma$ effect of the systematic parameters on the total number of e-like Super-K events with Run 1-8 POT for neutrino mode post-BANFF Asimov data set A. Only the systematic parameters which affect this sample are shown.

Parameter	1 σ value	BANFF tuned -3σ		BANFF tuned -1σ		BANFF tuned +1σ		BANFF tuned +3σ	
All syst		2.963 71	−62.2766(%)	5.462 14	−30.475 (%)	11.115	41.472(%)	21.274	170.785(%)
BANFF 0, SK numu flux, 0.0 - 0.7 GeV; RHC	0.065 643 2	7.723 62	−1.690 35	7.812 16	−0.563 45	7.900 69	0.563 45	7.989 22	1.690 35
BANFF 1, SK numu flux, 0.7 - 1.0 GeV; RHC	0.048 611 9	7.776 33	−1.019 45	7.829 73	−0.339 82	7.883 12	0.339 82	7.936 52	1.019 45
BANFF 2, SK numu flux, 1.0 - 1.5 GeV; RHC	0.045 404 8	7.812 29	−0.561 803	7.841 71	−0.187 27	7.871 14	0.187 27	7.900 56	0.561 803
BANFF 3, SK numu flux, 1.5 - 2.5 GeV; RHC	0.048 620 6	7.837 35	−0.242 765	7.850 07	−0.080 922	7.862 78	0.080 922	7.8755	0.242 765
BANFF 4, SK numu flux, 2.5 - 30.0 GeV; RHC	0.043 062 7	7.838 32	−0.230 369	7.850 39	−0.076 79	7.862 46	0.076 79	7.874 52	0.230 369
BANFF 5, SK numubar flux, 0.0 - 0.4 GeV; RHC	0.064 779 5	7.84	−0.209 058	7.850 95	−0.069 686	7.8619	0.069 686	7.872 85	0.209 058
BANFF 6, SK numubar flux, 0.4 - 0.5 GeV; RHC	0.052 486 4	7.807 95	−0.616 928	7.840 27	−0.205 64	7.872 58	0.205 64	7.904 89	0.616 928
BANFF 7, SK numubar flux, 0.5 - 0.6 GeV; RHC	0.044 828 8	7.746 07	−1.404 56	7.819 64	−0.468 19	7.893 21	0.468 19	7.966 77	1.404 56
BANFF 8, SK numubar flux, 0.6 - 0.7 GeV; RHC	0.040 954 3	7.720 03	−1.736 07	7.810 96	−0.578 69	7.901 89	0.578 69	7.992 82	1.736 07
BANFF 9, SK numubar flux, 0.7 - 1.0 GeV; RHC	0.052 165 1	7.640 76	−2.745	7.784 54	−0.915	7.928 31	0.915	8.072 08	2.745
BANFF 10, SK numubar flux, 1.0 - 1.5 GeV; RHC	0.047 032 3	7.816 42	−0.509 156	7.843 09	−0.169 72	7.869 76	0.169 72	7.896 42	0.509 156
BANFF 11, SK numubar flux, 1.5 - 2.5 GeV; RHC	0.042 404 3	7.844 95	−0.146 092	7.8526	−0.048 697	7.860 25	0.048 697	7.8679	0.146 092
BANFF 12, SK numubar flux, 2.5 - 3.5 GeV; RHC	0.046 242 6	7.850 33	−0.077 579 9	7.854 39	−0.025 86	7.858 45	0.025 86	7.862 52	0.077 579 9
BANFF 13, SK numubar flux, 3.5 - 5.0 GeV; RHC	0.062 880 7	7.849 05	−0.093 860 5	7.853 96	−0.031 287	7.858 88	0.031 287	7.8638	0.093 860 5
BANFF 14, SK numubar flux, 5.0 - 7.0 GeV; RHC	0.055 519 7	7.854 31	−0.026 909 5	7.855 72	−0.008 969 8	7.857 13	0.008 969 8	7.858 54	0.026 909 5
BANFF 15, SK numubar flux, 7.0 - 30.0 GeV; RHC	0.092 647 5	7.8547	−0.021 895 7	7.855 85	−0.007 298 6	7.857	0.007 298 6	7.858 14	0.021 895 7
BANFF 16, SK nue flux, 0.0 - 2.5 GeV; RHC	0.046 545 2	7.754 35	−1.299 28	7.8224	−0.433 09	7.890 45	0.433 09	7.9585	1.299 28
BANFF 17, SK nue flux, 2.5 - 30.0 GeV; RHC	0.064 639	7.854 84	−0.020 132 8	7.8559	−0.006 710 9	7.856 95	0.006 710 9	7.858	0.020 132 8
BANFF 18, SK nuebar flux, 0.0 - 0.5 GeV; RHC	0.051 375 5	7.824 84	−0.401 976	7.8459	−0.133 99	7.866 95	0.133 99	7.888	0.401 976
BANFF 19, SK nuebar flux, 0.5 - 0.7 GeV; RHC	0.043 268	7.8255	−0.393 588	7.846 12	−0.1312	7.866 73	0.1312	7.887 34	0.393 588
BANFF 20, SK nuebar flux, 0.7 - 0.8 GeV; RHC	0.043 836 5	7.839 41	−0.216 534	7.850 75	−0.072 178	7.862 09	0.072 178	7.873 43	0.216 534
BANFF 21, SK nuebar flux, 0.8 - 1.5 GeV; RHC	0.039 880 6	7.802 53	−0.685 932	7.838 46	−0.228 64	7.874 39	0.228 64	7.910 31	0.685 932
BANFF 22, SK nuebar flux, 1.5 - 2.5 GeV; RHC	0.051 444 5	7.852 38	−0.051 433 9	7.855 08	−0.017 145	7.857 77	0.017 145	7.860 46	0.051 433 9
BANFF 23, SK nuebar flux, 2.5 - 4.0 GeV; RHC	0.064 480 7	7.855 54	−0.011 252 1	7.856 13	−0.003 750 7	7.856 72	0.003 750 7	7.857 31	0.011 252 1
BANFF 24, SK nuebar flux, 4.0 - 30.0 GeV; RHC	0.132 852	7.855 62	−0.010 160 3	7.856 16	−0.003 386 8	7.856 69	0.003 386 8	7.857 22	0.010 160 3
BANFF; Norm; 2p2h	0.182 443	7.720 15	−1.7346	7.811	−0.5782	7.901 85	0.5782	7.9927	1.7346
BANFF; CA5 RES	0.059 470 4	7.633 37	−2.8391	7.770 72	−1.0909	7.953 48	1.2354	8.181 66	4.139 76
BANFF; Norm; BgRES Isospin 1/2	0.189 77	7.740 41	−1.476 65	7.807 18	−0.626 77	7.916 24	0.761 32	8.067 57	2.687 63
BANFF, Ma QE	0.056 648 3	7.380 72	−6.054 95	7.693 53	−2.0734	8.019 55	2.0764	8.338 05	6.130 37
BANFF, Ma RES	0.045 292 1	7.748 05	−1.379 41	7.8167	−0.505 59	7.899 09	0.543 13	7.991 45	1.718 63
BANFF; Fermi Momentum	0.071 668 1	7.7857	−0.900 157	7.8963	0.507 53	7.743 12	−1.4422	7.506 25	−4.457 13
BANFF; Shape; CC Oth	0.186 63	7.839 38	−0.216 893	7.850 74	−0.072 298	7.8621	0.072 298	7.873 46	0.216 893
BANFF; Norm, CC Coh	0.274 896	7.813 83	−0.542 185	7.842 22	−0.180 73	7.870 62	0.180 73	7.899 02	0.542 185
BANFF; Norm, NC Coh	0.297 426	7.6102	−3.134 05	7.774 35	−1.0447	7.9385	1.0447	8.102 65	3.134 05
BANFF; Norm, NC Oth	0.3	7.777 88	−0.999 766	7.830 24	−0.333 26	7.8826	0.333 26	7.934 97	0.999 766
BANFF; Norm, ν_e To ν_μ	0.028 284 3	7.6748	−2.311 78	7.795 88	−0.770 59	7.916 96	0.770 59	8.038 05	2.311 78
BANFF; Norm; NC 1 γ	1	7.325 03	−6.763 74	7.325 03	−6.7637	8.387 81	6.7637	9.450 59	20.2912
BANFF; Norm, $\bar{\nu}_e$ To $\bar{\nu}_\mu$	0.028 284 3	7.481 99	−4.765 99	7.731 61	−1.5887	7.981 24	1.5887	8.230 86	4.765 99
BANFF; Norm; 2p2hBar	0.201 069	7.662 82	−2.464 32	7.785 93	−0.8973	7.926 92	0.8973	8.067 91	2.6919
BANFF; BeRPA A	0.055 826 7	7.376 28	−6.111 45	7.696 38	−2.0371	8.016 47	2.0371	8.336 56	6.111 44
BANFF; BeRPA B	0.117 434	7.471 56	−4.898 73	7.728 13	−1.6329	7.984 71	1.6329	8.241 29	4.898 73
BANFF; BeRPA D	0.127 806	7.584 43	−3.461 99	7.765 76	−1.154	7.947 09	1.154	8.128 41	3.461 99
BANFF; BeRPA E	0.354 515	7.837 36	−0.242 58	7.848 65	−0.098 949	7.8642	0.098 955	7.879 75	0.296 901
BANFF; Shape; 2p2h	0.338 124	7.810 59	−0.583 371	7.833 51	−0.291 69	7.916 07	0.759 24	8.046	2.413 06
BANFF; Norm; 2p2h C to O	0.161 427	7.573 64	−3.599 42	7.762 16	−1.1998	7.950 68	1.1998	8.139 21	3.599 42
SKDet + FSI/SI 6; E_{reco}(0.00 - 0.35)GeV; Osc. ν_e CC (1R_e); RHC	0.108 165	7.719 43	−1.743 77	7.810 76	−0.581 26	7.902 09	0.581 26	7.993 42	1.743 77
SKDet + FSI/SI 7; E_{reco}(0.35 - 0.80)GeV; Osc. ν_e CC (1R_e); RHC	0.036 303 9	7.494 43	−4.607 64	7.735 76	−1.5359	7.977 09	1.5359	8.218 42	4.607 64
SKDet + FSI/SI 8; E_{reco}(0.80 - 1.25)GeV; Osc. ν_e CC (1R_e); RHC	0.056 731 5	7.687 41	−2.151 25	7.800 09	−0.717 08	7.912 76	0.717 08	8.025 43	2.151 25
SKDet + FSI/SI 9; E_{reco}(0.00 - 0.35)GeV; $\nu_\mu/\bar{\nu}_\mu$ CC (1R_e); RHC	0.348 644	7.8459	−0.133 966	7.852 91	−0.044 655	7.859 93	0.044 655	7.866 95	0.133 966
SKDet + FSI/SI 10; E_{reco}(0.35 - 0.80)GeV; $\nu_\mu/\bar{\nu}_\mu$ CC (1R_e); RHC	0.341 647	7.8176	−0.494 211	7.843 48	−0.164 74	7.869 37	0.164 74	7.895 25	0.494 211
SKDet + FSI/SI 11; E_{reco}(0.80 - 1.25)GeV; $\nu_\mu/\bar{\nu}_\mu$ CC (1R_e); RHC	0.417 164	7.840 41	−0.203 851	7.851 08	−0.067 95	7.861 76	0.067 95	7.872 44	0.203 851
SKDet + FSI/SI 12; E_{reco}(0.00 - 0.35)GeV; $\nu_e/\bar{\nu}_e$ CC (1R_e); RHC	0.084 556 3	7.805 85	−0.643 709	7.839 57	−0.214 57	7.873 28	0.214 57	7.907	0.643 709
SKDet + FSI/SI 13; E_{reco}(0.35 - 0.80)GeV; $\nu_e/\bar{\nu}_e$ CC (1R_e); RHC	0.056 069 7	7.704 77	−1.930 28	7.805 87	−0.643 43	7.906 97	0.643 43	8.008 07	1.930 28
SKDet + FSI/SI 14; E_{reco}(0.80 - 1.25)GeV; $\nu_e/\bar{\nu}_e$ CC (1R_e); RHC	0.078 024 1	7.689 46	−2.125 19	7.800 77	−0.7084	7.912 08	0.7084	8.023 39	2.125 19
SKDet + FSI/SI 15; E_{reco}(0.00 - 0.35)GeV; all NC (1R_e); RHC	0.214 066	7.571 17	−3.630 77	7.761 34	−1.2103	7.951 51	1.2103	8.141 67	3.630 77
SKDet + FSI/SI 16; E_{reco}(0.35 - 0.80)GeV; all NC (1R_e); RHC	0.190 575	7.487 66	−4.693 75	7.7335	−1.5646	7.979 34	1.5646	8.225 18	4.693 75
SKDet + FSI/SI 17; E_{reco}(0.80 - 1.25)GeV; all NC (1R_e); RHC	0.464 86	7.642 65	−2.721	7.785 17	−0.907	7.927 68	0.907	8.0702	2.721
SK energy scale	0.024	7.856 42	$2.261\,02 \times 10^{-14}$	7.856 42	2.261×10^{-14}	7.856 42	3.3915×10^{-14}	7.856 42	0

Table B.9: $\pm 1\sigma$ and $\pm 3\sigma$ effect of the systematic parameters on the total number of e-like Super-K events with Run 1-8 POT for antineutrino mode post-BANFF Asimov data set A. Only the systematic parameters which affect this sample are shown.

Parameter	1 σ value	BANFF tuned -3σ		BANFF tuned -1σ		BANFF tuned +1σ		BANFF tuned +3σ	
All syst		0.804 711	−88.4314(%)	4.008 33	−42.376 (%)	11.207	61.106(%)	25.0389	259.961(%)
BANFF 0, SK numu flux, 0.0 - 0.4 GeV	0.057 496 7	6.954 24	−0.025 206 3	6.955 41	−0.008 402 1	6.956 58	0.008 402 1	6.957 75	0.025 206 3
BANFF 1, SK numu flux, 0.4 - 0.5 GeV	0.051 936 3	6.910 04	−0.660 661	6.940 68	−0.220 22	6.971 31	0.220 22	7.001 95	0.660 661
BANFF 2, SK numu flux, 0.5 - 0.6 GeV	0.044 568 2	6.798 99	−2.257 11	6.903 66	−0.752 37	7.008 33	0.752 37	7.113	2.257 11
BANFF 3, SK numu flux, 0.6 - 0.7 GeV	0.041 886 1	6.727 93	−3.278 66	6.879 97	−1.0929	7.032 01	1.0929	7.184 06	3.278 66
BANFF 4, SK numu flux, 0.7 - 1.0 GeV	0.054 16	6.610 26	−4.970 27	6.840 75	−1.6568	7.071 24	1.6568	7.301 73	4.970 27
BANFF 5, SK numu flux, 1.0 - 1.5 GeV	0.049 026 1	6.906 32	−0.714 124	6.939 44	−0.238 04	6.972 55	0.238 04	7.005 67	0.714 124
BANFF 6, SK numu flux, 1.5 - 2.5 GeV	0.041 778 9	6.9436	−0.178 111	6.951 86	−0.059 37	6.960 12	0.059 37	6.968 38	0.178 111
BANFF 7, SK numu flux, 2.5 - 3.5 GeV	0.043 606 9	6.948 64	−0.105 658	6.953 54	−0.035 219	6.958 44	0.035 219	6.963 34	0.105 658
BANFF 8, SK numu flux, 3.5 - 5.0 GeV	0.040 772	6.944 79	−0.161 07	6.952 26	−0.053 69	6.959 73	0.053 69	6.9672	0.161 07
BANFF 9, SK numu flux, 5.0 - 7.0 GeV	0.040 095 8	6.951 21	−0.068 745 4	6.9544	−0.022 915	6.957 59	0.022 915	6.960 78	0.068 745 4
BANFF 10, SK numu flux, 7.0 - 30.0 GeV	0.048 214	6.9554	−0.008 540 26	6.9558	−0.002 846 8	6.956 19	0.002 846 8	6.956 59	0.008 540 26
BANFF 11, SK numubar flux, 0.0 - 0.7 GeV	0.073 717	6.955 31	−0.009 815 25	6.955 77	−0.003 271 8	6.956 22	0.003 271 8	6.956 68	0.009 815 25
BANFF 12, SK numubar flux, 0.7 - 1.0 GeV	0.0477	6.955 39	−0.008 743 09	6.955 79	−0.002 914 4	6.9562	0.002 914 4	6.9566	0.008 743 09
BANFF 13, SK numubar flux, 1.0 - 1.5 GeV	0.057 472 1	6.954 97	−0.014 683 7	6.955 65	−0.004 894 6	6.956 33	0.004 894 6	6.957 02	0.014 683 7
BANFF 14, SK numubar flux, 1.5 - 2.5 GeV	0.061 890 7	6.954 56	−0.020 658 8	6.955 51	−0.006 886 3	6.956 47	0.006 886 3	6.957 43	0.020 658 8
BANFF 15, SK numubar flux, 2.5 - 30.0 GeV	0.064 676 3	6.9542	−0.025 784 6	6.9554	−0.008 594 9	6.956 59	0.008 594 9	6.957 79	0.025 784 6
BANFF 16, SK nue flux, 0.0 - 0.5 GeV	0.046 471 9	6.950 48	−0.079 277 3	6.954 16	−0.026 426	6.957 83	0.026 426	6.961 51	0.079 277 3
BANFF 17, SK nue flux, 0.5 - 0.7 GeV	0.042 400 3	6.931 68	−0.349 548	6.947 89	−0.116 52	6.9641	0.116 52	6.980 31	0.349 548
BANFF 18, SK nue flux, 0.7 - 0.8 GeV	0.041 175	6.939 98	−0.230 278	6.950 65	−0.076 759	6.961 33	0.076 759	6.972 01	0.230 278
BANFF 19, SK nue flux, 0.8 - 1.5 GeV	0.039 056 6	6.896 41	−0.856 582	6.936 13	−0.285 53	6.975 86	0.285 53	7.015 58	0.856 582
BANFF 20, SK nue flux, 1.5 - 2.5 GeV	0.040 055 2	6.949 68	−0.090 741 5	6.953 89	−0.030 247	6.9581	0.030 247	6.962 31	0.090 741 5
BANFF 21, SK nue flux, 2.5 - 4.0 GeV	0.041 468 5	6.955 29	−0.010 118 7	6.955 76	−0.003 372 9	6.956 23	0.003 372 9	6.9567	0.010 118 7
BANFF 22, SK nue flux, 4.0 - 30.0 GeV	0.058 681 4	6.955 63	−0.005 302 11	6.955 87	−0.001 767 4	6.956 12	0.001 767 4	6.956 36	0.005 302 11
BANFF 23, SK nuebar flux, 0.0 - 2.5 GeV	0.053 829 3	6.954 56	−0.020 660 1	6.955 51	−0.006 886 7	6.956 47	0.006 886 7	6.957 43	0.020 660 1
BANFF 24, SK nuebar flux, 2.5 - 30.0 GeV	0.114 234	6.955 64	−0.005 042 17	6.955 88	−0.001 680 7	6.956 11	0.001 680 7	6.956 34	0.005 042 17
BANFF; Norm; 2p2h	0.182 443	6.886 67	−0.996 676	6.932 88	−0.332 23	6.9791	0.332 23	7.025 32	0.996 676
BANFF; CA5 RES	0.059 470 4	5.897 54	−15.2164	6.587 37	−5.2994	7.340 43	5.5266	8.156 71	17.2616
BANFF; Norm; BgRES Isospin 1/2	0.189 77	6.570 82	−5.537 26	6.792 51	−2.3503	7.154 58	2.8549	7.657 04	10.0783
BANFF, Ma QE	0.056 648 3	6.9079	−0.691 353	6.940 74	−0.219 33	6.970 39	0.206 94	6.996 54	0.582 87
BANFF, Ma RES	0.045 292 1	6.208 12	−10.7516	6.717 13	−3.4339	7.184 06	3.2788	7.608 06	9.374 09
BANFF; Fermi Momentum	0.071 668 1	6.954 02	−0.028 404 5	6.9574	0.020 253	6.951 51	−0.064 517	6.941 42	−0.209 459
BANFF; Shape; CC Oth	0.186 63	6.850 23	−1.520 53	6.920 74	−0.506 84	6.991 25	0.506 84	7.061 76	1.520 53
BANFF; Norm, CC Coh	0.274 896	6.832 07	−1.781 54	6.914 69	−0.593 85	6.9973	0.593 85	7.079 92	1.781 54
BANFF; Norm, NC Oth	0.3	6.7486	−2.9815	6.886 86	−0.993 83	7.025 12	0.993 83	7.163 39	2.9815
BANFF; Norm, ν_e To ν_μ	0.028 284 3	6.412 77	−7.809 49	6.774 92	−2.6032	7.137 07	2.6032	7.499 22	7.809 49
BANFF; Norm; NC 1 γ	1	6.896 95	−0.848 755	6.896 95	−0.848 76	7.015 03	0.848 76	7.133 11	2.546 27
BANFF; Norm, $\bar{\nu}_e$ To $\bar{\nu}_\mu$	0.028 284 3	6.954 62	−0.019 721 7	6.955 54	−0.006 573 9	6.956 45	0.006 573 9	6.957 37	0.019 721 7
BANFF; Norm; 2p2hBar	0.201 069	6.954 91	−0.015 515	6.9556	−0.005 649 2	6.956 39	0.005 649 2	6.957 17	0.016 947 7
BANFF; BeRPA A	0.055 826 7	6.935 41	−0.295 95	6.949 13	−0.098 65	6.962 86	0.098 65	6.976 58	0.295 95
BANFF; BeRPA B	0.117 434	6.9248	−0.448 374	6.9456	−0.149 46	6.966 39	0.149 46	6.987 18	0.448 374
BANFF; BeRPA D	0.127 806	6.923 23	−0.470 98	6.945 07	−0.156 99	6.966 91	0.156 99	6.988 76	0.470 98
BANFF; BeRPA E	0.354 515	6.953 69	−0.033 073 6	6.955 06	−0.013 489	6.956 93	0.013 489	6.958 81	0.040 466 6
BANFF; Shape; 2p2h	0.338 124	6.909 88	−0.662 967	6.932 94	−0.331 47	6.982 02	0.374 12	7.014 03	0.834 343
BANFF; Norm; 2p2h C to O	0.161 427	6.862 34	−1.346 41	6.924 78	−0.4488	6.987 21	0.4488	7.049 65	1.346 41
SKDet + FSI/SI 0; E_{reco}(0.30 - 0.80)GeV; Osc. ν_e CC ($MultiR_e$); MultiRing	0.248 951	4.116 61	−40.8193	6.009 53	−13.606	7.902 46	13.606	9.795 38	40.8193
SKDet + FSI/SI 1; E_{reco}(0.80 - 1.25)GeV; Osc. ν_e CC ($MultiR_e$); MultiRing	0.214 994	5.8806	−15.46	6.597 53	−5.1533	7.314 46	5.1533	8.031 39	15.46
SKDet + FSI/SI 2; E_{reco}(0.30 - 0.80)GeV; $\nu_\mu/\bar{\nu}_\mu$ CC ($MultiR_e$); MultiRing	0.507 403	6.789 88	−2.388 12	6.900 62	−0.796 04	7.011 37	0.796 04	7.122 11	2.388 12
SKDet + FSI/SI 3; E_{reco}(0.80 - 1.25)GeV; $\nu_\mu/\bar{\nu}_\mu$ CC ($MultiR_e$); MultiRing	0.236 118	6.9201	−0.516 076	6.944 03	−0.172 03	6.967 96	0.172 03	6.991 89	0.516 076
SKDet + FSI/SI 4; E_{reco}(0.30 - 0.80)GeV; $\nu_e/\bar{\nu}_e$ CC ($MultiR_e$); MultiRing	0.244 289	6.6652	−4.180 41	6.859 06	−1.3935	7.052 92	1.3935	7.246 78	4.180 41
SKDet + FSI/SI 5; E_{reco}(0.80 - 1.25)GeV; $\nu_e/\bar{\nu}_e$ CC ($MultiR_e$); MultiRing	0.234 55	6.5674	−5.586 39	6.826 46	−1.8621	7.085 52	1.8621	7.344 58	5.586 39
SKDet + FSI/SI 6; E_{reco}(0.30 - 0.80)GeV; all NC ($MultiR_e$); MultiRing	0.983 178	6.165 29	−11.3673	6.692 42	−3.7891	7.219 56	3.7891	7.7467	11.3673
SKDet + FSI/SI 7; E_{reco}(0.80 - 1.25)GeV; all NC ($MultiR_e$); MultiRing	0.523 609	6.783 29	−2.482 74	6.898 43	−0.827 58	7.013 56	0.827 58	7.128 69	2.482 74
SK energy scale	0.024	6.955 99	$-1.276\,85 \times 10^{-14}$	6.955 99	1.2769×10^{-14}	6.955 99	0	6.955 99	$1.276\,85 \times 10^{-14}$

Table B.10: $\pm1\sigma$ and $\pm3\sigma$ effect of the systematic parameters on the total number of e-like Super-K events with one decay electron with Run 1-8 POT for neutrino mode post-BANFF Asimov data set A. Only the systematic parameters which affect this sample are shown.

Appendix C

Marginalisation studies

The increase in sensitivity to δ_{CP} provided by a doubling of FHC statistics in Run 1-8 relative to Run 1-7c has made sampling of the tails of oscillation parameters (particularly $\sin^2\theta_{13}$) more significant for 1D fits. In previous analyses all fits were performed with 10K marginalisation toys, but in the present analysis this is no longer sufficient to ensure that fits return consistent results for independent sets of marginalisation toys. One can see the nature of the problem in fig. C.1, in which five independent sets of 10K marginalisation toys were fitted under the Asimov A oscillation parameter hypothesis without the reactor constraint; a large spread in $\Delta\chi^2$ contours is evident.

To determine a sufficient number of marginalisation toys to use checks of fit stability were carried out for different numbers of marginalisation toys. Figures C.2 to C.3 show the $\Delta\chi^2$ contours for the case of 40K and 80K marginalisation toys respectively. These studies indicate that good agreement among fits is achieved for 80K marginalisation toys 40k toys was found to be sufficient in the with reactor case due to the smaller marginalisation range for $\sin^2\theta_{13}$).

Further to the Asimov-based marginalisation studies, the stronger constraint seen in the data fits prompted a check of the data fit stability. Figures C.4 to C.4 show the result of fitting δ_{CP} with the reactor constraint for both normal and inverted hierarchy. Variations of $\Delta\chi^2 \sim 1$ are evident around the maximum in the region of $\delta_{CP} \sim \pi/2$, but that good stability is maintained in the preferred region and at the values of $\delta_{CP} = 0$ and π.

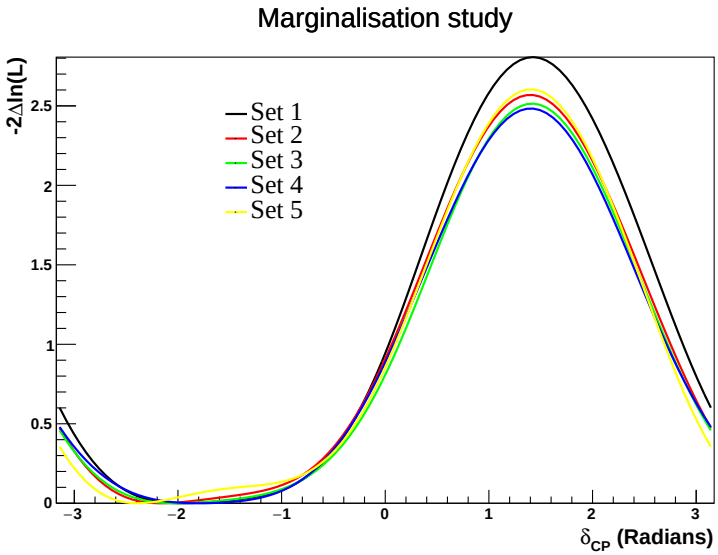

Figure C.1: Asimov A δ_{CP} normal hierarchy contours without reactor constraint for independent sets of 10K marginalisation toys

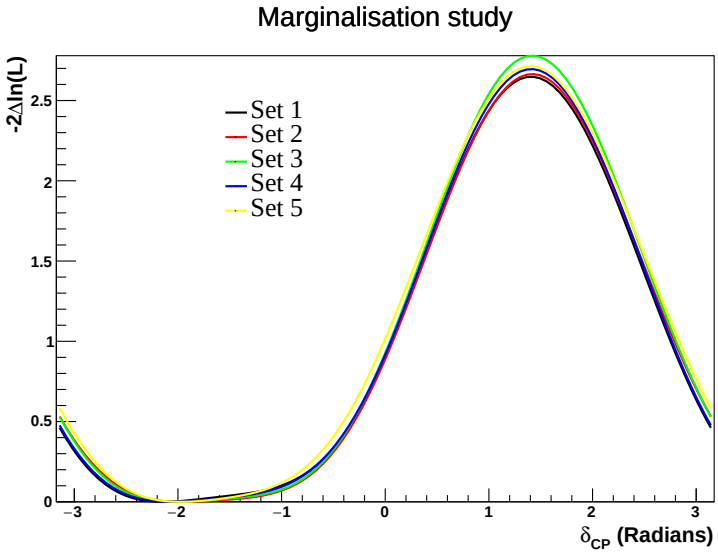

Figure C.2: Asimov A δ_{CP} normal hierarchy contours without reactor constraint for independent sets of 40K marginalisation toys

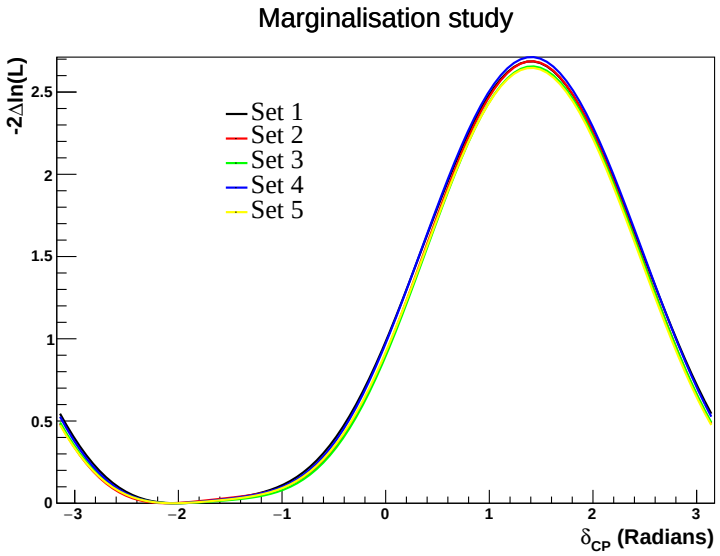

Figure C.3: Asimov A δ_{CP} normal hierarchy contours without reactor constraint for independent sets of 80K marginalisation toys

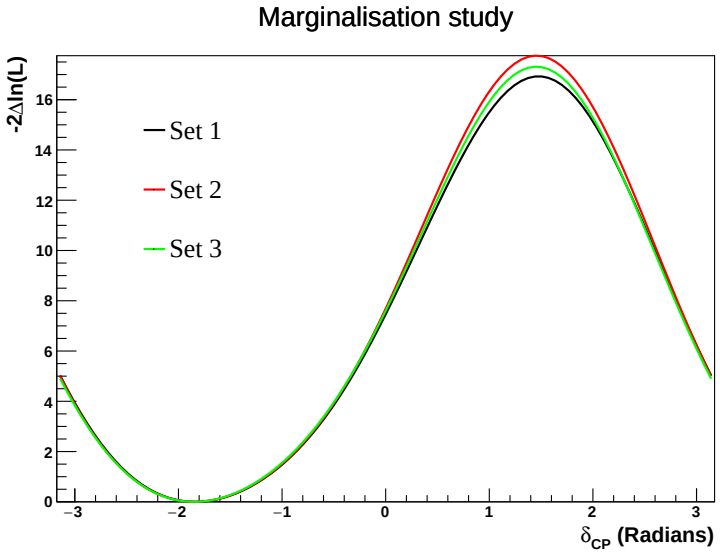

Figure C.4: Data fit of δ_{CP} normal hierarchy contours with reactor constraint for independent sets of 40K marginalisation toys

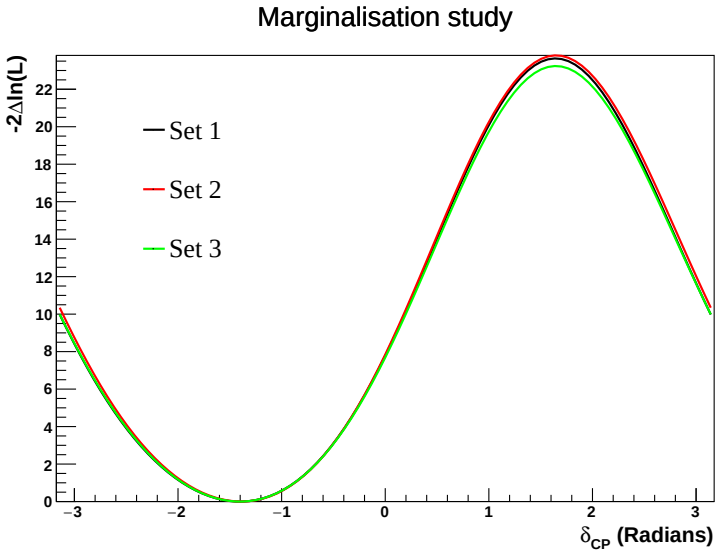

Figure C.5: Data fit of δ_{CP} inverted hierarchy contours with reactor constraint for independent sets of 40K marginalisation toys

Appendix D

Effect of systematic errors on Super-K predictions

	Pre-BANFF			Post-BANFF		
Group	Mean	1σ	%	Mean	1σ	%
SK Detector	-	-	-	269.11	5.01	1.86
SK FSI+SI+PN	-	-	-	268.38	5.91	2.20
Flux+Xsec constrained	250.34	35.35	14.12	266.68	8.60	3.22
$\sigma(\nu_e)/\sigma(\bar{\nu}_e)$	-	-	-	268.42	0.00	0.00
NC1γ	-	-	-	268.42	0.00	0.00
NC Other	-	-	-	268.42	0.67	0.25
Osc	-	-	-	268.42	0.09	0.04
All	250.95	35.71	14.23	267.78	11.79	4.40
All with osc	250.95	35.71	14.23	267.78	11.79	4.40

Table D.1: Average event rate and RMS error broken down by systematic parameter group for μ-like Super-K events with Run 1-8 POT for neutrino mode.

	Pre-BANFF			Post-BANFF		
Group	Mean	1σ	%	Mean	1σ	%
SK Detector	-	-	-	64.41	0.97	1.51
SK FSI+SI+PN	-	-	-	64.27	1.27	1.98
Flux+Xsec constrained	62.09	7.18	11.56	63.97	1.74	2.72
$\sigma(\nu_e)/\sigma(\bar{\nu}_e)$	-	-	-	64.28	0.00	0.00
NC1γ	-	-	-	64.28	0.00	0.00
NC Other	-	-	-	64.28	0.16	0.25
Osc	-	-	-	64.28	0.02	0.03
All	62.18	7.31	11.76	64.17	2.41	3.76
All with osc	62.18	7.31	11.76	64.17	2.41	3.76

Table D.2: Average event rate and RMS error broken down by systematic parameter group for μ-like Super-K events with Run 1-8 POT for antineutrino mode.

	Pre-BANFF			Post-BANFF		
Group	Mean	1σ	%	Mean	1σ	%
SK Detector	-	-	-	73.64	2.23	3.03
SK FSI+SI+PN	-	-	-	73.46	2.21	3.01
Flux+Xsec constrained	65.47	9.80	14.97	72.57	2.34	3.22
$\sigma(\nu_e)/\sigma(\bar{\nu}_e)$	-	-	-	73.46	1.93	2.63
NC1γ	-	-	-	73.76	0.80	1.08
NC Other	-	-	-	73.48	0.11	0.14
Osc	-	-	-	73.49	2.84	3.86
All	65.91	10.26	15.56	73.12	4.46	6.10
All with osc	65.92	10.57	16.03	73.14	5.32	7.27

Table D.3: Average event rate and RMS error broken down by systematic parameter group for e-like Super-K events with Run 1-8 POT for neutrino mode.

	Pre-BANFF			Post-BANFF		
Group	Mean	1σ	%	Mean	1σ	%
SK Detector	-	-	-	7.94	0.33	4.22
SK FSI+SI+PN	-	-	-	7.91	0.18	2.31
Flux+Xsec constrained	7.63	0.91	11.94	7.84	0.23	2.88
$\sigma(\nu_e)/\sigma(\bar{\nu}_e)$	-	-	-	7.91	0.12	1.46
NC1γ	-	-	-	7.98	0.21	2.59
NC Other	-	-	-	7.91	0.03	0.33
Osc	-	-	-	7.91	0.29	3.60
All	7.74	1.03	13.32	7.95	0.52	6.51
All with osc	7.74	1.07	13.79	7.96	0.59	7.44

Table D.4: Average event rate and RMS error broken down by systematic parameter group for e-like Super-K events with Run 1-8 POT for antineutrino mode.

	Pre-BANFF			Post-BANFF		
Group	Mean	1σ	%	Mean	1σ	%
SK Detector	-	-	-	7.02	1.17	16.69
SK FSI+SI+PN	-	-	-	6.92	0.79	11.43
Flux+Xsec constrained	7.71	0.91	11.79	6.91	0.28	4.05
$\sigma(\nu_e)/\sigma(\bar{\nu}_e)$	-	-	-	6.92	0.18	2.62
NC1γ	-	-	-	6.93	0.02	0.33
NC Other	-	-	-	6.92	0.07	0.98
Osc	-	-	-	6.92	0.26	3.78
All	7.79	1.85	23.71	7.00	1.47	20.94
All with osc	7.79	1.87	24.05	7.00	1.49	21.24

Table D.5: Average event rate and RMS error broken down by systematic parameter group for ν_e CC1π^+-like Super-K events with Run 1-8 POT for neutrino mode.

Appendix E

Effect of ν_e CC1π^+sample on constraint strength

Section 5.7 showed stronger than expected constraints from data for δ_{CP}, appearance and disappearance fits. To determine a potential explanation for this we chose to run an additional fit without the ν_e CC1π^+sample, hereafter creferred to as the 4-sample fit, with the fit using all samples being creferred to as the 5-sample fit. It should be noted that the full 5-sample marginalisation toys were used for all fits, rather than using 4-sample marginalisation toys for the 4-sample fit. This means that the correlations among samples for the 4-sample fit are not handled correctly, but the effect from this is expected to be small.

Figure E.1 shows comparisons of the aforementioned fits for normal hierarchy. It can be seen that the constraint on the δ_{CP} and appearance fits is weakened in the absence of the ν_e CC1π^+sample, while the disappearance contour is unaffected.

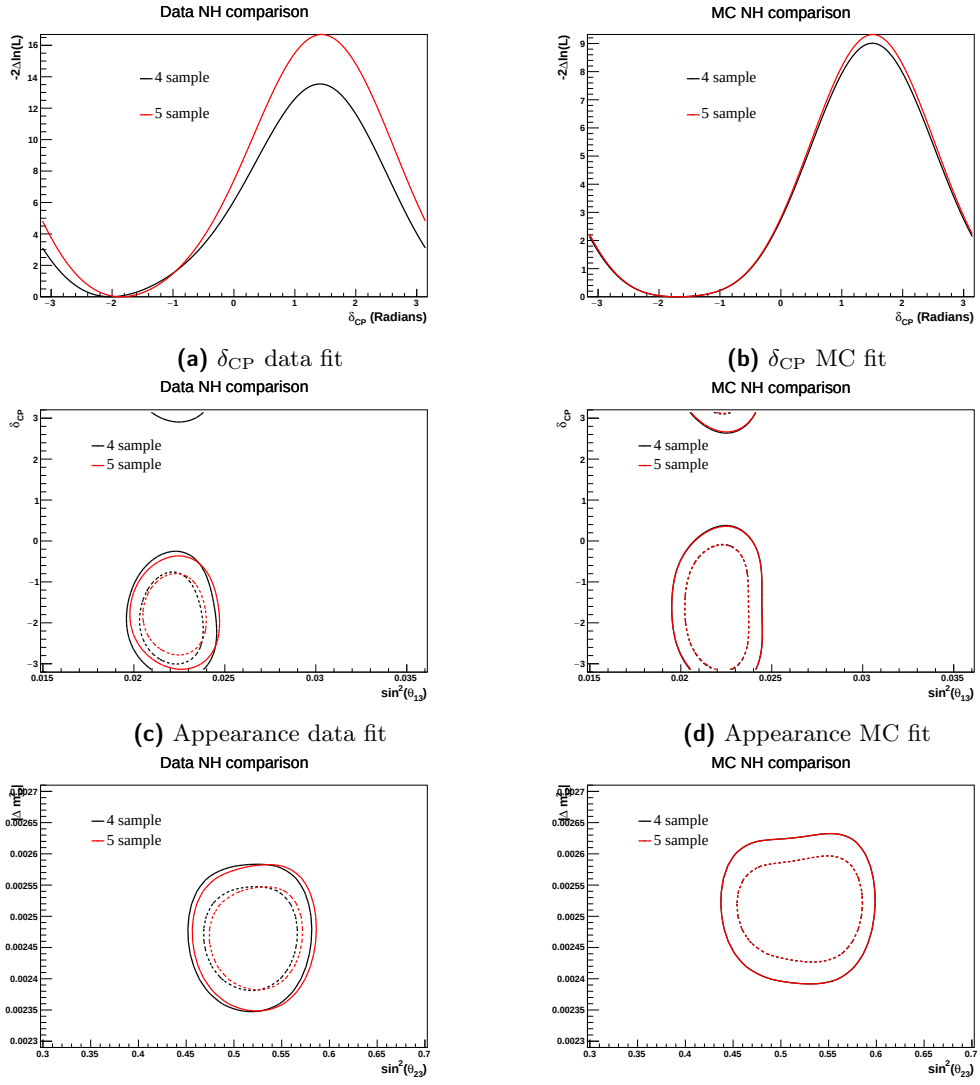

(a) δ_{CP} data fit

(b) δ_{CP} MC fit

(c) Appearance data fit

(d) Appearance MC fit

(e) Disappearance data fit

(f) Disappearance MC fit

Figure E.1: Fits of data and the Asimov A data set with four and five samples respectively.

Appendix F

Matter effects and crust density

To check the effect of the error on the average crust density [216] a number of fits of δ_{CP} were performed varying this value. Figures F.1 to F.2 show the effect of varying the average crust density between 2.5, 2.6 and 2.7 g cm^{-3} in normal and inverted hierarchy respectively. 1×10^4 marginalisation toys were generated with the average crust density fixed at the value of 2.6 g cm^{-3}, whilst fits were performed using the Asimov A data set where the crust density was varied using the aforementioned values. The effect on the fit of δ_{CP} can be seen to be small, supporting the use of a fixed value for the average crust density.

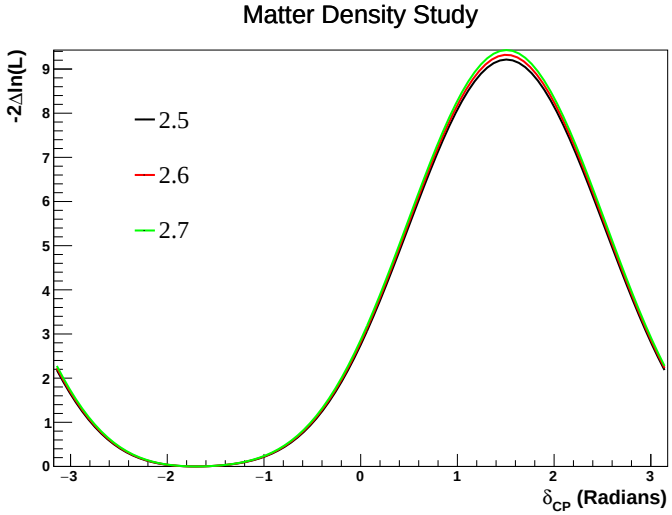

Figure F.1: Fits of δ_{CP} using the Asimov A data set whilst varying the average crust density in normal hierarchy for 10K marginalisation toys.

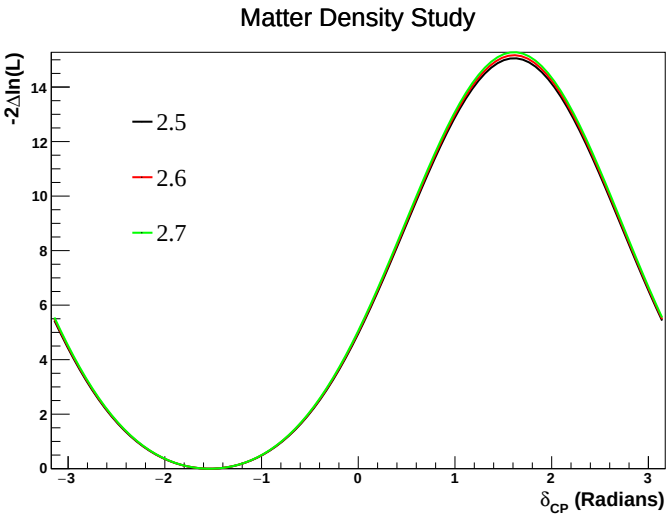

Figure F.2: Fits of δ_{CP} using the Asimov A data set whilst varying the average crust density in inverted hierarchy for 10K marginalisation toys.

Appendix G

Asimov B δ_{CP}/mass-hierarchy degeneracy

In section 5.6.1 it was noted that Asimov B fits are affected by a lack of sensitivity to distinguish $\delta_{CP} = 0$ and $\delta_{CP} = \pi$, for example, the fit of δ_{CP} shown in fig. 5.22 shows a best-fit point shifted away from the true value. fig. G.1 shows normalised one-ring e-like spectra for Asimov data set B with mass hierarchy and δ_{CP} varied to demonstrate the problem. It is clear from the plots that the spectrum for $\delta_{CP} = 0$ in normal hierarchy is similar in shape to the spectrum for $\delta_{CP} = \pi$ in inverted hierarchy and vice versa.

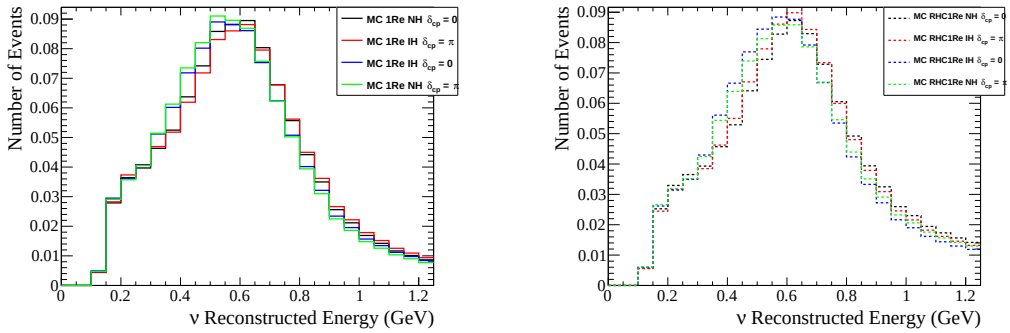

(a) MC one-ring FHC e-like spectra

(b) MC one-ring RHC e-like spectra

Figure G.1: Normalised spectra for one-ring e-like samples showing the effect of changing the mass hierarchy and true value of δ_{CP} for the Asimov B data set.

Bibliography

[1] M. E. Peskin and D. V. Schroeder. *An Introduction to Quantum Field Theory*. Addison-Wesley Reading, MA, 1995.

[2] M. Goldhaber, L. Grodzins, and A. W. Sunyar. "Helicity of Neutrinos". *Phys. Rev.* 109 (3 Feb. 1958), pp. 1015–1017.

[3] J. A. Formaggio and G. P. Zeller. "From eV to EeV: Neutrino Cross Sections Across Energy Scales". *Rev. Mod. Phys. 84, 1307 (2012)* (May 31, 2013). arXiv: `1305.7513v1 [hep-ex]`.

[4] E. Leader and E. Predazzi. *An Introduction to Gauge Theories and Modern Particle Physics*. Cambridge University Press, 1996.

[5] C. Andreopoulos et al. "The GENIE neutrino Monte Carlo generator". *Nuclear Instruments and Methods in Physics Research Section A: Accelerators, Spectrometers, Detectors and Associated Equipment* 614.1 (2010), pp. 87–104.

[6] E. Majorana. "Teoria simmetrica dell'elettrone e del positrone". *Il Nuovo Cimento (1924-1942)* 14.4 (Sept. 1937), pp. 171–184.

[7] C. Weinheimer. "KATRIN, a next generation tritium β decay experiment in search for the absolute neutrino mass scale". *Progress in Particle and Nuclear Physics* 48.1 (Jan. 2002), pp. 141–150.

[8] C. Kraus et al. "Final results from phase II of the Mainz neutrino mass search in tritium β decay". *The European Physical Journal C - Particles and Fields* 40.4 (Apr. 2005), pp. 447–468.

[9] V. N. Aseev et al. "Upper limit on the electron antineutrino mass from the Troitsk experiment". *Phys. Rev. D* 84 (11 Dec. 2011), p. 112003.

[10] KATRIN Collaboration. *KATRIN design report 2004*. 51.54.01; LK 01; Auch: NPI ASCR Rez EXP-01/2005; MS-KP-0501. Forschungszentrum, Karlsruhe, 2005. 245 pp.

[11] K. Assamagan et al. "Upper limit of the muon-neutrino mass and charged-pion mass from momentum analysis of a surface muon beam". *Phys. Rev. D* 53 (11 June 1996), pp. 6065–6077.

[12] KamLAND-Zen Collaboration, A. Gando et al. "Search for Majorana Neutrinos Near the Inverted Mass Hierarchy Region with KamLAND-Zen". *Phys. Rev. Lett.* 117 (8 Aug. 2016), p. 082503.

[13] GERDA Collaboration, M. Agostini et al. "Improved Limit on Neutrinoless Double-β Decay of ^{76}Ge from GERDA Phase II". *Phys. Rev. Lett.* 120 (13 Mar. 2018), p. 132503.

[14] CUORE Collaboration, C. Alduino et al. "First Results from CUORE: A Search for Lepton Number Violation via $0\nu\beta\beta$ Decay of ^{130}Te". *Phys. Rev. Lett.* 120 (13 Mar. 2018), p. 132501.

[15] CUORE Collaboration, K. Alfonso et al. "Search for Neutrinoless Double-Beta Decay of ^{130}Te with CUORE-0". *Phys. Rev. Lett.* 115 (10 Sept. 2015), p. 102502.

[16] E. Andreotti et al. "^{130}Te neutrinoless double-beta decay with CUORICINO". *Astroparticle Physics* 34.11 (2011), pp. 822–831.

[17] EXO-200 Collaboration, J. B. Albert et al. "Search for Neutrinoless Double-Beta Decay with the Upgraded EXO-200 Detector". *Phys. Rev. Lett.* 120 (7 Feb. 2018), p. 072701.

[18] Majorana Collaboration, C. E. Aalseth et al. "Search for Neutrinoless Double-β Decay in ^{76}Ge with the Majorana Demonstrator". *Phys. Rev. Lett.* 120 (13 Mar. 2018), p. 132502.

[19] G. Ellis. "The Standard Cosmological Model: Achievements and Issues". *Foundations of Physics* (June 2018).

[20] Planck, N. Aghanim et al. "Planck 2018 results. VI. Cosmological parameters" (2018). arXiv: `1807.06209 [astro-ph.CO]`.

[21] A. G. Riess et al. "New Parallaxes of Galactic Cepheids from Spatially Scanning the Hubble Space Telescope : Implications for the Hubble Constant". *The Astrophysical Journal* 855.2 (2018), p. 136.

[22] ALEPH Collaboration, DELPHI Collaboration, L3 Collaboration, OPAL Collaboration, SLD Collaboration, LEP Electroweak Working Group, SLD Electroweak Group, SLD Heavy Flavour Group, S. Schael et al. "Precision electroweak measurements on the Z resonance". *Phys.Rept.* 427 (2006), pp. 257–454. arXiv: `hep-ex/0509008 [hep-ex]`.

[23] B. Kayser. "On the quantum mechanics of neutrino oscillation". *Phys. Rev. D* 24 (1 July 1981), pp. 110–116.

[24] L. Wolfenstein. "Neutrino oscillations in matter". *Physical Review D* 17.9 (May 1978), pp. 2369–2374.

[25] H. Nunokawa, S. Parke, and J. W. Valle. "CP violation and neutrino oscillations". *Progress in Particle and Nuclear Physics* 60.2 (Apr. 2008), pp. 338–402.

[26] C. Giunti and C. W. Kim. *Fundamentals of neutrino physics and astrophysics*. Oxford University Press, 2007.

[27] S. P. Mikheyev and A. Y. Smirnov. "Resonance Amplification of Oscillations in Matter and Spectroscopy of Solar Neutrinos". *Sov. J. Nucl. Phys.* 42 (1985), pp. 913–917.

[28] S. P. Mikheyev and A. Y. Smirnov. "Resonant amplification of ν oscillations in matter and solar-neutrino spectroscopy". *Il Nuovo Cimento C* 9.1 (Jan. 1986), pp. 17–26.

[29] S. Turck-Chièze and S. Couvidat. "Solar neutrinos, helioseismology and the solar internal dynamics". *Reports on Progress in Physics* 74.8 (July 2011), p. 086901.

[30] S. Turck-Chièze et al. "Solar Neutrino Emission Deduced from a Seismic Model". *The Astrophysical Journal Letters* 555.1 (2001), p. L69.

[31] B. T. Cleveland et al. "Measurement of the Solar Electron Neutrino Flux with the Homestake Chlorine Detector". *The Astrophysical Journal* 496.1 (1998), p. 505.

[32] K. S. Hirata et al. "Observation of ^{8}B solar neutrinos in the Kamiokande-II detector". *Phys. Rev. Lett.* 63 (1 July 1989), pp. 16–19.

[33] M. Cribier et al. "Results of the whole GALLEX experiment". *Nuclear Physics B - Proceedings Supplements* 70.1 (1999). Proceedings of the Fifth International Workshop on topics in Astroparticle and Underground Physics, pp. 284–291.

[34] F. Kaether et al. "Reanalysis of the Gallex solar neutrino flux and source experiments". *Physics Letters B* 685.1 (2010), pp. 47–54.

[35] SAGE Collaboration, J. N. Abdurashitov et al. "Measurement of the solar neutrino capture rate with gallium metal". *Physical Review C* 60.5 (5 Oct. 1999), p. 055801.

[36] Super-Kamiokande Collaboration, K. Abe et al. "Solar neutrino measurements in Super-Kamiokande-IV". *Phys. Rev. D* 94 (5 Sept. 2016), p. 052010.

[37] G. Alimonti et al. "The Borexino detector at the Laboratori Nazionali del Gran Sasso". *Nuclear Instruments and Methods in Physics Research Section A: Accelerators, Spectrometers, Detectors and Associated Equipment* 600.3 (2009), pp. 568–593.

[38] G. Bellini et al. "Neutrinos from the primary proton–proton fusion process in the Sun". *Nature* 512.7515 (Aug. 2014), pp. 383–386.

[39] O. Y. Smirnov et al. "Measurement of neutrino flux from the primary proton–proton fusion process in the Sun with Borexino detector". *Physics of Particles and Nuclei* 47.6 (Nov. 2016), pp. 995–1002.

[40] Super-Kamiokande, S. Fukuda et al. "Determination of solar neutrino oscillation parameters using 1496 days of Super-Kamiokande I data". *Phys. Lett.* B539 (2002), pp. 179–187. arXiv: `hep-ex/0205075 [hep-ex]`.

[41] SNO Collaboration, B. Aharmim et al. "Electron energy spectra, fluxes, and day-night asymmetries of ^{8}B solar neutrinos from measurements with NaCl dissolved in the heavy-water detector at the Sudbury Neutrino Observatory". *Phys. Rev. C* 72 (5 Nov. 2005), p. 055502.

[42] Y. Fukuda et al. "Study of the atmospheric neutrino flux in the multi-GeV energy range". *Physics Letters B* 436.1 (1998), pp. 33–41.

[43] Super-Kamiokande Collaboration, Y. Fukuda et al. "Evidence for Oscillation of Atmospheric Neutrinos". *Phys. Rev. Lett.* 81.8 (8 Aug. 1998), pp. 1562–1567. eprint: `hep-ex/9807003`.

[44] IceCube Collaboration, M. G. Aartsen et al. "Determining neutrino oscillation parameters from atmospheric muon neutrino disappearance with three years of IceCube DeepCore data". *Phys. Rev. D* 91 (7 Apr. 2015), p. 072004.

[45] R. Abbasi et al. "The design and performance of IceCube DeepCore". *Astroparticle Physics* 35.10 (2012), pp. 615–624.

[46] IceCube PINGU, M. G. Aartsen et al. "Letter of Intent: The Precision IceCube Next Generation Upgrade (PINGU)" (2014). arXiv: `1401 . 2046 [physics.ins-det]`.

[47] H. Minakata et al. "Determining neutrino mass hierarchy by precision measurements in electron and muon neutrino disappearance experiments". *Phys. Rev. D* 74 (5 Sept. 2006), p. 053008.

[48] The KamLAND Collaboration, S. Abe et al. "Precision Measurement of Neutrino Oscillation Parameters with KamLAND". *Phys. Rev. Lett.* 100 (22 June 2008), p. 221803.

[49] CHOOZ, M. Apollonio et al. "Initial results from the CHOOZ long baseline reactor neutrino oscillation experiment". *Phys. Lett.* B420 (1998), pp. 397–404. arXiv: `hep-ex/9711002 [hep-ex]`.

[50] CHOOZ, M. Apollonio et al. "Search for neutrino oscillations on a long baseline at the CHOOZ nuclear power station". *Eur. Phys. J.* C27 (2003), pp. 331–374. arXiv: `hep-ex/0301017 [hep-ex]`.

[51] A. G. Piepke, S. Moser, and V. M. Novikov. "Development of a Gd loaded liquid scintillator for electron anti-neutrino spectroscopy". *Nuclear Instruments and Methods in Physics Research Section A: Accelerators, Spectrometers, Detectors and Associated Equipment* 432.2 (1999), pp. 392–398.

[52] F. Boehm et al. "Final results from the Palo Verde neutrino oscillation experiment". *Phys. Rev. D* 64 (11 Nov. 2001), p. 112001.

[53] The Double Chooz collaboration, Y. Abe et al. "Measurement of θ_{13} in Double Chooz using neutron captures on hydrogen with novel background rejection techniques". *Journal of High Energy Physics* 2016.1 (Jan. 2016), p. 163.

[54] Daya Bay Collaboration, F. P. An et al. "Measurement of electron antineutrino oscillation based on 1230 days of operation of the Daya Bay experiment". *Phys. Rev. D* 95 (7 Apr. 2017), p. 072006.

[55] RENO Collaboration, S. H. Seo et al. "Spectral measurement of the electron antineutrino oscillation amplitude and frequency using 500 live days of RENO data". *Phys. Rev. D* 98 (1 July 2018), p. 012002.

[56] MINOS, I. Ambats et al. *The MINOS Detectors Technical Design Report*. 1998.

[57] R. E. Kalman. "A New Approach to Linear Filtering and Prediction Problems". *Journal of Basic Engineering* 82.1 (1960), p. 35.

[58] N. S. Altman. "An Introduction to Kernel and Nearest-Neighbor Nonparametric Regression". *The American Statistician* 46.3 (1992), pp. 175–185. eprint: `https://www.tandfonline.com/doi/pdf/10.1080/00031305.1992.10475879`.

[59] NOvA Collaboration, M. A. Acero et al. "New constraints on oscillation parameters from ν_e appearance and ν_μ disappearance in the NOvA experiment". *Phys. Rev. D* 98 (3 Aug. 2018), p. 032012.

[60] LSND Collaboration, A. Aguilar et al. "Evidence for neutrino oscillations from the observation of $\overline{\nu}_e$ appearance in a $\overline{\nu}_\mu$ beam". *Phys. Rev. D* 64 (11 Nov. 2001), p. 112007. arXiv: `hep-ex/0104049 [hep-ex]`.

[61] MiniBooNE, A. A. Aguilar-Arevalo et al. "Observation of a Significant Excess of Electron-Like Events in the MiniBooNE Short-Baseline Neutrino Experiment" (2018). arXiv: `1805.12028 [hep-ex]`.

[62] MicroBooNE, LAr1-ND, ICARUS-WA104, R. Acciarri et al. "A Proposal for a Three Detector Short-Baseline Neutrino Oscillation Program in the Fermilab Booster Neutrino Beam" (2015). arXiv: `1503.01520 [physics]`.

[63] J. H. Christenson et al. "Evidence for the 2π Decay of the K_2^0 Meson". *Phys. Rev. Lett.* 13 (4 July 1964), pp. 138–140.

[64] The LHCb collaboration, R. Aaij et al. "Measurement of matter–antimatter differences in beauty baryon decays". *Nature Physics* 13 (Jan.), 391 EP -.

[65] A. D. Sakharov. "Violation of CP invariance, C asymmetry, and baryon asymmetry of the universe". *Soviet Physics Uspekhi* 34.5 (May 1991), pp. 392–393.

[66] R. Barbieri et al. "Baryogenesis through leptogenesis". *Nuclear Physics B* 575.1-2 (May 2000), pp. 61–77.

[67] C. S. Wu et al. "Experimental Test of Parity Conservation in Beta Decay". *Phys. Rev.* 105 (4 Feb. 1957), pp. 1413–1415.

[68] R. L. Garwin, L. M. Lederman, and M. Weinrich. "Observations of the Failure of Conservation of Parity and Charge Conjugation in Meson Decays: the Magnetic Moment of the Free Muon". *Phys. Rev.* 105 (4 Feb. 1957), pp. 1415–1417.

[69] G. Barenboim and J. Salvado. "Cosmology and CPT violating neutrinos". *Eur. Phys. J.* C77.11 (2017), p. 766. arXiv: 1707.08155 [hep-ph].

[70] C. Jarlskog. "Commutator of the Quark Mass Matrices in the Standard Electroweak Model and a Measure of Maximal CP Violation". *Phys. Rev. Lett.* 55 (1985), p. 1039.

[71] Particle Data Group, M. Tanabashi et al. "Review of Particle Physics". *Phys. Rev. D* 98 (3 Aug. 2018), p. 030001.

[72] I. Esteban et al. "Updated fit to three neutrino mixing: exploring the accelerator-reactor complementarity". *Journal of High Energy Physics* 2017.1 (Jan. 2017).

[73] F. Capozzi et al. "Global constraints on absolute neutrino masses and their ordering". *Phys. Rev. D* 95 (9 May 2017), p. 096014.

[74] *Proceedings, 27th International Conference on Neutrino Physics and Astrophysics (Neutrino 2016)*. Vol. 888. 1. 2017.

[75] T2K, K. Abe et al. "The T2K Experiment". *Nucl. Instrum. Meth.* A659 (2011), pp. 106–135. arXiv: 1106.1238 [physics.ins-det].

[76] H. Hotchi et al. "Achievement of a low-loss 1-MW beam operation in the 3-GeV rapid cycling synchrotron of the Japan Proton Accelerator Research Complex". *Physical Review Accelerators and Beams* 20.6 (June 2017).

[77] M. Friend. "J-PARC accelerator and neutrino beamline upgrade programme". *J. Phys. Conf. Ser.* 888.1 (2017), p. 012042.

[78] S. Bhadra et al. "Optical transition radiation monitor for the T2K experiment". *Nuclear Instruments and Methods in Physics Research Section A: Accelerators, Spectrometers, Detectors and Associated Equipment* 703 (Mar. 2013), pp. 45–58.

[79] T2K, T. Sekiguchi et al. "Development and operational experience of magnetic horn system for T2K experiment". *Nucl. Instrum. Meth.* A789 (2015), pp. 57–80. arXiv: 1502.01737 [physics.ins-det].

[80] T2K, K. Suzuki et al. "Measurement of the muon beam direction and muon flux for the T2K neutrino experiment". *PTEP* 2015.5 (2015), p. 053C01. arXiv: 1412.0194 [physics.ins-det].

[81] D. Beavis, A. Carroll, I. Chiang, et al. *Proposal of BNL AGS E-889*. Tech. Rep., BNL, 1995.

[82] UA1, J. Timmer. "The UA1 Detector". In: *ANTI-PROTON PROTON PHYSICS AND THE W DISCOVERY. PROCEEDINGS, INTERNATIONAL COLLOQUIUM OF THE CNRS, 3RD MORIOND WORKSHOP, LA PLAGNE, FRANCE, MARCH 13-19, 1983*. 1983, pp. 593–608.

[83] M. Yokoyama et al. "Application of Hamamatsu MPPCs to T2K neutrino detectors". *Nuclear Instruments and Methods in Physics Research Section A: Accelerators, Spectrometers, Detectors and Associated Equipment* 610.1 (Oct. 2009), pp. 128–130.

[84] S. Aoki et al. "The T2K Side Muon Range Detector (SMRD)". *Nucl. Instrum. Meth.* A698 (2013), pp. 135–146. arXiv: 1206.3553 [physics.ins-det].

[85] P.-A. Amaudruz et al. "The T2K fine-grained detectors". *Nuclear Instruments and Methods in Physics Research Section A: Accelerators, Spectrometers, Detectors and Associated Equipment* 696 (Dec. 2012), pp. 1–31.

[86] T2K Collaboration, S. Assylbekov et al. "The T2K ND280 Off-Axis Pi-Zero Detector". *Nucl. Instrum. Meth.* A686 (2012), pp. 48–63. arXiv: 1111.5030 [physics.ins-det].

[87] T2K UK, D. Allan et al. "The Electromagnetic Calorimeter for the T2K Near Detector ND280". *JINST* 8 (2013), P10019. arXiv: 1308.3445 [physics.ins-det].

[88] T2K Collaboration, K. Abe et al. "Measurements of the T2K neutrino beam properties using the INGRID on-axis near detector". *Nuclear Instruments and Methods in Physics Research Section A: Accelerators, Spectrometers, Detectors and Associated Equipment* 694 (Dec. 2012), pp. 211–223.

[89] S. Fukuda et al. "The Super-Kamiokande detector". *Nuclear Instruments and Methods in Physics Research Section A: Accelerators, Spectrometers, Detectors and Associated Equipment* 501.2-3 (Apr. 2003), pp. 418–462.

[90] C. Grupen and B. Shwartz. *Particle Detectors*. Cambridge University Press, 2008.

[91] T2K Collaboration, S. Berkman et al. *fiTQun: A New Reconstruction Algorithm for Super-K*. T2K-TN-146. 2013.

[92] A. D. Missert. "Improving the T2K Oscillation Analysis With fiTQun: A New Maximum-Likelihood Event Reconstruction for Super-Kamiokande". *Journal of Physics: Conference Series* 888 (Sept. 2017), p. 012066.

[93] E. Davies. *Computer and Machine Vision*. Elsevier, 2012.

[94] M. Shiozawa. "Reconstruction algorithms in the Super-Kamiokande large water Cherenkov detector". *Nuclear Instruments and Methods in Physics Research Section A: Accelerators, Spectrometers, Detectors and Associated Equipment* 433.1-2 (Aug. 1999), pp. 240–246.

[95] T2K Collaboration, R. Akutsu et al. *Super-Kamiokande events and data quality studies for T2K Run 8 Part I - fiTQun Samples*. T2K-TN-317. 2017.

[96] T2K Collaboration, K. Abe et al. "Indication of Electron Neutrino Appearance from an Accelerator-produced Off-axis Muon Neutrino Beam". *Phys.Rev.Lett.* 107 (2011), p. 041801. arXiv: 1106.2822 [hep-ex].

[97] T2K Collaboration, K. Abe et al. "Observation of Electron Neutrino Appearance in a Muon Neutrino Beam". *Physical Review Letters* 112.6 (Feb. 2014).

[98] T2K Collaboration, K. Abe et al. "Measurement of Muon Antineutrino Oscillations with an Accelerator-Produced Off-Axis Beam". *Physical Review Letters* 116.18 (May 2016).

[99] T2K Collaboration, K. Abe et al. "Measurement of neutrino and antineutrino oscillations by the T2K experiment including a new additional sample of νe interactions at the far detector". *Physical Review D* 96.9 (Nov. 2017).

[100] T2K Collaboration, K. Abe et al. "Search for short baseline ν_e disappearance with the T2K near detector". *Phys. Rev. D* 91 (5 Mar. 2015), p. 051102.

[101] T2K Collaboration, K. Abe et al. "Search for Lorentz and CPT violation using sidereal time dependence of neutrino flavor transitions over a short baseline". *Physical Review D* 95.11 (June 2017).

[102] T2K Collaboration, K. Abe et al. "First measurement of the muon neutrino charged current single pion production cross section on water with the T2K near detector". *Physical Review D* 95.1 (Jan. 2017).

[103] The T2K Collaboration, K. Abe et al. "Measurement of Coherent π^+ Production in Low Energy Neutrino-Carbon Scattering". *Phys. Rev. Lett.* 117 (19 Nov. 2016), p. 192501.

[104] T2K Collaboration, K. Abe et al. "Measurement of $\bar{\nu}_\mu$ and ν_μ charged current inclusive cross sections and their ratio with the T2K off-axis near detector". *Physical Review D* 96.5 (Sept. 2017).

[105] T2K Collaboration, K. Abe et al. "First measurement of the ν_μ charged-current cross section on a water target without pions in the final state". *Physical Review D* 97.1 (Jan. 2018).

[106] T2K Collaboration, K. Abe et al. "Measurement of the single π^0 production rate in neutral current neutrino interactions on water". *Phys. Rev. D* 97 (3 Feb. 2018), p. 032002.

[107] J. K. Ahn et al. "Observation of Reactor Electron Antineutrinos Disappearance in the RENO Experiment". *Physical Review Letters* 108.19 (May 2012).

[108] F. P. An et al. "Observation of Electron-Antineutrino Disappearance at Daya Bay". *Physical Review Letters* 108.17 (Apr. 2012).

[109] Y. Abe et al. "Indication of Reactor ν_eDisappearance in the Double Chooz Experiment". *Physical Review Letters* 108.13 (Mar. 2012).

[110] T2K Collaboration, K. Abe et al. "Sensitivity of the T2K accelerator-based neutrino experiment with an Extended run to 20×10^{21} POT" (July 27, 2016). arXiv: 1607.08004v1 [hep-ex].

[111] C. Giganti. "Latest results from T2K and T2K Phase II" (Mar. 30, 2018). arXiv: 1803.11513v1 [hep-ex].

[112] T. Mori. "Status of the Super-Kamiokande gadolinium project". *Nuclear Instruments and Methods in Physics Research Section A: Accelerators, Spectrometers, Detectors and Associated Equipment* 732 (Dec. 2013), pp. 316–319.

[113] J. F. Beacom and M. R. Vagins. "Antineutrino Spectroscopy with Large Water Čerenkov Detectors". *Physical Review Letters* 93.17 (Oct. 2004).

[114] C. Xu and the Super-Kamiokande Collaboration. "Current status of SK-Gd project and EGADS". *Journal of Physics: Conference Series* 718 (May 2016), p. 062070.

[115] G. Battistoni et al. "Overview of the FLUKA code". *Annals of Nuclear Energy* 82 (Aug. 2015), pp. 10–18.

[116] T. Böhlen et al. "The FLUKA Code: Developments and Challenges for High Energy and Medical Applications". *Nuclear Data Sheets* 120 (June 2014), pp. 211–214.

[117] T2K Collaboration, Beam Working Group. *Flux Release Summary.* T2K-TN-264v3. 2017.

[118] R. Brun et al. *GEANT: Detector Description and Simulation Tool; Oct 1994.* CERN Program Library. Long Writeup W5013. Geneva: CERN, 1993.

[119] C. Zeitnitz and T. A. Gabriel. "The GEANT-CALOR interface". In: *3rd International Conference on Calorimetry in High-energy Physics (Note: dates changed from Oct 6-9) Corpus Christi, Texas, September 29-October 2, 1992.* 1992, pp. 394–404.

[120] C. Zeitnitz and T. Gabriel. "The GEANT-CALOR interface and benchmark calculations of ZEUS test calorimeters". *Nuclear Instruments and Methods in Physics Research Section A: Accelerators, Spectrometers, Detectors and Associated Equipment* 349.1 (Sept. 1994), pp. 106–111.

[121] N. Abgrall et al. "NA61/SHINE facility at the CERN SPS: beams and detector system". *Journal of Instrumentation* 9.06 (June 2014), P06005–P06005.

[122] The NA61/SHINE Collaboration, N. Abgrall et al. "Measurements of cross sections and charged pion spectra in proton-carbon interactions at 31 GeV/c". *Phys. Rev. C* 84 (3 Sept. 2011), p. 034604. eprint: 1102.0983.

[123] NA61/SHINE Collaboration, N. Abgrall et al. "Measurement of production properties of positively charged kaons in proton-carbon interactions at 31 GeV/c". *Phys. Rev. C* 85 (3 Mar. 2012), p. 035210.

[124] NA61/SHINE Collaboration, N. Abgrall et al. "Measurements of production properties of K^0_S mesons and Λ hyperons in proton-carbon interactions at 31 GeV/c". *Phys. Rev. C* 89 (2 Feb. 2014), p. 025205.

[125] NA61/SHINE Collaboration, N. Abgrall et al. "Pion emission from the T2K replica target: Method, results and application". *Nuclear Instruments and Methods in Physics Research Section A: Accelerators, Spectrometers, Detectors and Associated Equipment* 701 (Feb. 2013), pp. 99–114.

[126] N. Abgrall et al. "Measurements of $\pi^{\pm}$ differential yields from the surface of the T2K replica target for incoming 31 GeV/c protons with the NA61/SHINE spectrometer at the CERN SPS". *The European Physical Journal C* 76.11 (Nov. 2016).

[127] NA61/SHINE Collaboration, A. Aduszkiewicz et al. "Measurements of total production cross sections for π^++C, π^++Al, K^++C, and K^++Al at 60 GeV/c and π^+ + C and π^+ + Al at 31 GeV/c". *Phys. Rev. D* 98 (5 Sept. 2018), p. 052001.

[128] T2K Collaboration, A. Fiorentini et al. *Flux Prediction and Uncertainty Updates with NA61 2009 Thin Target Data and Negative Focussing Mode Predictions.* T2K-TN-217. 2017.

[129] NA61/SHINE collaboration, N. Abgrall et al. "Measurements of $\pi^{\pm}$, $K^{\pm}$, K^0_S, Λ and proton production in proton-carbon interactions at 31 GeV/c with the NA61/SHINE spectrometer at the CERN SPS". *The European Physical Journal C, 76(2), 1-49 (2016)* (Oct. 9, 2015). arXiv: `1510.02703v2 [hep-ex]`.

[130] T2K Collaboration, N. Abgrall et al. *Neutrino flux prediction.* T2K-TN-038. 2011.

[131] T2K Collaboration, N. Abgrall et al. *Flux Prediction and Uncertainties for the 2012a Oscillation Analysis.* T2K-TN-099. 2013.

[132] Y. Hayato. "A neutrino interaction simulation program library NEUT". *Acta Phys. Polon.* B40 (2009), pp. 2477–2489.

[133] T2K Collaboration, Y. Hayato, S. Cao, and V. Nguyen. *The NEUT Neutrino Monte Carlo Generator: Physics and User Manual.* T2K-TN-351. 2018.

[134] T2K Collaboration, S. Bolognesi et al. *NIWG model and uncertainties for the 2017 oscillation analysis.* T2K-TN-315. 2017.

[135] J. Nieves, I. R. Simo, and M. V. Vacas. "Inclusive charged-current neutrino-nucleus reactions". *Physical Review C* 83.4 (Apr. 2011), p. 045501.

[136] S. Dulat et al. "New parton distribution functions from a global analysis of quantum chromodynamics". *Phys. Rev. D* 93 (3 Feb. 2016), p. 033006.

[137] C. H. Llewellyn Smith. "Neutrino Reactions at Accelerator Energies". *Phys. Rept.* 3 (1972), pp. 261–379.

[138] K. L. Miller et al. "Study of the reaction $\nu_\mu d \to \mu^- pp_s$". *Phys. Rev. D* 26 (3 Aug. 1982), pp. 537–542.

[139] S. J. Barish et al. "Study of neutrino interactions in hydrogen and deuterium: Description of the experiment and study of the reaction $\nu + d \to \mu^- + p + p_s$". *Phys. Rev. D* 16 (11 Dec. 1977), pp. 3103–3121.

[140] N. J. Baker et al. "Quasielastic neutrino scattering: A measurement of the weak nucleon axial-vector form factor". *Phys. Rev. D* 23 (11 June 1981), pp. 2499–2505.

[141] T. Kitagaki et al. "High-energy quasielastic $\nu_\mu n \to \mu^- p$ scattering in deuterium". *Phys. Rev. D* 28 (3 Aug. 1983), pp. 436–442.

[142] D. Allasia et al. "Investigation of exclusive channels in $\nu/\bar{\nu}$-deuteron charged current interactions". *Nuclear Physics B* 343.2 (Oct. 1990), pp. 285–309.

[143] C. Adamuščín et al. "Two-component model for the axial form factor of the nucleon". *Physical Review C* 78.3 (3 Sept. 2008), p. 035201.

[144] B. Bhattacharya, G. Paz, and A. J. Tropiano. "Model-independent determination of the axial mass parameter in quasielastic antineutrino-nucleon scattering". *Phys. Rev. D* 92 (11 Dec. 2015), p. 113011.

[145] B. Bhattacharya, R. J. Hill, and G. Paz. "Model-independent determination of the axial mass parameter in quasielastic neutrino-nucleon scattering". *Phys. Rev. D* 84 (7 Oct. 2011), p. 073006.

[146] M. Martini et al. "Unified approach for nucleon knock-out and coherent and incoherent pion production in neutrino interactions with nuclei". *Phys. Rev. C* 80 (6 Dec. 2009), p. 065501.

[147] M. Martini, M. Ericson, and G. Chanfray. "Neutrino quasielastic interaction and nuclear dynamics". *Phys. Rev. C* 84 (5 Nov. 2011), p. 055502.

[148] B. Mecking et al. "The CEBAF large acceptance spectrometer (CLAS)". *Nuclear Instruments and Methods in Physics Research Section A: Accelerators, Spectrometers, Detectors and Associated Equipment* 503.3 (May 2003), pp. 513–553.

[149] D. Rein and L. M. Sehgal. "Neutrino Excitation of Baryon Resonances and Single Pion Production". *Annals Phys.* 133 (1981), pp. 79–153.

[150] T2K Collaboration, P. de Perio et al. *NEUT Systematic Studies for 2010a Analysis*. T2K-TN-032. Version 1.0. 2011.

[151] T2K Collaboration, P. de Perio et al. *Cross section parameters for the 2012a oscillation analysis*. T2K-TN-108(v1.5). 2012.

[152] T2K Collaboration, A. Bercellie et al. *Cross section parameters for 2014 oscillation analysis*. T2K-TN-192. Version 2.2. 2015.

[153] A. Aguilar-Arevalo et al. "The MiniBooNE detector". *Nuclear Instruments and Methods in Physics Research Section A: Accelerators, Spectrometers, Detectors and Associated Equipment* 599.1 (2009), pp. 28–46.

[154] K2K Collaboration, A. Rodriguez et al. "Measurement of single charged pion production in the charged-current interactions of neutrinos in a 1.3 GeV wide band beam". *Phys. Rev. D* 78 (3 Aug. 2008), p. 032003.

[155] K. M. Graczyk and J. T. Sobczyk. "Form factors in the quark resonance model". *Phys. Rev. D* 77 (5 Mar. 2008), p. 053001.

[156] T2K Collaboration, T. Feusels et al. *Tuning of the NEUT Cascade Model using $\pi^\pm$-A Scattering External Data to Improve Final State Interaction and Secondary Interaction Systematic Uncertainties*. T2K-TN-325. Version 1.0. 2017.

[157] R. D. Woods and D. S. Saxon. "Diffuse Surface Optical Model for Nucleon-Nuclei Scattering". *Phys. Rev.* 95 (2 July 1954), pp. 577–578.

[158] DUET Collaboration, E. S. Pinzon Guerra et al. "Measurement of σ_{ABS} and σ_{CX} of π^+ on carbon by the Dual Use Experiment at TRIUMF (DUET)". *Phys. Rev. C* 95 (4 Apr. 2017), p. 045203.

[159] T2K Collaboration, P. de Perio et al. *Constraining the Flux and Cross Section Models with Data from the ND280 Detector for the 2012a Oscillation Analysis*. T2K-TN-106. Version 8.0. 2012.

[160] G. Cowan et al. "Asymptotic formulae for likelihood-based tests of new physics". *The European Physical Journal C* 71.2 (Feb. 2011), p. 1554. eprint: `arXiv:1007.1727`.

[161] NA61/SHINE Collaboration, N. Abgrall et al. *Measurements of $\pi^{\pm}$, $K^{\pm}$ and proton yields from the surface of the T2K replica target for incoming 31 GeV/c protons with the NA61/SHINE spectrometer at the CERN SPS*. arXiv:1808.04927. 54 pages, 55 figures. Geneva: CERN, Aug. 2018.

[162] T2K Collaboration, C. Giganti and M. Zito. *Particle Identification with the T2K TPC*. T2K-TN-001. Version v2. 2009.

[163] T2K Collaboration, C. Licciardi and M. Barbi. *Particle identification with the Fine Grained Detectors*. T2K-TN-103. 2012.

[164] T2K Collaboration, A. Hillairet et al. *ND280 Reconstruction*. T2K-TN-072. 2011.

[165] T2K Collaboration, V. Berardi et al. *CC $\bar{\nu}_\mu$ event selection in the ND280 tracker using Run 5c and Run 6 anti-neutrino beam data*. T2K-TN-246. Version 1.0. 2015.

[166] T2K Collaboration, V. Berardi et al. *CC ν_μ background event selection in the ND280 tracker using Run 5c and Run 6 anti-neutrino beam data*. T2K-TN-248. Version 1.2. 2015.

[167] T2K Collaboration, P. Bartet et al. *ν_μ CC event selections in the ND280 tracker using Run 2+3+4 data*. T2K-TN-212. Version 2.1.1. 2015.

[168] T2K Collaboration, S. Bienstock et al. *Constraining the Flux and Cross Section Models with Data from the ND280 Detector using FGD1 and FGD2 for the 2017 Joint Oscillation Analysis*. T2K-TN-324. Version 3. 2017.

[169] T2K Collaboration, A. Missert. *Fit to Super-K Atmospheric Neutrino Data for Optimization of the fiTQun Fiducial Volume Cuts and Estimation of Detector Uncertainties*. T2K-TN-318. 2017.

[170] A. M. Ankowski, O. Benhar, and M. Sakuda. "Improving the accuracy of neutrino energy reconstruction in charged-current quasielastic scattering off nuclear targets". *Phys. Rev.* D91.3 (2015), p. 033005. arXiv: `1404.5687 [nucl-th]`.

[171] T2K Collaboration, K. Iwamoto et al. *Inelastic Single Pion Signal Study in Electron Neutrino Appearance using Modified Decay Electron Cut*. T2K-TN-233. Version 0.5. 2016.

[172] T2K Collaboration, J. Kameda. *Updated study of the systematic error in ν_μ disappearance analysis from Super-Kamiokande*. T2K-TN-159v2. 2013.

[173] T2K Collaboration, M. Friend and M. Ikeda. *Future Sensitivity Task Force – Three Flavor Log Likelihood Fitter using a Realistic Systematic Error Covariance Matrix*. T2K-TN-151. Version 5.2. 2013.

[174] *Prob3++ 3-flavour oscillation probability software*. `http://webhome.phy.duke.edu/~raw22/public/Prob3++/`.

[175] T2K Collaboration, K. Duffy et al. *A Joint ND280-SK 1Rμ-SK 1Re fit of neutrino and antineutrino-mode data using MCMC*. T2K-TN-269. Version 3.2. 2016.

[176] T2K Collaboration, X. Li and M. Wilking. *FiTQun event selection optimization*. T2K-TN-319. 2017.

[177] T2K Collaboration, J. Imber et al. *T2K-SK Systematic Error Summary for the 2017 Oscillation Analysis*. T2K-TN-326. Version 1.2. 2017.

[178] W. K. Hastings. "Monte Carlo sampling methods using Markov chains and their applications". *Biometrika* 57.1 (Apr. 1970), pp. 97–109.

[179] C. J. F. T. Braak. "A Markov Chain Monte Carlo version of the genetic algorithm Differential Evolution: easy Bayesian computing for real parameter spaces". *Statistics and Computing* 16.3 (Sept. 2006), pp. 239–249.

[180] T2K Collaboration, P. de Perio and J. Imber. *Super-K Systematic Uncertainties for RUN1-4 Joint ν_e + ν_μ Analyses*. T2K-TN-186. Version 4.0. 2014.

[181] T2K Collaboration, C. Andreopoulos et al. *T2K 7.482×10^{20}-POT FHC and 7.471×10^{20}-POT RHC (1-7c) Joint 3-Flavour $\nu_\mu/\bar{\nu}_\mu$ Disappearance and $\nu_e/\bar{\nu}_e$ Appearance Analysis with additional ν_e CC$1\pi^+$-like sample*. T2K-TN-306.

[182] T2K Collaboration, C. Andreopoulos et al. *T2K Neutrino and Anti-Neutrino 3-Flavour Joint Analysis of Run 1-6 (6.914×10^{20}-POT ν 4.011×10^{20}-POT $\bar{\nu}$), Run 1-7b (7.002×10^{20}-POT ν 7.471×10^{20}-POT $\bar{\nu}$) and Run 1-7c (7.482×10^{20}-POT ν 7.471×10^{20}-POT $\bar{\nu}$) data sets*. T2K-TN-266.

[183] T2K Collaboration, C. Andreopoulos et al. *T2K 3.23×10^{19}-POT Muon-Neutrino Disappearance Analysis*. T2K-TN-036(v4).

[184] T2K Collaboration, C. Andreopoulos et al. *T2K 1.431×10^{20}-POT Muon-Neutrino Disappearance Analysis*. T2K-TN-064(v3).

[185] T2K Collaboration, C. Andreopoulos et al. *T2K 1.431×10^{20}-POT 3-Flavour Muon-Neutrino Disappearance Analysis*. T2K-TN-087(v1).

[186] T2K Collaboration, C. Andreopoulos et al. *T2K 3.010×10^{20}-POT 3-Flavour Muon-Neutrino Disappearance Analysis*. T2K-TN-141(v10).

[187] T2K Collaboration, C. Andreopoulos et al. *T2K 3.010×10^{20}-POT Joint 3-Flavour Oscillation Analysis*. T2K-TN-154(v3).

[188] T2K Collaboration, C. Andreopoulos et al. *T2K 6.57×10^{20}-POT 3-Flavour Muon-Neutrino Disappearance Analysis*. T2K-TN-183(v3).

[189] T2K Collaboration, C. Andreopoulos et al. *T2K 6.57×10^{20}-POT Joint 3-Flavour Oscillation Analysis*. T2K-TN-175.

[190] T2K Collaboration, C. Andreopoulos et al. *T2K 2.315×10^{20}-POT 3-Flavour Muon-Antineutrino Disappearance Analysis*. T2K-TN-243.

[191] T2K Collaboration, C. Andreopoulos et al. *T2K 4.0108×10^{20}-POT 3-Flavour Electron-Antineutrino Appearance Analysis*. T2K-TN-252.

[192] R. D. Cousins and V. L. Highland. "Incorporating systematic uncertainties into an upper limit". *Nucl. Instrum. Meth.* A320 (1992), pp. 331–335.

[193] G. Cowan. *Statistical Data Analysis*. Oxford University Press, Oxford, 1998.

[194] T2K Collaboration, Beam Working Group. *Flux tuning (13a v2)*.

[195] W. Press et al. *Numerical Recipes 3rd Edition: The Art of Scientific Computing*. Cambridge University Press, 2007.

[196] G. J. Feldman and R. D. Cousins. "Unified approach to the classical statistical analysis of small signals". *Physical Review D* 57.7 (Apr. 1998), pp. 3873–3889.

[197] T2K Collaboration, D. Sgalaberna. *Proposal for Feldman & Cousins method*.

[198] Particle Data Group, C. Patrignani et al. "Review of Particle Physics". *Chin. Phys.* C40.10 (2016), p. 100001.

[199] Particle Data Group, K. Olive et al. "Review of Particle Physics". *Chin.Phys.* C38 (2014), p. 090001.

[200] T2K Collaboration, K. Abe et al. "Measurements of neutrino oscillation in appearance and disappearance channels by the T2K experiment with 6.6×10^{20} protons on target". *Physical Review D* 91.7 (Apr. 2015).

[201] T2K Collaboration, S. Bolognesi et al. *Updates to T2KReWeight for the 2017 analysis*. T2K-TN-309.

[202] T2K Collaboration, Y. Nishimura and H.-K. Tanaka. *Super-K systematic uncertainties for the ν_e analysis with T2K 6.393$\times 10^{20}$ POT (RUN1-4) data*. T2K-TN-157v2. 2013.

[203] T2K Collaboration, P. de Perio et al. *Pion Hadronic Secondary Interactions in Super-Kamiokande*. T2K-TN-105(v1.1). 2012.

[204] T2K Collaboration, R. T. Patrick de Perio Yoshinari Hayato. *NEUT Nuclear Effects (FSI)*. T2K-TN-033(v2.0). 2012.

[205] T2K Collaboration, J. Hignight et al. *Super-Kamiokande events and data quality studies for T2K Run4*. T2K-TN-148(v2r3). 2013.

[206] K. Olive. "Review of Particle Physics". *Chinese Physics C* 40.10 (Oct. 2016), p. 100001.

[207] T2K Collaboration, K. Duffy et al. *A Joint ND280-SK 1R_μ-SK 1R_e fit of neutrino and antineutrino-mode data using MCMC*. T2K-TN-320. 2017.

[208] T2K Collaboration, K. Abe et al. "Search for CP Violation in Neutrino and Antineutrino Oscillations by the T2K Experiment with 2.2×10^{21} Protons on Target". *Phys. Rev. Lett.* 121 (17 Oct. 2018), p. 171802.

[209] P. Fernández and Super-Kamiokande collaboration. "Benefits of Gd for High Energy Neutrinos in SuperK-Gd". *Journal of Physics: Conference Series* 888.1 (2017), p. 012054.

[210] P. Huber, M. Lindner, and W. Winter. "Simulation of long-baseline neutrino oscillation experiments with GLoBES: (General Long Baseline Experiment Simulator)". *Computer Physics Communications* 167.3 (2005), pp. 195–202.

[211] K. Abe et al. "Proposal for an Extended Run of T2K to 20×10^{21} POT" (2016). arXiv: 1609.04111 [hep-ex].

[212] Hyper-Kamiokande Working Group, K. Abe et al. "A Long Baseline Neutrino Oscillation Experiment Using J-PARC Neutrino Beam and Hyper-Kamiokande". In: 2014. arXiv: 1412.4673 [physics.ins-det].

[213] Hyper-Kamiokande, K. Abe et al. "Hyper-Kamiokande Design Report" (2018). arXiv: 1805.04163 [physics.ins-det].

[214] DUNE Collaboration, B. Abi et al. "The DUNE Far Detector Interim Design Report Volume 1: Physics, Technology and Strategies" (July 26, 2018). arXiv: 1807.10334v1 [physics.ins-det].

[215] DUNE Collaboration, R. Acciarri et al. "Long-Baseline Neutrino Facility (LBNF) and Deep Underground Neutrino Experiment (DUNE)" (Dec. 18, 2015). arXiv: 1512.06148v2 [physics.ins-det].

[216] K. Hagiwara, N. Okamura, and K.-i. Senda. "The earth matter effects in neutrino oscillation experiments from Tokai to Kamioka and Korea". *JHEP* 1109 (July 29, 2011), p. 082. arXiv: 1107.5857v2 [hep-ph].